MULTI-PHYSICS MODELING AND DESIGN OF SWITCHED RELUCTANCE MACHINES AND LARGE SYNCHRONOUS GENERATORS

A Dissertation
Presented to
The Academic Faculty

by

Sufei Li

In Partial Fulfillment
of the Requirements for the Degree
Doctor of Philosophy in the
School of Electrical and Computer Engineering

Georgia Institute of Technology
May 2019

COPYRIGHT © 2019 BY SUFEI LI

MULTI-PHYSICS MODELING AND DESIGN OF SWITCHED RELUCTANCE MACHINES AND LARGE SYNCHRONOUS GENERATORS

Approved by:

Dr. Thomas G. Habetler, Advisor
School of Electrical and Computer Engineering
Georgia Institute of Technology

Dr. J. Rhett Mayor
The George W. Woodruff School of Mechanical Engineering
Georgia Institute of Technology

Dr. Lukas Graber
School of Electrical and Computer Engineering
Georgia Institute of Technology

Dr. Lijun He
Global Research Center
General Electric

Dr. Maryam Saeedifard
School of Electrical and Computer Engineering
Georgia Institute of Technology

Date Approved: November 26, 2018

To my dear parents,

Jingdong Li and Yu Song,

for their unconditional and endless love and support.

ACKNOWLEDGEMENTS

First of all, I would like to give my deepest thanks to my advisor, Dr. Thomas G. Habetler. I am so honored to be one of the graduate students of such a scholar with a high reputation. His invaluable guidance, great personality and trust in my abilities allow me to explore my research freely. Particularly, I wish to express my sincerest gratitude to him for taking over the responsibilities as a Ph.D. research advisor upon the passing of my former advisor, Dr. Ronald G. Harley in October 2017. It would not have been possible for me to finish this doctoral dissertation without the encouragement and support from Dr. Habetler.

I would also like to give my deepest and special thanks to my former Ph.D. advisor, Dr. Ronald G. Harley, for his guidance and support to me during the first three years of my Ph.D. study. His profound knowledge, patience, rigorous attitude towards research, and perfect personality helped me make significant progress and improve my technical skills as a professional researcher. None of the achievements in this dissertation would be possible without him, and he will always live in my heart. I also wish to thank Dr. J. Rhett Mayor, for his long-term technical support and academic collaboration. Dr. Mayor sets up the communication bridge between the electric machine group and the corporate sponsor, and I benefit a lot from our teamwork. I also wish to express my thanks to the corporate sponsor for the financial support of my Ph.D. study.

I would also like to thank Prof. Maryam Saeedifard, Prof. Lukas Graber, and Dr. Lijun He for serving as my Ph.D. dissertation committee members and their insightful comments and suggestions.

It is honored for me to have worked with so many talented and exceptional fellow students at Georgia Tech. Among them, I wish to give my special thanks to the senior Ph.D. graduates Dr. Jie Dang, Dr. Lijun He, and Dr. Yi Deng, for their generous help in the first few years of my Ph.D. study, and the fellow students Shen Zhang, Cheng Gong, and Hang Shao for the helpful discussions and productive collaborations in my research.

My gratitude is also given to other fellow Ph.D. graduates and labmates, Nan Liu, Chen Jiang, Liang Du, Genyi Luo, Morteza Rezaee, Omer Lateef, Raeey Regassa, Yao Duan, Andrew Semidey, Noris A. Gallandat, and many more, for their friendship and support. The family members of Dr. Harley and Dr. Habetler, who gave me the courage to overcome the difficulties and face the challenges in my study and life, are gratefully acknowledged.

Most of all, I owe my greatest debt of gratitude to my parents, my dear Mom and Dad, who have been the source of love and courage throughout my life.

TABLE OF CONTENTS

LIST OF TABLES

LIST OF FIGURES

SUMMARY

Electric machines are primary energy conversion devices and therefore advances in electric machine design and manufacturing can significantly increase the efficiency and reduce the cost of industrial and residential energy systems. Electric machine design is a comprehensive process and generally involves the multi-physics modeling of the behaviors of machines and multi-objective optimization in terms of various specified performance indices. Among many types of electric machines, switched reluctance machines (SRMs) are gaining interests and have become a feasible alternative to conventional machines owing to the advantages of rigid structures, high reliability, the absence of permanent magnets, robustness, fast dynamic response, and low cost. On the other hand, in a power system, large synchronous generators (LSGs) are a major source of electrical energy production and their safe and stable operation is essential for the system stability. The modeling and optimization of SRMs and LSGs are research hot spots in the field of electric machine design.

The objective of the dissertation is to develop multi-physics models for SRMs and the end regions of LSGs, so as to further exploit effective and efficient methods for the design optimization that improve their torque, thermal performance, efficiency, stability and robustness. In particular, for SRMs, a generalized and fast analytical model based on Maxwell's equations and magnetic equivalent circuits (MECs) that predicts the electromagnetic (EM) behaviors of SRMs with arbitrary geometries, materials and current profiles is developed and validated by its finite-element analysis (FEA) counterpart and measured results; then, a hybrid thermal model combining 2-dimensional (2D) finite-

difference (FD) formulation and thermal circuits is applied to estimate the temperature based on the loss distribution calculated by the EM model. Based on the multi-physics model, the methods of design of experiments (DoE) and evolutionary algorithms are used for the multi-objective optimization (MOO) of SRMs. For the design of the end regions of LSGs, 3-dimensional (3D) EM and thermal models are constructed to estimate the magnetic field, loss density and temperature distributions in the end region with different structures and operating conditions and are verified by the agreement between the predicted and measured temperature values. To improve the computational efficiency, a harmonic quasi-3D FD formulation of the LSG end regions is developed that can provide acceptable solutions of the distributions of magnetic field and loss density within a short period of time and is thus an appropriate tool at the initial design stage. In addition, parametric studies are adopted to evaluate and investigate the influences of different design parameters of the LSG end regions, including the material and inner diameter of the press plate, the distance between the press plate and stator, metallic shield property, the stepped profile of end core packets, the assignment of end tooth slits, the angle of inclined armature end windings, and the relative axial lengths of the stator and rotor.

CHAPTER 1. INTRODUCTION

1.1 Background

Electric machines are primary energy conversion devices and therefore advances in electric machine design and manufacturing can significantly increase the efficiency and reduce the cost of industrial/residential energy systems.

Among various types of electric machines, switched reluctance machines (SRMs) are gaining interests owing to the advantages of rigid structures, high reliability, the absence of permanent magnets, robustness, fast dynamic response, and low cost. They become a feasible alternative to conventional electric machines in various applications. However, high torque ripple, high noise and vibrations are the critical drawbacks of SRMs. The optimization aiming at improving their performances has attracted attention. However, previous research efforts are mostly conducted to address only one performance index (PI), e.g., torque ripple, efficiency, torque density and acoustic noise. The implementation of multi-objective optimization (MOO) is necessary and such approaches have been investigated in recent years. One of the main issues with most existing MOO methods is that they only predict the electromagnetic (EM) behaviors based on SRM geometries, and as a result the control and thermal effects are not rigorously integrated. On the other hand, since they employ stochastic evolutionary methods that involve simulations for a huge number of design candidates coupled with a time-consuming finite element analysis (FEA) solver, the overall computational cost can be intensive. Therefore, developing a fast and generalized multi-physics model and efficient MOO algorithms is crucial for SRM design.

In a power system, large synchronous generators (LSGs) are a major source of electrical energy production and their safe and stable operation is essential for the system stability. A major issue in LSG design is that with the increasing capacity of LSGs, the

leakage magnetic flux due to the mmfs of armature and field end windings strengthens in the end region. This leakage flux leads to significant eddy current losses in the end metallic components, such as the press plate and finger plates. Moreover, the axial flux impinging normally to the core end lamination packets induces eddy currents that flow in the radial-tangential plane of these laminations, resulting in extra losses. The eddy current losses lead to partial overheating that can potentially damage the insulations between laminations thus threatening safe operation of LSGs. Accurately predicting the magnetic field, loss and temperature distributions in the end region and optimize the end structures to minimize the losses and make sure that the temperatures are within thermal limits is an essential aspect in LSG design.

1.2 Problem Statement

The objective of the proposed research is to develop the multi-physics models for SRMs and the end regions of LSGs, so as to further exploit fast and efficient methods for the design optimization that improve their performances and robustness. In particular, for SRMs, a generalized and fast analytical model based on Maxwell's equations and magnetic equivalent circuits (MECs) that predicts the EM behaviors of SRMs with arbitrary geometries, materials and current profiles is developed and validated by its FEA counterpart and measured results; then, a hybrid thermal model combining 2-dimensional (2D) finite-difference (FD) formulation and thermal circuits is applied to estimate the temperature based on the loss distribution calculated by the EM model. Based on the multi-physics model, the methods of design of experiments (DoE) and evolutionary algorithms are used for the MOO of SRMs. For LSGs, 3-dimensional (3D) EM and thermal models are constructed to estimate the magnetic field, loss and temperature distributions in the end region and are verified by the agreement between the predicted and measured temperature values. To improve the computational efficiency, a quasi-3D FD formulation of the LSG end regions is developed that can provide acceptable solutions within a short period of time

and is thus an appropriate tool at the initial design stage. In addition, parametric studies and MOO algorithms are adopted to evaluate and investigate different design concepts of the LSG end regions.

1.3 Dissertation Outline

The dissertation is organized as follows:

Chapter 2 presents a comprehensive literature review on the existing methods and techniques associated with the proposed research in this dissertation.

Chapter 3 proposes a generalized and fast-solving model that predicts the EM and thermal behaviors of an SRM with arbitrary materials, topologies and dimensions, which facilitates rapid evaluation of an SRM design and efficient optimization of SRMs.

Chapter 4 presents a comprehensive approach for the multi-objective design optimization of SRMs based on the multi-physics model described in Chapter 3.

Chapter 5 describes a 3D FEA method to estimate the magnetic field, loss and temperature distributions in the end region of large synchronous generators.

Chapter 6 carries out a systematic parametric study on the influences of various factors on the magnetic field and losses in the large generator end region based on the 3D FEA approach in Chapter 5.

Chapter 7 proposes a fast-solving quasi-3D-FD-formulation-based model of the end region of large generators that estimates the field and loss distributions in the end stator core, end metallic components and stator copper strands.

Chapter 8 summarizes the conclusions and contributions of the dissertation work and recommendations for future investigations.

CHAPTER 2. REVIEW OF LITERATURE

This chapter presents a literature review on the existing techniques associated with the work of this dissertation, including: 1) electromagnetic (EM) and thermal modeling methods for switched reluctance machines (SRMs); 2) single-objective and multi-objective optimization (MOO) approaches to improve the performances of SRMs; 3) multi-physics modeling methods for the end regions of large synchronous generators (LSGs); 4) design concepts of the end region of LSGs to enhance their thermal performance and reliability.

2.1 Electromagnetic and Thermal Modeling of SRMs

The first step in computing-aided design optimization of an SRM is to establish a general mathematical model that predicts the performances of SRMs. Two paramount criteria to evaluate the validity of a model are the accuracy and computational speed. The accuracy depends on the level of conformity of the behaviors of an SRM predicted by the model with the values of the corresponding real machine, while the computational speed is scaled by the simulation time for a single design given a specific set of machine parameters. Clearly, a compromise between the accuracy and rapidity of the simulation model should be accomplished for the design optimization of an SRM that requires the evaluation of multiple design candidates.

In traditional design procedures, only the magnetic behaviors of an SRM is emphasized without a comprehensive simulation of other physical fields, such as the temperature and mechanical stress distributions in an SRM. Overheating caused by the excessive losses can potentially impair the insulation materials between stator coils and laminations, while concentrated stress can lead to the deformation of stator/rotor structures, especially in high-speed SRMs. Safety margins of critical machine parameters, e.g., current density, are often employed to prevent overheating or overstress, which often leads to over-

or under-design with reduced performance or higher cost. Therefore, parallel simulation that couples different physical fields becomes popular in recent years. This section focuses on the overview of modeling techniques for two important physical fields in an SRM, the electromagnetic and thermal fields.

2.1.1 Electromagnetic Modelling Methods of SRMs

Accurate modeling of the electromagnetic (EM) behaviors of an SRM is the foundation for the design optimization or torque control. Typical indices include average torque, torque ripple, loss density and radial/tangential forces on stators/rotors. Generally, the model to predict the performance of an SRM system is given by:

$$\frac{d\psi}{dt} = V - Ri \tag{2.1}$$

where ψ is the flux linkage of a phase, V is the voltage applied to a phase winding, i is the phase current, R is the stator phase resistance, and t is the time. Obviously predicting the variation of ψ is the key to modeling the dynamic behaviors and thus the performance indices of an SRM. It is more difficult to describe the magnetic characteristics of an SRM than conventional three-phase electric machines since its flux linkage exhibits nonlinear relations with respect to both the rotor position and phase current, which naturally makes the modeling of the SRM by the first-order differential voltage equation (2.1) nonlinear. There are two primary causes for the nonlinearity of ψ: the airgap is inconsistently distributed in the peripheral direction due to the doubly salient poles of the stator and rotor, which leads to the dimensional variation of flux paths in the airgap and thus nonlinear relation between ψ and rotor position; an SRM usually operates in the magnetic saturation region to achieve a high torque density, rendering ψ nonlinear with respect to the phase current.

A number of studies have focused on the modeling of the EM characteristics in SRMs. These approaches of EM analyses are basically classified into numerical and analytical methods.

2.1.1.1 Numerical Methods

Numerical methods mainly include finite-element analysis (FEA) [1]-[9] and boundary element method (BEM) [10]-[16].

a) FEA: The FEA is a general and the most popular numerical analysis tool, since it can offer trustworthy EM analyses for almost any machine topologies and geometries without the assumptions imposed by analytical methods. The FEA subdivides the entire solution domain into small, simpler parts called finite elements, assembles the equations associated with each element into a larger system of algebraic equations, and yields approximate values of the unknowns at discrete number of points over the domain. Figure 2.1 shows a typical assignment of meshes with triangular elements in a 2-Dimensional finite element analysis for SRMs. The two most popular approaches to derive the finite element equations are the variational method and the Galerkin method, which is a special form of the method of weighted residuals (MWR) [1]. Because it is difficult or even impossible to obtain the variational expression in some particular cases of machinery analysis, the Galerkin approach is more popular due to the greater generality and is employed in most commercial FEA solvers.

The merits of the FEA for SRM design lie in the following aspects: the assignment of the elements is flexible and covers the entire solution domain, making it adaptable to any complex or irregular machine geometries; it can provide an accurate solution of the magnetic field distribution in the subdomains with inhomogeneous properties, e.g., the laminated core with anisotropic and nonlinear permeability, by applying iterative algorithms; the FEA system matrix is sparse, symmetric and diagonal dominant, which

facilitates faster solution algorithms and allows reduced memory occupation. However, when using the multi-objective optimization techniques that accommodate large parameter spaces, complex constraints and the evaluation of numerous design candidates for SRM design, including the evolutionary algorithms, rapidity becomes the primary criterion for the assessment of an analysis tool. The main drawback of the FEA when applied for optimization-based design is the need to volume-mesh the entire solution domain, which is generally a computationally expensive procedure. This obstacle is particularly salient when the volume-meshing is applied to structures with small dimensions, e.g., the airgap region of electric machines, which necessitates an extensive refinement of the mesh in the relevant regions and results in a large number of high-resolution elements. On the other hand, the predefined mesh cannot be modified substantially as machine geometry changes and remeshing the solution domain is required for each design. In addition, to improve the accuracy of field solution by performing FEAs, the number of elements in simulations can be remarkably large, which ultimately involves the inversion of a huge system matrix and brings about heavy computational workload to the analyses.

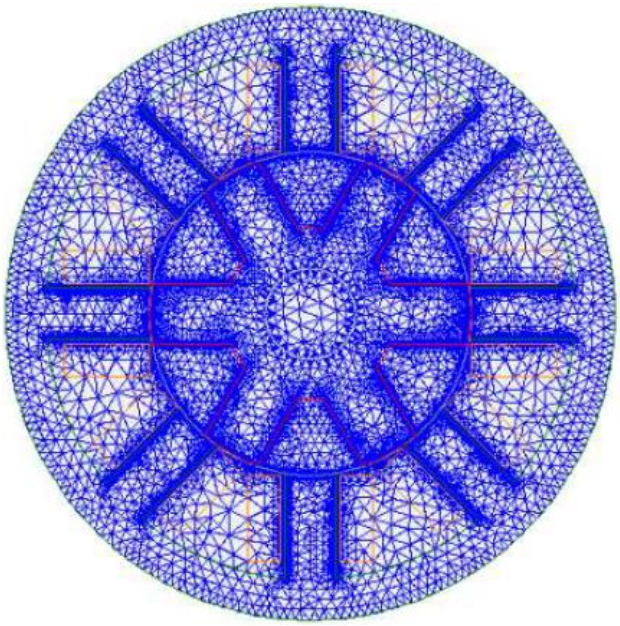

Figure 2.1 Meshing of the 2-D solution domain of an SRM.

Many techniques have been proposed to improve the rapidity of FEAs. A common method for 3-dimensional (3D) transient time-domain analyses is to apply **T**-Ω (electric vector potential – magnetic scalar potential) formulation in which the scalar potential Ω is normally represented by nodal shape functions in the entire domain while the vector potential **T** is restricted to the regions subject to eddy current conduction only [6]. It is much more efficient compared to **A**-φ (magnetic vector potential – electric scalar potential) formulation that includes the solution of all three components of vector potential **A** over the entire domain. The **T**-Ω formulation is particularly effective when analyzing SRMs, since the effects of the in-plane eddy currents in stator/rotor laminations can be represented by an additional equivalent field component and the terms associated with the vector potential **T** is eliminated in almost the entire domain [7]. With the rapid development of computer hardware and parallel computing algorithms in recent years, domain decomposition method (DDM) is a popular technique applied to improve the efficiency of FEAs for electric machine design [8]. In the DDM, the original large-scale problem is decomposed into many subdomain problems and then these subdomain problems are treated concurrently in parallel computing schemes using multiple processors to significantly reduce the total simulation time. Another form of matrix decomposition technique for the acceleration of transient FEAs, the time decomposition method (TDM) is proposed to solve the magnetic fields at all time steps simultaneously in parallel so as to achieve better scalability rather than to treat the time-domain problem sequentially one time-step by one time-step [9].

b) BEM: BEM is an alternative numerical method and has attracted growing interests in the field of the EM analysis of SRMs. In contrast to FEA formulations, BEM forms the boundary value problem (BVP) as integral equations with the boundary conditions approximated by certain basis functions, rather than differential equations with the unknowns solved throughout the entire space, and then uses the integral equations again to

calculate numerically the solution at any location in the interior of the solution domain in post-processing [13]. The benefit of BEM over FEA is that BEM only requires a surface mesh along the boundaries a volume mesh defined over the entire space, which averts the difficulty in the mesh generation for the airgap and reduces the dimensionality of the system matrix and thus the overall computational effort.

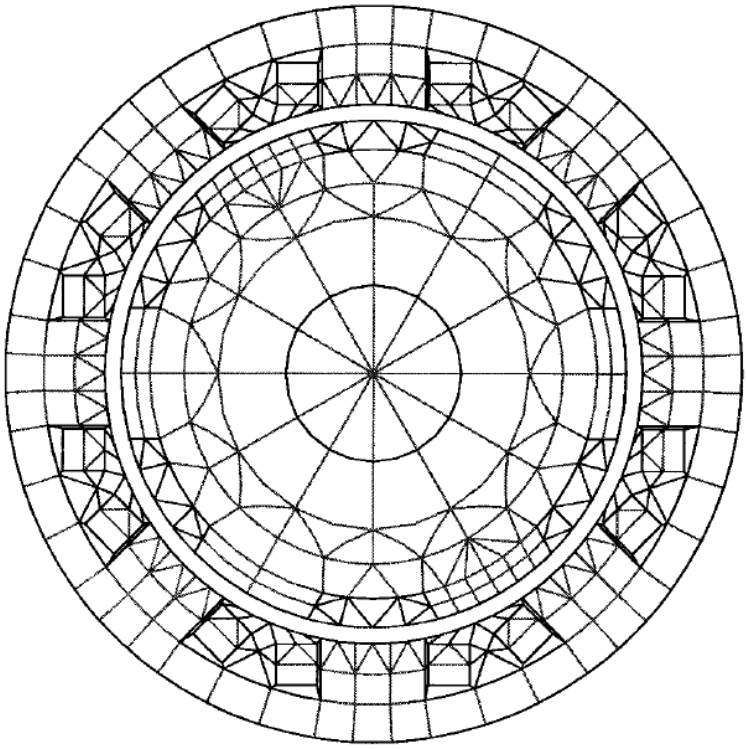

Figure 2.2 Finite element and boundary element meshes in an SRM [12].

The weaknesses of BEM lie in the following two aspects. The first is that the system matrix of BEM is dense and lacks symmetry and diagonal dominance [14]. The order of the required memory for the storage of the BEM system matrix and the computational complexity is $\mathcal{O}(N^2)$, compared to $\mathcal{O}(N)$ for FEA. Recent fast solver algorithms, such as the multilevel fast multipole algorithm, can reduce the system matrix storage and operational complexity to $\mathcal{O}(N\log N)$ [13]-[15]. The second weakness of BEM, which is also the paramount obstacle to its application in electric machine designs, is the lack of rigorous treatment of the effect of inhomogeneous material properties, e.g., nonlinear

permeability of stator/rotor steel [14]. The solution for the SRM EM analysis is the hybridization with approaches capable of nonlinear analysis, such as FEA [11], [12] and magnetic equivalent circuit (MEC) method [16]. As an example of hybridization between FEA and BEM, Fig. 1 shows the assignment of the meshes in the solution domain in [12]. In Figure 2.2, the homogeneous airgap ring is treated using BEM formulation, while the quadrangular FEA elements in the heterogeneous stator and rotor regions are defined separately. The uncoupling between the FEA solutions in the stator and rotor reduces the dimensionality of their system matrices and facilitates the nonlinear analysis, while the BEM applied to the airgap region avoids the mesh generation issues. The idea of the hybridization between BEM and MEC is similar in which the stator and rotor regions are formulated by reluctance circuits. Without the need to solve the FEA matrices, it can further save the computational effort at the expense of the detriment to the accuracy.

2.1.1.2 Analytical Methods

Compared to numerical methods, analytical models can significantly reduce the computational complexity without or with the reduced need to solve a high-dimension system matrix at the cost of lower accuracies due to the assumptions made to facilitate the analyses. The analytical methods can be generally classified into three categories: curve-fitting methods, MECs and Maxwell's-equation-based approaches.

a) Curve-fitting methods: Curve-fitting models approximate the variation of the phase inductance or flux linkage profile with respect to both phase current and rotor position with closed-form analytical functions, interpolation models, or computationally intelligent models based on the limited data collected from either FEAs or experiments. Fourier-series based model is a representative type of close-form functions to characterize the nonlinearity of the flux linkage of an SRM [17]-[21]. In [17], the flux linkages at three different rotor angles are estimated based on the recorded dc voltage and phase current

waveforms and then used to calculate the coefficients of a second-order Fourier series flux linkage model. Song *et al.* presented a similar second-order Fourier series flux linkage model determined by 21 measured data points from five rotor positions, which is then used to obtain the static torque characteristics of an SRM [18]. In [19], the coefficients of Fourier series with flexible terms are determined in terms of machine geometry-dependent flux linkage at aligned and unaligned positions, and the existence of inverse models makes the model suitable for real-time controller implementation. Chi *et al.* proposed a model built with only five data points in which the position dependency of the flux linkage is represented by a limited number of Fourier series terms and the variation of the flux linkage with stator current is expressed by an arc-tangent function [20]. Later in [21], Ding *et al.* proposed an extended Chi model which utilizes the first five components of Fourier series in expression of arctangent function dependent upon current to express the flux linkage curve and is built with only nine data points at five positions through experiment. There are several other classes of analytical functions adopted for the approximation of flux linkage profile of SRMs. In [22], the nonlinear variation of inductance with the phase current is expressed by means of polynomial functions. A least square data reduction algorithm is proposed in [23] to generate bivariate polynomials to express the flux linkage. Stephenson and Corda presented a model with a polynomial function in current and a cosine function in rotor position [24]. Roux and Sudhoff proposed an improved model in which the reciprocal of inductance is expressed as a polynomial of the flux linkage with the coefficients expressed by Fourier series of the rotor position, which incorporates the effects of mutual inductances in an SRM [25]. Xue *et al.* developed a model of magnetic characteristics that consists of 2-D orthogonal polynomials with the coefficients determined by the 2-D least squares method [26]. Compound functions including exponential terms to approximate the phase inductance are presented in [27], [28], and Loop *et al.* proposed a nonlinear average value model in [29].

The principle of interpolation models is to approximate the nonlinear flux linkage or inductance by appropriate piecewise interpolation functions based on the stored magnetic data. Xue *et al*. presented a 2-D bicubic spline interpolation function to describe the nonlinear magnetic behaviors in SRMs [30]. In [24], the flux linkage with respect to the phase current is interpolated using a quadratic interpolation method, while its relationship with the rotor position is expressed by a linear function for a specific current. Quadratic interpolation is also adopted in [31] to determine the relationship between the flux linkage and rotor position with certain specified current values. Bilinear-interpolation-based models are proposed in [32], [33].

In computationally intelligent schemes, the coefficients of the intelligent models that express the nonlinear nature of the flux linkage, such as the artificial neural network (ANN), are determined by training a larger number of given magnetic data obtained from either experiments or numerical methods. The accuracy of an intelligent model is highly associated with the size of the data for the training of the model coefficients and the structure of the model, e.g., the number of the neurons in the hidden layer of an ANN [34]. A 2-D B-spline neural network (BSNN) is designed in [35] to learn the nonlinear flux linkage characteristics of an SRM online and in real-time. Belfore and Arkadan developed an SRM model based on evolutionary neural networks (ENNs) [36]. Song *et al.* proposed a model in which the flux linkage characteristics are obtained by training support vector machine (SVM) with the measured few samples, and back-propagation neural network (BPNN) is adopted to describe the reconstructed flux linkage and calculated static torque characteristics [37].

Field reconstruction method (FRM) is a special type of curve-fitting approaches. Rather than model the flux linkage or inductance of an SRM, FRMs aim to compute the magnetic field at desired positions in an SRM by employing closed-form analytical functions based on the data collected from numerical analyses [38], [39]. Reference [38]

demonstrates an extended FRM that uses the snapshots of a limited number of magnetic field solutions from an FEA to develop the basis functions necessary to compute the magnetic field under arbitrary stator excitation and at any desired rotor position. In this model, a truncated Fourier series expansion dependent upon the rotor position is used to compute basis functions under unsaturated condition, while polynomial saturation multipliers associated with excitation current are applied to these Fourier coefficients in saturation condition to include the nonlinear effects of steel.

In general, the major advantage of curve-fitting methods applied to the design optimization of SRMs is that they can estimate the flux linkage profile or any magnetic behaviors of an SRM only based on a limited set of data obtained from either FEAs or experiments, so as to significantly reduce the computational efforts compared to pure numerical analyses which require a full set of data. The drawbacks of curve-fitting methods are the following: they are inherently empirical and heuristic, and there is no rigorous proof of their generality for an SRM with any type of topology or geometry; they only fit the curves of flux linkage or inductance rather than actually analyze the nature of the magnetic field in an SRM; they still require the data collected from FEAs, thus the computational complexity of curve-fitting methods is higher than the other analytical approaches without the need to solve large system matrices.

b) MEC: The MEC approach is a popular and powerful tool for the EM analysis and design of various electric machines [40]-[51]. The MEC is analogous to an electric circuit except that the voltage sources are replaced by the sources of magneto-motive force (mmf) generated by phase winding currents in an SRM, admittances are replaced by permeances of flux paths, and currents are replaced by fluxes in the permeance components [41]. Figure 2.3 and Figure 2.4 demonstrate the physical structure and the circuit diagram of the MEC of an 8/6 SRM when the rotor and excited stator poles partially overlap, respectively. In an MEC, each region of the machine is represented by a permeance/reluctance that is a

function of the permeability and geometry. Typically for the MEC of an SRM, the permeances/reluctances in the steel are nonideal and allowed to saturate, and separately assigned to represent the rotor/stator poles and yokes. The permeances in the air region are assumed to be ideal and are associated with three types of fluxes: the overlapping flux between rotor and excited stator poles, the fringing flux and the leakage flux [41]. The air-region permeances are determined by flux tube analysis and assumptions should be made on the geometries of the flux paths [40]. The topology of the MEC of an SRM usually changes with the rotor angle. One solution approach for an MEC is to solve the flux in each element, which is analogous to solving an electric circuit by using Kirchhoff's voltage law. A better and more popular method is to solve the magnetic scalar potential at each node in the MEC and determine the flux through every element based on its element and mmf drop, which resembles the solution of an electric circuit with Kirchhoff's current low. To incorporate the nonlinear effects of steel, an iterative process is required to update the permeances and flux densities in the stator and rotor elements [41].

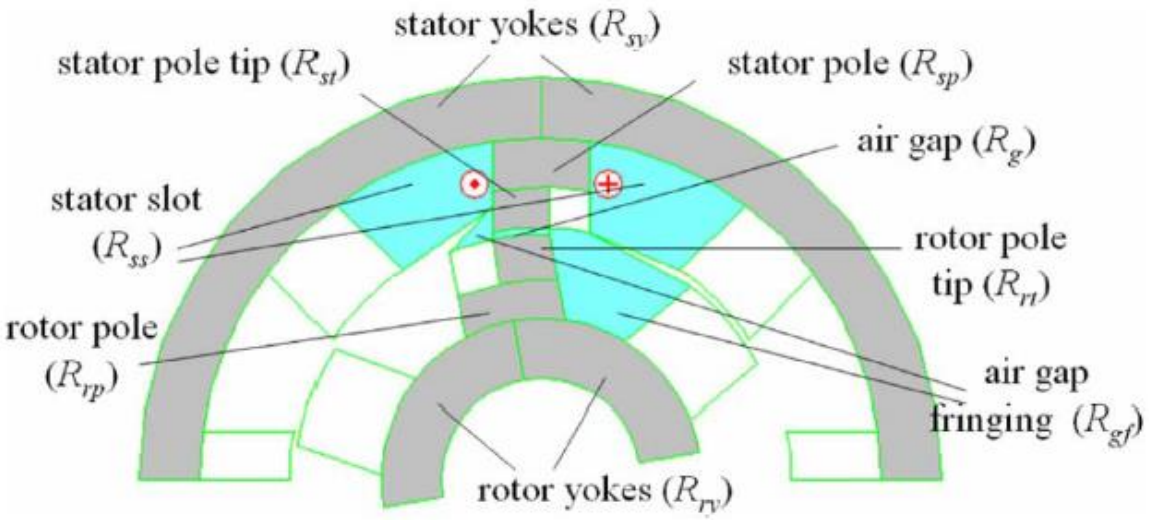

Figure 2.3 Physical structure of the magnetic circuit of an 8/6 SRM [40].

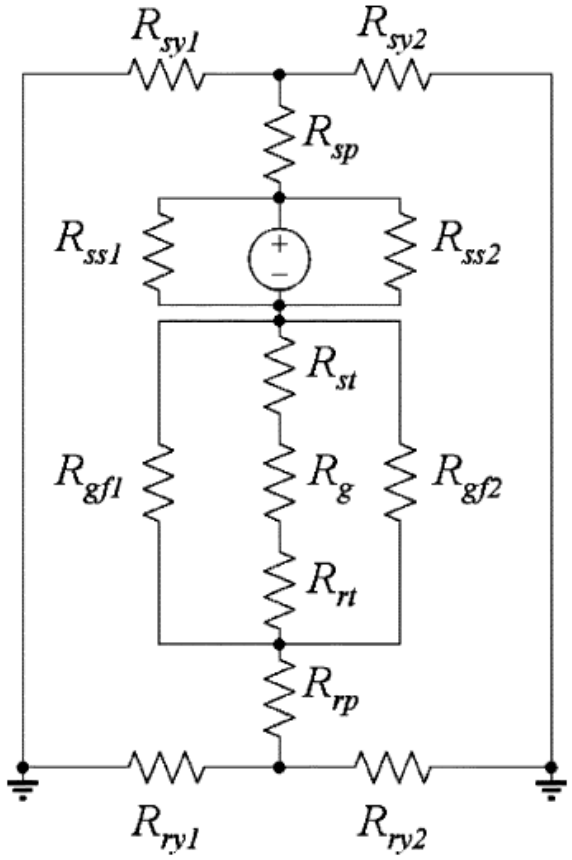

Figure 2.4 MEC of the SRM when the stator and rotor poles partially overlap [40].

The advantage of MEC methods is the highest computational speed, since the number of elements and thus the dimension of the system matrix in an MEC are smaller than numerical methods, and they do not need to solve the boundary conditions in the form of series in Maxwell's-equation-based methods, which is discussed in the following section. However, the assignment of the MEC structure of an SRM is empirical and different assumptions on the magnetic flux paths, especially the areas and lengths of fringing/leakage reluctances in the air region that are parametrically nonlinear, have to be selected for different rotor positions based on prior experiences obtained from FEA results, which confines their accuracy and generality applied to the analysis of SRMs with arbitrary geometries.

c) Maxwell's-equation-based methods: Unlike curve-fitting methods and MECs that aim to directly obtain the magnetic characteristics of an SRM, e.g., phase inductance and flux linkage, the methods in this category are capable of providing a detailed magnetic field analysis in an SRM based on Maxwell's equations. The formulation of Maxwell's equations is usually based on the magnetic scalar potential or vector potential that lead to a unique solution of the distributions of the unknowns and facilitate the definition of boundary conditions. The Laplace equation of the magnetic scalar potential can be used to simplify the analysis in non-conductive regions, while the Poisson equation of the magnetic vector potential should be applied to the regions with source or eddy currents [52], [53].

References [51], [54] present an approach to calculate the magnetic field in the air region and phase inductance of an SRM at the unaligned position. In [51], [54], the stator and rotor slots are reshaped into rectangular dimensions to simplify the analysis in Cartesian coordinates, and boundary conditions of the tangential flux on the edges of stator/rotor slots are defined separately to facilitate the solution of magnetic vector potential. This method is generalized to analyze the magnetic field at any rotor angle in [52] by assigning flexible boundary conditions of the airgap, rotor slot and stator slot sub-regions dependent on the rotor position, and the formulation is based on the polar coordinates to reduce the error caused by reshaping the stator and rotor slots. This method is further developed in [53] where the error introduced by the misrepresentation of the geometry is eliminated by employing conformal mappings individually in the stator/rotor slots. In [51]-[54], the assumption of consistent tangential field intensity on the boundaries between the stator and rotor slots is made to simplify the analysis. To eliminate the error caused by this assumption, [55], [56] propose to use conformal mapping for an air sub-region within a pole pitch that connects the stator and rotor slots, and periodic boundary condition is applied to the peripheral borders of the pole-pitch region. The drawback of this method is the significantly higher complexity due to the need to solve a set of high-order

transcendental equations associated with a larger number of vertices in the Schwarz-Christoffel transformation. The subdomain method in [57] establishes three sub-regions, and all Laplace and Poisson equations in the form of Fourier series in the peripheral direction are solved analytically with boundary conditions between sub-regions obtained from the continuity of the circumferential magnetic field intensity and vector potential in the interface.

The treatment of the nonlinear property of steel is a critical issue in the Maxwell's-equation-based methods because it is difficult to derive an accurate closed-form solution for a partial differential equation with an undetermined heterogeneous coefficient associated with nonlinear permeability. For this reason, only the magnetic field in the air region is solved based on Maxwell's equations in [51]-[56]. It is recommended in [47], [51], [55] that the solution of the magnetic field in the air region is substituted into an MEC which accommodates the effects of nonlinear of steel. In [57], the saturation in the stator/rotor poles is considered in the subdomain harmonic modeling through an iterative process, but the permeability in the stator/rotor yokes is assumed to be infinite and the nonuniform circumferential distribution of steel permeability in the poles is not modeled.

2.1.2 Thermal Modelling Methods of SRMs

Since the life of winding and lamination insulation materials is determined by the temperature rise, it is necessary to perform thermal analyses during the SRM design process to meet the requirement of insulation life and make the full utilization of the motor thermal limit or cooling capability. The methods for modeling the thermal conditions in electric machines include thermal circuit approaches and numerical techniques such as thermal FEA and computational fluid dynamics (CFD).

In a thermal circuit, different parts of the machine are represented as lumped parameters of inter-connected thermal resistors and capacitors. In the early studies of

thermal circuits, some resistances can be directly solved or experimentally measured. Simplified thermal resistance networks were proposed afterwards to reduce the formulation complexity for different exterior boundary conditions and machine topologies. The simplest thermal network uses three thermal resistances (frame, stator and rotor) that are calculated from experimental temperature and loss data. Extensive research is conducted in formulating the experimentally fit or analytically determined thermal resistance values for use in thermal circuits. Among the thermal-circuit based methods for SRMs, references [58]-[60] determine the heat distribution in SRMs for natural and forced cooling conditions. A lumped parameter transient thermal model during driving cycles is proposed in [61]. Figure 2.5 presents a typical thermal circuit network model for the transient analysis of an SRM.

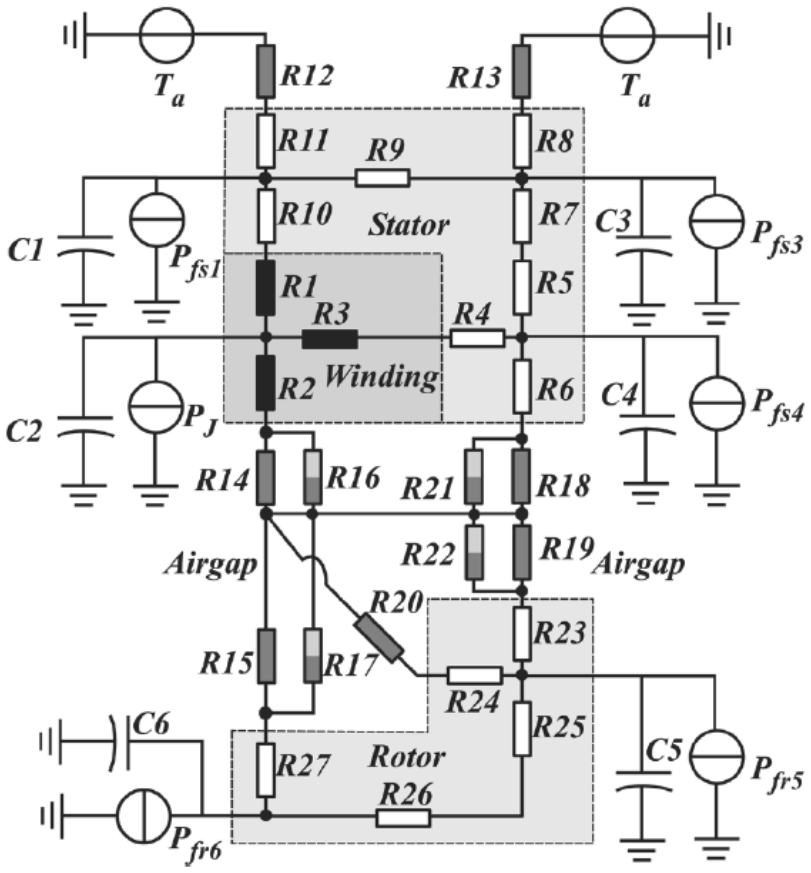

Figure 2.5 Lumped-parameter thermal circuit model of an SRM [61].

The thermal resistance network is computationally efficient, but the drawback is that its accuracy relies on the approximation of the thermal resistance parameters, making it a predictive model rather than a design tool due to the required calibration process. FEA tools that are independent of experimental data to model thermal transport have attracted significant interest from machine designers. FEA proves to possess the capability to accurately predict the temperature distribution in electric machines [62]-[64]. CFD is primarily utilized to find the heat transfer coefficients in different air/water coolant flow conditions for thermal circuits or FEAs, instead of the well-known heat transfer relationships [62]-[64]. FEA and CFD are geometrically generic and can accurately predict the temperature field in SRMs, but they generally require extended setup and computation times, which limits their integration into the EM design and optimization process.

References [65], [66] propose a hybrid method that combines a 2-D finite-difference (FD) numerical technique and a thermal circuit for temperature estimation to achieve a balance between the computational speed and accuracy. In [65], [66], the steady-state temperature distribution within a radial-peripheral cross-section in the center of an SRM is predicted by the 2-D FD method, and a thermal circuit is set up to determine the boundary conditions of the 2-D FD solution domain associated with the axial heat dissipation through the shaft, frame and end windings.

The coupling between the EM and thermal fields is an essential topic for the analysis of SRMs. The distribution of the copper and iron loss density obtained in an EM simulation is substituted into the thermal model as the heat source. Also, in the thermal analysis, the material properties of the copper, lamination steel and air are temperature-dependent. As the temperature increases, the copper/lamination steel resistivities, air conductivity and viscosity increase, while the air density decreases [67]. On the other hand, in the EM analysis, it is indispensable to incorporate the temperature-dependent resistivities of copper windings and steel into the calculation of the copper losses and

stator/rotor eddy current losses and update the thermal field backwards with iterations [66], [67].

2.2 Design Optimization of SRMs

2.2.1 Single-Objective Performance Improvement of SRMs

2.2.1.1 Torque Ripple

The torque ripple in SRMs is relatively higher than that in sinusoidal three-phase machines due to the doubly salient structures and the nonlinear discrete torque production mechanism. The torque-current-rotor position characteristic curve of the SRM and the current profile of individual stator phases determine the torque ripple in dynamic operation. Both electronic control approaches and machine electromagnetic design have been proposed to reduce the level of torque ripple in SRMs. Various techniques based on current control have been carried out to reduce the torque ripple, including introducing torque sharing functions (TSF) to coordinate the torque production of individual phases [68]-[71], linearization and decoupling techniques (LDTs) that linearize the SRM and load characteristics and decouple the control objectives for each phase [72], [73], optimum phase current profiling strategies [74]-[76], optimum harmonic current injection [77], direct torque control (DTC) schemes [78], [79], and wide-speed-range methods [71], [80]. Intelligent algorithms are also employed for optimizing the current profile, such as the iterative learning method [81], [82], neural-network-based techniques [83], [84], and adaptive fuzzy control schemes [85].

Shape optimization is also a common approach to reduce torque pulsation. Torque ripple minimization can be achieved by selecting appropriate rotor and stator diameters, pole arcs/shapes, stack length and the number of phases. Some special geometric designs for torque ripple minimization include introducing a notched tooth rotor in the forward

rotating direction [86] and a non-uniform air gap structure [87], [88]. Emadi *et al.* studied the effects of geometric points of molding pins in SRMs [89]. A new family of SRMs which have higher number of rotor poles than stator poles are also proposed in [90]. In [91], optimal design is achieved by neural-network method with finite-element (FE) simulation.

2.2.1.2 Acoustic Noise

The main source of acoustic noise is the radial magnetic force inducing resonant vibration with circumferential mode shapes of the stator [92]. The acoustic noise can be mitigated by optimizing the geometries and control strategies. The impact of various geometry parameters and the number of stator/rotor poles is analyzed in [92]. The acoustic noise can be reduced by properly selecting the ratio between the stator yoke thickness and the stator lateral pole width, and the ratio between the rotor and stator pole heights, the stator pole shape [93], and the cylindrical outer rotor shape [94]. The impacts of different frame types and cooling ribs are discussed in [95]. A variety of electronic control strategies can be applied to reduce acoustic noise, including voltage smoothing [96], two/three-stage commutation [96], [97], current waveform profiling reduced harmonic order [98] and hybrid excitation method [99].

Because the higher levels of the torque ripple and acoustic noise are the major disadvantages of SRMs compared to conventional three-phase electric machines, there are several review papers already published in the past decade about the techniques for the reduction of the torque ripple or acoustic noise of SRMs [100], [101].

2.2.1.3 Efficiency Improvement

The losses in SRMs mainly consist of core losses, copper losses and losses generated by power electronic drives. Core losses are significantly affected by the

properties of stator/rotor material. Different types of low-loss magnetic steels can be utilized to reduce the core losses, such as high silicon steel Super E-Core [102], laminated amorphous alloy, general-purpose low-loss silicon steel and 6.5% high silicon steel [103]-[105]. Geometric design is an alternative approach to improve the SRM efficiency. Reference [106] presents the detailed procedures to select the machine parameters, including the stator bore diameter, stator/rotor pole arc, stator yoke thickness and rotor slot depth for a 5-phase SRM. In the study of [107], the design variables such as the stack length, turns of winding and width of air gap are optimized using the response surface model and kriging model. A type of SRM with stepped-skewing rotor (SSR) with selected skew angle is proposed in [108]. Various methods of current control are carried out for efficiency improvement. The use of adaptive fuzzy systems to learn current profiles suitable for minimizing copper losses is demonstrated in [109]. The turn-on and turn-off switching angles are optimized in [110], [111]. The method to improve the SRM efficiency by minimizing the dc-link current ripple in real time appears in [112]. Reference [113] investigates the relationship between SRM efficiency and zero-voltage loop (ZVL) current commutation. The design and control strategy of drive systems is another factor that influences the efficiency. Soft-switching converters [114], split ac drive systems with a single-switch-per-phase topology [115], asymmetric half-bridge converter with mixed parallel IGBT/MOSFET operation [116] are proposed and investigated.

2.2.1.4 Torque Density

SRMs that have competitive torque density for electric vehicle applications have appeared during recent years [117]. The torque density can be enhanced by optimizing the mechanical structure, the distribution of stator windings, and the control strategy of SRMs. Shape optimization can be achieved by adjusting the physical dimensions such as stator/rotor pole arcs, rotor diameter and stack length [118]. Some special types of geometries have been proposed such as a quintuple-set SRM [119], segmental rotor

structure, circular slot segmented SRM (CSSSRM) [120] and axial-flux SRM with separately wound c-cores [121]. Emadi *et al.* presented a novel SRM configuration with more rotor poles than the stator poles [90]. A wider rotor pole width and skewing can enhance the average torque of SRMs [122]. Winding design and control strategy also have an impact on the torque density of SRMs. A new SRM with fractionally-pitched coils and with bipolar currents is proposed in [123]. Switched reluctance motors using auxiliary DC windings to achieve the built-in field excitation in the SR structures can greatly improve the output torque density [124]. Regarding the influence of control strategies on the output torque of SRMs, the turn-on and turn-off angles are optimized in [125]. A modified direct instantaneous torque control (DITC) proposed in [126] improves the torque per ampere ratio.

2.2.2 Multi-Objective Optimization of SRMs

As discussed in section 2.2.1, previous research efforts on SRM design and optimization are mostly done to address only one performance index. However, the problem with this single-objective optimization is the potential unfavorable downgrading of other important performance indices, as *trade-offs* to some initiated improvements on one single objective. Therefore, the implementation of multi-objective optimization on SRMs [127]-[140] is necessary to accommodate the needs for different applications.

While the enumeration method (direct search) [127], [128] and response surface method [129] have been applied to solve SRM multi-objective design and optimization problems, the majority of literatures employ certain stochastic algorithms to perform the optimal design search by evaluating a large number of design candidates based on several randomly generated independent prime design variables. These variables typically involve some crucial SRM geometric parameters, including the air gap diameter, stack length, stator/rotor pole heights and pole arc angles, as well as other non-geometric quantities,

such as the current density and the number of turns. Then the complete SRM geometry is designed and various performance indices are evaluated by either FEA simulations [127]-[135], [139], [140], surrogate models as kriging [135] or analytical models based on the magnetic equivalent circuit [136] or Maxwell's equations [138]. After all the performance indices are assessed in a scalar or vector objective function, the next-generation prime design variables are generated by the multi-objective optimization algorithms of genetic algorithms (GA) [131], [132], [137], [139], particle swarm optimization (PSO) [134]-[136], [138], and differential evolutions (DE) [133], [140]. The entire process is repeated until the end of the iterations. It is reported in [127]-[140] that significant improvement can be made on one or two targeted performance indices, with minimal impact on others.

Table 2.1 – Comparison of different multi-objective design and optimization methods of switched reluctance machines.

References	Modeling method	Optimization method	Average torque	Torque density	Efficiency	Torque ripple	Acoustic noise	Integration of current profile	Objective function dimension	Computational speed / accuracy
Xue [127]	FEA	Enumeration	Yes	Yes	Partial	No	No	No	Scalar	Slow / high
Omekanda [128]	FEA	Enumeration	Yes	No	Yes	Yes	No	Yes	N/A	Slow / high
Choi [129]	FEA	RS	Yes	No	No	Yes	No	No	N/A	Slow / high
Cheng [130]	FEA	N/A	Yes	Yes	Partial	Yes	No	No	Scalar	Slow / high
Jiang [131]	FEA	GA	Yes	No	No	Yes	No	No	Vector	Slow / high
Smaka [132]	FEA	GA	Yes	Yes	No	Yes	No	No	Scalar	Slow / high
Öksüztepe [133]	FEA	DE	Yes	Yes	Yes	No	No	No	Vector	Slow / high
Ma [134]	FEA	PSO	Yes	Yes	Yes	Yes	No	No	Scalar	Slow / high
Ren [135]	Surrogate model	PSO	Yes	No	No	Yes	No	No	Vector	Fast / low
Ilea [136]	MEC	PSO	Yes	No	Yes	No	No	No	Scalar	Fast / modest
Mirzaeian [137]	Fuzzy system	GA	No	No	Yes	Yes	No	No	Scalar	Fast / low
Zhang [138]	Maxwell's equations	PSO	Yes	Yes	Yes	No	No	No	Scalar	Fast / modest
Pisch [139]	FEA	GA	Yes	No	Yes	No	No	Yes	Vector	Slow / high
Ma [140]	FEA	DE	No	No	No	Yes	Yes	Yes	Scalar	Slow / high

Aside from the geometry design aspect, multi-objective optimizations have also been performed on the control of SRMs. Multiple Fourier Series coefficients approximating the current profile are optimized by DE to simultaneously reduce the torque ripple and acoustic noise [140]. In addition, the PI controller gains, steady-state phase current and its turn-on and turn-off angles can be also adjusted as prime design variables with PSO, as reported in [141], [142].

The aforementioned SRM multi-objective design and optimization approaches are summarized and compared in Table I, in terms of specific modeling/optimization methods, various performance indices to be optimized, integration of current profile or control related issues, dimension of objective functions and computational efficiency [127]-[140]. The comparison demonstrates that the integration of acoustic noise and current profile into the multi-objective design and optimization processes are still largely unexplored in the existing literatures, and there is always a demand for fast and highly-accurate machine performance evaluation approaches.

For the emerging trend of multi-objective design and optimization of SRMs, coupling the multi-physics and the control aspects with the electromagnetic part is becoming increasing popular, which will largely increase the number of design variables at the very first stage of SRM design and optimization. Therefore, the development of computationally efficient FEA methods, parallel computing or pure analytical design models [130] will be vital for maintaining a reasonable optimization efficiency.

2.3 Mathematical Modeling of the Fields in the End Region of Large Synchronous Generators

One of the major topics in the research on the large synchronous generators is the electromagnetic (EM) field calculation and the design optimization of the end-region as

shown in Figure 2.6 to reduce the eddy current losses and temperature [143], [144]. Basically, there are two types of calculation methods: the analytical methods and the numerical methods. Analytical methods possess a relatively faster calculation speed but with low accuracy because of the assumptions made for deriving the closed-form solutions and the over-simplifications of the representation of the end structures, while numerical methods have a high level of accuracy but are extremely time-consuming. In the literature review of this section, the existing different techniques in both analytical and numerical method are first introduced. Then, a review of some state-of-art techniques and possible solutions to the design optimization for the end region of large turbine generators is presented.

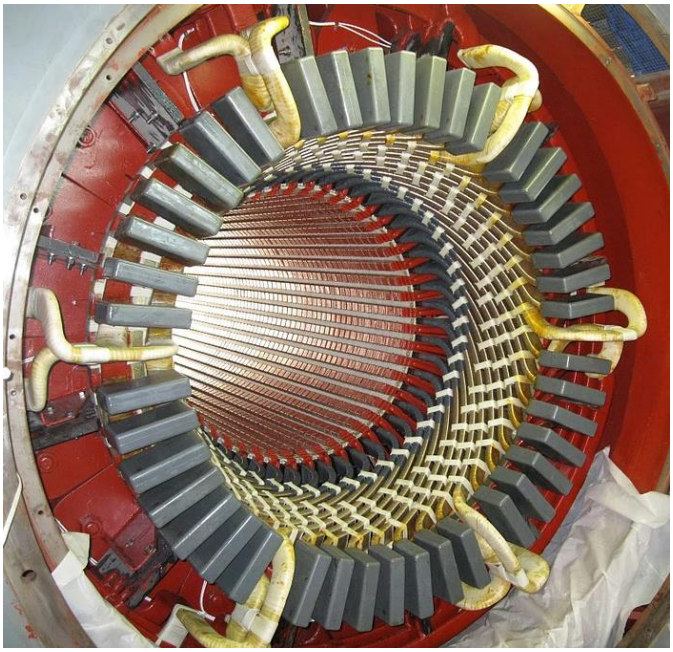

Figure 2.6 End region of a large synchronous generator.

2.3.1 Analytical Methods

2.3.1.1 End-winding geometric modelling

The most important part of the analytical calculation of the end-region magnetic field is the geometric modelling of the end windings. Many researchers have developed different kinds of models for the analytical calculation [145]-[155]. For example, in 1961, P. Hammond modeled the stator conductor as tubular current similar to the rotor current system of a squirrel-cage induction motor with cylindrical symmetry [145]. Then method to analyze the magnetic field at the surface of the stator-core end-plate of large turbo-generator is applied, based on a cylinder and cone model of the end-winding [146]. In 1963, J.A Tegopoulos proposed a closed loop model that separates the stator and rotor current into four components of peripheral, axial, radial and return current, of which the return current represents the effect of the air gap [149]. Four years later, ABJ Reece proposed a model that divided the coil end into two parts: the actual coil end lying on a cylinder closed by a conductor on the core end surface and a fictitious coil lying on the core end surface taking account of the radial displacement between air gap and the coil end [152]. In 2005, Drago Ban precisely gave the analytical 3D geometric model of the end-winding in which each coil is modeled as a set of serially connected straight filaments and an involute line lying on the surface of a frustum of a cone [155].

2.3.1.2 Boundary Conditions

Boundary conditions are another important part in determining the magnetic field. The field due to the winding alone can be obtained by integration with proper aforementioned model, but the magnetic effect of the iron and of any other magnetic surfaces which may be close to the end-winding cannot be dealt with so directly. In 1963, J.A. Tegopoulos determined the magnetic field in the end zone of turbine generators in cylindrical co-ordinates taking into account all boundaries with the assumption that the field is normal on all of them. The flux density is calculated by superposition of one part due to end-windings and a second because of the cylindrical boundaries, which includes four parts: the end core plane, the rotor shaft surface, the cylindrical outer boundary and

the end-bell plane [150]. Among these boundaries, the one that affects most the magnetic field is the end core plane. In 1960, C.J. Carpenter first introduced the method of images to the machine end-winding field calculation to solve this problem. The image principle, as applied to a closed current-carrying circuit in the vicinity of a semi-infinite block of iron, states that the magnetic field in the air is the same as that which would result if the iron were removed and replaced by the mirror image of the circuit [156]. After that, many researchers have applied this method to determine the boundary conditions in the end-region field calculation [146]-[148], [155]-[162].

2.3.2 Numerical Methods

Before the 1980's, researchers focused on the analytical solutions for the modeling of the large generator end regions. However, with the development and aid of high-speed computers, numerical methods become popular and are widely adopted in the solution of the problem.

The mathematical formulations of the electromagnetic field in existing numerical approaches are based on different dimensionalities. These methods can be classified into 2-dimensional (2D), quasi-3-dimensional (quasi-3D) and 3-demensional (3D) modellings. The 2-dimensional models are the simplest and fastest among the numerical approaches. However, 2D models are inadequate for an accurate solution of the practical large generator end-region problem, because they simply map the end geometries onto multiple cross-sectional planes without considering the variation of the magnetic field in the peripheral or axial direction, thus introducing unacceptable errors to the calculation. Quasi-3D models that include the treatment of complex end-geometries appeared in the late 1970s [163], [164]. However, a key assumption of quasi-3D methods is that the end geometries are peripherally consistent and the magnetic field varies sinusoidally in the circumferential direction, which constrains the calculation accuracy. 3D FEA based methods later emerged

based on different governing equations. Frequency-domain harmonic FEA was introduced with reduced magnetic scalar potential φ_r modelling [165], $\boldsymbol{A}$-φ (magnetic vector potential – electric scalar potential) formulation [166], and $\boldsymbol{T}$-Ω (electric vector potential – magnetic scalar potential) formulation [167]. Although the complexity is lower, linearizing the field equations at fundamental frequency without considering the saturation of nonlinear materials bring about unacceptable errors. Transient time-domain FEA methods appeared in recent years with $\boldsymbol{A}$-φ formulation [168], $\boldsymbol{T}$-Ω formulation [169] and reduced magnetic potential formulation [170]. The $\boldsymbol{T}$-Ω formulation is much more efficient than **A**-φ formulation that includes the solution of all three components of vector potential **A** over the entire domain. The **T**-Ω formulation is particularly effective when analyzing the end region of large generators, since the eddy current effects only exist in the end metallic components within a limited space, and in most of the solution domain the terms associated with the vector potential **T** can be eliminated. There are some inherent deficiencies in the existing full 3D FEA based methods, such as the over-simplifications of the end geometries, and the ignorance of the anisotropic property of stator structures and the in-plane eddy current reaction in the classical laminated core models.

2.4 Design of the End Region of Large Synchronous Generators

Table 2.2 – Geometry parameters with an influence on the end-region field and losses.

Part	Parameter	Way to Lower Losses	Reference
end-winding	cone angle	smaller	[146]
	length of the axial portion	longer	[146]
end-plates	core-end stepping	effective	[163], [175]
	slitting the tooth	effective	[163]
	packets width	thin near core-end	[163]

stator core	Radial cooling ducts	effective	[163], [175]
	relative length of rotor core	minor effect	[171], [175]
operation condition	short-circuit ratio	higher	[171]
	power factor	lagging	[146], [169]
flux shunt	length	half-tooth	[171]
	thickness	minor effect	[171]
copper shield structure		effective	[176]
copper screen thickness		thicker	[176]
retaining ring		non-magnetic	[175]
metal screen material		effective	[173], [177]

Various design concepts have been proposed to reduce the electromagnetic losses in the end components of large generators. In [171], Ito *et al.* analyzed the influences of the flux shunts and the stator/rotor core lengths. In 1978 Tavner *et al*. examined the impact of end-winding designs [172]. Reference [163] discusses the effectiveness of the tooth slits and core-end stepping in reducing the losses in end core packets. The impacts of the material, location, thickness and metal shield of the press plate on the loss distribution in the large generator end region are analyzed in [173]. Changing the materials of the clamping ring and finger plates is discussed in [174]. However, a common issue with the existing design methods for the large generator end region is that they only analyze the influence of one single design parameter without a precise definition of the full design space of multiple critical variables. Multi-objective optimization of the large generator end structures has not been performed in the existing literature due to the high computational complexity.

Table 2.2 lists the geometry parameters investigated in literatures that may have an influence on the end-region field and losses.

2.5 Chapter Summary

This chapter presents a comprehensive literature review on existing methods and techniques related to the dissertation work. First, various numerical and analytical methods for the electromagnetic and thermal modeling of SRMs are summarized. This facilitates the development of design optimization techniques aiming to enhance the performances of SRMs. Next, the existing single-objective and multi-objective optimization methods for SRMs are introduced and compared. Then, for the design of large synchronous generators, the existing analytical and numerical approaches that estimate the magnetic field and loss distributions in the large generator end region are reviewed. Finally, the concepts of the large generator end region design are summarized and discussed.

CHAPTER 3. MULTI-PHYSICS MODELLING OF SWITCHED RELUCTANCE MACHINES

As demonstrated in Chapter 1 and 2, accurate estimation of the performances of an arbitrary design candidate is the foundation for SRM design. This chapter describes a comprehensive method that predicts the EM and thermal behaviors of SRMs. A generalized analytical model that predicts the EM behaviors of SRMs with arbitrary geometries, materials or current profiles is first developed and validated by its FEA counterpart in terms of various performance indices and experimental results. In addition, an enhanced EM model with conformal mappings is applied to eliminate the negative effects of the approximations of the non-radial or non-peripheral geometric structures when calculating the air-region permeance parameters. Then, a hybrid thermal model combining a 2-dimensional (2D) finite-difference (FD) formulation and thermal equivalent circuits is used to estimate the temperature distribution within an SRM based on the loss distribution calculated by the analytical EM model.

3.1 Generalized Analytical Electromagnetic Model of SRMs

In an SRM EM model, phase inductance is a key parameter because the performance indices such as torque, torque ripple, losses and the dynamics of phase voltages and currents are related to the phase inductance. Therefore, accurate calculation of the inductance profile of an SRM is important in determining the SRM behavior. Instead of using the time-consuming finite element analyses (FEAs), or the analytical methods that require prior knowledge of flux linkage from either an FEA simulation or an experimental test such as the curve fitting and flux-path-based methods, this section presents a fast, generalized and accurate analytical approach to determine the magnetic field, phase inductance and thus the associated EM behaviors of an SRM with any common topologies,

dimensions and phase currents at any rotor position. In this method, the magnetic field distribution and the permeance parameters in the air region are firstly determined by solving the partial differential equations of magnetic potentials based on Maxwell's equations. The air-region permeance parameters are then substituted into a magnetic circuit network to include the impact of the saturation effects of steel on the phase inductance profile. The agreement between the results of the proposed analytical method and 2D/3D FEAs and experimental results validates the analysis.

3.1.1 Determining the Magnetic Field and Permeances in the Air Region

3.1.1.1 Assumptions

The assumptions of the proposed approach to determine the magnetic field and permeances in the air region are as follows:

1) The permeability of steel is assumed to be infinite and the magnetic intensity vector (**H**) is orthogonal to the surfaces of the stator and rotor. The mmf drop in each steel segment due to saturation will be analyzed by the magnetic circuit network presented in Section III.
2) The cross-sectional geometry of an SRM is consistent in the axial direction, so a 2D analysis of the magnetic field is sufficient for deriving the air-region permeances.
3) Since the SRM geometric dimensions are far smaller than the electromagnetic wavelengths at the fundamental and lower-order harmonic frequencies, the magnetic field is considered to be quasi-static, and the displacement current and the time delay of field transmission is neglected. A magnetostatic analysis is carried out at each rotor position.

4) For the convenience of assigning the boundary conditions of the magnetic potentials in the air region, the side surfaces of the rotor slot and stator slot sub-regions are assumed to be directed in the radial direction.

3.1.1.2 General Descriptions and the List of Machine Parameters

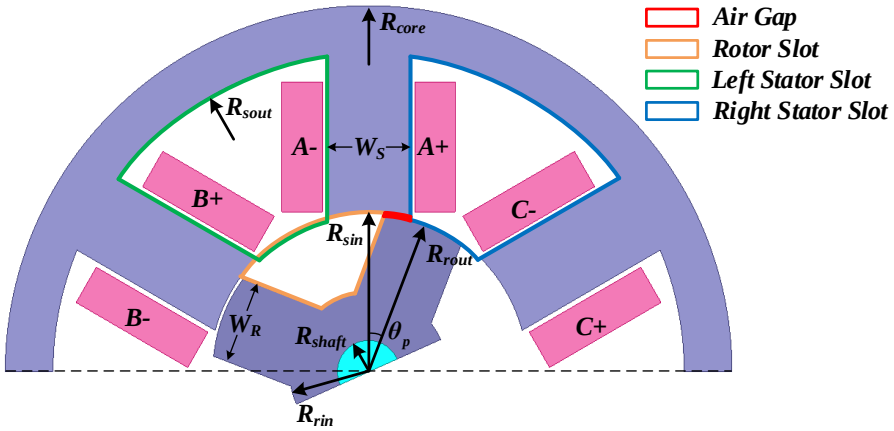

Figure 3.1 Cross-section view of the upper half solution domain of an SRM.

This section describes the method to determine the magnetic field and permeance parameters for the air region. This allows the first step of the solution process for the magnetic circuit of an SRM with any geometry. Because it is infeasible to formulate a precise analytical model of the magnetic field in the region of the air and windings as a whole, due to the complex geometries, the region is thus divided into three types of sub-regions: air gap sub-regions, rotor slot sub-regions, and stator slot sub-regions. Figure 3.1 shows an example of the three types of sub-regions in a 6/4 SRM. To calculate the inductance of phase A of the SRM in Figure 3.1, the magnetic field in the air gap region in the red frame, the rotor slot region in the orange frame, and the left/right stator slot regions in the green/blue frames should be analyzed individually. In the analysis of the magnetic field in the air region, that is, the combination of the air gap, rotor slot and stator slot sub-regions, the boundaries on the edges of the stator and rotor steel are subject to the ideal magnetic boundary conditions, which implies that the magnetic flux density vectors are

orthogonal to these boundaries. This is a reasonable assumption because the permeability of steel is much greater than that of the air. Note that this assumption is made only for the purpose of simplifying the analysis for the air region, and the saturation effects of the rotor and stator steel are rigorously considered in the magnetic circuit network model described in Section 3.1.2.

The inductance of an SRM at an arbitrary rotor position is related to the variables listed in Table 3.1. There are four additional parameters dependent on the variables in Table 3.1 that are useful in the derivation of the permeances in the air region: half stator pole angle θ_S, half rotor pole angle θ_R, half angular span of the stator slot at inner diameter (ID) θ_{ST}, and half angular span of rotor slot at outer diameter (OD) θ_{RT}. The expressions of these dependent parameters are presented in Table 3.2. At a certain time instant the rotor position θ_p is defined as the angle between the centers of the stator pole and rotor pole. The range of θ_p is $[0, \pi/N_R]$.

Table 3.1 – Independent machine parameters.

Parameter	Parameter
Stator slot outer radius R_{sout}	Stator pole width W_S
Stator pole inner radius R_{sin}	Rotor pole width W_R
Rotor pole outer radius R_{rout}	Shaft outer radius R_{shaft}
Rotor slot inner radius R_{rin}	Stator yoke outer radius R_{core}
Stator length l_s	Number of turns/pole/phase N_t
Number of stator poles N_S	Number of rotor poles N_R
Number of stator poles per phase N_{sp}	Stator phase current I_p

Table 3.2 – Expressions of the dependent parameters.

Parameter	Expression
θ_S	$sin^{-1}[W_S/(2R_{sin})]$
θ_R	$sin^{-1}[W_R/(2R_{rout})]$
θ_{ST}	$\pi/N_S - sin^{-1}[W_S/(2R_{rout})]$
θ_{RT}	$\pi/N_R - sin^{-1}[W_R/(2R_{sin})]$

3.1.1.3 Determining the Magnetic Field and Permeances in the Air Gap Sub-region

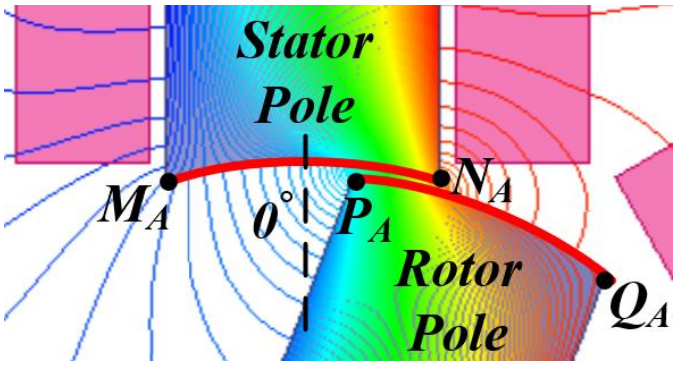

Figure 3.2 Air gap region of an SRM.

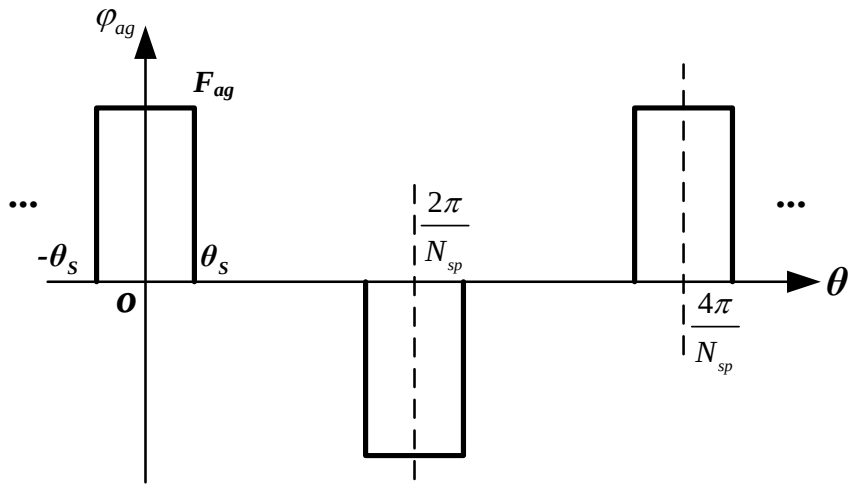

Figure 3.3 Boundary condition at $r=R_{sin}$ of the air gap region.

For the convenience of discussion, the critical vertices of the air gap sub-region have a subscript "A". Similarly, the vertices of the rotor slot sub-region and stator slot sub-regions are associated with a subscript "R" and "S" respectively, although some vertices are located on the boundaries of more than one sub-regions. The air gap permeance represents the flux that travels between the rotor pole P_AQ_A and stator pole M_AN_A shown in Figure 3.2. Because there are no windings carrying currents in the air gap region, the magnetic field intensity **H** in the non-conductive air gap region where **J**=0 can be expressed in 2D polar coordinates by the magnetic scalar potential φ as follows [178]:

$$\mathbf{H} = -\nabla\varphi = -\left(\frac{\partial\varphi}{\partial r}\mathbf{a}_{\mathbf{r}} + \frac{1}{r}\frac{\partial\varphi}{\partial\theta}\mathbf{a}_{\boldsymbol{\theta}}\right) \tag{3.1}$$

where $\mathbf{a_r}$ is the unit radial vector, $\mathbf{a_\theta}$ is the unit tangential vector, and r and θ are the radial and tangential coordinates respectively.

According to Gauss's law for magnetism, the Laplace equation of φ in 2D polar coordinates is [178]

$$\nabla^2\varphi = \frac{\partial^2\varphi}{\partial r^2} + \frac{1}{r}\frac{\partial\varphi}{\partial r} + \frac{1}{r^2}\frac{\partial^2\varphi}{\partial\theta^2} = \frac{1}{\mu_0}\nabla\cdot\left(\mu_0\nabla\varphi\right) = -\frac{1}{\mu_0}\nabla\cdot\left(\mu_0\mathbf{H}\right) = -\frac{1}{\mu_0}\nabla\cdot\mathbf{B} = 0 \tag{3.2}$$

where μ_0 is the permeability of air. The method of separating variables is used to solve (3.2) for the air gap sub-region. The homogeneous solution of φ in 2D polar coordinates for the Laplace equation (3.2) is

$$\varphi(r,\theta) = \sum_{n=1}^{\infty}(A_n r^{m_n} + B_n r^{-m_n})(C_n\cos m_n\theta + D_n\sin m_n\theta) \tag{3.3}$$

where the coefficients A_n, B_n, C_n, D_n and m_n are determined by the boundary conditions.

Selecting the center of the stator tooth to be at the zero angle as illustrated inFigure 3.2, the boundary conditions of φ are:

1) Due to the symmetry of the machine geometry, assume that on the surface of the rotor pole:

$$\varphi_{ag}\left(R_{rout},\theta\right) = 0 \tag{3.4}$$

where φ_{ag} is the magnetic scalar potential in the air gap region.

2) The boundary condition of φ_{ag} on the surface of the stator pole $r=R_{sin}$ is demonstrated in Figure 3.3. It has a magnitude of F_{ag}, which is the drop of magnetomotive force (mmf) across the air gap, and a period of $4\pi/N_{sp}$ in polar coordinates. Performing the Fourier expansion on φ_{ag} yields:

$$\varphi_{ag}\left(R_{sin},\theta\right)=\sum_{nodd}\left[\frac{4F_{ag}}{n\pi}\sin\left(\frac{N_{sp}n}{2}\theta_S\right)\right]\cos\left(\frac{N_{sp}n}{2}\theta\right)=\sum_{n=1}^{\infty}F_{ag\_an}\cos\left(\frac{N_{sp}n}{2}\theta\right). \quad (3.5)$$

Substitute the boundary conditions 2) into (3.3) to yield

$$D_n=0,\ m_n=\frac{N_{sp}n}{2}. \quad (3.6)$$

Define $A_nC_n=A_n'$ and $B_nC_n=B_n'$, then (3.3) reduces to

$$\varphi_{ag}\left(r,\theta\right)=\sum_{n=1}^{\infty}(A_n'r^{m_n}+B_n'r^{-m_n})\cos m_n\theta. \quad (3.7)$$

According to the boundary conditions 1), 2) and (3.7):

$$\begin{cases}A_n'R_{sin}^{m_n}+B_n'R_{sin}^{-m_n}=F_{ag\_an}\\ A_n'R_{rout}^{m_n}+B_n'R_{rout}^{-m_n}=0\end{cases}. \quad (3.8)$$

The expression of φ_{ag} after solving (3.8) is

$$\varphi_{ag}(r,\theta)=\sum_{nodd}\left[F_{ag\_an}\cdot\frac{\left(\frac{r}{R_{rout}}\right)^{m_n}-\left(\frac{r}{R_{rout}}\right)^{-m_n}}{\left(\frac{R_{sin}}{R_{rout}}\right)^{m_n}-\left(\frac{R_{sin}}{R_{rout}}\right)^{-m_n}}\right]\cos\left(m_n\theta\right). \quad (3.9)$$

The magnetic field intensity **H** is obtained by substituting $\varphi_{ag}(r,\theta)$ into (3.1). The flux intensity on the rotor pole surface is

$$\mathbf{H}(R_{rout},\theta) = -\sum_{nodd}\left\{F_{ag\_an}\cdot\frac{2m_n}{R_{rout}}\left[\frac{\left(\frac{R_{rout}}{R_{sin}}\right)^{m_n}}{1-\left(\frac{R_{rout}}{R_{sin}}\right)^{2m_n}}\right]\cdot\cos\left(m_n\theta\right)\right\}\mathbf{a_r}. \tag{3.10}$$

The airgap flux that links the rotor pole surface P_AQ_A and stator pole surface M_AN_A is

$$\begin{aligned}\phi_{ag} &= -\mu_0 l_s R_{rout}\int_{\theta_p-\theta_R}^{\theta_p+\theta_R} H_r\left(R_{rout},\theta\right)d\theta \\ &= 2\mu_0 l_s\cdot\sum_{n=1}^{\infty}\left\{F_{ag\_an}\left[\frac{\left(R_{rout}/R_{sin}\right)^{m_n}}{1-\left(R_{rout}/R_{sin}\right)^{2m_n}}\right]\cdot\sin\left(m_n\theta\right)\Big|_{\theta_p-\theta_R}^{\theta_p+\theta_R}\right\}.\end{aligned} \tag{3.11}$$

The air gap permeance is

$$P_{ag} = \frac{\phi_{ag}}{F_{ag}}. \tag{3.12}$$

3.1.1.4 Determining the Magnetic Field and Permeances in the Rotor Slot Sub-Region

The permeances in the rotor slot sub-regions determine the flux that flows across the rotor slot shown in the orange frame in Figure 3.4 between the stator poles and the rotor poles and back iron. For the rotor slot sub-region in Figure 3.4, this flux composes the fringing flux impinging the rotor pole side surface M_RN_R and yoke surface P_RN_R, and the pole-pole flux entering the other rotor pole surface P_RQ_R. The permeances in the rotor slot sub-regions are especially significant when the stator pole and rotor pole partially overlap. Similar to the air gap, there are no windings carrying currents in the rotor slots so that the Laplace equation (3.2) of magnetic scalar potential φ is utilized to calculate the field distribution in this region. Define the center line of the rotor slot to be at the zero-degree angle as demonstrated in Figure 3.4.

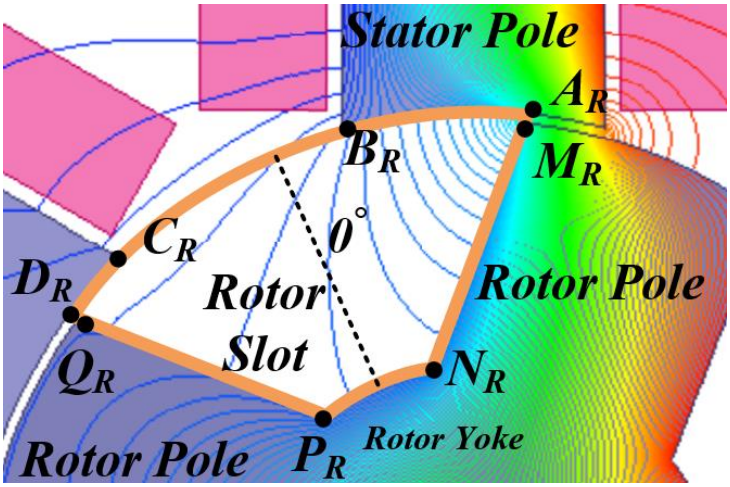

Figure 3.4 Rotor slot sub-region of an SRM.

Take the homogeneous solution (3.3) and the corresponding rotor-slot boundary conditions are as follows:

1) Due to the symmetry of the machine geometry and the assumption of orthogonal flux density vector on steel surfaces, the tangential component of the flux density on the inner surface of the rotor slot P_RN_R is zero and the corresponding boundary condition satisfies

$$\varphi_{rt}\left(R_{rin},\theta\right)=0 \tag{3.13}$$

where φ_{rt} is the magnetic scalar potential in the rotor slot region.

2) The magnetic scalar potential φ_{rt} on the two side surfaces N_RA_R and P_RD_R of the rotor slot is zero:

$$\varphi_{rt}\left(r,\theta_{RT}\right)=0,\ \varphi_{rt}\left(r,-\theta_{RT}\right)=0. \tag{3.14}$$

In fact, this boundary condition reshapes the rotor slot region a little bit because the angle spans of the two tangential edges P_RN_R and A_RD_R are different and the boundary

condition forces the angle span of the edge P_RN_R to be $2\theta_{RT}$ and the lines N_RA_R and P_RD_R to be in the radial direction according to the assumption 4). Deriving a precise boundary condition for the original N_RA_R and P_RD_R is almost impossible and this approximation leads to satisfactory results.

3) The magnetic scalar potential φ_{rt} on the outer surface of the rotor slot where $r=R_{sin}$, $-\theta_{RT}\leq\theta\leq\theta_{RT}$ is defined with respect to the rotor angle θ_p. For the case shown in Figure 3.4 where the stator pole and the rotor pole partially overlap, the tangential component of flux density on the boundary A_RB_R and C_RD_R is defined to be zero. The boundary condition of the tangential flux density on B_RC_R should also be determined to uniquely solve the distribution of φ_{rt}. It is difficult to obtain a precise solution of this boundary condition with an analytical approach. To obtain an approximate solution of the magnetic field, it is assumed that the tangential component of flux density is constant and φ_{rt} linearly decreases from F_{ag} to zero on B_RC_R. Then for the case of the SRM in Figure 3.4 the boundary condition of $\varphi_{rt}(R_{sin},\theta)$ can be expressed as the following piecewise linear function:

$$\varphi_{rt}\left(R_{sin},\theta\right)=\begin{cases}F_{ag},\ \theta_{B_R}\leq\theta\leq\theta_{RT}\\ \dfrac{F_{ag}\left(\theta-\theta_{C_R}\right)}{\theta_{B_R}-\theta_{C_R}},\ \theta_{C_R}\leq\theta\leq\theta_{B_R}\\ 0,\ -\theta_{RT}\leq\theta\leq\theta_{C_R}\end{cases} \tag{3.15}$$

where θ_{B_R} and θ_{C_R} are the angular positions of the points B_R and C_R with respect to the zero-degree center line respectively. The boundary condition in (3.15) is demonstrated in Figure 3.5(a) and is suitable for the rotor positions when the rotor pole and stator pole partially overlap for an SRM. The boundary condition of $\varphi_{rt}(R_{sin},\theta)$ for another typical case

where the rotor is at the unaligned position is shown in Figure 3.5(b). The boundary condition of φ_{rt} on A_RD_R should be derived for the other rotor positions or for an SRM with another topology in a similar way. The basic principle is that on the surface of the stator pole with current excitations, $\varphi_{rt}=F_{ag}$, while on the surface of another pole, $\varphi_{rt}=0$, and φ_{rt} linearly drops from F_{ag} to 0 along the edge between them.

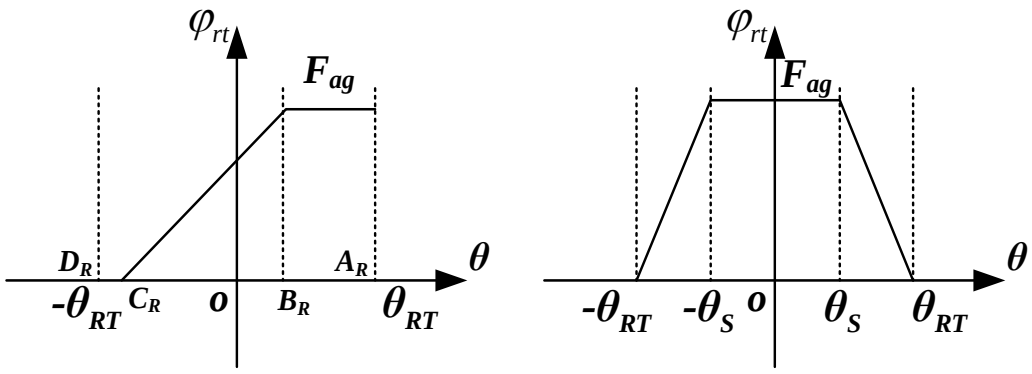

(a) (b)

Figure 3.5 Boundary condition at $r=R_{sin}$ of the rotor slot sub-region. (a) At the rotor position when the stator pole and rotor pole partially overlap; (b) When the rotor is at the unaligned position.

The homogeneous solution of the Laplace equation (3.3) can be transformed into the form for the rotor slot sub-region:

$$\varphi_{rt}(r,\theta)=\sum_{n=1}^{\infty}\left[\left(A_{nr}r^{m_{nr}}+B_{nr}r^{-m_{nr}}\right)\cos m_{nr}\theta+\left(C_{nr}r^{m_{nr}}+D_{nr}r^{-m_{nr}}\right)\sin m_{nr}\theta\right]. \quad (3.16)$$

Apply the boundary condition 1) to φ_{rt} in (3.16) to yield

$$\begin{cases} A_{nr}R_{rin}^{m_{nr}}+B_{nr}R_{rin}^{-m_{nr}}=0 \\ C_{nr}R_{rin}^{m_{nr}}+D_{nr}R_{rin}^{-m_{nr}}=0 \end{cases}. \quad (3.17)$$

It can be inferred from the rotor-slot boundary condition 2):

$$\begin{cases} m_{nr} = \dfrac{n\pi}{2\theta_{RT}} \\ A_{nr} = 0,\ B_{nr} = 0,\ for\ n = even. \\ C_{nr} = 0,\ D_{nr} = 0,\ for\ n = odd \end{cases} \tag{3.18}$$

Then φ_{rt} in (3.16) is simplified to the following form:

$$\varphi_{rt}(r,\theta) = \sum_{nodd}\left(A_{nr}r^{m_{nr}} + B_{nr}r^{-m_{nr}}\right)\cos\left(m_{nr}\theta\right) + \sum_{neven}\left(C_{nr}r^{m_{nr}} + D_{nr}r^{-m_{nr}}\right)\sin\left(m_{nr}\theta\right). \tag{3.19}$$

For a certain rotor position θ_p, expand $\varphi_{rt}(R_{sin},\theta)$ defined in the boundary condition 3) into the following Fourier series:

$$\varphi_{rt}(R_{sin},\theta) = \sum_{nodd} F_{rt\_an}\cos\left(\frac{\pi n\theta}{2\theta_{RT}}\right) + \sum_{neven} F_{rt\_bn}\sin\left(\frac{\pi n\theta}{2\theta_{RT}}\right) \tag{3.20}$$

where

$$\begin{cases} F_{rt\_an} = \dfrac{1}{\theta_{RT}}\displaystyle\int_{-\theta_{RT}}^{\theta_{RT}} \varphi_{rt}\left(R_{sin},\theta\right)\cos\left(\frac{\pi n\theta}{2\theta_{RT}}\right)d\theta,\ n = odd \\ F_{rt\_bn} = \dfrac{1}{\theta_{RT}}\displaystyle\int_{-\theta_{RT}}^{\theta_{RT}} \varphi_{rt}\left(R_{sin},\theta\right)\sin\left(\frac{\pi n\theta}{2\theta_{RT}}\right)d\theta,\ n = even \end{cases}.$$

Substituting the Fourier coefficients solved by (3.20) into (3.19) yields

$$\begin{cases} A_{nr}R_{sin}^{m_{nr}} + B_{nr}R_{sin}^{-m_{nr}} = F_{rt\_an} \\ C_{nr}R_{sin}^{m_{nr}} + D_{nr}R_{sin}^{-m_{nr}} = F_{rt\_bn} \end{cases}. \tag{3.21}$$

The coefficients A_{nr}, B_{nr}, C_{nr} and D_{nr} are obtained by solving linear equations (3.17), (3.18) and (3.21). After calculating all the boundary conditions for each rotor angle θ_p, the distribution of the scalar potential in the rotor slot sub-region is

$$\varphi_{rt}(r,\theta)=\sum_{nodd}F_{rt\_an}\cdot\left[\frac{\left(\frac{r}{R_{rin}}\right)^{m_{nr}}-\left(\frac{r}{R_{rin}}\right)^{-m_{nr}}}{\left(\frac{R_{sin}}{R_{rin}}\right)^{m_{nr}}-\left(\frac{R_{sin}}{R_{rin}}\right)^{-m_{nr}}}\right]\cos\left(\frac{\pi n\theta}{2\theta_{RT}}\right)$$
$$+\sum_{neven}F_{rt\_bn}\cdot\left[\frac{\left(\frac{r}{R_{rin}}\right)^{m_{nr}}-\left(\frac{r}{R_{rin}}\right)^{-m_{nr}}}{\left(\frac{R_{sin}}{R_{rin}}\right)^{m_{nr}}-\left(\frac{R_{sin}}{R_{rin}}\right)^{-m_{nr}}}\right]\sin\left(\frac{\pi n\theta}{2\theta_{RT}}\right). \tag{3.22}$$

The corresponding magnetic field **H** in the rotor slot region is calculated by substituting φ_{rt} into (3.1). The total flux that impinges the surface P_RN_R of the rotor yoke is

$$\begin{aligned}\phi_{P_RN_R}&=-\mu_0 l_s R_{rin}\int_{-\theta_{RT}}^{\theta_{RT}}H_r\left(R_{rin},\theta\right)d\theta\\&=\mu_0 l_s\left\{\begin{array}{l}\displaystyle\sum_{nodd}\frac{F_{rt\_an}}{K_n}\left[\sin\left(m_{nr}\theta_{RT}\right)-\sin\left(-m_{nr}\theta_{RT}\right)\right]\\\qquad\displaystyle-\sum_{neven}\frac{F_{rt\_bn}}{K_n}\left[\cos\left(m_{nr}\theta_{RT}\right)-\cos\left(-m_{nr}\theta_{RT}\right)\right]\end{array}\right\}\end{aligned} \tag{3.23}$$

where

$$K_n=\left(\frac{R_{sin}}{R_{rin}}\right)^{m_{nr}}-\left(\frac{R_{sin}}{R_{rin}}\right)^{-m_{nr}}.$$

The fringing flux impinging the rotor pole surface M_RN_R is

$$\begin{aligned}\phi_{M_RN_R}&=\mu_0 l_s\int_{R_{rin}}^{R_{rout}}H_t\left(r,\theta_{RT}\right)dr\\&=\mu_0 l_s\left\{\begin{array}{l}\displaystyle\sum_{nodd}\frac{F_{rt\_an}}{K_n}\sin\left(m_{nr}\theta_{RT}\right)\left[\left(\frac{R_{rout}}{R_{rin}}\right)^{m_{nr}}+\left(\frac{R_{rout}}{R_{rin}}\right)^{-m_{nr}}-2\right]\\\displaystyle-\sum_{neven}\frac{F_{rt\_bn}}{K_n}\cos\left(m_{nr}\theta_{RT}\right)\left[\left(\frac{R_{rout}}{R_{rin}}\right)^{m_{nr}}+\left(\frac{R_{rout}}{R_{rin}}\right)^{-m_{nr}}-2\right]\end{array}\right\}.\end{aligned} \tag{3.24}$$

Similarly, the pole-pole flux entering the surface P_RQ_R of another rotor pole is

$$\begin{aligned}\phi_{P_RQ_R} &= -\mu_0 l_s \int_{R_{rin}}^{R_{rout}} H_t\left(r, -\theta_{RT}\right) dr \\ &= -\mu_0 l_s \left\{ \begin{array}{l} \sum_{nodd} \frac{F_{rt\_an}}{K_n} \sin\left(-m_{nr}\theta_{RT}\right) \left[\left(\frac{R_{rout}}{R_{rin}}\right)^{m_{nr}} + \left(\frac{R_{rout}}{R_{rin}}\right)^{-m_{nr}} - 2 \right] \\ -\sum_{neven} \frac{F_{rt\_bn}}{K_n} \cos\left(-m_{nr}\theta_{RT}\right) \left[\left(\frac{R_{rout}}{R_{rin}}\right)^{m_{nr}} + \left(\frac{R_{rout}}{R_{rin}}\right)^{-m_{nr}} - 2 \right] \end{array} \right\}. \end{aligned} \tag{3.25}$$

The fringing permeance of the rotor slot sub-region is

$$P_{fr} = \frac{\phi_{P_RN_R} + \phi_{M_RN_R}}{F_{ag}}. \tag{3.26}$$

And the pole-to-pole permeance is

$$P_{pp} = \frac{\phi_{P_RQ_R}}{F_{ag}}. \tag{3.27}$$

3.1.1.5 Determining the Magnetic Field and Permeances in the Stator Slot Sub-Regions

The permeances in the stator slot sub-region generally consist of two components: the fringing permeances and the slot leakage permeances. Figure 3.6(a) and Figure 3.6(b) demonstrate the geometry and the flux lines of the right stator slot sub-region for the SRM in Figure 3.1 when the stator pole of phase A and rotor pole partially overlap and when the rotor pole is close to the unaligned position of phase A, respectively. The fringing permeance is related to the flux that flows between the stator pole surface M_SP_S and the rotor pole surface, which is N_SA_S in Figure 3.6(a) and A_SB_S in Figure 3.6(b). The slot leakage flux flows out of the stator pole surface M_SP_S into the stator yoke surface P_SQ_S and the surface of another pole B_SQ_S. The magnetic field should be solved in both the left and right stator slots for a stator pole of the SRM in Figure 3.1. Due to the presence of stator

windings carrying currents in the stator slots, the Laplace equation of magnetic scalar potential does not hold in the stator slot sub-regions. Consequently the magnetic field in the stator slot sub-regions is formulated by the Poisson equation of the magnetic vector potential **A**. Because solving the 2D magnetic field is sufficient for the analysis, only the axial component of **A** should be considered in the mathematical modelling. For the convenience of the following discussions, define $\mathbf{A}=A\mathbf{a}_z$. The flux density vector **B** can be expressed by **A** in 2D polar coordinates [178]:

$$\mathbf{B}=\nabla\times\mathbf{A}=\frac{1}{r}\frac{\partial A}{\partial\theta}\mathbf{a}_r-\frac{\partial A}{\partial r}\mathbf{a}_\theta. \tag{3.28}$$

The Poisson equation of **A** in the stator slot sub-regions is

$$\begin{aligned}\left(\nabla^2 A\right)\mathbf{a}_z&=\left(\frac{\partial^2 A}{\partial r^2}+\frac{1}{r}\frac{\partial A}{\partial r}+\frac{1}{r^2}\frac{\partial^2 A}{\partial\theta^2}\right)\mathbf{a}_z=-\mu_0\nabla\times\left(\frac{1}{\mu_0}\nabla\times\mathbf{A}\right)=-\mu_0\nabla\times\frac{1}{\mu_0}\mathbf{B}\\&=-\mu_0\nabla\times\mathbf{H}=\left(-\mu_0 J\right)\mathbf{a}_z\end{aligned} \tag{3.29}$$

where J is the current density in A/m^2.

The solution of the vector potential in (3.29) is the combination of a particular solution and a homogeneous solution. The particular solution satisfies the Poisson equation and corresponds to the source current but does not necessarily satisfy the boundary conditions, while the homogeneous solution satisfies the Laplace equation and has a similar form to that of the magnetic scalar potential in (3.3), and is selected so that their summation satisfies the specified boundary conditions.

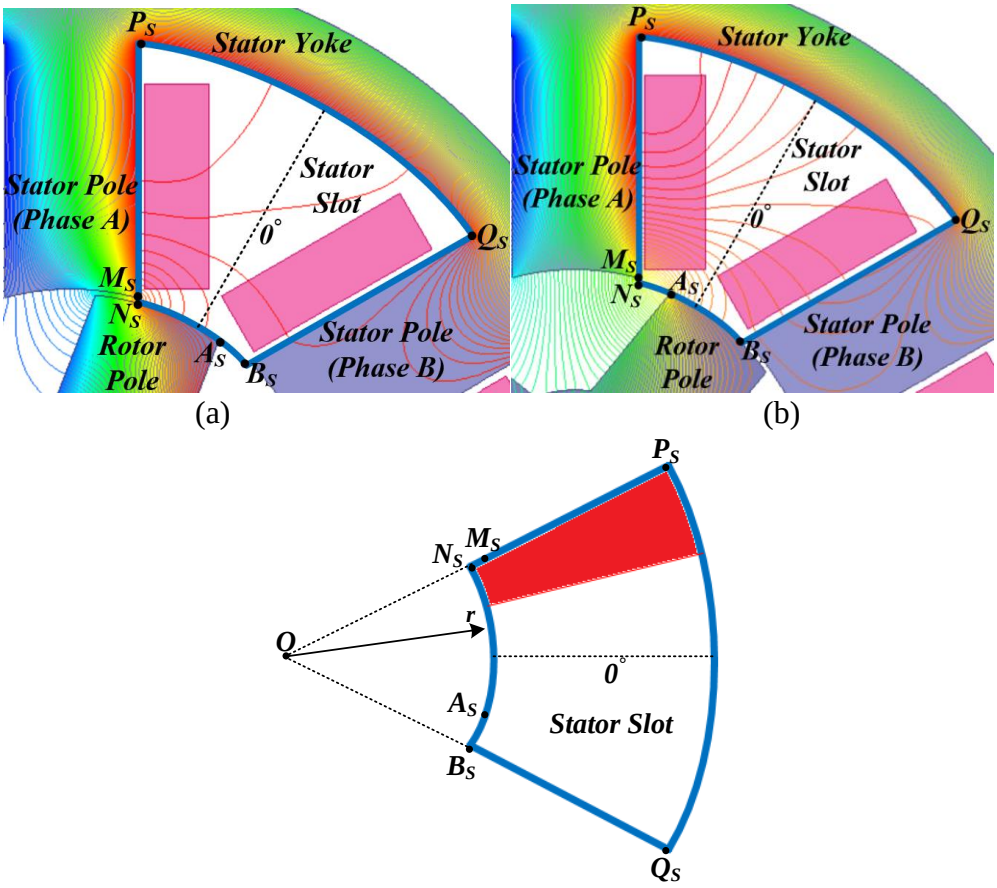

Figure 3.6 Stator slot sub-region of an SRM. (a) When the stator pole of phase A and rotor pole partially overlap; (b) When the rotor pole is close to the unaligned position of phase A; (c) The simplified stator slot region geometry for the case when the stator pole and rotor pole partially overlap.

It is necessary to determine a mathematical model for the distribution of the stator current to find the particular solution for the magnetic vector potential. The original geometries of the stator slot and the winding are approximated into the dimensions presented in Figure 3.6(c). The edges B_SQ_S and N_SP_S are in the radial direction and the angle span of the stator slot is $2\theta_{ST}$. The stator windings are modeled as circular sectors instead of the original rectangles in Figure 3.6(c), and it is assumed that the stator windings fill the region in a stator slot from the back iron to the stator pole tip. The current density is inversely proportional to the distance between a certain position and the center of the

circular sector to guarantee an even current distribution in the radial direction. The current density can be expressed as

$$J\left(r,\theta\right)=\begin{cases}\dfrac{J_m}{r},\theta_{ST}-\theta_w\le\theta\le\theta_{ST}\\ 0,-\theta_{ST}\le\theta\le\theta_{ST}-\theta_w\end{cases} \tag{3.30}$$

where θ_w is the equivalent winding span angle, and J_m is the equivalent stator winding current density when $r=1$ m given by

$$J_m=\frac{N_tI_p}{\int_{R_{rout}}^{R_{sout}}\left(\frac{1}{r}\int_{\theta_{ST}-\theta_w}^{\theta_{ST}}rd\theta\right)dr}=\frac{N_tI_p}{\left(R_{sout}-R_{rout}\right)\theta_w}. \tag{3.31}$$

Therefore, this circular-sector-shaped current density is transformed into a Fourier series with respect to the angle θ:

$$J\left(r,\theta\right)=\frac{1}{r}\left[J_{a0}+\sum_{neven}J_{an}\cos m_{ns}\theta+\sum_{nodd}J_{bn}\sin m_{ns}\theta\right] \tag{3.32}$$

where

$$\begin{cases}m_{ns}=\dfrac{n\pi}{2\theta_{ST}}\\ J_{a0}=\dfrac{\theta_w}{2\theta_{ST}}J_m,\ J_{an}=-\dfrac{2J_m}{n\pi}\sin\left(\dfrac{n\pi\left(\theta_{ST}-\theta_w\right)}{2\theta_{ST}}\right)\\ J_{bn}=\dfrac{2J_m}{n\pi}\cos\left(\dfrac{n\pi\left(\theta_{ST}-\theta_w\right)}{2\theta_{ST}}\right)\end{cases}.$$

A feasible particular solution that satisfies the Poisson equation (3.29) and the Fourier expansion of the current density distribution (3.32) is

$$A_p(r,\theta) = P_{0s} r + \sum_{neven} P_{ns} r \cos(m_{ns}\theta) + \sum_{nodd} Q_{ns} r \sin(m_{ns}\theta) \tag{3.33}$$

where

$$P_{0s} = -\mu_0 J_{a0},\ P_{ns} = \frac{1}{m_{ns}^{\ 2} - 1}\mu_0 J_{an},\ Q_{ns} = \frac{1}{m_{ns}^{\ 2} - 1}\mu_0 J_{bn}.$$

The next step is to specify the stator-slot boundary conditions of A in (3.29) to derive the expression of the homogeneous solution. For the right stator slot sub-region in Figure 3.6(c), the boundary conditions are defined as

1) Due to the assumption of orthogonal flux density vector on the steel surfaces, the tangential component of the field intensity on the stator yoke surface $P_S Q_S$ is zero, and the radial component of the field intensity on the pole surfaces $N_S P_S$ and $B_S Q_S$ is zero:

$$\begin{cases} H_r(r,\theta_{ST}) = H_r(r,-\theta_{ST}) = 0 \\ H_t(R_{sout},\theta) = 0 \end{cases}. \tag{3.34}$$

2) The boundary conditions of the field intensity on the edge $B_S N_S$ is more complex and is defined with respect to the rotor position θ_p. For the case presented in Figure 3.6(a) where the rotor pole and stator pole overlap or partially overlap, the tangential component of magnetic field on the rotor pole surface is zero. On the other hand, in the air gap the mmf drops by F_{ag} from the stator pole surface to the rotor pole surface. To approximate the instant mmf drop in the air gap, the tangential component of the field intensity is defined as the following delta function:

$$H_t(R_{rout},\theta) = -\frac{F_{ag}}{R_{rout}}\delta(\theta - \theta_{ST}). \tag{3.35}$$

For the case in Figure 3.6(b) where the rotor pole and stator pole do not overlap, the tangential component of flux on the rotor pole surface A_SB_S is zero, and the tangential flux density on the edge N_SA_S is assumed to be constant, so in this situation

$$\begin{cases} H_t\left(R_{rout},\theta\right) = -\dfrac{F_{ag}}{R_{rout}\left(\theta_{ST}-\theta_{A_S}\right)}, \theta_{A_S} \le \theta \le \theta_{ST} \\ H_t\left(R_{rout},\theta\right) = 0, -\theta_{ST} \le \theta < \theta_{A_S} \end{cases} \tag{3.36}$$

where θ_{A_S} is the angular position of the point A_S with respect to the zero-degree line in Figure 3.6(b). The boundary condition of the tangential field intensity on the edge $r=R_{rout}$ for the left stator slot region, and the stator slot regions for the SRMs with another geometry or rotor position is calculated similarly.

Performing the Fourier expansion on the magnetic field intensity of boundary condition 2) yields

$$H_t\left(R_{rout},\theta\right) = H_{a0} + \sum_{neven} H_{an}\cos\left(m_{ns}\theta\right) + \sum_{nodd} H_{bn}\sin\left(m_{ns}\theta\right). \tag{3.37}$$

The homogeneous solution A_h that satisfies the Laplace equation in 2D polar coordinates can be expressed in the following form

$$\begin{aligned} A_h(r,\theta) = &\left(A_{0s}\ln r + B_{0s}\right)\left(C_{0s}\theta + D_{0s}\right) + \sum_{n=1}^{\infty}\left(A_{ns}r^{m_{ns}} + B_{ns}r^{-m_{ns}}\right)\cos\left(m_{ns}\theta\right) \\ &+ \sum_{n=1}^{\infty}\left(C_{ns}r^{m_{ns}} + D_{ns}r^{-m_{ns}}\right)\sin\left(m_{ns}\theta\right). \end{aligned} \tag{3.38}$$

Therefore, the final expression of magnetic potential **A** is

$$
\begin{aligned}
A(r,\theta) &= A_p(r,\theta) + A_h(r,\theta) \\
&= \left[P_{0s} r + \left(A_{0s} \ln r + B_{0s} \right) \left(C_{0s}\theta + D_{0s} \right) \right] + \sum_{n=1}^{\infty} \left(A_{ns} r^{m_{ns}} + B_{ns} r^{-m_{ns}} + P_{ns} r \right) \cos\left(m_{ns}\theta \right) \\
&\quad + \sum_{n=1}^{\infty} \left(C_{ns} r^{m_{ns}} + D_{ns} r^{-m_{ns}} + Q_{ns} r \right) \sin\left(m_{ns}\theta \right).
\end{aligned} \tag{3.39}
$$

According to boundary condition 1), $C_{0s}=0$, and the constant term does not make a difference to the calculation of final magnetic field. Define $B_{0s}=0$, $D_{0s}=1$ and the equivalent 0^{th} order component is

$$
A_{0th} = P_{0s} r + A_{0s} \ln r. \tag{3.40}
$$

It can be inferred by substituting the boundary condition 1) into (3.40), that:

$$
A_{0s} = -R_{sout} P_{0s}. \tag{3.41}
$$

The next step is to determine the Fourier coefficients A_{ns}, B_{ns}, C_{ns} and D_{ns}. According to the boundary condition 1):

$$
\begin{cases}
m_{ns} A_{ns} R_{sout}^{m_{ns}-1} - m_{ns} B_{ns} R_{sout}^{-m_{ns}-1} + P_{ns} = 0, \ for\ n = even \\
m_{ns} C_{ns} R_{sout}^{m_{ns}-1} - m_{ns} D_{ns} R_{sout}^{-m_{ns}-1} + Q_{ns} = 0, \ for\ n = odd
\end{cases}. \tag{3.42}
$$

It can be obtained from the boundary condition 2) that:

$$
\begin{cases}
m_{ns} A_{ns} R_{rout}^{m_{ns}-1} - m_{ns} B_{ns} R_{rout}^{-m_{ns}-1} + P_{ns} = -\mu_0 H_{an}, \ for\ n = even \\
m_{ns} C_{ns} R_{rout}^{m_{ns}-1} - m_{ns} D_{ns} R_{rout}^{-m_{ns}-1} + Q_{ns} = -\mu_0 H_{bn}, \ for\ n = odd
\end{cases}. \tag{3.43}
$$

Then the Fourier coefficients A_{ns}, B_{ns}, C_{ns} and D_{ns} are obtained by solving linear equations (3.42) and (3.43). The flux density is solved by substituting the magnetic vector potential in (3.39) into (3.28).

The slot leakage flux flowing between the stator pole surface M_SP_S and the stator yoke surface P_SQ_S is

$$\begin{aligned}\phi_{P_SQ_S} &= l_s R_{sout}\int_{-\theta_{ST}}^{\theta_{ST}} B_r\left(R_{sout},\theta\right)d\theta \\ &= l_s\left[\begin{array}{l}\sum_{neven}\left(A_{ns}{R_{sout}}^{m_{ns}}+B_{ns}{R_{sout}}^{-m_{ns}}+P_{ns}R_{sout}\right)\cos\left(m_{ns}\theta\right)\Big|_{-\theta_{ST}}^{\theta_{ST}} \\ \quad+\sum_{nodd}\left(C_{ns}{R_{sout}}^{m_{ns}}+D_{ns}{R_{sout}}^{-m_{ns}}+Q_{ns}R_{sout}\right)\sin\left(m_{ns}\theta\right)\Big|_{-\theta_{ST}}^{\theta_{ST}}\end{array}\right].\end{aligned} \tag{3.44}$$

The slot leakage flux that links the stator pole surface M_SP_S and the surface of another pole B_SQ_S is

$$\begin{aligned}\phi_{B_SQ_S} &= -l_s\int_{R_{rout}}^{R_{sout}} B_t\left(r,-\theta_{ST}\right)dr \\ &= l_s\left[\begin{array}{l}P_{0s}r\,|_{R_{rout}}^{R_{sout}}+A_{0s}\ln r\,|_{R_{rout}}^{R_{sout}} \\ \quad+\sum_{neven}\left(A_{ns}r^{m_{ns}}\,|_{R_{rout}}^{R_{sout}}+B_{ns}r^{-m_{ns}}\,|_{R_{rout}}^{R_{sout}}+P_{ns}r\,|_{R_{rout}}^{R_{sout}}\right)\cos\left(-m_{ns}\theta_{ST}\right) \\ \quad+\sum_{nodd}\left(C_{ns}r^{m_{ns}}\,|_{R_{rout}}^{R_{sout}}+D_{ns}r^{-m_{ns}}\,|_{R_{rout}}^{R_{sout}}+Q_{ns}r\,|_{R_{rout}}^{R_{sout}}\right)\sin\left(-m_{ns}\theta_{ST}\right)\end{array}\right].\end{aligned} \tag{3.45}$$

The fringing flux that links the rotor pole surface in the stator slot region is

$$\phi_{fs} = -l_s R_{rout}\int_{-\theta_{ST}}^{\theta_K} B_r\left(R_{rout},\theta\right)d\theta \tag{3.46}$$

where θ_K is the upper bound of the integration and is dependent on the rotor position θ_p. For the case in Figure 3.6(a) when the stator pole and rotor pole overlap or partially overlap, $\theta_K=\theta_{ST}$, while for the case shown in Figure 3.6(b) when the rotor pole is around the unaligned position, $\theta_K=\theta_{As}$.

The slot leakage permeance of the rotor slot sub-region is

$$P_{sl} = \frac{\phi_{P_SQ_S}+\phi_{B_SQ_S}}{F_{ag}}. \tag{3.47}$$

The fringing permeance of the stator slot sub-region is

$$P_{fs} = \frac{\phi_{fs}}{F_{ag}}. \tag{3.48}$$

It can be concluded from (3.30)-(3.33) that the particular solution A_p is related to the phase current I_p, while (3.34)-(3.43) indicate that the homogeneous solution A_h depends on both the phase current I_p and the airgap mmf drop F_{ag}, so the final distribution of magnetic vector potential **A** and the magnetic field **B** are determined by both I_p and F_{ag}. Because the level of saturation in the stator/rotor steel varies with the rotor positions and phase currents, the permeances in the stator/rotor steel are not constants and the relationship between I_p and F_{ag} is nonlinear. Thus, the fringing permeance in (3.48) and the slot leakage permeance in (3.47) of the stator slot regions may vary with the phase current. However, generally under normal operation, the mmf drop in the SRMs is concentrated in the air gap, so for simplicity it is assumed that in the stator slot sub-regions

$$F_{ag} \approx N_t I_p. \tag{3.49}$$

In this way, the permeances in the stator slot sub-regions have constant values that are independent of the phase currents.

3.1.2 Nonlinear Solution and Lumped-Parameter Magnetic Circuit Network

This section describes the development of the magnetic circuit network model for an SRM with any geometry and topology that allows for the saturation effects of the rotor and stator steel on the phase inductance profile. Magnetic-circuit-based methods have been applied to the analyses of SRMs and some other types of machines. In a magnetic circuit network of an SRM, the mmf sources are stator windings. The permeances in the magnetic circuit network of an SRM consist of the permeances in the air region and the permeances in the rotor and stator steel. The difficulty in deriving the permeances in the air region lies

in the fact that they are parametrically nonlinear because of the dimensional variation of flux paths with respect to the rotor position, which is overcome by solving the partial differential equations of magnetic scalar or vector potentials based on the Maxwell's equations as discussed in Section 3.1.1. However, it is infeasible to derive precise closed-form solutions for the permeances and the magnetic field distribution at each location in the steel by solving the nonlinear partial differential equations of magnetic potentials. Fortunately, the cross-sectional areas and lengths of flux paths in steel segments are easy to determine and the methods to calculate the lumped-parameter rotor/stator permeances in conventional magnetic circuits of SRMs are utilized in this chapter.

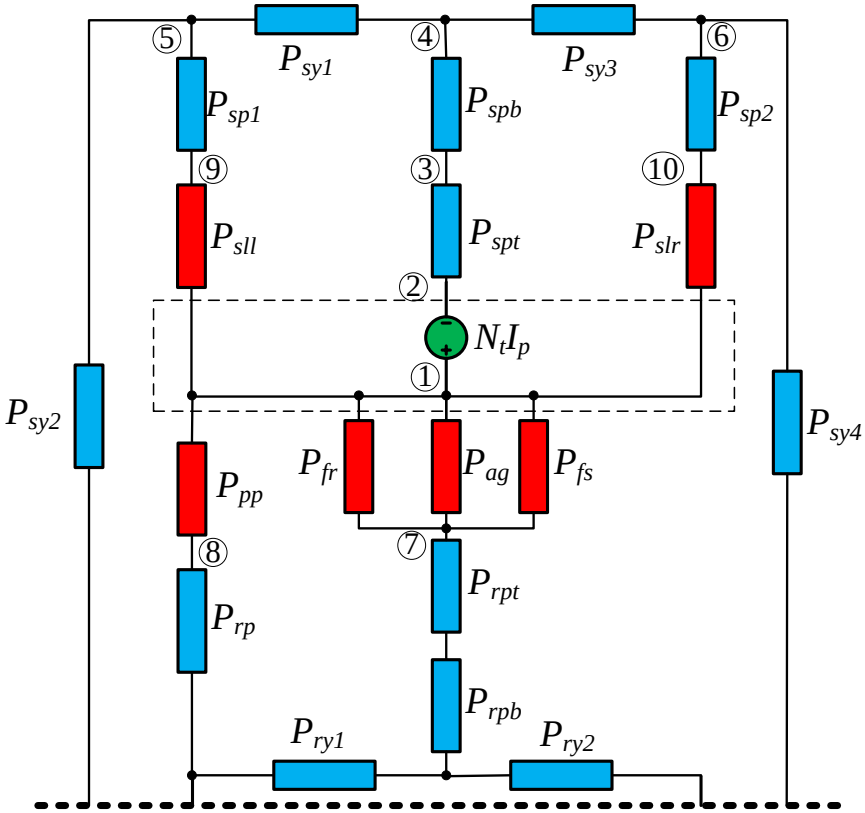

Figure 3.7 Magnetic circuit network model including all types of permeances in the upper half of the SRM in Figure 3.1 when the stator pole and rotor pole partially overlap.

The structure of the magnetic circuit network should be determined based on the SRM topology and geometry, as well as the instantaneous rotor angle. Figure 3.7

demonstrates an example of a magnetic equivalent circuit model for the upper half of the SRM in Figure 3.1 when its stator pole and rotor pole partially overlap. The source of mmf is the stator phase current represented by $F=N_tI_p$ in Figure 3.7. Aside from the air-region permeances represented by the red blocks in Figure 3.7 that have been solved in Section 3.1.1, the permeances in the blue blocks are the steel-region permeances that are functions of the cross-sectional areas, lengths and relative permeabilities of the corresponding steel segments. In Figure 3.7, separate permeance parameters are introduced to represent the stator/rotor poles, stator/rotor yokes, stator/rotor pole tips and pole bottoms. The permeability associated with the permeance of each steel segment is assumed to be non-ideal and exhibits a nonlinear relationship with the local flux density based on the manufacturer provided **B**-**H** curve of stator/rotor laminations.

The permeance parameters of the stator poles and rotor poles that overlap or partially overlap should be carefully determined. It can be concluded from Figure 3.2, Figure 3.4 and Figure 3.6(a) that when a rotor pole and a stator pole partially overlap, the magnetic flux travels through a small section in the tips of the rotor pole and stator pole, and the flux density in the pole tips exhibits a significant nonuniform distribution. The local saturation of the pole tips where magnetic flux concentrates can possibly lead to an error if the cross-sectional areas of the stator and rotor poles are assumed to be constant when calculating the permeances of the corresponding stator/rotor poles [41]. To deal with the problem caused by the local saturation, the permeance of the partially-overlapped pole is divided into two permeances representing the pole tip and pole bottom respectively. In Figure 3.7, P_{spt}, P_{spb}, P_{rpt} and P_{rpb} are the permeances of the stator pole tip, stator pole bottom, rotor pole tip and rotor pole bottom respectively. The cross-sectional area of the pole tip is less than that of the pole and varies with the overlap region. It is assumed that the cross-sectional area of stator pole tips at the inner diameter is the overlapped area between the stator and rotor poles, while at the outer diameter it is equal to the cross-

sectional area of the entire stator pole. Thus, the average cross-sectional area of a stator pole tip is

$$A_{spt} = \frac{1}{2}\left(\frac{\theta_{olp}}{2\theta_S}+1\right)W_S l_s = \frac{1}{2}\left(\frac{\theta_S+\theta_R-\theta_p}{2\theta_S}+1\right)W_S l_s \tag{3.50}$$

where θ_{olp} is the overlapped angle between the stator and rotor poles. The areas of rotor pole tips are calculated in the same way. Simulations show accurate predictions of inductance in highly saturated regions when the length of a pole tip is half of the pole width.

The flux in each element of the magnetic circuit should be calculated. This is achieved by solving the equations of the magnetic scalar potential at each node of the magnetic circuit network. Kirchhoff's Current Law is utilized to determine the relationship between the potentials at different nodes. For example, using V to express the potential at the nodes in the magnetic circuit in Figure 3.7, the equation associated with node 4 is

$$\left(V_5 - V_4\right)P_{sy1} + \left(V_6 - V_4\right)P_{sy3} + \left(V_3 - V_4\right)P_{spb} = 0. \tag{3.51}$$

The nodes adjacent to a mmf source are treated as a "pseudo" node to apply the Kirchhoff's Current Law. In Figure 3.7, node 1, node 2 and the mmf source form a "pseudo" node represented by the dashed block and the associated equations are

$$\begin{cases} V_1 - V_2 = N_t I_p \\ \left(V_1 - V_7\right)\cdot\left(P_{ag} + P_{fr} + P_{fs}\right) + \left(V_1 - V_8\right)P_{pp} + \left(V_1 - V_9\right)P_{sll} \\ \quad + \left(V_1 - V_{10}\right)P_{slr} + \left(V_2 - V_3\right)P_{spt} = 0 \end{cases}. \tag{3.52}$$

The equations at the other nodes should be set up in the same form as (3.51) or (3.52). The combination of the node equations can be integrated into the matrix form:

$$\mathbf{P}\cdot\mathbf{V} = \mathbf{f} \tag{3.53}$$

where **P** is the matrix related to the permeances, **V** is the vector of the potentials at the nodes in the magnetic circuit, and **f** is the vector associated with the constant terms in the node equations, mainly the mmf sources.

The fluxes in the elements of the magnetic circuit can be determined once the potential vector **V** is obtained. However, since the steel permeances are dependent on the local flux densities, an iterative method should be adopted to ensure the convergence of solution. The matrix **P** is updated and then a new potential vector **V** is solved in each iteration. The iterative procedure terminates when $\|\mathbf{V_c}-\mathbf{V_p}\|/\|\mathbf{V_c}\| \le \delta$, where $\mathbf{V_c}$ and $\mathbf{V_p}$ are the potential vector **V** at the current iteration and the previous iteration respectively, and δ is the precision threshold.

After the solution converges, the total flux of the stator pole in Figure 3.7 can be expressed as

$$\phi_P = (V_1 - V_7)\cdot(P_{ag} + P_{fr} + P_{fs}) + (V_1 - V_8)P_{pp} + (V_1 - V_9)P_{sll} + (V_1 - V_{10})P_{slr}. \quad (3.54)$$

And the phase inductance is

$$L = \frac{N_{sp} N_t \phi_P}{I_p}. \quad (3.55)$$

Figure 3.7 illustrates the magnetic circuit of the SRM in the scenario where only one phase winding is excited with currents. The structure of the magnetic circuit should be determined based on the SRM topology and geometry, as well as the instantaneous rotor position and the currents of each phase. Figure 3.8 illustrates an example of the magnetic circuit model for the upper half of the SRM in Figure 3.1 when the rotor is rotating clockwise and phase B and phase C are simultaneously excited. The mmf sources are the stator currents represented by green circles with the values $F=N_t I_{pP}$ *(P=A,B,C)* in Figure 3.8.

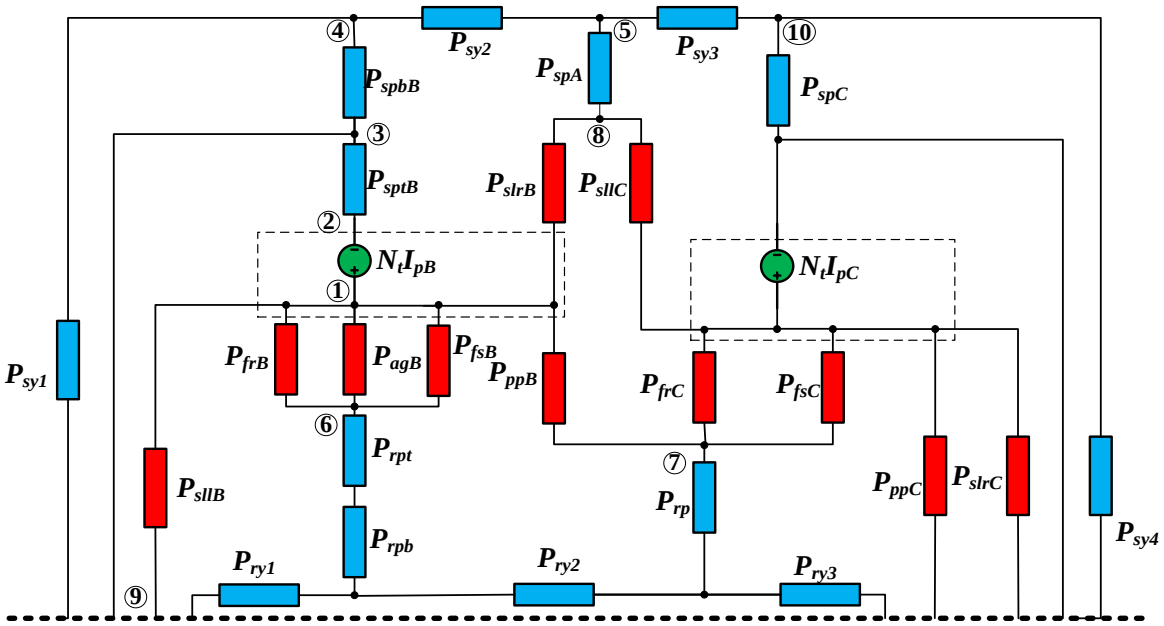

Figure 3.8 Magnetic circuit network model of the upper half of the 6/4 SRM shown in Figure 3.1 when the phase B and phase C are excited.

Similar to the analysis for the scenario with single-phase excitation, Kirchhoff's Current Law is used to compute the magnetic potentials at the nodes. For example, using *V* to express the potential at the nodes, the equation associated with node 5 in Figure 3.8 is

$$\left(V_4 - V_5\right)P_{sy2} + \left(V_{10} - V_5\right)P_{sy3} + \left(V_8 - V_5\right)P_{spA} = 0. \tag{3.56}$$

The nodes connected to an mmf source are treated as a single "dummy" node. In Figure 3.8, the dashed block containing the phase B mmf source and the nodes 1 and 2 constitutes a dummy node and the associated nodal equation becomes

$$\begin{cases} V_1 - V_2 = N_t I_{pB} \\ \left(V_1 - V_6\right)\cdot\left(P_{agB} + P_{frB} + P_{fsB}\right) + \left(V_1 - V_7\right)P_{ppB} \\ \quad + \left(V_1 - V_9\right)P_{sllB} + \left(V_1 - V_8\right)P_{slrB} + \left(V_2 - V_3\right)P_{sptB} = 0 \end{cases}. \tag{3.57}$$

The fluxes in the elements of the magnetic circuit are determined based on the magnetic potential vector **V** solved in the same way. The phase B inductance of the SRM in Figure 3.1 with the magnetic circuit in Figure 3.8 is

$$L_B = \frac{N_{sp} N_t}{i_{pB}} \left[\left(V_1 - V_6 \right) \cdot \left(P_{agB} + P_{frB} + P_{fsB} \right) + \left(V_1 - V_7 \right) P_{ppB} + \left(V_1 - V_9 \right) P_{sllB} + \left(V_1 - V_8 \right) P_{slrB} \right]. \quad (3.58)$$

The flowchart of the phase inductance profile prediction for SRMs appears in Figure 3.9.

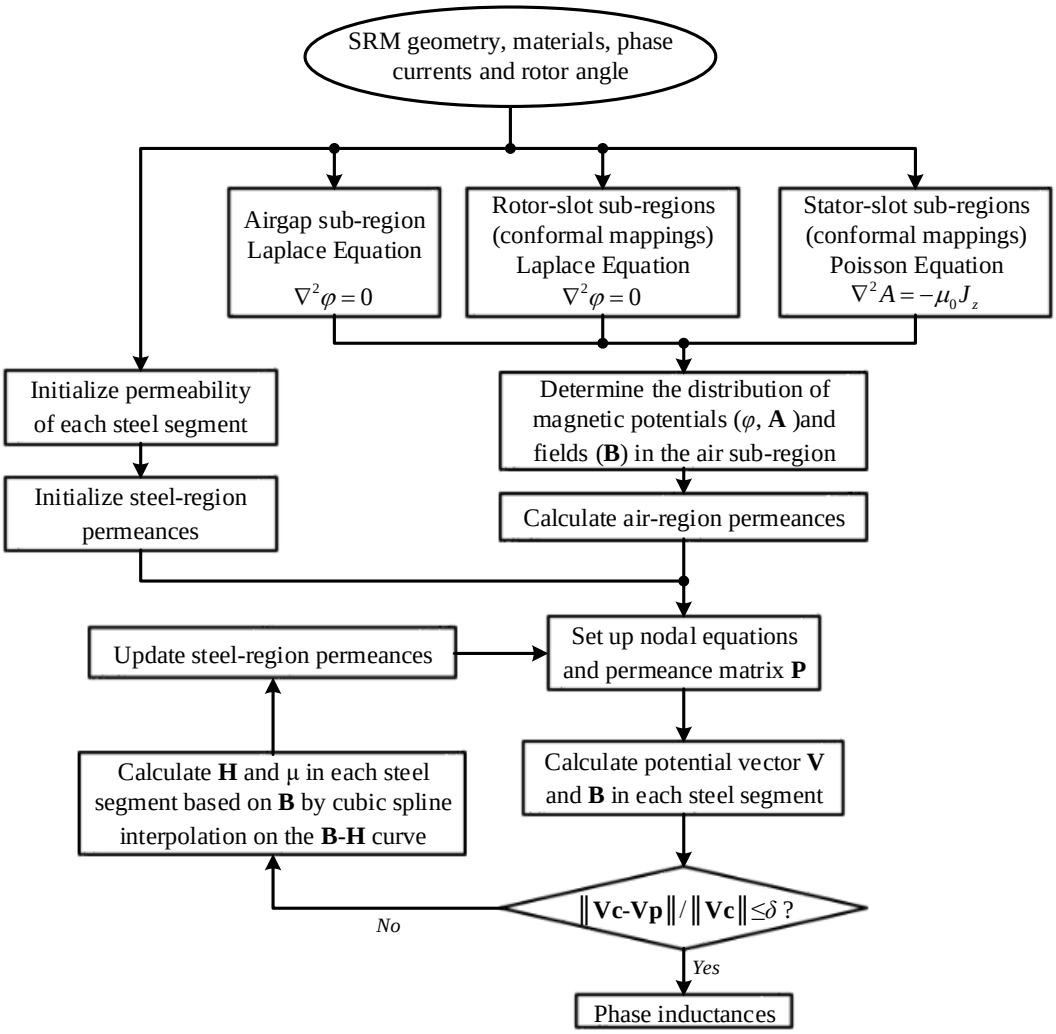

Figure 3.9 Flowchart of the phase inductance prediction.

3.1.3 Comparison between the Simulation Results of the Generalized Analytical Method and 2D/3D FEAs and Experimental Validation

3.1.3.1 Comparison between the Proposed Analytical Method and 2D FEAs

Calculations of the phase inductance profiles with different phase currents are performed for a 6/4 SRM and an 8/6 SRM. To validate the effectiveness of the above novel analytical approach, corresponding 2D FEAs are implemented in AnSys Maxwell 2D for the two SRMs with the same geometries, stator/rotor lamination materials and stator phase currents. The geometry parameters of the 6/4 SRM and the 8/6 SRM are given in Table 3.3 and Table 3.4 respectively.

Table 3.3 – Geometry parameters of the 6/4 SRM.

Parameter	**Value**	**Parameter**	**Value**
R_{sout}	27 mm	W_S	7.93 mm
R_{sin}	17 mm	W_R	8.83 mm
R_{rout}	16.5 mm	l_s	35 mm
R_{rin}	12 mm	N_t	62
R_{shaft}	6 mm	R_{core}	30.5 mm

Table 3.4 – Geometry parameters of the 8/6 SRM.

Parameter	**Value**	**Parameter**	**Value**
R_{sout}	22.8 mm	W_S	4.87 mm
R_{sin}	12.5 mm	W_R	5.11 mm
R_{rout}	12.3 mm	l_s	40 mm
R_{rin}	6.35 mm	N_t	100
R_{shaft}	3 mm	R_{core}	26 mm

Figure 3.10 and Figure 3.11 show the phase inductance profiles of the 6/4 and the 8/6 SRM respectively with respect to the rotor position calculated by using 2D FEA and the proposed analytical approach with different stator currents. In Figure 3.10 and Figure

3.11, the aligned position corresponds to the 0-degree rotor angle, and at the unaligned position the rotor angle is 45 degrees for the 6/4 SRM and 30 degrees for the 8/6 SRM. For the two SRMs, all segments of the stator and rotor steel do not saturate and operate in the linear region of the B-H curve when the stator phase current is 1 A. The agreement between the phase inductance profiles when the stator current is 1 A predicted by FEA and the analytical approach indicates that the method proposed in Section 3.1.1 of this chapter to calculate the air-region permeances is reliable and accurate. The proposed method slightly overestimates the inductance at the aligned position in the unsaturated region, but the percentage error is still less than 5%. The results of the inductance profiles in the saturation region are also given in Figure 3.10 and Figure 3.11. For either the 6/4 SRM or the 8/6 SRM, the values of inductance in the region close to the unaligned position are almost identical with different stator currents because the steel is less saturated in these situations and the mmf drop in the stator and rotor segments is small. There is some discrepancy between the results predicted by 2D FEA and the analytical method in the region where the rotor pole and stator pole partially overlap. This is compensated by introducing additional pole tip permeances in the magnetic circuit network as discussed in Section 3.1.2. The percentage error of the inductance prediction is less than 5% at all rotor positions and operating conditions for both machines. Therefore, the proposed method is suitable for SRMs with different topologies and geometries.

There are two main types of error in the proposed method. One is the error of the air-region permeances described in Section 3.1.1, and the other one is the error produced in the nonlinear iterations discussed in Section 3.1.2. To quantitatively analyze the first type of error, an additional 2D FEA and the corresponding analytical calculation are performed for the 6/4 SRM with the parameters shown in Table 3.3 assuming the steel relative permeability μ_r=1,000,000. In this situation, steel is ideal and infinitely permeable, thus the reluctances of steel segments are almost zero and the mmf drop is primarily

concentrated in the air gap, and the error is due to imperfections in computing the air-region permeances. The results of the inductance calculated by using the proposed method and 2D FEA are shown in Table 3.5. In the case when ideal magnetic steel is assumed, the analytical method overestimates the inductance at the aligned position and the error decreases as the rotor moves out of alignment. Thus, when calculating the air-region permeances, the largest discrepancy occurs at the aligned position. In the cases with non-ideal steel, as the stator current increases, the error of the predicted saturated inductance becomes even smaller as demonstrated in Table 3.5. In the highly saturated region, the discrepancy exacerbates in the region when the rotor pole and stator pole partially overlap if the pole tip permeances are not represented. If each rotor pole or stator pole is represented by only one permeance parameter without considering the reduced cross sectional area of flux at the pole tip, for θ_p=15°, the computed inductance is 4.09 mH when I_p=8 A and 3.61 mH when I_p=11 A, and the error is 3.02% and 2.84% respectively in these two cases, compared to 2.01% and 0.28% in Table 3.5.

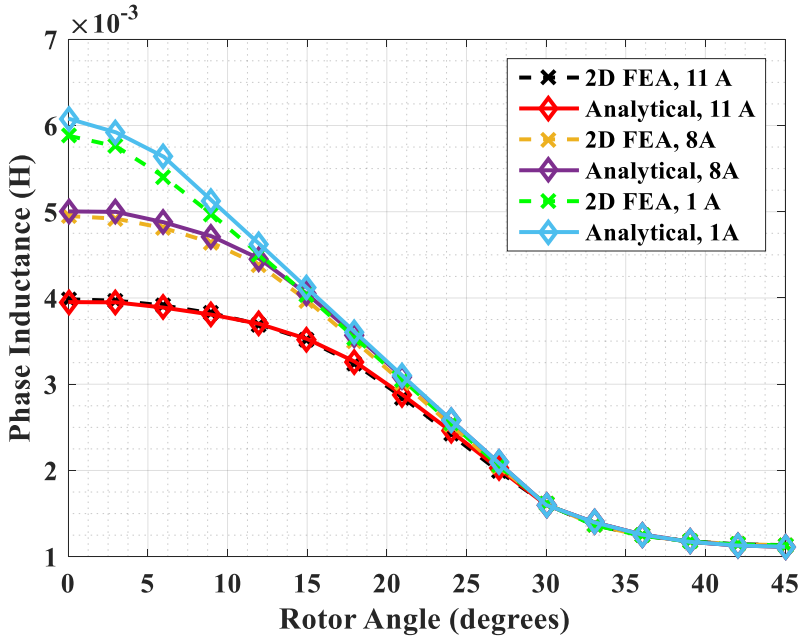

Figure 3.10 Comparison between the phase inductance profiles of the 6/4 SRM calculated by 2D FEA and the analytical method with different stator phase currents.

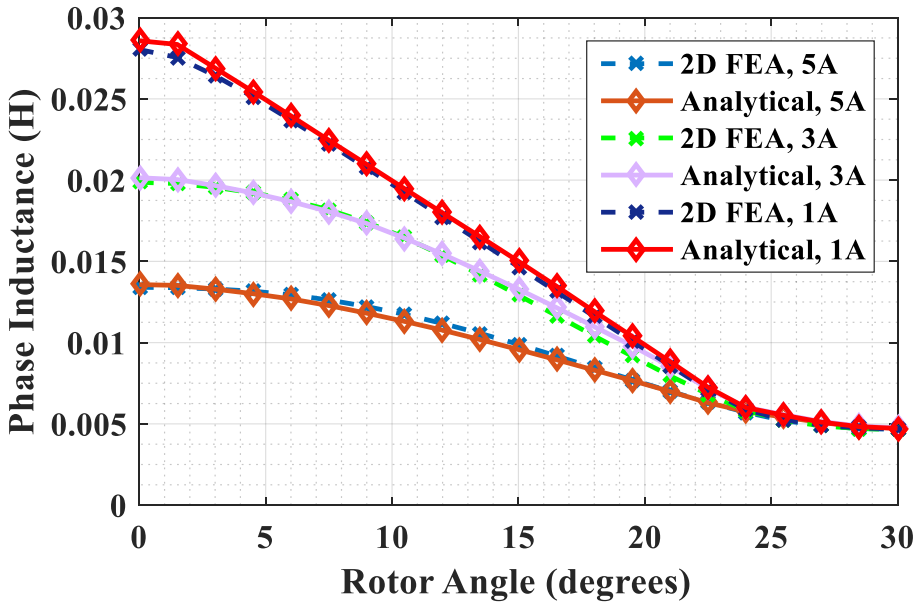

Figure 3.11 Comparison between the phase inductance profiles of the 8/6 SRM calculated by 2D FEA and the analytical method with different stator phase currents.

Table 3.5 – The Inductance Computed Using the Analytical Method and 2D FEA of a 6/4 SRM with Different Currents and Rotor Angles.

Rotor Angle		**0°**	**15°**	**30°**	**45°**
Ideal	**Analytical (mH)**	6.21	4.11	1.60	1.12
	2D FEA (mH)	5.98	4.08	1.62	1.14
	Error (%)	3.85	0.74	-1.23	-1.75
1 A	**Analytical (mH)**	6.08	4.11	1.59	1.12
	2D FEA (mH)	5.88	4.03	1.61	1.13
	Error (%)	3.40	1.99	-1.24	-0.88
8 A	**Analytical (mH)**	5.00	4.05	1.59	1.12
	2D FEA (mH)	4.95	3.97	1.61	1.13
	Error (%)	1.01	2.01	-1.24	-0.88
11 A	**Analytical (mH)**	3.95	3.52	1.59	1.12
	2D FEA (mH)	3.98	3.51	1.61	1.13
	Error (%)	-0.75	0.28	-1.24	-0.88

The proposed method can also be applied to calculate the inductance profile with multi-phase excitation. Figure 3.12 shows the phase A inductance profiles of the SRM in

Figure 3.1 (with the parameters in Table 3.3) predicted by the analytical method and the 2D FEA with multi-phase or single-phase excitation. In the case of multi-phase excitation, the rotor moves counter- clockwise from the unaligned position to the aligned position of phase A and the stator currents of phase A and phase B are 8 A and 4 A respectively. In this case, mmf sources representing the phase A and phase B currents and the associated air-region permeances are substituted into the magnetic circuit in Figure 3.8 with proper adjustments of the MEC structure. In the single-phase excitation scenario, the phase A current is 8 A and there are no currents in phases B and C. Figure 3.12 shows good agreement between the phase inductances calculated by the proposed method and 2D FEA. Figure 3.12 indicates that in the region close to the aligned position, the phase A inductance is smaller when phase B is also excited. This is because in some segments of the stator yoke, e.g., P_{sy1}, P_{sy2} and P_{sy4} in Figure 3.7, the fluxes produced by phase A and phase B currents strengthen each other, thus increasing the saturation level and the steel reluctances in the magnetic circuit.

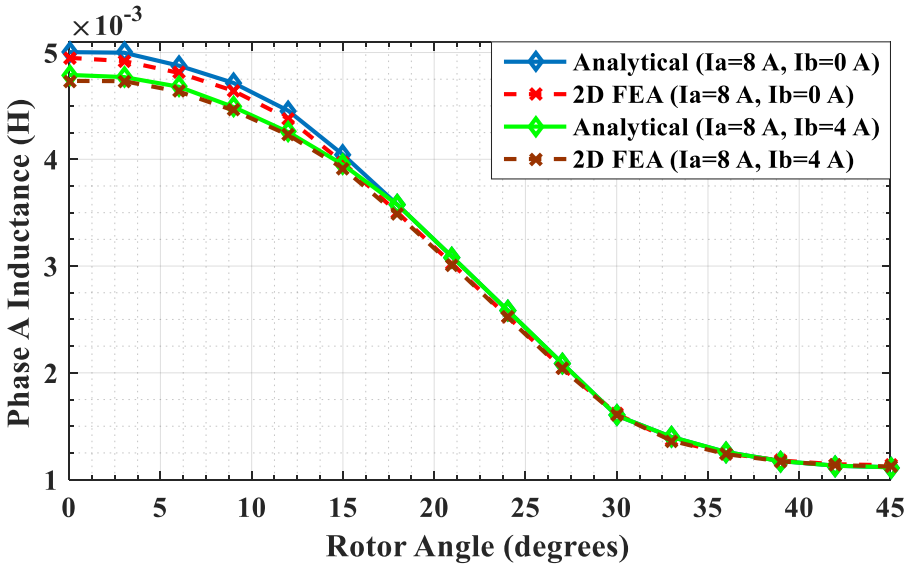

Figure 3.12 Comparison between the phase A inductances with respect to the rotor angle of the 6/4 SRM calculated by 2D FEA and the proposed analytical method with and without multi-phase excitation.

Once the inductance is obtained, the torque in dynamic operation is given by

$$T = \frac{1}{2}\frac{dL\left(\theta_p, i_p\right)}{d\theta_p} {i_p}^2. \tag{3.59}$$

As an example, the torque profiles of the 6/4 SRM obtained by 2D FEA and the analytical method are illustrated in Figure 3.13. In the simulations, the rotor speed is 10,000 rpm and the three phases are sequentially excited with a maximum current 7 A. The average torque calculated by 2D FEA is 179.3 mN·m, while the value with analytical prediction is 182.6 mN·m with an error of 1.84%. Therefore, the proposed method is an effective tool to predict the dynamic performances of SRMs.

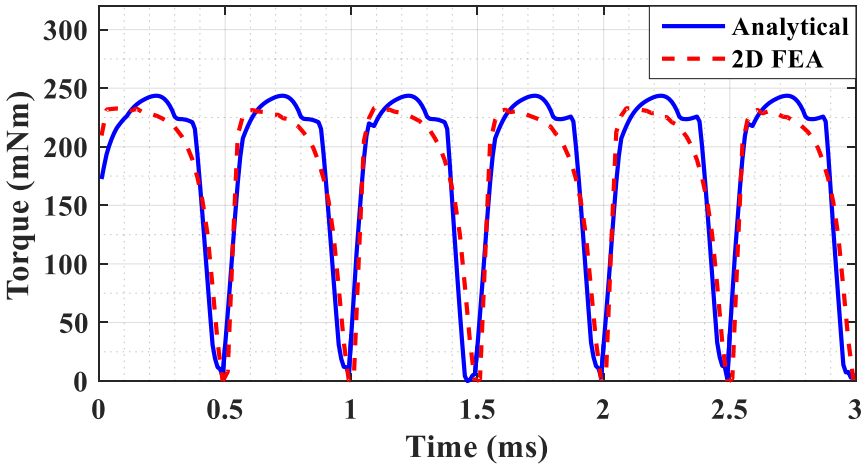

Figure 3.13 Torque profiles of the 6/4 SRM calculated by 2D FEAs and the proposed analytical method.

3.1.3.2 Comparison between the Proposed Analytical Method and 3D FEAs

3D FEAs are conducted for the 6/4 SRM with the same parameters in TABLE III to further validate the proposed analytical method. Figure 3.14 presents the inductance profiles of the SRM with respect to the rotor position computed by using the analytical approach and 2D/3D FEAs. The inductance calculated by 3D FEA is larger than that by

2D FEA for all rotor positions, because in 3D FEAs the effect of fringing flux in the end region is included when calculating inductance, which cannot be modeled in any 2D magnetic analysis. Correspondingly, the discrepancy between the results of the analytical method and 3D FEA becomes smaller at the aligned position but increases at the unaligned position. When I_p=8 A the absolute error is -0.12 mH at the unaligned position and the percentage error is -9.6%. When compared to 3D FEA, the error of the analytical method is acceptable.

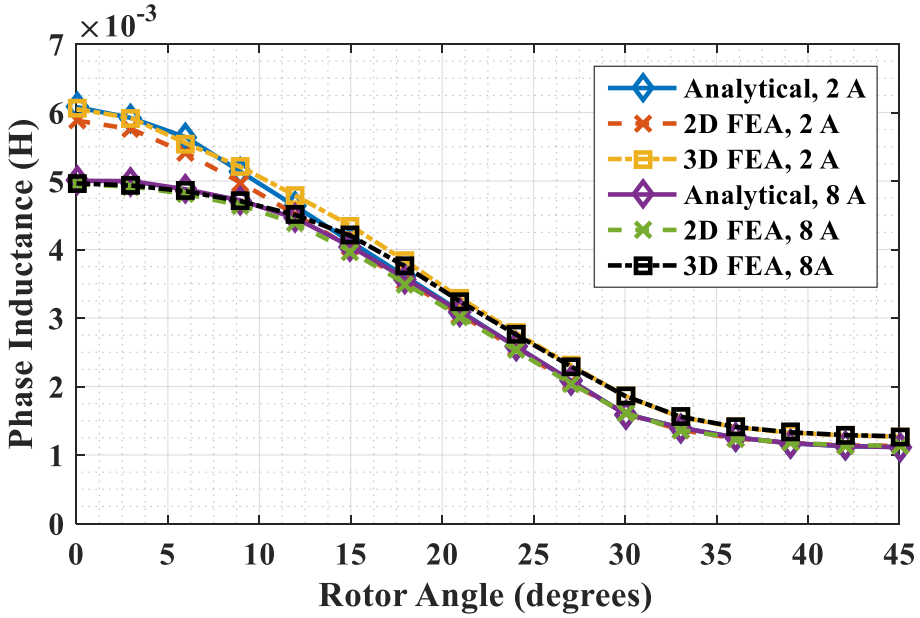

Figure 3.14 Comparison between the phase inductance profiles with respect to the rotor angle of the 6/4 SRM calculated by 2D/3D FEAs and the proposed analytical method.

3.1.3.3 Experimental Validation

The flux linkage of a 6/4 SRM with the parameters in Table 3.3 is measured at different rotor positions with respect to phase current. The rated speed of the SRM is 8,000 rpm and its rated power is 200 W. In the measurement, the rotor is locked in a specific position, and ac voltage is applied to the relevant stator windings of one phase, and thus flux linkage is calculated by using the voltage and current data in that position. The ac

voltage is provided by a single-phase transformer connected to the power system, so the magnitude of the ac voltage is adjustable and its frequency is locked at 60 Hz. The experimental data of phase voltages and currents are recorded by a digital oscilloscope Tektronix TDS5034B and transferred to a computer. The rotor position is then changed and the same process is repeated.

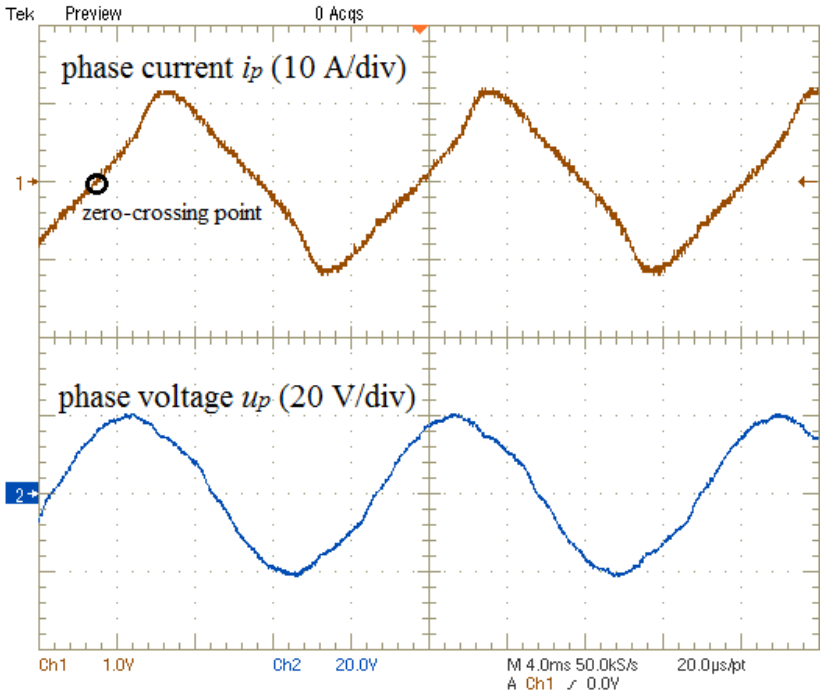

Figure 3.15 Measured phase current and voltage of a 6/4 SRM at the aligned position.

The flux linkage in an SRM is estimated from the voltage and current data:

$$\lambda = \int_{t_0}^{t_1} \left(u_p - i_p R_S \right) dt \tag{3.60}$$

where u_p is the phase voltage and R_S is the phase resistance. To obtain the value of R_S, a small ac voltage is applied to make sure that the steel does not saturate, and the waveforms of phase voltage and current should be sinusoidal at 60 Hz. Then a Fourier transform is performed to calculate the phasor $\mathbf{u_p}$ of the phase voltage and $\mathbf{i_p}$ of the stator current at fundamental frequency, and R_S can be expressed by

$$R_S = \mathrm{Re}(Z_S) = \mathrm{Re}\left(\frac{\mathbf{u}_p}{\mathbf{i}_p}\right) \tag{3.61}$$

where Z_S is the equivalent stator impedance. In real-time measurements, higher-order harmonics appear in the current waveform when the magnitude of the ac voltage increases leading to steel saturation, as illustrated in Figure 3.15. The starting point t_0 and the ending point t_1 of the integration interval should also be determined for the flux linkage calculation in (3.60). The ending point t_1 is selected when phase current is equal to the desired value, and the starting time t_0 is the current zero-crossing point in Figure 3.15 when there is no flux linkage of the phase winding.

Figure 3.16 presents the comparison between the measured flux linkages of this 6/4 SRM and the predicted values by using the proposed method. The corresponding inductances when the stator phase current is 4A, 8A and 12 A are shown in Table 3.6. The percentage error of all predicted values shown in Figure 3.16 and Table 3.6 is below 10%. Therefore, the analytical model presented in this section gives acceptable results.

Table 3.6 – The Inductance Obtained by the Analytical Method and Physical Measurements of a 6/4 SRM with Different Currents and Rotor Angles.

Rotor Angle		**0°**	**15°**	**30°**	**45°**
4 A	**Analytical (mH)**	6.01	4.12	1.59	1.12
	Measured (mH)	6.19	4.03	1.69	1.23
	Error (%)	-2.91	2.23	-5.92	-8.94
8 A	**Analytical (mH)**	5.00	4.05	1.59	1.12
	Measured (mH)	4.89	3.97	1.72	1.23
	Error (%)	2.25	2.02	-7.56	-8.94
12 A	**Analytical (mH)**	3.55	3.22	1.59	1.12
	Measured (mH)	3.63	3.13	1.65	1.21
	Error (%)	-2.20	2.88	-3.64	-7.44

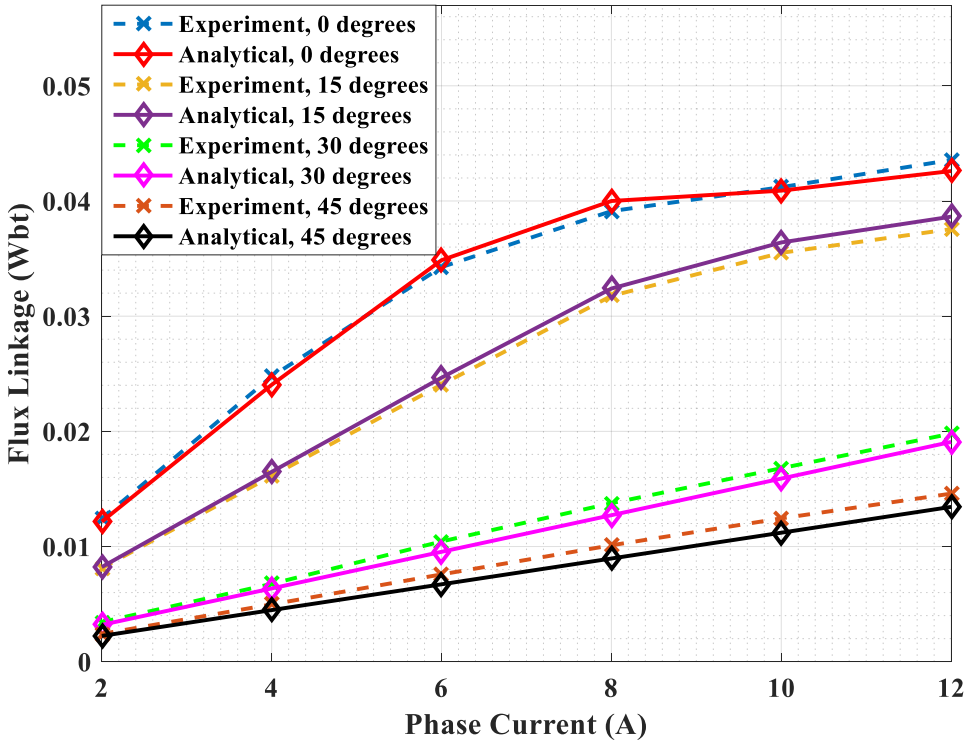

Figure 3.16 Comparison between the measured and analytically predicted flux linkages of the 6/4 SRM.

3.2 Enhanced Analytical Electromagnetic Model of SRMs

In the generalized SRM analytical EM model described in Section 3.1, to enable the closed-form expressions of magnetic potentials, the side boundaries of the stator/rotor slots are forced to be radially directed, which introduces error to the performance estimation due to the slight difference from a real SRM geometry. This section presents an enhanced analytical approach to predict the electromagnetic behaviors of SRMs. Based on the method proposed in Section 3.1, a series of conformal mappings, including the Schwarz-Christoffel (S-C) transformation is adopted to map the rotor slots and stator slots to rectangular regions in a magnetically equivalent manner and thus makes it possible to carry out an accurate analysis on the magnetic field in these regions. Hence the errors

caused by the regularization of geometries in the process of deriving the closed-form solutions are eliminated.

3.2.1 Determining the Magnetic Field and Permeances in the Air Region

3.2.1.1 General Descriptions and the List of Machine Parameters

The assumptions of the enhanced EM model are the same as those in Section 3.1.1, except that the assumption 4) is removed and the associated errors caused by this assumption are eliminated in this improved model.

Because it is difficult to formulate a precise analytical model of the magnetic field in the region of the air and windings with complex geometries as a whole, this region is thus divided into three types of sub-regions as illustrated in Figure 3.17, which is similar to the method in Section 3.1: the air gap sub-regions, rotor slot sub-regions, and stator slot sub-regions. To calculate the phase A inductance of the 6/4 SRM in Figure 3.17, the magnetic field in the air gap region (red), the rotor slot region (orange), and the left/right stator slot regions (green/blue) should be analyzed separately. Owing to the symmetry of the magnetic field, only the upper half of the SRM in Figure 3.17 is analyzed to accelerate the simulation by using the anti-periodic boundary conditions when calculating the permeances in the relevant magnetic circuit and in FEAs [179].

The SRM phase inductance at an arbitrary rotor position is associated with the variables in Table 3.7. The last 6 parameters are dependent on the other variables above in TABLE I and the expressions of these dependencies are presented in

Table 3.8. Assuming that the rotor of the SRM in Figure 3.17 is rotating clockwise, at one time instant the rotor position θ_p is defined as the angle between the centers of the stator pole and rotor pole. The value range of θ_p is $[0, \pi/N_R]$.

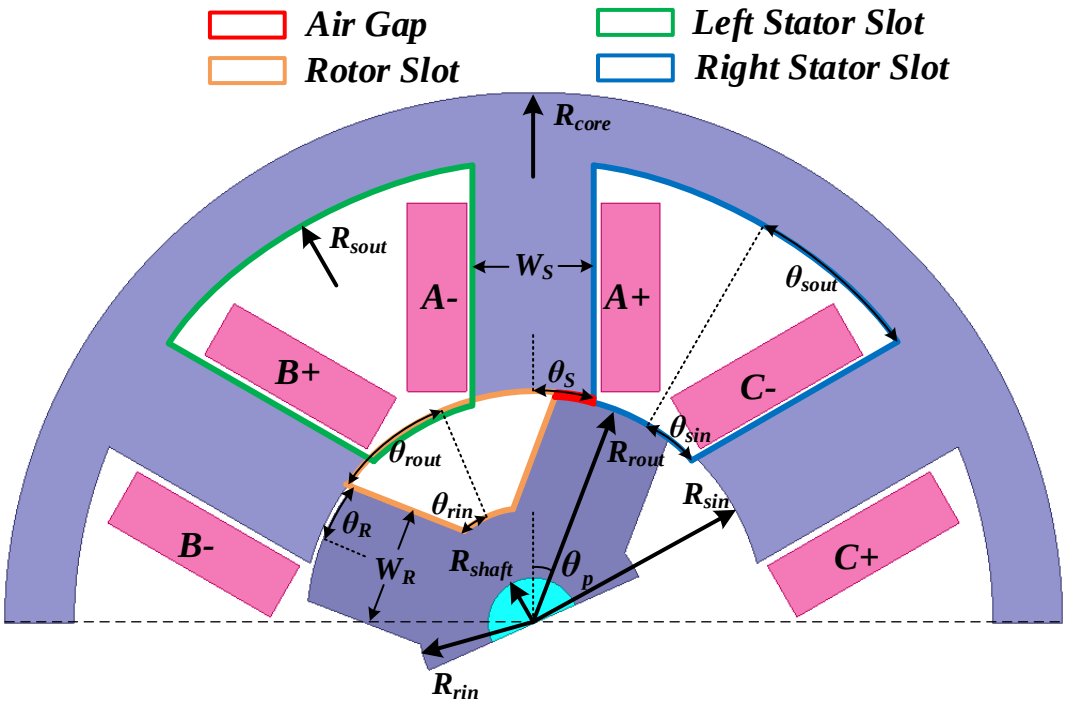

Figure 3.17 Cross-section view of the upper half of an SRM and the representation of geometric parameters.

Table 3.7 – Independent SRM geometric parameters.

Parameter	Parameter
Stator slot outer radius R_{sout}	Stator pole width W_S
Stator pole inner radius R_{sin}	Rotor pole width W_R
Rotor pole outer radius R_{rout}	Shaft outer radius R_{shaft}
Rotor slot inner radius R_{rin}	Stator yoke outer radius R_{core}
Stator length l_s	No. turns/pole/phase N_t
No. stator poles N_S	No. rotor poles N_R
No. phases N_p	Stator phase current I_p
half stator pole angle θ_S	half rotor pole angle θR
half angular span of rotor slots at ID θrin	half angular span of rotor slots at OD $\theta rout$
half angular span of stator slots at inner diameter (ID) θsin	half angular span of stator slots at outer diameter (OD) $\theta sout$

Table 3.8 – Dependencies of the SRM parameters.

Parameter	Expression
θ_S	$sin^{-1}[W_S/(2R_{sin})]$
θ_R	$sin^{-1}[W_R/(2R_{rout})]$
θ_{sin}	$\pi/N_S - sin^{-1}[W_S/(2R_{rout})]$
θ_{sout}	$\pi/N_S - sin^{-1}[W_S/(2R_{sout})]$
θ_{rin}	$\pi/N_R - sin^{-1}[W_R/(2R_{rin})]$
θ_{rout}	$\pi/N_R - sin^{-1}[W_R/(2R_{sin})]$

The method to determine the magnetic field and permeance parameters in the air-gap sub-region in the enhanced method is the same as the generalized method in Section 3.1, but there exist significant differences between them in the approach to estimate the magnetic fields in the rotor slot and stator slot sub-regions.

3.2.1.2 Rotor Slot Sub-Region

Since there are no windings in the rotor slots, so the Laplace equation (3.2) of magnetic scalar potential also holds in the rotor slot sub-region. However, directly specifying of the boundary conditions analytically on the two non-radial side surfaces A_SB_S and D_SC_S in the S plane with the original geometry in Figure 3.18 is infeasible under the scheme of separating variables since $\theta_{rin} \neq \theta_{rout}$. To deal with this problem, in Section 3.1 the two side surfaces are modified to be parallel with the radial direction and θ_{rin} is forced to be equal to θ_{rout}, which brings intrinsic inaccuracy due to this geometry change. This section, however, takes a more rigorous and precise approach that utilizes the method of conformal mapping, a useful tool to assist solving the Laplace or Poisson equations in a complicated region by transforming the original solution domain to a simpler domain for easier calculations without sacrificing the accuracy. Once the solution is obtained in the simpler domain, it can then be mapped back to the original domain [180]. The rotor slot region is eventually transformed to a rectangular region.

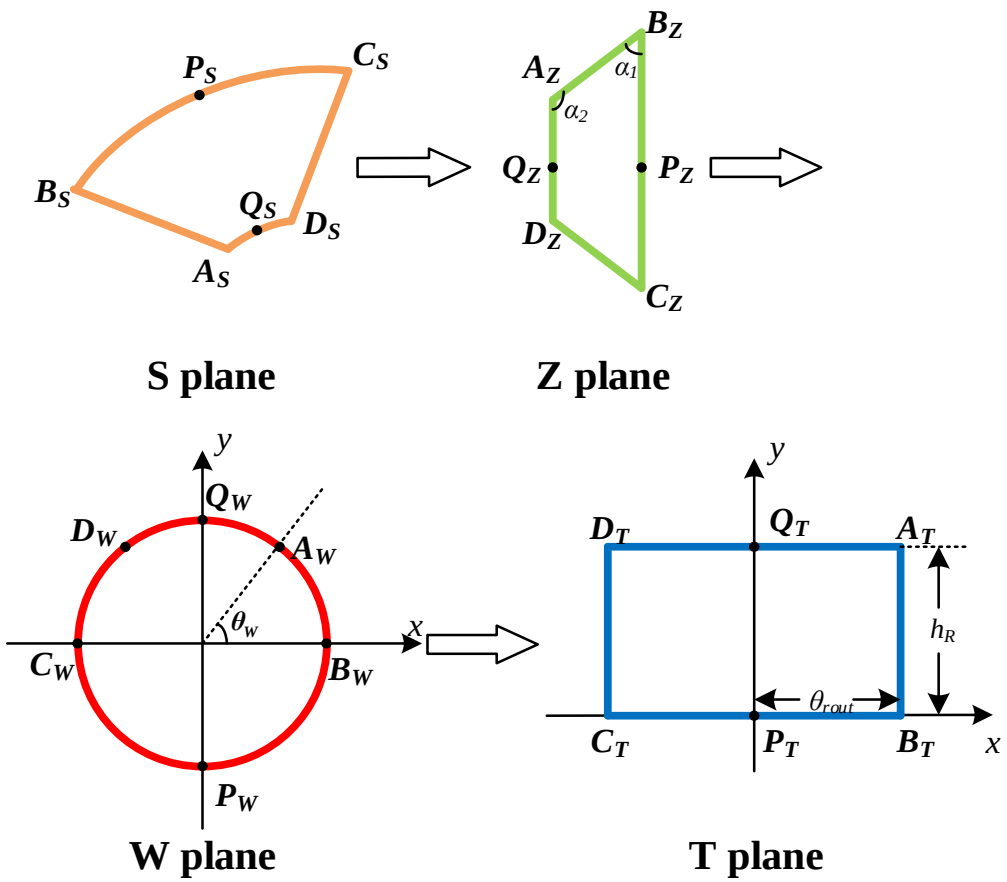

Figure 3.18 Sequence of conformal mappings on the rotor slot sub-region.

S-C transformation is the essential component of the serial conformal mappings in Figure 3.18. The S-C mapping theorem is stated as follows [56]. Let P be the interior of a polygon Γ having n vertices w_1, w_2, …, w_n, and interior angles $\alpha_1\pi$, $\alpha_2\pi$, …, $\alpha_n\pi$, in the counterclockwise order. Let f be any conformal map from the upper half-plane H^+ to P with $f(\infty)=w_n$. Then, for some complex constants A_0 and C_0, where $w_k=f(z_k)$ for 1, …, $n-1$

$$w = f(z) = A_0 + C_0 \int_{z_0}^{z} \prod_{k=1}^{n-1} (\zeta - z_k)^{\alpha_k - 1} \, d\zeta \tag{3.62}$$

where $z = x + yi$ and $w = u + vi$ denote complex numbers in the z- and w-planes, respectively in Figure 3.19. This theorem states that a conformal map (a complex map that

preservers angles locally) can always be constructed that maps the upper (lower) half-plane to the interior (exterior) of any polygon, and that the mapping will have the above form (3.62). The theorem is useful because it allows a boundary value problem in a irregular arbitrary polygon-shaped domain to solved by first solving a simpler problem in a canonical domain and then mapping the result back to the original domain.

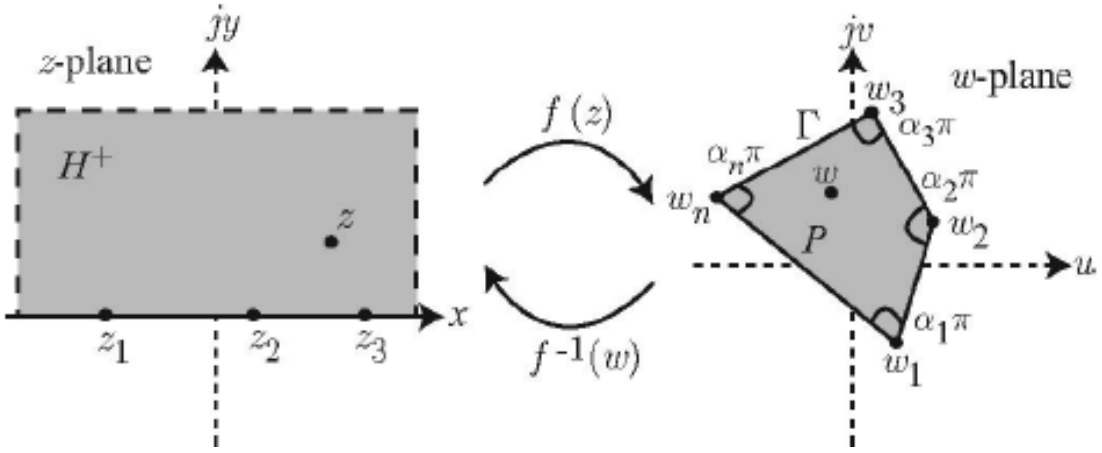

Figure 3.19 Illustration of the S-C mapping theorem showing the upper half-plane H^+ mapped to the interior P of a polygon Γ [56].

Figure 3.18 shows the sequential conformal mappings. The original geometry of the rotor slot (orange frame in Figure 3.17) in the S plane is firstly transformed into its linear model in the Z plane by a logarithmic conformal transformation [180]:

$$z = \ln(s);\ \frac{\partial z}{\partial s} = \frac{1}{s}. \tag{3.63}$$

In the Z plane, the x-coordinate represents the logarithm of the radius and the y-coordinate indicates the angular position of a point. Then the geometry in the Z plane is mapped to a unit disk in the W plane by the following S-C transformation [56]:

$$\frac{\partial z}{\partial w} = C_0 \cdot (w-1)^{\frac{\alpha_1}{\pi}-1} (w+1)^{\frac{\alpha_1}{\pi}-1} \left(w - e^{i\theta_w}\right)^{\frac{\alpha_2}{\pi}-1} \left(w + e^{-i\theta_w}\right)^{\frac{\alpha_2}{\pi}-1} \tag{3.64}$$

where C_0 is a complex constant to be determined, α_1 and α_2 are the interior angles in the Z plane at the points B_Z (or C_Z) and A_Z (or D_Z) respectively, and θ_W is the phase angle of the point A_W in the W plane. The interior angles α_1 and α_2 are

$$\begin{cases} \alpha_1 = \tan^{-1}\left(\dfrac{\ln\left(R_{sin}\right) - \ln\left(R_{rin}\right)}{\theta_{rout} - \theta_{rin}} \right). \\ \alpha_2 = \pi - \alpha_1 \end{cases} \tag{3.65}$$

The constants C_0 and θ_W can be determined by integrating along the intervals P_W~B_W and B_W~ A_W on the unit disk in the W plane and comparing the integrations to the corresponding intervals P_Z~B_Z and B_Z~ A_Z on the polygon in the Z plane:

$$\begin{cases} C_0 \cdot \int_{-i}^{1} \left(w-1\right)^{\frac{\alpha_1}{\pi}-1} \left(w+1\right)^{\frac{\alpha_1}{\pi}-1} \left(w-e^{i\theta_W}\right)^{\frac{\alpha_2}{\pi}-1} \left(w+e^{-i\theta_W}\right)^{\frac{\alpha_2}{\pi}-1} dw = i\theta_{rout} \\ C_0 \cdot \int_{1}^{e^{i\theta_W}} \left(w-1\right)^{\frac{\alpha_1}{\pi}-1} \left(w+1\right)^{\frac{\alpha_1}{\pi}-1} \left(w-e^{i\theta_W}\right)^{\frac{\alpha_2}{\pi}-1} \left(w+e^{-i\theta_W}\right)^{\frac{\alpha_2}{\pi}-1} dw \\ = \ln\left(\dfrac{R_{rin}}{R_{sin}}\right) + i\left(\theta_{rin} - \theta_{rout}\right) \end{cases} . \tag{3.66}$$

Finally, another S-C transformation is performed to map the unit disk to a rectangular region in the T plane. All the interior angles of the polygon in the T plane are $\pi/2$, so the S-C transformation is given by

$$\frac{\partial t}{\partial w} = C_1 \cdot \left[\left(w-1\right)\left(w+1\right)\left(w-e^{i\theta_W}\right)\left(w+e^{-i\theta_W}\right) \right]^{-0.5}. \tag{3.67}$$

For the convenience of assigning the boundary conditions in the T plane, regulate the distance between P_T and B_T to be θ_{rout}. Then the complex constant C_1 and the height of the rectangle h_R (the distance between A_T and B_T) in the T plane are

$$\begin{cases} C_1 = \theta_{rout} \Big/ \int_{-i}^{1} \left[(w-1)(w+1)\left(w-e^{i\theta_W}\right)\left(w+e^{-i\theta_W}\right) \right]^{-0.5} dw \\ h_R = \left(-C_1 \cdot i\right) \cdot \int_{1}^{e^{i\theta_W}} \left[(w-1)(w+1)\left(w-e^{i\theta_W}\right)\left(w+e^{-i\theta_W}\right) \right]^{-0.5} dw \end{cases}. \tag{3.68}$$

Before the analytical expressions of the magnetic field are given, the following lemma is introduced that significantly simplifies the calculation of the flux and permeances.

***Lemma 1*:** Suppose that *t=f(s)* is the conformal mapping that transforms the magnetic scalar potential φ from the *S* plane to the *T* plane, then the magnetic flux on the ideal magnetic iron boundaries of the region calculated in the *T* plane is equivalent to that solved on the corresponding boundaries in the *S* plane.

***Proof*:** Suppose $\mathbf{B}_S$ and $\mathbf{B}_T$ are the flux density vector calculated in the *S* plane and *T* plane respectively, and **dS** and **dT** are the element tangential vector on the boundaries in the *S* plane and *T* plane respectively. The equations that map the magnetic field solution and the element vectors from the *T* plane to the *S* plane are [180]:

$$\begin{cases} \mathbf{B}_S = \mathbf{B}_T \left(\dfrac{\partial t}{\partial w} \cdot \dfrac{\partial w}{\partial z} \cdot \dfrac{\partial z}{\partial s} \right)^* = \mathbf{B}_T \left(\dfrac{\partial t}{\partial s} \right)^* \\ \mathbf{dS} = \left(\dfrac{\partial s}{\partial z} \cdot \dfrac{\partial z}{\partial w} \cdot \dfrac{\partial w}{\partial t} \right) \mathbf{dT} = \left(\dfrac{\partial s}{\partial t} \right) \mathbf{dT} \end{cases}. \tag{3.69}$$

On the ideal magnetic iron boundaries where $\mu_{fe} \approx \infty$, the **B** vectors are orthogonal to the geometric boundaries. Suppose that $\mathbf{dT} = a + jb$ and $\partial s/\partial t = c + jd$, then $\mathbf{B}_T = \lambda(-b + ja)$, where *a*, *b*, *c*, *d* and λ are real numbers. Define $\mathbf{a}_z$ to be the unit vector in the axial direction, then

$$\mathbf{B}_S \times \mathbf{dS} = \left[\mathbf{B}_T \cdot \left(\frac{\partial t}{\partial s} \right)^* \right] \times \left[\mathbf{dT} \cdot \left(\frac{\partial s}{\partial t} \right) \right] = \lambda \left(a^2 + b^2 \right) \mathbf{a}_z = \mathbf{B}_T \times \mathbf{dT}. \tag{3.70}$$

Therefore, the flux on the ideal magnetic iron boundaries in the *S* plane and *T* plane are equal:

$$\Phi_S = l_s \left\| \int_{\Gamma_S} \mathbf{B_S} \times \mathbf{dS} \right\| = l_s \left\| \int_{\Gamma_T} \mathbf{B_T} \times \mathbf{dT} \right\| = \Phi_T \tag{3.71}$$

where Γ_S and Γ_T are the corresponding integration interval on the ideal magnetic iron boundaries in the *S* plane and *T* plane respectively. Since the calculation of the air-region permeances are associated with the flux on these iron boundaries, *Lemma 1* indicates that after the magnetic field in the rotor slot region in the *T* plane is solved, it is not necessary to map the field back to the *S* plane to estimate the flux linkage or permeances.

Denote the magnetic scalar potential in the rotor slot sub-region as φ_{rotor}. The distribution of φ_{rotor} in the *T* plane can be expressed by the homogeneous solution of the Laplace equation of the magnetic scalar potential in 2D Cartesian coordinates without the component of particular solution [178]:

$$\varphi_{rotor}(x,y) = \sum_{n=1}^{\infty} \left[\begin{array}{r} \left(A_n \sinh m_n y + B_n \cosh m_n y\right) \cdot \cos m_n x \\ + \left(C_n \sinh m_n y + D_n \cosh m_n y\right) \cdot \sin m_n x \end{array} \right] \tag{3.72}$$

where the coefficients A_n, B_n, C_n, D_n and m_n are determined by the boundary conditions specified as follows:

1) Since the rotor is assumed to be ideal magnetic iron in this section, the tangential **B** field on the radially inner surface of the rotor slot (A_SD_S in the *S* plane) is zero, and the corresponding magnetic scalar potential on the boundary A_TD_T in the *T* plane satisfies

$$\varphi_{rotor}(x, h_R) = 0. \tag{3.73}$$

2) Similarly, the φ_{rotor} on the two side surfaces C_TD_T and A_TB_T in the *T* plane is also defined to be zero:

$$\varphi_{rotor}\left(\theta_{rout}, y\right)=0, \varphi_{rotor}\left(-\theta_{rout}, y\right)=0. \tag{3.74}$$

3) The boundary condition of φ_{rotor} on the radially outer surface of the rotor slot (C_TB_T in the T plane) is defined with respect to the rotor position θ_p. The entire value range of θ_p should be divided into several intervals based on the topology and geometry of the SRM and the boundary conditions are specified for each interval individually. For example, for the 6/4 SRM shown in Figure 3.17, for the rotor position interval [π/4 - θ_{rout} - θ_S, θ_S + θ_{rout} - π/12] when the rotor pole and stator pole partially overlap, the boundary condition $\varphi_{rotor}(x,0)$ is defined as the following piecewise linear function:

$$\varphi_{rotor}\left(x,0\right)=\begin{cases} F_{ag}, -\theta_{rout} \le x \le \theta_p+\theta_S-\pi/4 \\ -F_{ag}\left(x+\theta_S-\theta_p-\pi/12\right)\Big/\left(\pi/3-2\theta_S\right), \\ \qquad\qquad \theta_p+\theta_S-\pi/4 \le x \le \theta_p-\theta_S+\pi/12 \\ 0, \theta_p-\theta_S+\pi/12 \le x \le \theta_{rout} \end{cases}. \tag{3.75}$$

The boundary condition of φ_{rotor} on C_TB_T should be derived for the other scenarios depending on the rotor position or for an SRM with different numbers of stator and rotor poles in a similar way. The basic principle is that on the surface of the stator pole with phase current and hence an mmf source, $\varphi_{rotor}=F_{ag}$, while on the surface of another stator pole without current or a rotor pole, φ_{rotor}=0. It is difficult to derive a precise expression of the boundary condition of φ_{rotor} along the peripheral edge between poles with an analytical approach. To obtain an approximate solution of the magnetic field, it is assumed that the tangential **B** field is constant and φ_{rotor} linearly drops from F_{ag} to 0 along the edge between the two poles.

According to the boundary condition 1),

$$\begin{cases} A_n \sinh\left(m_n h_R\right)+B_n \cosh\left(m_n h_R\right)=0 \\ C_n \sinh\left(m_n h_R\right)+D_n \cosh\left(m_n h_R\right)=0 \end{cases}. \tag{3.76}$$

Applying the boundary condition 2) to (3.72) yields

$$\begin{cases} m_n = (n\pi)/(2\theta_{rout}) \\ A_n = B_n = 0,\ n = \text{even} \\ C_n = D_n = 0,\ n = \text{odd} \end{cases}. \tag{3.77}$$

For a certain rotor position θ_p, expand $\varphi_{rotor}(x,0)$ defined in the boundary condition 3) into the following Fourier series:

$$\varphi_{rotor}(x,0) = \sum_{nodd} F_{rotor\_an} \cos\left(\frac{n\pi}{2\theta_{rout}} x\right) + \sum_{neven} F_{rotor\_bn} \sin\left(\frac{n\pi}{2\theta_{rout}} x\right) \tag{3.78}$$

where

$$\begin{cases} F_{rotor\_an} = \dfrac{1}{\theta_{rout}} \int_{-\theta_{rout}}^{\theta_{rout}} \varphi_{rotor}(x,0) \cos\left(\dfrac{n\pi}{2\theta_{rout}} x\right) dx,\ n = \text{odd} \\ F_{rotor\_bn} = \dfrac{1}{\theta_{rout}} \int_{-\theta_{rout}}^{\theta_{rout}} \varphi_{rotor}(x,0) \sin\left(\dfrac{n\pi}{2\theta_{rout}} x\right) dx,\ n = \text{even} \end{cases}.$$

Substituting the Fourier coefficients F_{rotor_an} and F_{rotor_bn} solved in (3.78) and (3.77) into (3.72) yields

$$\begin{cases} B_n = F_{rotor\_an} \\ D_n = F_{rotor\_bn} \end{cases}. \tag{3.79}$$

The coefficients A_n and C_n can be solved by combining (3.76), (3.77) and (3.79). Then the distribution of the magnetic scalar potential φ_{rotor} in (3.72) is determined for each rotor position θ_p and the corresponding **H** field in the rotor slot sub-region is predicted by taking the negative gradient of φ_{rotor}.

The rotor-slot fringing flux is defined as the flux impinging the rotor pole/yoke surfaces C_SD_S and A_SD_S in the original S plane. According to *Lemma 1*, this flux is equal

to the total flux on the boundaries C_TD_T and A_TD_T in the T plane. Thus, the rotor-slot fringing flux and permeance are calculated based on the transformed T plane:

$$\begin{cases} \Phi_{fr} = \Phi_{A_TD_T} + \Phi_{C_TD_T} \\ \quad = \mu_0 l_s \left[\int_{-\theta_{rout}}^{\theta_{rout}} H_y\left(x, h_R\right) dx - \int_0^{h_R} H_x\left(-\theta_{rout}, y\right) dy \right] \\ \quad = \mu_0 l_s \left[-\int_{-\theta_{rout}}^{\theta_{rout}} \left(\frac{\partial \varphi_{rotor}}{\partial y} \right)\left(x, h_R\right) dx + \int_0^{h_R} \left(\frac{\partial \varphi_{rotor}}{\partial x} \right)\left(-\theta_{rout}, y\right) dy \right]. \\ P_{fr} = \dfrac{\Phi_{fr}}{F_{ag}} \end{cases} \tag{3.80}$$

Similarly, the rotor-slot pole-to-pole flux entering the surface A_SB_S of another rotor pole and the related permeance are

$$\begin{cases} \Phi_{pp} = \Phi_{A_TB_T} = \mu_0 l_s \int_0^{h_R} H_x\left(\theta_{rout}, y\right) dy \\ \qquad = -\mu_0 l_s \int_0^{h_R} \left(\frac{\partial \varphi_{rotor}}{\partial x} \right)\left(\theta_{rout}, y\right) dy \\ P_{pp} = \dfrac{\Phi_{pp}}{F_{ag}} \end{cases}. \tag{3.81}$$

3.2.1.3 Stator Slot Sub-Regions

The magnetic field should be solved in both the left and right stator slots in Figure 3.17. Similar to the rotor slot region, sequential conformal mappings are performed on the stator slot regions. Figure 3.20 shows the conformal mapping from the original S plane to the final T plane for the right stator slot sub-region in Figure 3.17, where the intermediate transformations (Z plane and W plane in Figure 3.18) are omitted. For the convenience of specifying the boundary conditions of the transformed region in the T plane, the distance between P_T and B_T is regulated to be θ_{sin}. Then the height of the transformed rectangle h_S in the T plane (the length of A_TB_T in Figure 3.20) is determined in a similar way to the calculation of h_R in (3.68) for the rotor slot sub-region.

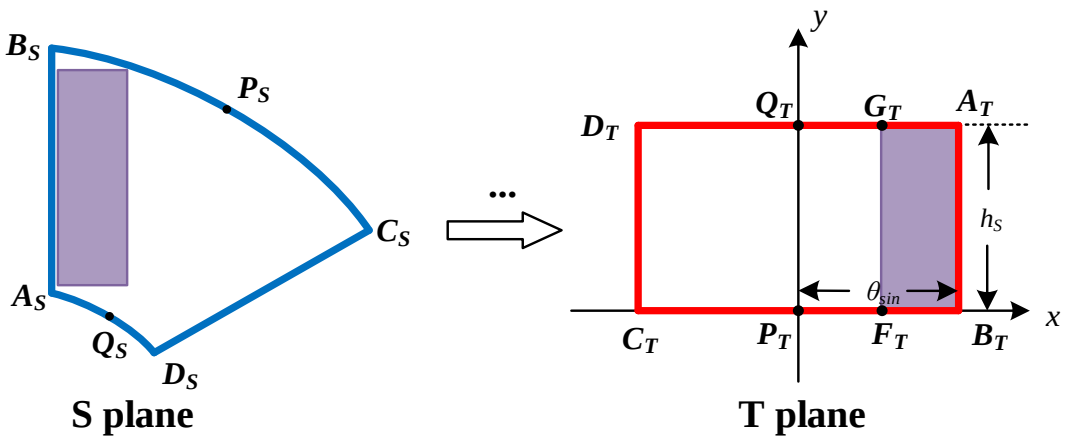

Figure 3.20 Conformal mapping on the right stator slot sub-region.

Because of the presence of stator windings carrying currents in stator slots, the Laplace equation of the magnetic scalar potential φ does not hold in stator slot regions. Consequently, the magnetic field in the stator slot sub-regions is formulated by the Poisson equation of the magnetic vector potential **A**. According to the assumption 2) in Section 3.1.1, only the axial component of **A** is considered in mathematical modelling. For the convenience of the following discussions, define $\mathbf{A}=A\mathbf{a}_z$. The flux density vector **B** can thus be expressed by **A** in 2D Cartesian coordinates [178]:

$$\mathbf{B}=\nabla\times\mathbf{A}=\frac{\partial A}{\partial y}\mathbf{a}_x-\frac{\partial A}{\partial x}\mathbf{a}_y \tag{3.82}$$

where $\mathbf{a}_x$ and $\mathbf{a}_y$ are the unit vector in the *x*-direction and *y*-direction respectively. The Poisson equation of A in the stator slot sub-regions is derived as follows:

$$\begin{aligned}\left(\nabla^2 A\right)\mathbf{a}_z&=\left(\frac{\partial^2 A}{\partial x^2}+\frac{\partial^2 A}{\partial y^2}\right)\mathbf{a}_z=-\mu_0\nabla\times\left(\frac{1}{\mu_0}\nabla\times\mathbf{A}\right)\\&=-\mu_0\nabla\times\frac{1}{\mu_0}\mathbf{B}=-\mu_0\nabla\times\mathbf{H}=\left(-\mu_0 J\right)\mathbf{a}_z\end{aligned} \tag{3.83}$$

where J is the current density in A/m^2. Similarly, *Lemma 2* is introduced to simplify the calculation of the permeances and fluxes in the stator slot sub-regions.

***Lemma 2*:** Suppose that $t=f(s)$ is the conformal mapping that transforms the axial component of **A** from the S plane ($s = u + jv$) to the T plane ($t = x + jy$), then the magnetic flux on the ideal magnetic iron boundaries of the region calculated in the T plane is equivalent to that solved in the S plane.

***Proof*:** The Poisson equation of A in the S plane is

$$\frac{\partial^2 A}{\partial u^2}+\frac{\partial^2 A}{\partial v^2}=-\mu_0 J_S \tag{3.84}$$

where J_S is the source current density in the S plane. Then the corresponding Poisson equation of A in the T plane is [181]

$$\frac{\partial^2 A}{\partial x^2}+\frac{\partial^2 A}{\partial y^2}=-\mu_0 J_S \left| f'(s)\right|^{-2}=-\mu_0 J_T \tag{3.85}$$

where J_T is the transformed current density in the T plane. Equation (3.85) indicates that the current density in the T plane is different from that in the S plane. But the total currents in the S plane and T plane are identical, because

$$\begin{aligned}\int_T J_T(x,y)\,dxdy &= \int_S \left| f'(s)\right|^{-2} J_S(u,v)\left|\frac{\partial(x,y)}{\partial(u,v)}dudv\right| \\ &= \int_S \left| f'(s)\right|^{-2} J_S(u,v)\left[\left(\frac{\partial x}{\partial u}\right)^2+\left(\frac{\partial x}{\partial v}\right)^2\right]dudv \\ &= \int_S J_S(u,v)dudv.\end{aligned} \tag{3.86}$$

The next step is to discuss the relationship between the **B** vectors solved by A in the S plane and in the T plane. The flux density is the curl of **A**, so in the T plane

$$\mathbf{B_T} = B_x + jB_y = \frac{\partial A}{\partial y} - j\frac{\partial A}{\partial x}. \tag{3.87}$$

And flux density in the *S* plane is

$$\begin{aligned}\mathbf{B_S} &= B_u + jB_v = \frac{\partial A}{\partial v} - j\frac{\partial A}{\partial u} \\ &= \left(-B_y\frac{\partial x}{\partial v} + B_x\frac{\partial y}{\partial v}\right) - j\left(-B_y\frac{\partial x}{\partial u} + B_x\frac{\partial y}{\partial u}\right).\end{aligned} \tag{3.88}$$

Applying the Cauchy-Riemann conditions [180] to (37):

$$\mathbf{B_S} = \left(B_x + jB_y\right)\left(\frac{\partial x}{\partial u} - j\frac{\partial y}{\partial u}\right) = \mathbf{B_T}\left(\frac{\partial t}{\partial s}\right)^*. \tag{3.89}$$

Equation (3.89) in which **B** is represented by *A* has the same form as that of (3.69) when the magnetic field is formulated by φ. Then *Lemma 2* can be proven by following the same procedures described in the proof of *Lemma 1*.

The solution of the vector potential in (3.83) is the combination of a homogeneous solution and a particular solution. The homogeneous solution satisfies the Laplace equation and is selected to satisfy the specified boundary conditions, while the particular solution complies with the Poisson equation that corresponds to the source current distribution but is allowed to be determined regardless of the boundary conditions. It is necessary to define the distribution of the stator current density in the *T* plane to find the particular solution of *A* in (3.83). Rigorously mapping the current density from the *S* plane to the *T* plane is complex and difficult. For simplicity, the winding is modeled as a rectangular block $F_TB_TA_TG_T$ in the *T* plane. The width of the winding is θ_e (the distance between F_T and B_T). The total currents in the *S* and *T* planes are equal (N_tI_p). Then the distribution of the current density in the *T* plane is defined as

$$J_T(x,y)=\begin{cases}\dfrac{N_t I_p}{\theta_e h_S}, \theta_{sin}-\theta_e \le x \le \theta_{sin} \\ 0, \text{otherwise}\end{cases}. \tag{3.90}$$

The Fourier expansion of current density with respect to x is

$$\begin{aligned} J_T(x,y) &= \frac{NI}{2\theta_{sin}h_S}+\sum_{neven}\left(-\frac{2NI}{\theta_e h_S n\pi}\right)\sin\left(\frac{n\pi(\theta_{sin}-\theta_e)}{2\theta_{sin}}\right)\cos\left(\frac{n\pi}{2\theta_{sin}}x\right) \\ &+\sum_{nodd}\left(\frac{2NI}{\theta_e h_S n\pi}\right)\cos\left(\frac{n\pi(\theta_{sin}-\theta_e)}{2\theta_{sin}}\right)\sin\left(\frac{n\pi}{2\theta_{sin}}x\right) \\ &= J_{a0}+\sum_{neven}J_{an}\cos(m_n x)+\sum_{nodd}J_{bn}\sin(m_n x). \end{aligned} \tag{3.91}$$

A feasible particular solution that satisfies (3.85) and (3.91) is

$$A_p(x,y)=-\frac{\mu_0 J_{a0}}{2}y^2+\sum_{neven}\frac{\mu_0 J_{an}}{m_n^{\,2}}\cos(m_n x)+\sum_{nodd}\frac{\mu_0 J_{bn}}{m_n^{\,2}}\sin(m_n x). \tag{3.92}$$

The next step is to define the boundary conditions of A in (3.85) to derive the homogeneous solution. For the right stator slot in Figure 3.20, the boundary conditions are defined as:

1) Due to the assumption 1) in Section 3.1.1, the peripheral component of the **H** vector on the stator yoke surface $B_S C_S$ is zero, and the **H** field tangential to the stator pole surfaces $A_S B_S$ and $C_S D_S$ is zero in the S plane. Equivalently, in the T plane:

$$\begin{cases} H_y(\theta_{sin},y)=H_y(-\theta_{sin},y)=0 \\ H_x(x,0)=0 \end{cases}. \tag{3.93}$$

2) On the edge $A_T D_T$ (radially inner surface $A_S D_S$ of stator slot in the S plane), the boundary conditions of **H** field should be defined with respect to the rotor position θ_p. For the scenario where the rotor pole and stator pole overlap or partially overlap, e.g., when θ_p is within the interval $[0, \pi/6-\theta_{sin}+\theta_R]$ for the 6/4 SRM in Figure 3.17, the tangential **H**

field (H_θ in the S plane and H_x in the T plane) on the rotor pole surface is zero. To approximate the MMF drop in the air gap by F_{ag} from the stator pole surface to the rotor pole surface, the tangential **H** field H_x in the T plane is expressed by the delta function:

$$H_x\left(x,h_S\right)=-F_{ag}\delta\left(x-\theta_{sin}\right) \tag{3.94}$$

For the scenario where the rotor pole is close to the unaligned position and the rotor pole and stator pole do not overlap, the tangential **H** field is zero on the rotor surface and is assumed to be constant on the edge between the stator and rotor poles with an mmf drop F_{ag}. For the example of the 6/4 SRM in Figure 3.17 when θ_p is within $[\pi/6\text{-}\theta_{sin}+\theta_R,\ \pi/4]$:

$$H_x\left(x,h_S\right)=\begin{cases}-\dfrac{F_{ag}}{\theta_p+\theta_{sin}-\theta_R-\pi/6}, x\in\left[\theta_R-\theta_p+\dfrac{\pi}{6},\theta_{sin}\right]\\ 0, x\in\left[-\theta_{sin},\theta_R-\theta_p+\pi/6\right]\end{cases}. \tag{3.95}$$

Performing Fourier expansion on H_x in boundary condition 2) with respect to x yields

$$H_x\left(x,h_S\right)=H_{a0}+\sum_{neven}H_{an}\cos\left(m_nx\right)+\sum_{nodd}H_{bn}\sin\left(m_nx\right). \tag{3.96}$$

The homogeneous solution A_h that satisfies the Laplace equation can be expressed in the following form:

$$\begin{aligned}A_h\left(x,y\right)&=A_0xy+B_0x+C_0y+D_0\\&\quad+\sum_{n=1}^{\infty}\left[\begin{array}{l}\left(A_n\sinh m_ny+B_n\cosh m_ny\right)\cdot\cos m_nx\\ \quad+\left(C_n\sinh m_ny+D_n\cosh m_ny\right)\cdot\sin m_nx\end{array}\right].\end{aligned} \tag{3.97}$$

Since $A = A_p + A_h$, it can be inferred from the boundary conditions 1) and 2) that

$$\begin{cases} A_0 = B_0 = C_0 = 0 \\ A_n = C_n = 0 \\ B_n = 0,\ n = \text{odd} \\ D_n = 0,\ n = \text{even} \\ B_n = \left(\mu_0 H_{an}\right) \Big/ \left[m_n \sinh\left(m_n h_S\right) \right],\ n = \text{even} \\ D_n = \left(\mu_0 H_{bn}\right) \Big/ \left[m_n \sinh\left(m_n h_S\right) \right],\ n = \text{odd} \end{cases} . \tag{3.98}$$

The parameter D_0 does not make a difference to the field solution so define D_0=0. Then A in the right stator slot is

$$A(x,y) = A_p(x,y) + A_h(x,y) = -\frac{\mu_0 J_{a0}}{2} y^2 + \sum_{neven} \left[B_n \cosh\left(m_n y\right) + \frac{\mu_0 J_{an}}{m_n^{\,2}} \right] \cos\left(m_n x\right) + \sum_{nodd} \left[D_n \cosh\left(m_n y\right) + \frac{\mu_0 J_{bn}}{m_n^{\,2}} \right] \sin\left(m_n x\right). \tag{3.99}$$

The slot leakage flux is the flux flowing between the surface $A_S B_S$ and the surfaces $B_S C_S$ and $C_S D_S$ in the original S plane. In the T plane, its value and the permeance are

$$\begin{cases} \Phi_{slr} = \Phi_{C_T B_T} + \Phi_{C_T D_T} = l_s \left[\int_{-\theta_{sin}}^{\theta_{sin}} \left(-B_y\left(x,0\right) \right) dx + \int_0^{h_S} \left(-B_x\left(-\theta_{sin}, y\right) \right) dy \right] \\ \qquad = l_s \left[\int_{-\theta_{sin}}^{\theta_{sin}} \left(\frac{\partial A}{\partial x} \right)(x,0)\, dx + \int_0^{h_S} \left(-\frac{\partial A}{\partial y} \right)\left(-\theta_{sin}, y\right) dy \right] \\ P_{slr} = \dfrac{\Phi_{slr}}{F_{ag}} \end{cases} . \tag{3.100}$$

The stator-slot fringing flux that travels between the stator pole surface $A_S B_S$ and the rotor pole located on the edge $A_S D_S$ in the S plane and the related permeance are

$$\begin{cases} \Phi_{fsr} = \Phi_{D_T K_T} = l_s \int_{-\theta_{sin}}^{\theta_K} B_y\left(x, h_S\right) dx = l_s \int_{-\theta_{sin}}^{\theta_K} \left(-\frac{\partial A}{\partial x} \right)\left(x, h_S\right) dx \\ P_{fsr} = \Phi_{fsr} \big/ F_{ag} \end{cases} \tag{3.101}$$

where θ_K is a variable about the rotor position θ_p, depending on different scenarios discussed in the description of the boundary condition 2). For the 6/4 SRM in Figure 3.17,

$$\begin{cases} \theta_K = \theta_{sin}, \theta_p \in [0, \pi/6 - \theta_{sin} + \theta_R] \\ \theta_K = \theta_R - \theta_p + \pi/6, \theta_p \in [\pi/6 - \theta_{sin} + \theta_R, \pi/4] \end{cases}. \tag{3.102}$$

A similar analysis can be carried out for the left stator slot sub-region to obtain the slot leakage and fringing permeances P_{sll} and P_{frl}.

3.2.2 Simulation and Experimental Validation

3.2.2.1 Comparison between the Results of the Proposed Method and FEAs

The method of nonlinear solution and lumped-parameter MEC model of the SRM in the enhanced method that incorporates the effects of saturation is the same as the model described in Section 3.1.2. To validate the effectiveness of the novel analytical approach, corresponding 2D FEAs are performed in Ansys Maxwell for a 6/4 and an 8/6 SRM with the same geometries and material properties. The parameters of the two SRMs appear in Table 3.9 and Table 3.4, respectively.

Table 3.9 – Parameters of the simulated 6/4 SRM.

Parameter	Value	Parameter	Value
R_{sout}	30.4 mm	θ_S	0.2618 rad
R_{sin}	15.3 mm	θ_R	0.2672 rad
R_{rout}	15 mm	l_s	40 mm
R_{rin}	7.6 mm	N_t	95
R_{shaft}	3 mm	R_{core}	35 mm

The comparison between the phase inductances of the two SRMs calculated by the proposed analytical method and FEA with different current and rotor positions is presented in Figure 3.21. The stator current only flows in the windings of one phase. For both SRMs,

the zero-degree indicates the aligned rotor position and the unaligned rotor angle is 45° for the 6/4 SRM or 30° for the 8/6 SRM. The steel is not saturated and operates in the linear region when the current I_p = 1 A. The agreement between the results of the proposed analytical method and 2D FEA when I_p = 1 A proves the reliability and accuracy of the approach in Section II that estimates the magnetic field distribution and permeances in the air region. The inductance decreases as the stator current increases and the steel becomes saturated when the stator and rotor poles overlap or partially overlap. Figure 3.21 confirms that the magnetic circuit method described in Section 3.1.2 possesses a good performance of incorporating the saturation effects of steel in the inductance prediction for SRMs with different geometries and topologies.

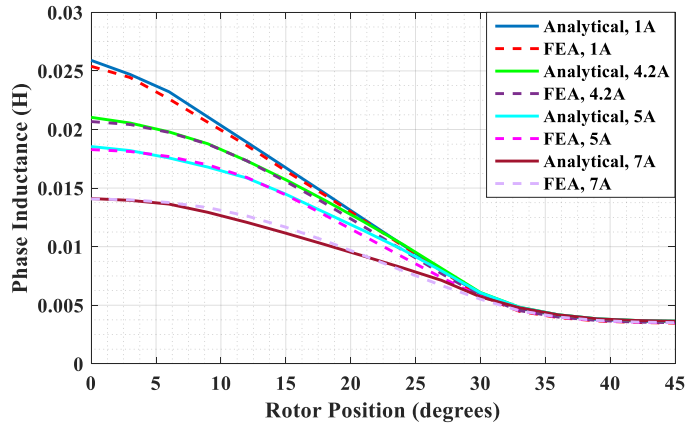

(a)

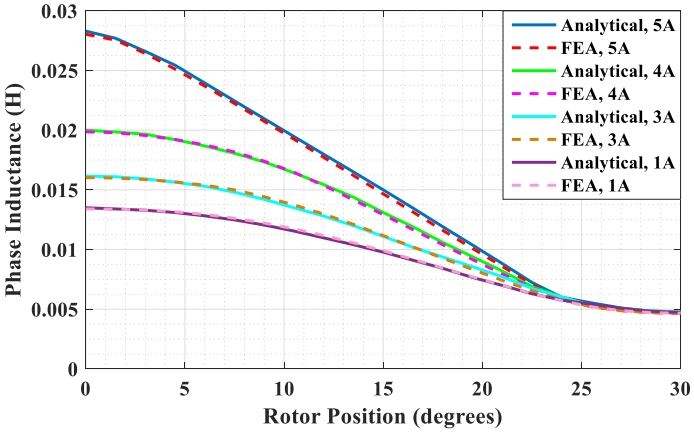

(b)

Figure 3.21 Comparison between the phase inductances of the (a) 6/4 SRM; (b) 8/6 SRM calculated by the proposed analytical method and FEA.

The magnetic circuit method presented in Section 3.1.2 can also be utilized to calculate the phase inductance for the scenarios where the windings of multiple phases are excited, and the relevant results of phase A inductance are demonstrated in Figure 3.22 for the 6/4 SRM with the parameters in Table 3.9. In these simulations, the rotor of the SRM in Figure 3.17 moves clockwise from the aligned position to the unaligned position of phase A. Figure 3.22 shows that when the rotor and stator poles overlap and I_{pA} = 5 A, the phase A inductance with a 5-A current fed into the phase B windings is smaller than that without multi-phase excitation, which is because the fluxes contributed by the phase B winding MMF reinforce the fluxes generated by phase A current in the stator back-iron segments P_{sy1}, P_{sy3} and P_{sy4} in Figure 3.8, thus rendering them more saturated and less permeable. However, when I_{pA} = 7 A, the inductance close to the aligned position is slightly larger when the same 5-A current is applied to phase B. This is because the fluxes produced by phase B current do not considerably increase the reluctances of the segments P_{sy1}, P_{sy3} and P_{sy4} that are already highly saturated, but rather cancel the flux generated by phase A current in the segment P_{sy2} and significantly decrease its reluctance. Figure 3.22 demonstrates that the magnetic circuit method in Section 3.1.2 can effectively capture these small changes in the phase inductance of an SRM when multi-phase excitation occurs.

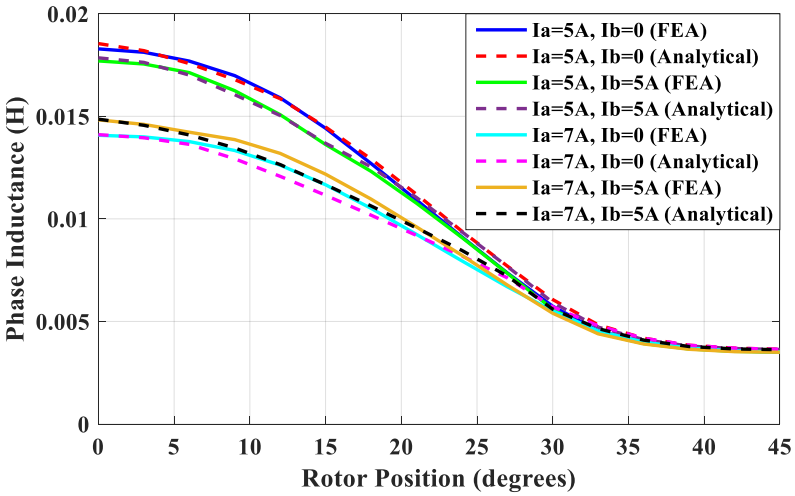

Figure 3.22 Comparison between the phase A inductances of the 6/4 SRM calculated by the proposed analytical method and FEA with and without multi-phase excitation.

Table 3.10 – The permeances computed using the two analytical methods and 2D FEA of the 6/4 SRM.

Rotor Angle		15°	30°	45°
P_{fr}	**2D FEA (μH)**	0.1244	0.1395	0.125
	Method 1 (μH)	0.1159	0.1245	0.1234
	Error 1 (%)	-6.83	-7.89	-1.28
	Method 2 (μH)	0.1023	0.1136	0.11
	Error 2 (%)	-17.8	-18.6	-12.0
P_{fsr}	**2D FEA (μH)**	0.0812	0.0829	0.0139
	Method 1 (μH)	0.0869	0.0869	0.0135
	Error 1 (%)	7.02	4.83	-2.88
	Method 2 (μH)	0.0944	0.0944	0.0149
	Error 2 (%)	16.3	13.9	7.19
P_{slr}	**2D FEA (μH)**	0.0251	0.0236	0.0272
	Method 1 (μH)	0.0242	0.0242	0.0294
	Error 1 (%)	-3.59	2.54	8.09
	Method 2 (μH)	0.0297	0.0297	0.0318
	Error 2 (%)	18.3	25.9	16.9

To show the superiority and improvement of the proposed method to predict the magnetic field and permeances in rotor slot and stator slot sub-regions compared to the approach presented in Section 3.1 based on cylindrical coordinates without conformal mapping, another 2D FEA, together with the two analytical methods, are performed on the 6/4 SRM with the parameters in Table 3.9 assuming the relative permeability of steel μ_r = 1,000,000. In this situation, the mmf drop in the stator and rotor segments can be neglected and is concentrated in the air gap. The permeances in the rotor-slot and stator-slot regions are obtained by taking the integration of the impinging fluxes on the corresponding surfaces of steel in the 2D FEA. The values of P_{fr} of the rotor slot, and P_{fsr} and P_{slr} of the right stator slot at the rotor angles 15°, 30° and 45° predicted by the 2D FEA and the two analytical

methods are shown in Table 3.10. It can be observed from Table 3.10 that although the method in Section 3.1 without conformal mapping can provide an accurate solution of overall phase inductance, it underestimates the flux and permeances in the rotor slot sub-region and overestimates the relevant components in the stator slot sub-regions. The primary reason for this phenomenon is that the surfaces A_SB_S and C_SD_S of the rotor slot in Figure 3.18 are forced to be radially directed to acquire a closed-form solution in cylindrical coordinates, which increases the angle between A_SB_S and B_SC_S, and between C_SD_S and B_SC_S, thus extending the lengths of the fringing flux paths and underestimating the permeances; similarly, in the right stator slot, the angle between A_SB_S and A_SD_S in Figure 3.20 is decreased, which shortens the fringing flux paths with a reduced reluctance in this region. Conversely, the conformal mapping method proposed in this Section 3.2 eliminates the error caused by geometry misrepresentation and Table 3.10 indicates that the errors of rotor-slot and stator-slot permeance prediction are significantly decreased by the enhanced method.

3.2.2.2 Experimental Validation

Table 3.11 – The inductance obtained by the enhanced analytical method and physical measurements of a 6/4 SRM.

Rotor Angle		**0°**	**15°**	**30°**	**45°**
4 A	**Measured (mH)**	6.19	4.03	1.69	1.23
	Analytical (mH)	6.04	4.06	1.58	1.12
	Error A (%)	-2.42	0.74	-6.51	-8.94
	Modified (mH)	6.14	4.16	1.68	1.22
	Error M (%)	-0.81	3.23	-0.59	-0.81
8 A	**Measured (mH)**	4.89	3.97	1.72	1.23
	Analytical (mH)	4.96	3.99	1.58	1.12
	Error A (%)	1.43	0.50	-8.14	-8.94
	Modified (mH)	5.03	4.07	1.68	1.22

	Error M (%)	2.86	2.52	-2.33	-0.81
12 A	**Measured (mH)**	3.63	3.13	1.65	1.21
	Analytical (mH)	3.55	3.16	1.57	1.12
	Error A (%)	-2.20	0.96	-4.85	-7.44
	Modified (mH)	3.61	3.23	1.66	1.22
	Error M (%)	-0.55	3.19	0.61	0.83

The inductances of a 6/4 SRM are measured at several rotor positions with different phase currents. The parameters of the SRM are listed in Table 3.3. In the measurement, the rotor is locked at a specific position, and an ac voltage is supplied to the stator windings of one phase, and flux linkage is then calculated by using the measured voltage and current data. The method to compute the phase inductance in the experiments is the same as the approach described in Section 3.1. The measured and estimated inductances when the phase current is 4 A, 8 A and 12 A are shown in Table 3.11. The percentage error of all predicted values is less than 10%, which validates the effectiveness of the analytical model proposed in this section. However, Table 3.11 shows that the inductance is underestimated at the unaligned position and in some cases at the aligned position with larger percentage errors, which is essentially because of the neglect of end fringing flux in the calculation. There are several approaches to calculate the end fringing flux or permeance with consideration of the end coil thickness, length and filamentary conductors. An approximate and simple equation for the end fringing permeance assuming circular end coils is given in [51], [182] as below:

$$P_{end} = \mu_0 a \left[\ln\left(1 + \frac{\pi a}{b}\right) + \left(\frac{a^2}{2.3a^2 + 1.6ab + 0.44b^2} \right) \right] \tag{3.103}$$

where a is the mean coil radius and b is the thickness of the coil in the radial direction. Once the value of P_{end} is obtained, it is then substituted into the magnetic circuit in Figure

3.8 and shunted parallel to P_{ag}. With this compensation of the end fringing inductance, the modified results are also presented in Table 3.11. The overall accuracy of the analytical method is better when the end fringing inductance is considered. It can be seen from Table 3.11 that the inductances at θ_p=15°are already overestimated without end leakage inductance compensation, and the errors are even slightly larger when this modification is applied. The primary reason for this phenomenon is that when the rotor pole and stator pole partially overlap, it is difficult to analytically predict the exact distribution of the non-uniform flux in saturated pole tips, the effect of which is approximated by defining reduced cross-sectional areas for the corresponding pole tip permeances P_{spt} and P_{rpt}; this procedure may lead to some error due to this approximation.

Table 3.11 indicates that when the rotor angle is 0° and 15°, which are within the region close to the aligned position, the inductance of the 6/4 SRM gradually becomes smaller when the phase current increases from 4 A to 12 A. This is because the larger current increases the flux density in the stator and rotor steel, leading to high saturation levels and thus the increases of the reluctances of the steel segments. Figure 3.23 illustrates the measured trajectory of the flux linkage versus the stator current of the 6/4 SRM at different rotor angles. Figure 3.23 shows that the machine still operates in the linear region when the current is 4 A, but the steel segments become highly saturated as the phase current increases and the flux linkage characteristic exhibits significant nonlinearity accordingly when the rotor angle is 0° and 15°. The agreement between the results of the analytical model and experiment in Table 3.11 proves that the phase inductance can be accurately predicted by the proposed method in both linear and saturation region of SRMs.

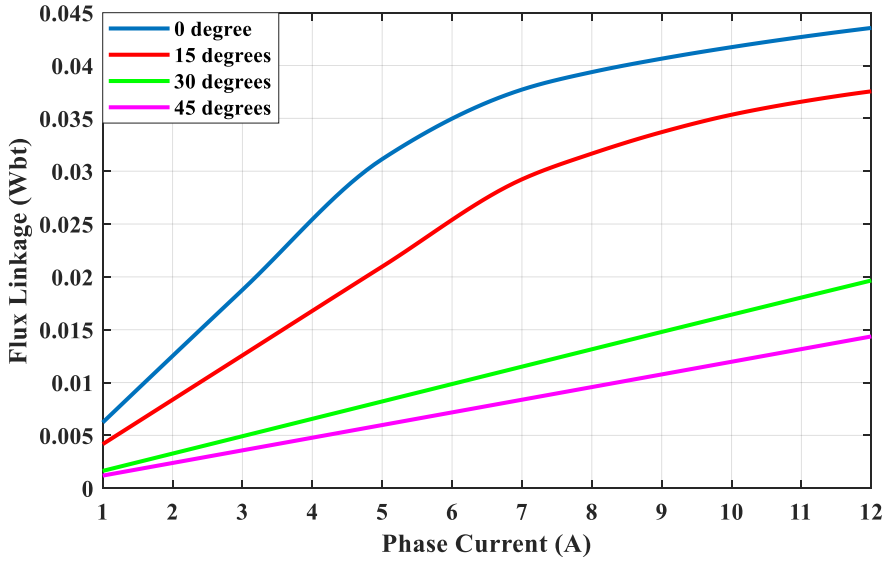

Figure 3.23 Characteristic of the flux linkage with respect to phase current at different rotor positions of the 6/4 SRM.

To validate the effectiveness of the proposed method in predicting the dynamic electromagnetic behaviors of SRMs with different topologies, another experiment is conducted on a 4/2 SRM prototype with the parameters in Table 3.12, and the measured performances of the SRM in steady-state operation are compared with the behaviors predicted by the FEA and the proposed analytical method. The variable-speed SRM drive test system is set up and consists of an Analog Device 21369 as the controller, a Xilinx Spartan-3 FPGA as the data communication hub, 12-bit A/D converters that sample the phase currents and dc-link voltage for closed-loop control, and a two-level converter with an asymmetric bridge in each phase [42]. The speed closed-loop control is achieved to drive the motor at 50,000 r/min in steady state, and the single-pulse control is adopted since it is a classical control strategy for high-speed SRMs [183], [184]. Figure 3.24 shows the measured waveforms of phase voltage and currents of the 4/2 SRM.

The dynamic responses of the phase current and torque are also predicted by the corresponding FEA and analytical model. In the simulations, the waveforms of the phase voltages in Figure 3.24 determined by the dc-link voltage and the turn-on and -off angles

are substituted into the FEA and analytical model. In this experiment, the core loss increases due to a higher fundamental frequency of stator current 1,667 Hz associated with the high rotor speed 50,000 r/min. In FEA simulations, the impact of core loss on the magnetic field is rigorously incorporated by introducing additional field intensity terms $\mathbf{H_{ph}}$, $\mathbf{H_{pc}}$ and $\mathbf{H_{pe}}$ that represent the effects of hysteresis loss, eddy current loss and excess core loss respectively into the governing equations [185]. A modified equivalent circuit model of SRMs shown in Figure 3.25 that contains a parallel resistor R_{FE} representing the core loss is used to capture the SRM dynamic behaviors and core loss effects. In Figure 3.25, i_p denotes the total phase current corresponding to the measured current waveform in Figure 3.24, while i_{pM} is the magnetizing current that generates the magnetic field and i_{pFE} is the equivalent current term producing the core loss [186]. The mathematical model of the circuit in Figure 3.25 is as follows [186]:

$$\begin{cases} u_p = R_S i_p + \dfrac{d\lambda_p\left(\theta_p, i_{pM}\right)}{dt} \\ i_p = i_{pM} + i_{pFE} = i_{pM} + \dfrac{1}{R_{FE}} \cdot \dfrac{d\lambda_p\left(\theta_p, i_{pM}\right)}{dt} \\ \dfrac{d\lambda_p\left(\theta_p, i_{pM}\right)}{dt} = L_p\left(\theta_p, i_{pM}\right)\dfrac{di_{pM}}{dt} + i_{pM}\dfrac{d\theta_p}{dt} \cdot \dfrac{\partial L_p\left(\theta_p, i_{pM}\right)}{\partial \theta_p} + i_{pM}\dfrac{di_{pM}}{dt} \cdot \dfrac{\partial L_p\left(\theta_p, i_{pM}\right)}{\partial i_{pM}} \end{cases} . \tag{3.104}$$

Table 3.12 – Parameters of the measured 4/2 SRM.

Parameter	Value	Parameter	Value
R_{sout}	26.57 mm	θ_S	0.5236
R_{sin}	12.5 mm	θ_R	0.6981
R_{rout}	11.981 mm	l_s	20 mm
R_{rin}	6.5 mm	N_t	90
R_{shaft}	3.374 mm	R_{core}	32.5 mm

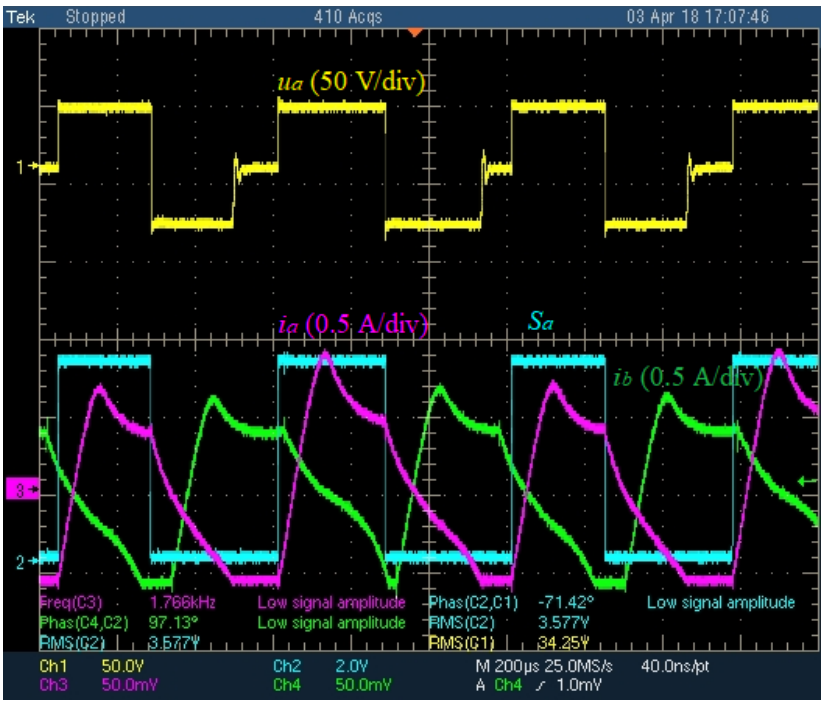

Figure 3.24 Measured phase currents and voltage of the 4/2 SRM in operation.

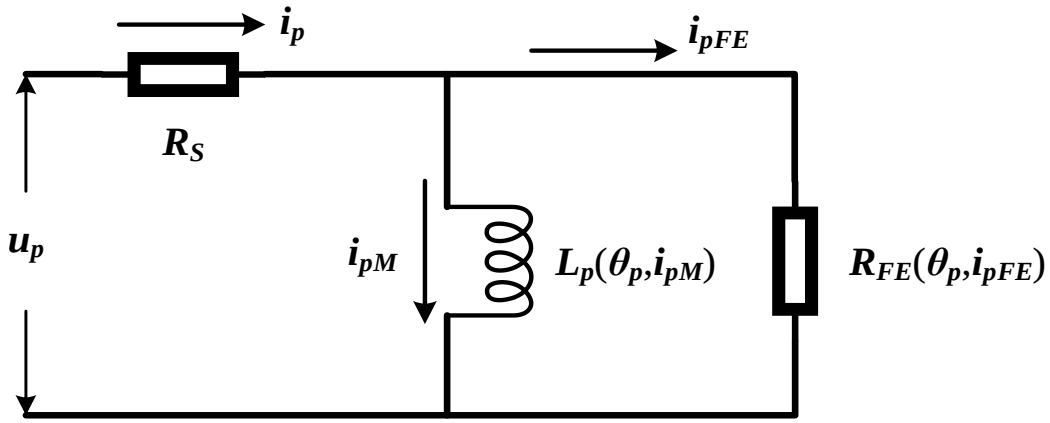

Figure 3.25 Modified SRM phase equivalent circuit model including the magnetizing inductance and core-loss resistance.

In (3.104), the phase inductance L_p with respect to the rotor angle and phase magnetizing current is predicted by the method proposed in Section 3.2. The equivalent

core-loss resistance R_{FE} can be either linear that expresses the average core loss [187], or nonlinear and incremental dependent on the phase current and time-varying core loss. The latter technique with nonlinear R_{FE} is utilized to improve the accuracy of the analytical model. The time-varying hysteresis loss density p_h, eddy current loss density p_c, and excess loss density p_e of each steel segment in the stator and rotor are determined at each time step based on the magnetic field solved in the MEC, as follows [188]:

$$p_h(t) = \left| H \cdot \frac{dB}{dt} \right|,\ p_c(t) = \frac{1}{2\pi^2} k_c \left(\frac{dB}{dt} \right)^2,\ p_e(t) = \frac{1}{C_e} k_e \left(\frac{dB}{dt} \right)^{1.5} \tag{3.105}$$

where k_c and k_e are the eddy current and excess loss coefficients, and in the calculation

$$k_c = \frac{\pi^2 \sigma d^2}{6},\ C_e = (2\pi)^{1.5} \cdot \frac{2}{\pi} \int_0^{\frac{\pi}{2}} \cos^{1.5}\theta d\theta \tag{3.106}$$

where σ and d are the conductivity and thickness of steel laminations, respectively. The value of k_e is determined by regression based on the loss curve (B_i, p_i) at the fundamental frequency f_1 [188]. The total core loss can be computed based on the loss densities (3.105) in each steel segment. The value of R_{FE} is updated iteratively at each time step to make sure that the total core loss and the loss produced by the equivalent core-loss resistor R_{FE} in the circuit diagram in Figure 3.25 are equal. When L_p and R_{FE} are determined, the phase current at each time step can be solved by differentiating (3.104).

Then the electromagnetic torque is derived as [189]:

$$T_e(\theta_p) = \sum_p \left(\frac{1}{2} \cdot \frac{\partial L_p}{\partial \theta_p} {i_{pM}}^2 \right) + \sum_{j \neq k} \left(\frac{\partial M_{jk}}{\partial \theta_p} i_{jM} i_{kM} \right) \tag{3.107}$$

where M_{jk} is the mutual inductance between phases j and k. In a common SRM, the mutual inductance between phases is much smaller than the self-inductance. To simplify the

calculations, generally the impact of mutual inductance can be neglected, and the torque is approximated by [190]

$$T_e\left(\theta_p\right) \approx \sum_p \left(\frac{1}{2} \cdot \frac{\partial L_p}{\partial \theta_p} {i_{pM}}^2 \right). \tag{3.108}$$

Figure 3.26 and Figure 3.27 compare the waveforms of phase A current and instantaneous torque obtained from the experiment, FEA and the analytical approach, respectively. The average torque in experiment, FEA and predicted by the analytical method is 2.41 mN·m, 2.46 mN·m and 2.44 mN·m, respectively. The peak instantaneous torque obtained in the experiment, FEA and the analytical model is 5.06 mN·m, 4.37 mN·m and 4.32 mN·m respectively. These results indicate that the proposed method can effectively predict the phase inductance and the associated dynamic electromagnetic behaviors of SRMs in operation.

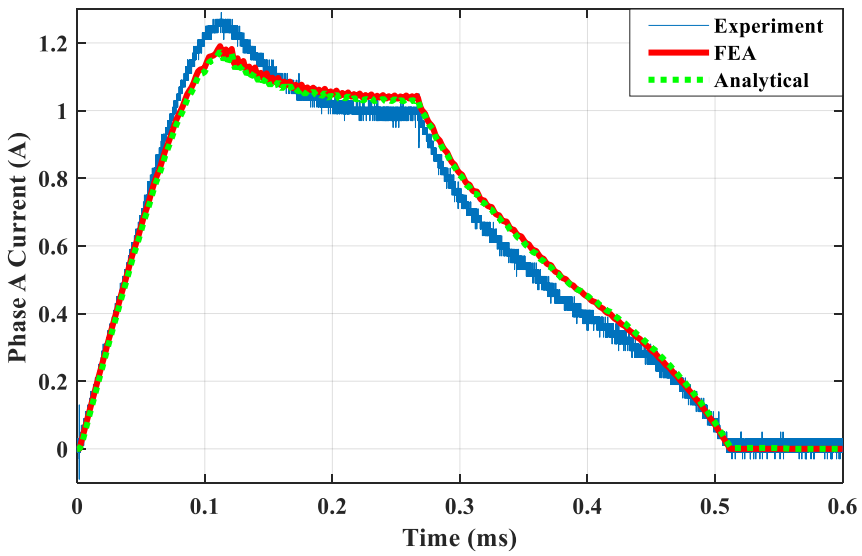

Figure 3.26 Waveforms of the phase current obtained from the experiment, FEA and the analytical method during a half electrical cycle at steady state.

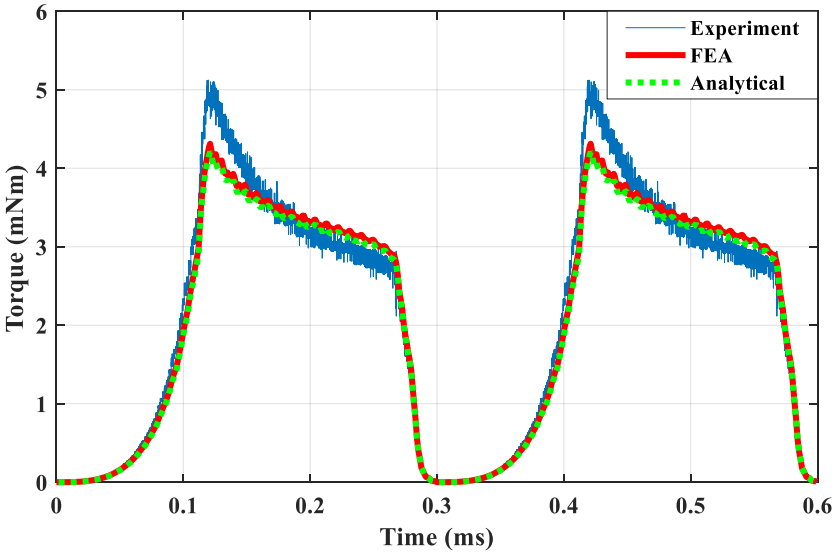

Figure 3.27 Instantaneous torque obtained from the experiment, FEA and analytical method during a half electrical cycle at steady state.

3.3 Hybrid Thermal Model of SRMs

Since the winding insulation life is determined by the winding temperature rise, it is necessary to perform thermal analyses during the design process to meet the requirement of the insulation life and make the full utilization of the motor thermal limit or cooling capability. The existing methods for SRM thermal modeling include thermal circuit methods [59], [61] and numerical techniques such as thermal FEA and computational fluid dynamics (CFD) [64]. The thermal resistance network is computationally efficient, but the drawback is that its accuracy relies on the approximation of the thermal resistances and capacitances, thus it is a predictive tool rather than a design tool due to the required calibration by experiments. FEA and CFD are geometrically generic and can accurately predict the temperature field in SRMs, but they generally need long setup and computation times, which limits their capability in design optimization. To achieve the balance between the computational speed and accuracy, this section uses a hybrid approach that combines FD and thermal circuit for temperature estimation [65].

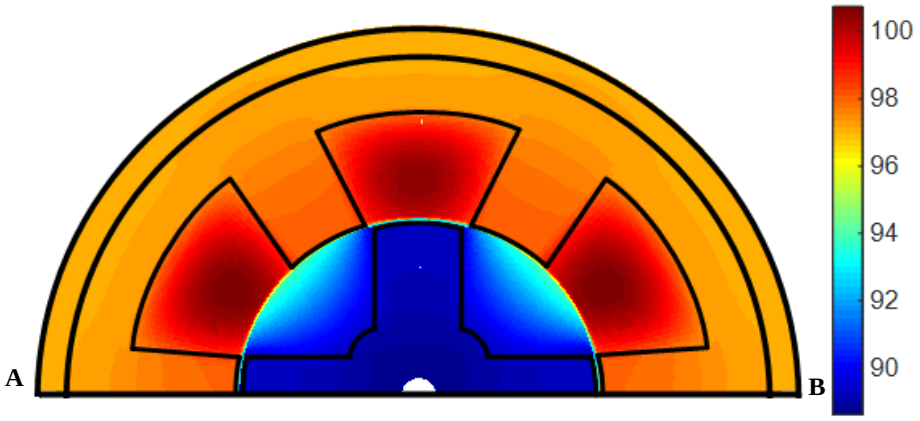

Figure 3.28 FD solution domain and the temperature distribution in the *R-θ* cross section half plane of a 6/4 SRM.

The objective of the hybrid method is to precisely capture the steady-state temperature within a radial-peripheral (*R-θ*) cross-section in the center of an SRM. The analysis should be performed for a half of the *R-θ* cross section at the axial midpoint of an SRM due to the geometric symmetry as illustrated in Figure 3.28, and the edge *AB* is subject to the adiabatic boundary condition [65]. The 2D FD method begins by distributing the nodes throughout the half cross section plane that represents the parametric SRM model using a "center node" distribution in cylindrical coordinates. An energy balance equation is imposed to each node that accounts for the energy entering, exiting and generated from the node as follows

$$\sum \dot{E}_{in} - \sum \dot{E}_{out} + \sum \dot{E}_{generated} = 0 \tag{3.109}$$

where

$$\sum \dot{E}_{in} - \sum \dot{E}_{out} = \frac{\Delta T_{R,\theta}}{R_{tot}}, \sum \dot{E}_{generated} = \dot{q}_{R,\theta} V_{R,\theta}$$

where $\Delta T_{R,\theta}$ and R_{tot} are the temperature difference and thermal resistance between an adjacent node and the target node respectively, $\dot{q}_{R,\theta}$ is the heat generation density at the node, i.e., core losses in the stator and rotor and copper losses in the windings, and $V_{R,\theta}$ is

the volume of the node. Thus, the expanded energy balance equation, or the governing equation of the stationary FD analysis is

$$\begin{aligned} &\frac{T_{R,\theta+d\theta}-T_{R,\theta}}{R_{tot|R,\theta+d\theta}}+\frac{T_{R,\theta-d\theta}-T_{R,\theta}}{R_{tot|R,\theta-d\theta}}+\frac{T_{R+dr,\theta}-T_{R,\theta}}{R_{tot|R+dr,\theta}}+\frac{T_{R-dr,\theta}-T_{R,\theta}}{R_{tot|R-dr,\theta}}=-\dot{q}_{R,\theta}V_{R,\theta} \\ &\Rightarrow \frac{T_{R,\theta}}{\sum R_{tot}}-\frac{T_{R,\theta+d\theta}}{R_{tot|R,\theta+d\theta}}-\frac{T_{R,\theta-d\theta}}{R_{tot|R,\theta-d\theta}}-\frac{T_{R+dr,\theta}}{R_{tot|R+dr,\theta}}-\frac{T_{R-dr,\theta}}{R_{tot|R-dr,\theta}}=\dot{q}_{R,\theta}V_{R,\theta} \end{aligned} \tag{3.110}$$

where

$$\begin{cases} R_{tot|R,\theta\pm d\theta}=\dfrac{R\cdot d\theta}{k\cdot dr} \\ R_{tot|R+dr,\theta}=\ln\left[\left(R+dr\right)/R\right]\Big/\left[k\cdot d\theta\cdot\left(R+\dfrac{dr}{2}\right)\right] \\ R_{tot|R+dr,\theta}=\ln\left[R/\left(R-dr\right)\right]\Big/\left[k\cdot d\theta\cdot\left(R-\dfrac{dr}{2}\right)\right] \end{cases}.$$

The governing energy balance equations (3.110) for all nodes lead to a system of linear equations, and its matrix form is $\mathbf{K}\cdot\mathbf{T}=\mathbf{Q}$, where **K** is a sparse tridiagonal matrix with five non-zero diagonals related to the coefficients of the nodal temperatures, **T** is the vector of nodal temperatures, and **Q** is the vector associated with the heat generation or boundary conditions at the nodes. The linear equations can be solved by using Cholesky decomposition. The thermal conductivity *k* of each node (element) should be specified to uniquely determine the matrix **K**. The thermal conductivity of the stator windings is estimated by taking a weighted average of the insulation k_{is} and the copper k_{cu}:

$$k_w=k_f k_{cu}+\left(1-k_f\right)k_{is} \tag{3.111}$$

where k_f is the fractional slot fill factor. Depending on the slot fill factor and winding configuration, k_f is in the range from 0.6 to 0.9 W/m^2/°C. The heat generation are assigned to each node to determine the vector **Q**. The copper loss, stator core loss and rotor core loss

distributions obtained from the EM model are mapped to the stator windings, stator iron and rotor iron respectively.

The heat generated within the FD solution plane is dissipated through three dimensional paths. Whilst the FD model encompasses the heat transfer in the radial and peripheral directions, the axial heat dissipation through the shaft, frame and end windings is captured by the thermal circuit approach [65]. The thermal resistances are assigned as boundary conditions in the FD model. The thermal circuit is selected due to its computational efficiency and the ability to accurately capture heat transfer with linear temperature gradients. The thermal resistance for the frame boundary includes the convection on the surfaces of the frame and end plates. For a horizontally placed SRM cooled by natural convection, the Nusselt numbers on the horizontal cylindrical frame surface and vertical end plates, Nu_{cn} and Nu_{pn} are [59]

$$\begin{cases} Nu_{cn} = \dfrac{hD}{k} = \left\{ 0.6 + \dfrac{0.387 Ra^{1/6}}{\left[1 + \left(0.559/\mathrm{Pr} \right)^{9/16} \right]^{8/27}} \right\}^2 \\ Nu_{pn} = \dfrac{hD}{k} = \left\{ 0.825 + \dfrac{0.387 Ra^{1/6}}{\left[1 + \left(0.492/\mathrm{Pr} \right)^{9/16} \right]^{8/27}} \right\}^2 \end{cases} \tag{3.112}$$

where Ra is the Rayleigh number and Pr is the Prandtl number. The axial heat transfer from the innermost nodes of the FD solution domain (rotor iron ID) through the shaft to ambient is modelled by a series of thermal resistances. When the heat is transported through the shaft from the motor midpoint to the bearing interface, the heat transfer is split into two parallel paths: heat dissipation through the shaft extension and convection on the surface of the end caps. The associated shaft transport model is described in [65]. The air gap is modelled as a single layer of nodes in the radial direction representing the heat transfer between the stator and rotor, and the associated Nusselt numbers for determining the convection thermal resistance values at the nodes can be computed as [61]

$$\begin{cases} Nu = 2 \ (Ta < 1700) \\ Nu = 0.128 Ta^{0.367} \ (1700 < Ta < 10^4) \\ Nu = 0.409 Ta^{0.241} \ (10^4 < Ta < 10^7) \end{cases} \tag{3.113}$$

where $Ta = (\rho^2 \omega^2 r_a \delta^3)/\mu^2$, and Ta, ρ, μ, ω, δ, r_a are the Taylor number, density and viscosity of the air, angular velocity of the rotor, radial airgap length, and average value of the stator and rotor radii, respectively.

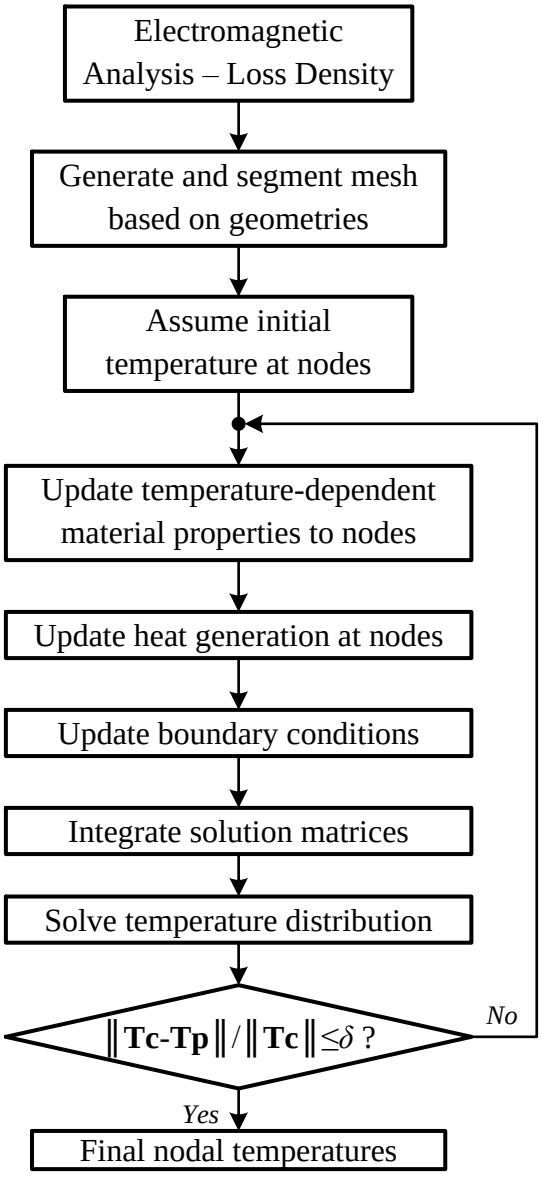

Figure 3.29 Flowchart of the thermal model.

The material properties of the copper, lamination steel and air are temperature-dependent in the thermal analysis. As temperature increases, the copper and lamination steel resistivities, air conductivity and viscosity increase, while the air density decreases [67]. The permeability of the lamination remains nearly constant, so it is unnecessary to update the entire EM analysis according to the temperature variation. However, it is indispensable to incorporate the temperature-dependent resistivities into the calculation of the copper losses and stator/rotor eddy current losses and update the thermal field by iterations. The flowchart of the thermal analysis is presented in Figure 3.29.

3.4 Chapter Summary

This chapter presents a multi-physics modelling approach for SRMs. First, a fast and accurate analytical approach to determine the phase inductance and associated EM behaviors of an SRM is proposed, where the magnetic field distribution and the permeance parameters in the air region are first determined by solving the partial differential equations of magnetic potentials based on Maxwell's equations, and the air-region permeance parameters are then substituted into a magnetic circuit network to include the impact of the saturation effects of steel on the phase inductance profile. Then, an enhanced SRM EM model is proposed to improve the accuracy, in which conformal mappings that deal with the non-radial/non-peripheral geometric structures are applied when calculating the air-region permeance parameters. Finally, a hybrid thermal model combining the 2D FD formulation and thermal equivalent circuits is used to estimate the temperature distribution within an SRM based on the loss distribution calculated by the analytical EM model. Finite-element analyses and experimental results validate the proposed multi-physics model of SRMs in this chapter.

CHAPTER 4. DESIGN OPTIMIZATION OF SWITCHED RELUCTANCE MACHINES

The optimization of structure design and control strategy aiming at improving the performances of SRMs has attracted attention. However, previous research efforts on SRM design optimization are mostly conducted to address only one performance index, e.g., torque ripple, efficiency, torque density and acoustic noise. The implementation of multi-objective optimization is necessary and such approaches have been investigated in recent years. One of the main issues with most of the existing multi-objective optimization methods is that they only predict the electromagnetic (EM) behaviors explicitly based on the SRM geometries, and as a result the machine control and thermal effects are not rigorously integrated in the design process. Generally, in these methods, the current profile is pre-defined by either the designer's own experience or heuristic curves and may not be the optimal solution corresponding to each design candidate, and the thermal effects are considered only by constraining the maximal current density or post evaluations of the optimal candidates by experimentally fit thermal-circuit-based models. On the other hand, since an optimization process usually simply employs stochastic evolutionary methods, e.g., particle swarm optimization (PSO), genetic algorithm (GA) and differential evolution (DE), which involve the simulations for a huge number of SRM design candidates and are coupled with a time-consuming FEA solver, the overall computational cost of such methods can be intensive. Design of experiments (DoE) based methods are an alternative for multi-objective optimization which require the assessment of a controllable number of candidates. However, the number of experiments can be impractically large with more design variables to be considered if the design method is not carefully chosen, and the optimal design selected directly from the sample points does not sufficiently lead to the global optimal solution because the experiments may not be uniformly and randomly

distributed over the design space. A class of approaches emerged recently that find the optimal solution based on the response surface models (RSMs) constructed by performing DoE, but the RSMs only express the relationship between the design variables and the performance indices with several pre-defined regression terms and are not adaptive and accurate within a wide design space.

This chapter presents a comprehensive approach for the multi-objective design optimization of switched reluctance machines (SRMs). A fast-solving multi-physics model that predicts the electromagnetic (EM) and thermal behaviors of an SRM with arbitrary geometries, materials or current profiles is developed in Chapter 3 and validated by its finite-element analysis (FEA) and experimental set-up counterpart in terms of various performance indices. Compared with the over-simplified traditional experience-based methods and the evolutionary algorithms that require the evaluation of numerous design candidates by FEAs, to achieve a balance between accuracy and computational complexity, artificial neural networks (ANNs) are constructed based on the maximin Latin hypercube design (MLHD) to identify the relationship between the SRM performance indices and the selected design variables within the entire predefined design space; then, incorporating the pre-trained ANN models, a particle swarm optimization (PSO) based multi-objective optimization approach is utilized to identify the Pareto optimal design candidates in terms of maximizing the efficiency and torque density, and minimizing the torque ripple. The thermal constraints as well as the effects of current profiles are incorporated in the design process. Simulation results demonstrate that the proposed method can effectively generate the Pareto front within a short period of time with the evaluation of a large number of design candidates.

4.1 Constructing Regression Models by MLHD and ANN

Although it only takes a few seconds to perform the multi-physics modeling for each candidate design, it is still computationally intensive to directly couple the model with an evolutionary algorithm for optimization. Instead, this section proposes a method to integrate regression models into PSO, in which ANNs are trained by performing DoE and used to predict the SRM performances in optimization.

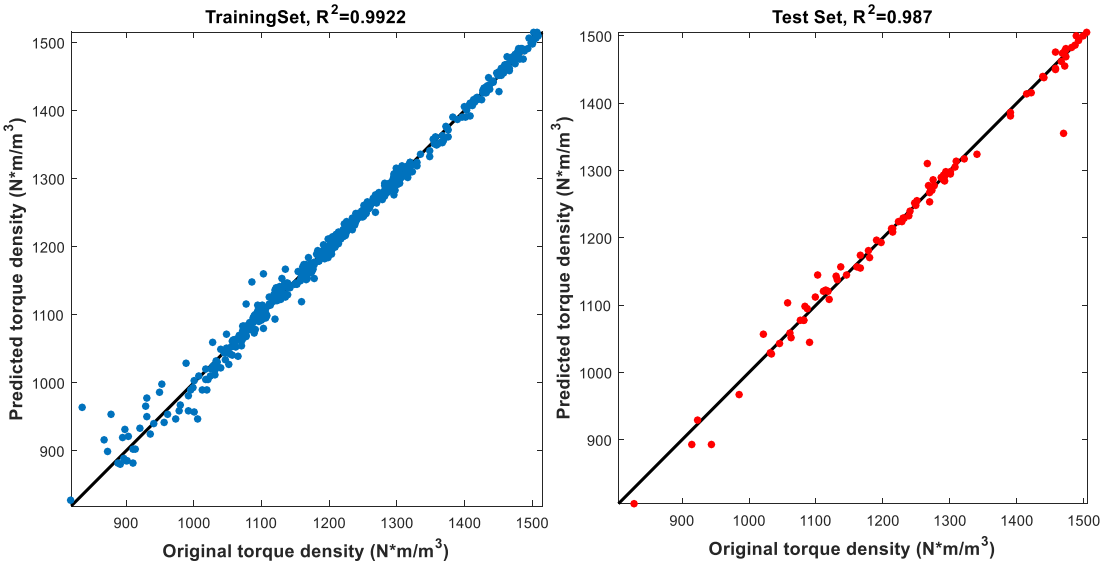

Figure 4.1 Comparison between the original and the predicted values of torque density for the training set and test set.

During the optimization process, the stator bore diameter D, stator length L_s, the angular spans of stator and rotor poles θ_s and θ_r, and the current density of the stator windings J, are selected as the prime design variables. The performance indices are the torque density T_d, efficiency η [191], [192], torque ripple T_r and maximum winding temperature T_{max}. In order to replace the multi-physics model in the optimization search process, the regression models should be able to accurately and adaptively predict the machine responses. This section employs the MLHD to ensure a nearly random and uniform space sampling within a wide design space, in which experimental points are spread out over the domain by maximizing the minimal distance between the points:

$$\psi_p(L) = \min_{\substack{i,j=1,\ldots,n \\ i \neq j}} \left\| \mathbf{x_i} - \mathbf{x_j} \right\|_p = \min_{\substack{i,j=1,\ldots,n \\ i \neq j}} \left(\sum_{s=1}^{N} \left| x_{s,i} - x_{s,j} \right|^p \right)^{1/p} \tag{4.1}$$

where N denotes the dimension of the n input vectors $\mathbf{x_1},\ldots,\mathbf{x_n}$ and $p=2$ in this design. The quality of Latin hypercube designs (LHDs) relies on the number of sample points n. A large-size MLHD is applied to better fit the regression model [193]. Therefore, the number of experiments to be performed is $n=420$ with a vector dimension $N=5$. In this study, the performance indices T_d, η, T_r and T_{max} should be solved based on the approach in Chapter 3 for each experiment.

The optimization of the current profiles is integrated in the design procedures, and the most important variables pertaining to the current control, the turn-on angle θ_{on} and turn-off angle θ_{off}, should be optimized for each sampled design candidate. This can be accomplished by using DoE, evolutionary methods or sweeping. To uniquely determine the angles, the objective at this stage can be expressed as

$$\min R(\mathbf{x}) = w_1 \cdot \frac{T_d^{\,B}}{T_d} + w_2 \cdot \frac{\eta^B}{\eta} + w_3 \cdot \frac{T_r}{T_r^{\,B}} \tag{4.2}$$

where w_1, w_2 and w_3 are weights, and T_d^B,η^B and T_r^B are the indices of the benchmark design. The outputs corresponding to the optimal θ_{on} and θ_{off} for each sampled candidate are further used to train the ANNs.

One of the most popular types of feed-forward ANNs, the multilayer perceptron neural network (MLPN), is selected to construct the regression model which consists of three layers of neurons, the input, hidden and output layers, interconnected by weight vectors. The weights of the MLPN are trained using the gradient-descent-based backpropagation algorithm. The activation function of the hidden-layer neurons is the following tangent sigmoid transfer function:

$$\phi(x) = \tanh(x) = \frac{2}{1+\exp(-2x)} - 1. \tag{4.3}$$

The neurons in the output layer are formed by the inner products between the nonlinear regression vector from the hidden-layer neurons and the output weight matrix [194].

In addition to the set of 420 experiments gathered by MLHD for the MLPN training, another 84 samples are randomly collected from the design space to test the effectiveness of the MLHD-MLPN regression model. The coefficient of determination R^2 is selected as the criterion to evaluate the quality of the regression model [134]. It can be found in Figure 4.1 that the value of R^2 of the MLPN that predicts the torque density is 0.9922 and 0.987 for the training set and test set respectively, which validates the proposed MLHD-MLPN regression model.

4.2 Vector-Based Multi-Objective PSO (MOPSO)

The MOPSO should simultaneously optimize the vector function and produce Pareto optimal solutions. Pareto front is a set of Pareto optimal (non-dominated) solutions, if no objective can be improved without sacrificing at least one other objective. A description of the procedures of MOPSO is presented in [134]. In this study, maximizing the torque density and efficiency, and minimizing the torque ripple are the objectives of the optimization. The maximum temperature is treated as a penalty function, which means that if the maximum temperature exceeds a certain value (120°C), the design candidate will be excluded from the set of Pareto optimal solutions. In addition to the thermal constraint, some other constraints include the minimum airgap length due to the manufacturing limitation, and the spatial constraints such as the maximum shaft radius and rotor pole and stator pole angles.

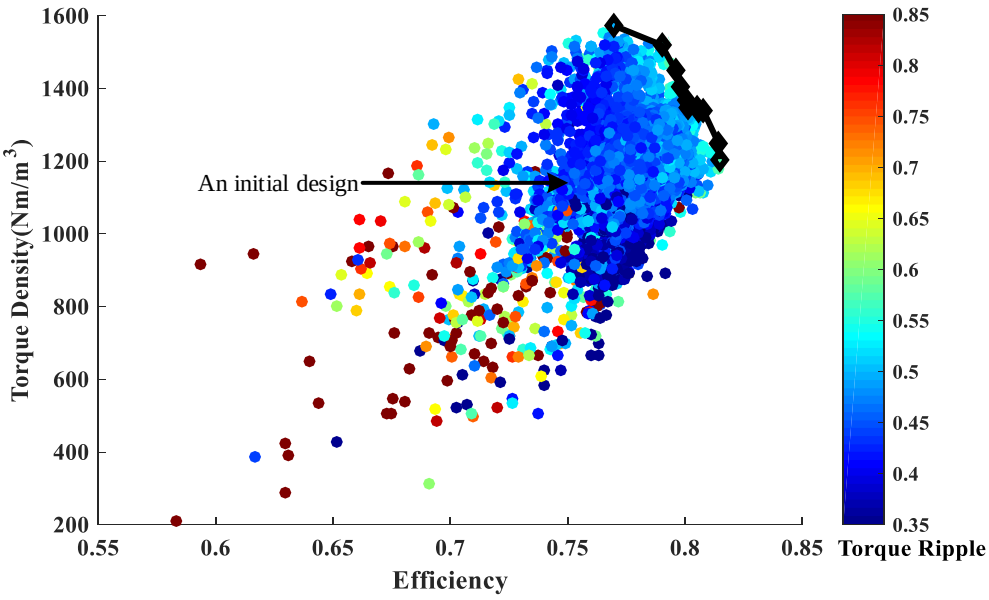

Figure 4.2 Pareto front of the MOPSO.

Figure 4.2 shows the Pareto front on the torque density – efficiency plane obtained by the MOPSO based on the MLHD-MLPN model for a 3A-excited 2000 rpm 6/4 SRM. There are 300 particles and 200 iterations in the MOPSO. It can be observed that the performances of the torque density, efficiency and torque ripple can be effectively improved compared to the initial benchmark design by applying the proposed method. It only takes about half an hour to go through the entire process of optimization, including the evaluation of the sampled candidates, setting up the regression model, and performing the MOPSO, so it is much faster than most of the existing methods of design optimization which typically take hours or even days to solve.

4.3 Chapter Summary

This chapter presents a comprehensive framework of the multi-physics based and multi-objective optimization of SRMs. The optimization of current profiles and the thermal constraints are rigorously incorporated in the method. To further accelerate the design

optimization, MLHD-MLPN based regression models are proposed and integrated into the MOPSO to find the Pareto optimal solutions.

CHAPTER 5. 3-DIMENSIONAL MULTI-PHYSICS NUMERICAL MODEL OF LARGE GENERATOR END REGIONS

As demonstrated in Chapter 1 and 2, the significant losses in the end components due to the leakage flux excited by the armature and field end windings can result in partial overheating and are important for the design of large synchronous generators. This chapter describes a method based on three-dimensional (3D) finite element analysis (FEA) to determine the magnetic field, and loss density and temperature distributions in the generator end region. Taking the nonlinear and anisotropic properties and the induced in-plane eddy currents in stator into consideration, the electromagnetic (EM) field and loss distributions in the end region are calculated. The method is validated by the agreement between the temperatures predicted by a corresponding 3D thermal FEA and the temperatures obtained from a physical measurement at different locations in the generator end region.

5.1 Introduction to the 3D Numerical Model

The overarching goal of this chapter is to develop a 3D numerical model that estimates the magnetic field, loss density and temperature distribution in the end region of large scale electrical generators in the 250 MVA – 750 MVA class.

Figure 5.1 shows the flowchart of the overall approach. The magnetic field and the eddy current in the end plate and finger plates are computed in the 3D Transient EM FEA model. The distribution of ohmic heating distribution in the stator end packets, end plate, finger plates and stator coils are obtained by post-processing the data collected from the 3D simulations. The data of the time-average loss density distribution is then translated into a localized heat source. The thermal boundary conditions are calculated using

analytical correlations, local computational fluid dynamics (CFD) studies and experimental data. The heat conduction equation within the end components, step-iron region and the stator coils is then solved in a stationary 3D thermal FEA simulation. The method described in this chapter is validated by the agreement between the predicted and measured temperature results.

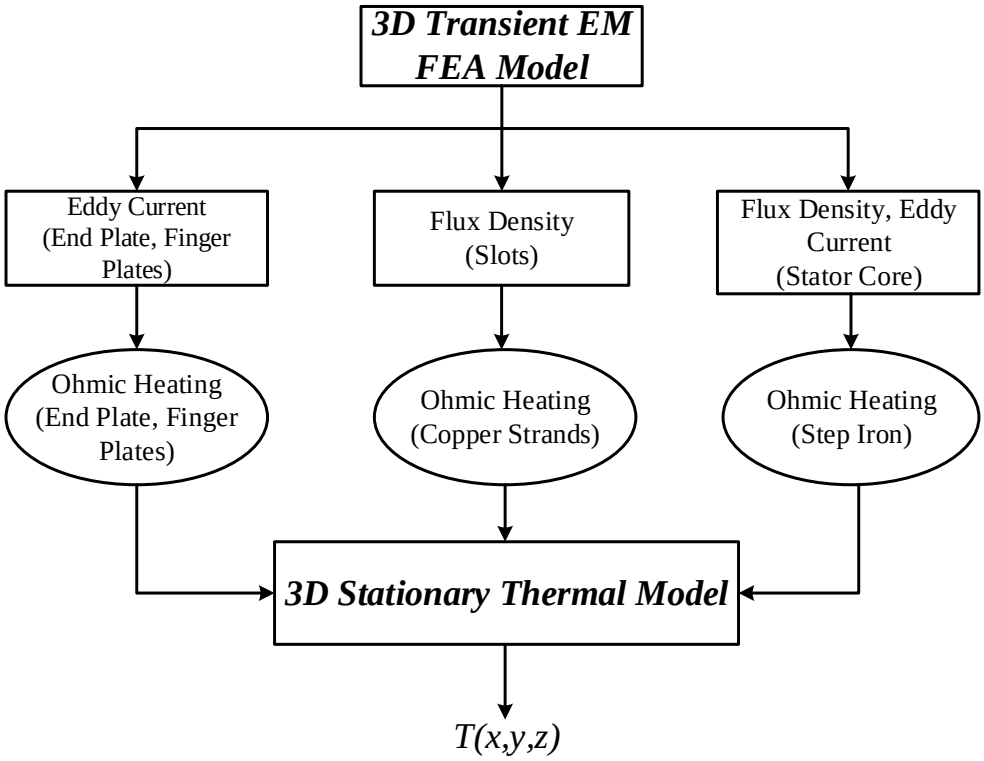

Figure 5.1 Flowchart of the overall 3D numerical modelling approach.

5.2 General Descriptions of the Transient 3D Electromagnetic FEA Model

5.2.1 Determination of Operating Conditions

5.2.1.1 Phasor Diagram Method

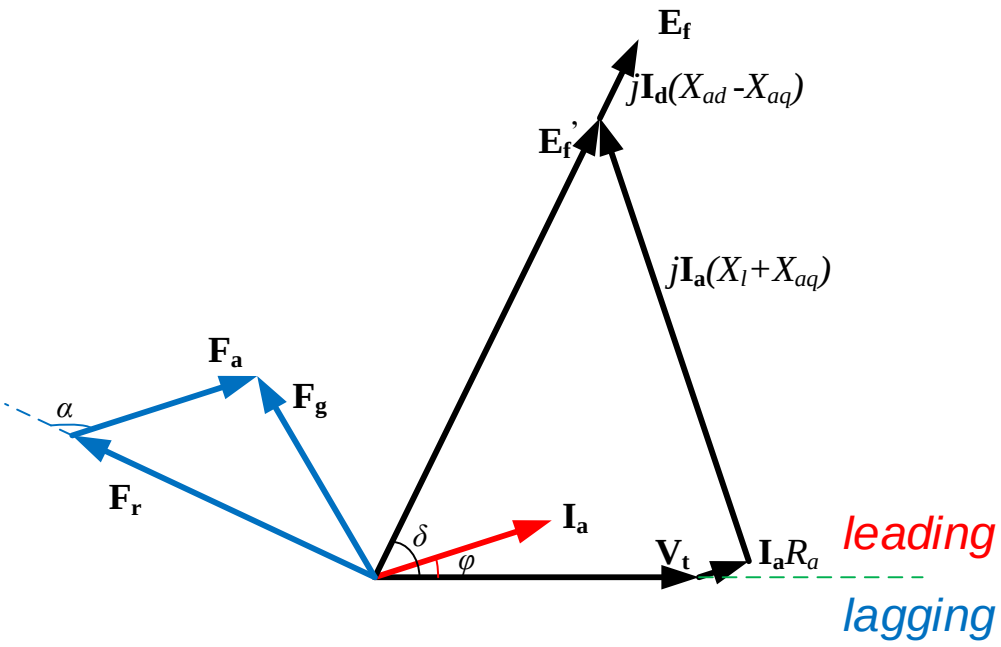

Figure 5.2 Phasor diagram of synchronous generators.

Phasor diagrams are used to determine the operating points of the generator as shown in Figure 5.2. In Figure 5.2, X_l is the armature leakage reactance, X_{ad} is the *d*-axis armature reaction reactance, X_{aq} is the *q*-axis armature reaction reactance, R_a is the armature resistance, $\mathbf{I_a}$ is the armature current, $\mathbf{I_d}$ is the d-axis armature current (all quantities are per phase); $\mathbf{V_t}$ is the line-to-neutral terminal voltage, $\mathbf{E_f}$ is the excitation voltage, $\mathbf{F_g}$ is the resultant air-gap mmf, $\mathbf{F_a}$ is the armature winding mmf, and $\mathbf{F_r}$ is the field winding mmf. The angle φ between $\mathbf{V_t}$ and $\mathbf{I_a}$ is the power factor angle and the angle δ between $\mathbf{E_f}$ and $\mathbf{V_t}$ is the load angle. The angle φ is greater than zero if the power factor is lagging, while it has a negative value if the power factor is leading. All of the components of voltages, currents and mmfs in the phasor diagram are based on the fundamental frequency and all higher-order harmonics are neglected in the analysis. The values of X_l, X_{ad}, X_{aq}, and R_a are obtained from the parameter table of the machine. At steady state, $\mathbf{I_a}$ and $\mathbf{E_f}$ are given by

$$I_a = \frac{S}{\sqrt{3}V_{l-l}} \tag{5.1}$$

$$\mathbf{E_f} = \mathbf{V}_t + \mathbf{I}_a R_a + j\mathbf{I_a}\left(X_l + X_{aq}\right) + j\mathbf{I_d}\left(X_{ad} - X_{aq}\right) \tag{5.2}$$

where S is the three-phase apparent power rating of the generator.

The air-gap mmf $\mathbf{F_g}$ is the vector sum of armature mmf $\mathbf{F_a}$ and field mmf $\mathbf{F_r}$. $\mathbf{F_r}$ is 90° ahead of $\mathbf{E_f}$, while $\mathbf{F_a}$ is in phase with $\mathbf{I_a}$. In the transient simulation, the angle α between $\mathbf{F_r}$ and $\mathbf{F_a}$ determines the position of the rotor at each time step. The field current $\mathbf{I_f}$ is obtained from its actual values under different operating conditions, while I_a is determined by (5.1). The magnitudes of $\mathbf{I_a}$ and $\mathbf{I_f}$ and the angle α at steady state uniquely determine the conditions of current excitations at the initial and all subsequent time steps in the 3D FEAs.

5.2.1.2 Iterative 2D FEA Method

An alternative method to determine the operating conditions is the iterative 2D FEA simulation. For a certain operating condition, the field current $\boldsymbol{I_f}$ and the angle α between the field mmf $\boldsymbol{F_r}$ and the armature mmf $\boldsymbol{F_a}$ need to be defined. Since a 3D FEA model merely reflects the magnetic field in the end region, and setting up a 3D model for the entire generator can result in unaccepted long simulation times, two-dimensional (2D) FEA can be used to determine operating points, and a flowchart appears in Figure 5.3. Figure 5.4 shows the phasor diagram of a generator operating with a lagging factor, which is generally the case for the rated conditions. In Figure 5.4, R_e is the equivalent phase resistance representing the copper loss and mechanical losses of the generator, X_l, X_{aq} and X_{ad} are the leakage reactance, the q-axis and d-axis armature reaction reactance respectively, and X_{le} is the end leakage reactance. In 2D FEAs, the fundamental component of armature currents is fed into the stator windings and the induced voltage $\boldsymbol{U'}$ can be obtained. The stator

terminal voltage phasor $\boldsymbol{U}$ and the power factor angle θ can be calculated based on the values of $\boldsymbol{U'}$, $\boldsymbol{I_a}$, R_e and X_{le} in Figure 5.4:

$$\mathbf{U} = \mathbf{U}^{'} - \mathbf{I_a} R_e - j\mathbf{I_a} X_{le}, \theta = \cos^{-1}\left[\left(\mathbf{U}\cdot\mathbf{I_a}\right)/\left(|\mathbf{U}||\mathbf{I_a}|\right)\right]. \tag{5.3}$$

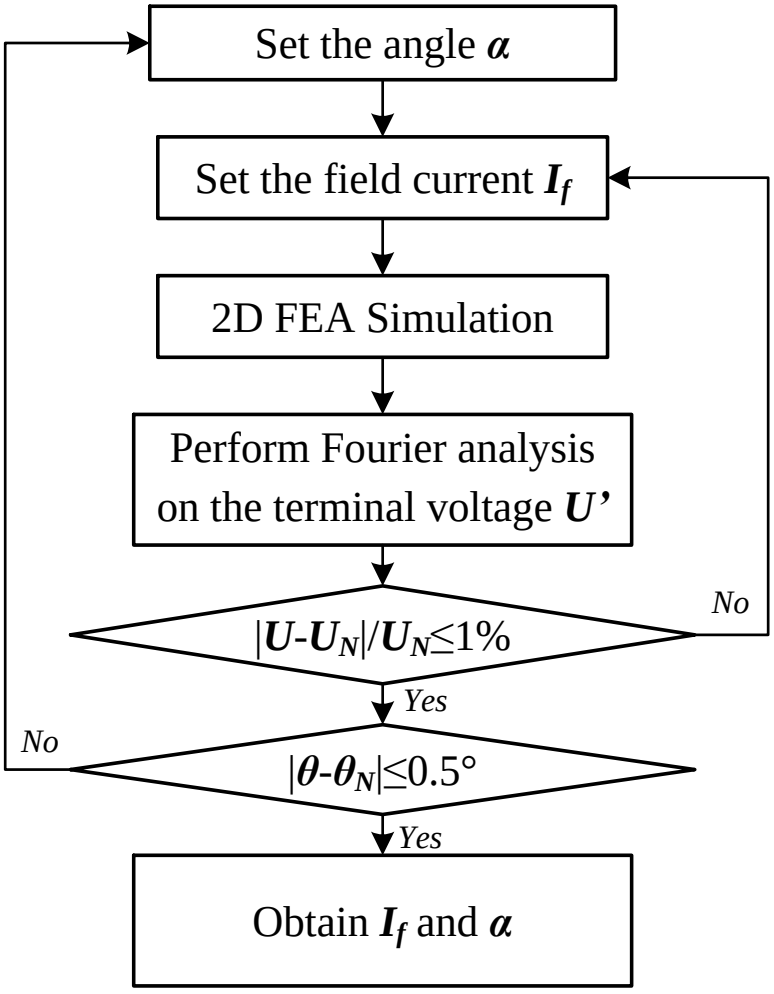

Figure 5.3 Flowchart of determining the operating conditions by iterative 2D FEA.

All of the quantities are on a per phase basis. The values of the field current $\boldsymbol{I_f}$ and the angle α are refined by iterations until the following convergence criterion is satisfied:

$$\left|U - U_N\right| \le 1\%, \left|\theta - \theta_N\right| \le 0.5^{\circ} \tag{5.4}$$

where U and U_N are the calculated and theoretical values of the stator fundamental terminal voltage respectively, and θ_N is the theoretical power factor angle.

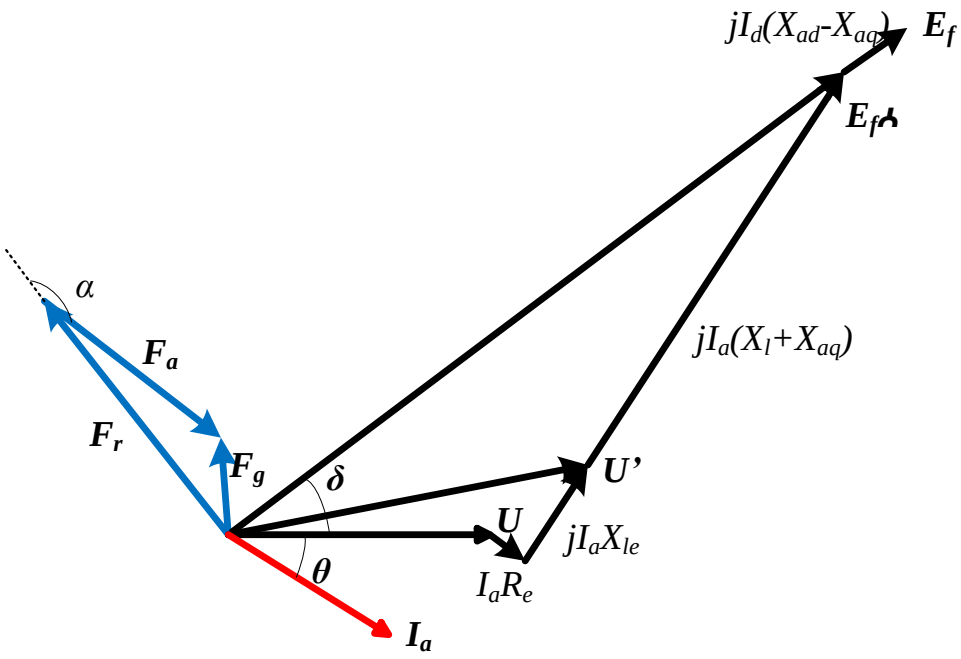

Figure 5.4 Phasor diagram of the generator in the power-factor-lagging condition.

In 2D FEAs, the impact of the radial cooling vents is considered by modifying the stacking factor of the stator core. An additional field term $\mathbf{H_p}$ is introduced in the governing equations for the stator core to include the effects of the hysteresis, excess and classical eddy current loss on the magnetic field [185].

Compared to the phasor diagram method, the iterative 2D FEA method is much more time-consuming since it requires multiple 2D FEA simulations, but its reliability and accuracy of calculation are higher because the effects of saturation, core losses on the magnetic field are rigorously incorporated.

5.2.2 Geometric Model

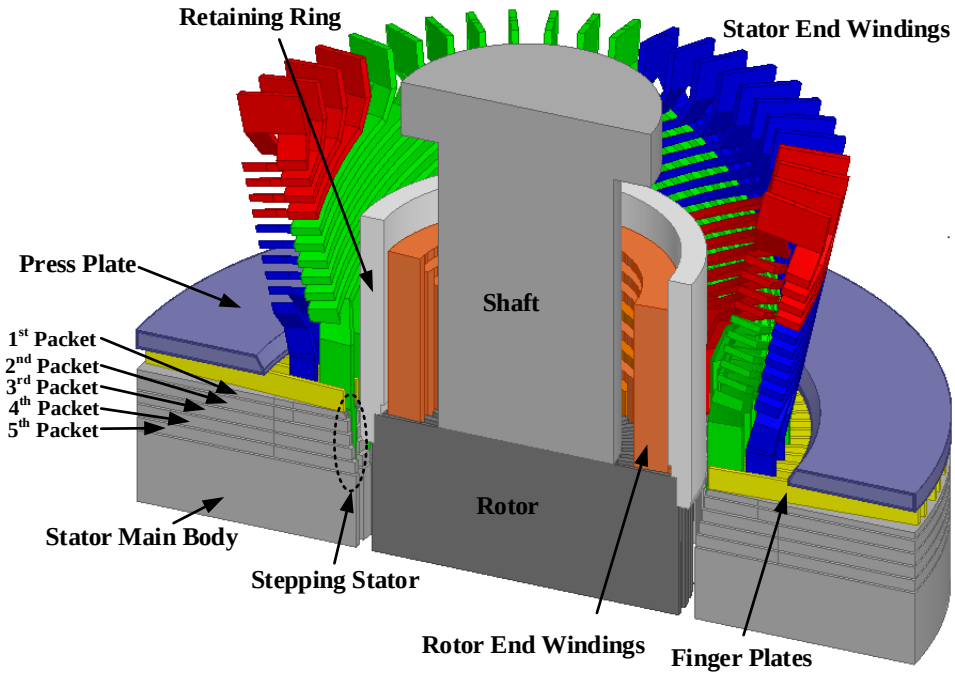

Figure 5.5 End components of the large synchronous generator.

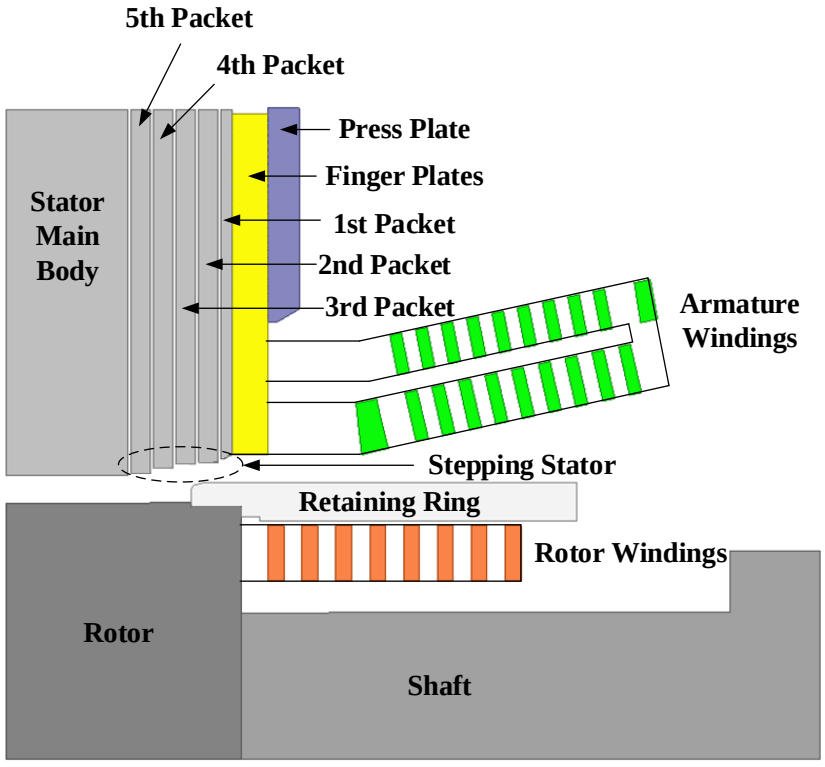

Figure 5.6 Radial-axial cross-section view of the end region of the generator.

A 370-MVA air-cooled two-pole turbo-generator with a 20-kV rated line-to-line voltage is used as the example for the 3D FEA. Figure 5.5 shows the geometries of the end region in the 3D model. The major end components are the stator end packets and main body, rotor, shaft, field/armature end windings, retaining ring, press plate, and finger plates. The inner diameter of the stator gradually increases from the 5th packet to the 1st packet. There is a slit in the middle of each stator tooth in the 1st and the 2nd end packet to reduce the eddy current losses induced by axial flux. Figure 5.6 is the cross-section plot of the end region in a *radial-axial* cross-sectional plane. The inner diameter of the stator gradually increases from the 5^{th} packet to the 1^{st} packet. In addition, there is a slit in the middle of each stator tooth in the 1^{st} and 2^{nd} packet.

Geometries of the end components are simplified due to the large number of finite elements introduced by their complexity. Only the electromagnetic field of one pole is analyzed by applying the anti-periodic boundary conditions [179]. In addition, the trivial but unimportant structures of the stator, e.g., round corners, slot wedges on top of windings and slits in the back yoke are eliminated from the original geometry. The tightening bolts and steel frames are also removed from the model.

5.2.3 Winding Layout

Figure 5.7 shows the layout of the field and armature windings. On the rotor side, the orange blocks represent the field windings; on the stator side, the red, blue and green blocks indicate the armature windings of phases A, B and C respectively. The armature windings are short-pitched by 4 slots. The simulated large generator has 48 stator slots and 32 rotor slots.

The armature windings have 2 parallel branches per phase and 8 turns in series per parallel branch. Define the stator bar or the rotor bar to be one block indicating stator or rotor windings in Figure 5.7. There are plenty of copper strands in each stator or rotor bar.

Each of the 8 turns is formed into two bars before inserting it into the stator slot. These windings are double layer, 60 degrees phase spread and short pitched by 4 slots. There are 16 stator bars of each phase in Figure 5.7, so the current flowing in each stator bar is half of the corresponding phase current. There is one parallel branch for the rotor windings and the number of turns in series per parallel branch is 208. In the simulation, the armature currents are sinusoidal at fundamental frequency and the field current only has the dc component.

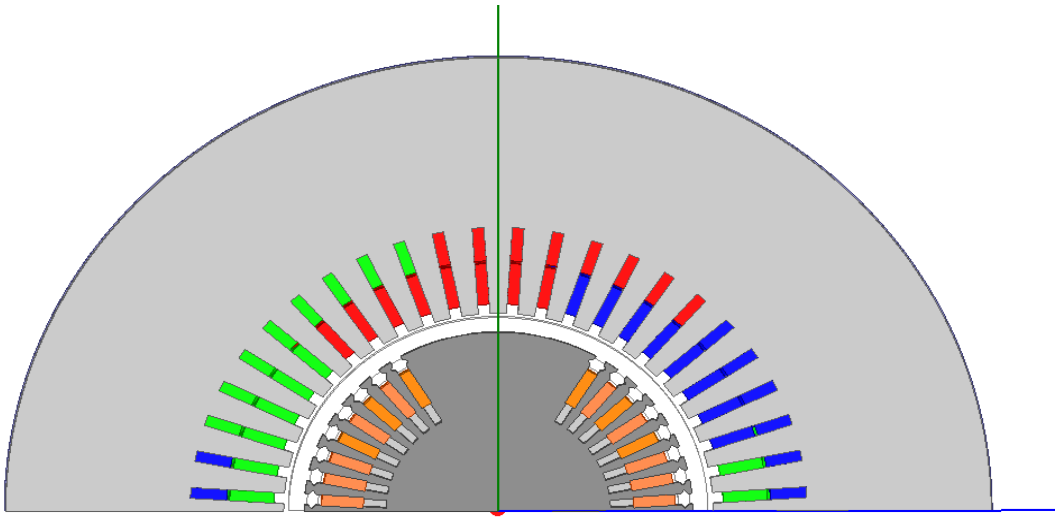

Figure 5.7 Field and armature winding layouts for one pole of a two-pole generator.

5.2.4 Boundary Conditions

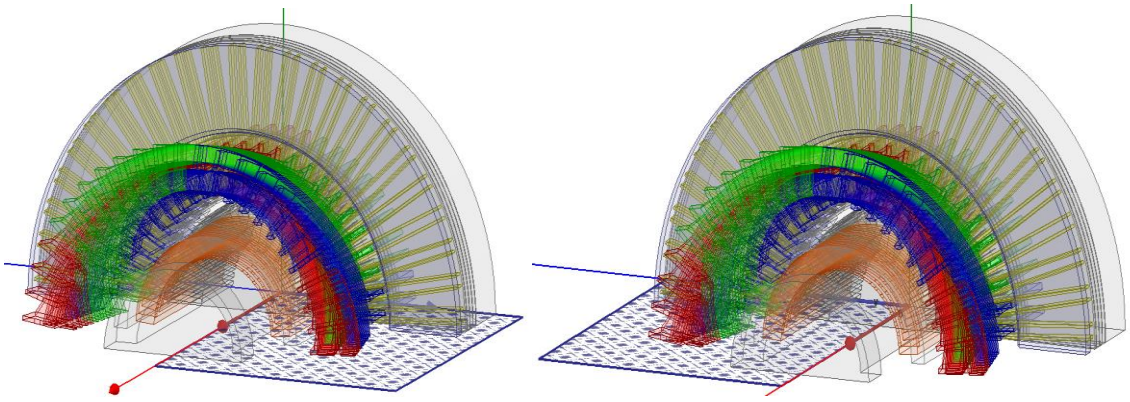

(a) (b)

Figure 5.8 (a) Master boundary plane; (b) slave boundary plane.

Insulation boundary conditions are specified on the surfaces between the armature windings and the stator core to prevent the leakage of the stator winding currents into the stator core.

The anti-periodic boundary condition is applied to the simulation in order to simplify the calculation as shown in Figure 5.8, where the magnetic field vector on the slave boundary plane is in the opposite direction to that on the master boundary plane with the same magnitude ($\mathbf{H}_s = -\mathbf{H}_m$). Only the analysis of the electromagnetic field of one pole is sufficient when this boundary condition is applied.

A Neumann boundary condition, also known as "natural boundary condition" is applied to the outer surfaces of the solving region, indicating tangential magnetic field on those surfaces and that the flux cannot travel across them.

5.2.5 Mesh Operations

Selecting the size of the finite elements is important when forming meshes of elements in the various regions of the generator. The solving region is discretized by second-order tetrahedral elements with a total number of 3,589,230. To improve the accuracy while minimizing the number of elements accordingly, the meshes are refined adaptively with the elements possessing the largest energy error refined in each iteration until the total energy error is within the acceptable limits, and dense elements are assigned in the regions where flux density varies rapidly or the induced eddy currents are pronounced, e.g., in the press plate, finger plates and stator teeth. The elements of the stator and rotor are defined separately and coupled with the sliding elements in the air gap so as to simulate the rotational motion of the rotor/field windings at each time step.

For the press plate, considering the significant skin-depth effect and the phenomenon that the eddy current is concentrated in the region beneath the surfaces, the density of elements is much higher in this region. There are four different mesh layers beneath the surface of the press plate illustrated in Figure 5.9. The thicknesses of the layers from the 1st to the 4th layer are 0.9 mm, 1.2 mm, 2.4 mm and 4.8 mm respectively. The length of the elements in the four mesh layers should not be greater than 25 mm; this limitation assures that computer simulation time does not become too large. For a press plate made of steel with a nonlinear B-H curve, the principle of drawing the mesh layers is that the thickness of the 1st mesh layer should not exceed the skin depth in the linear region, while the sum of the thicknesses of the four mesh layers should be no smaller than the skin depth in the highly saturated region.

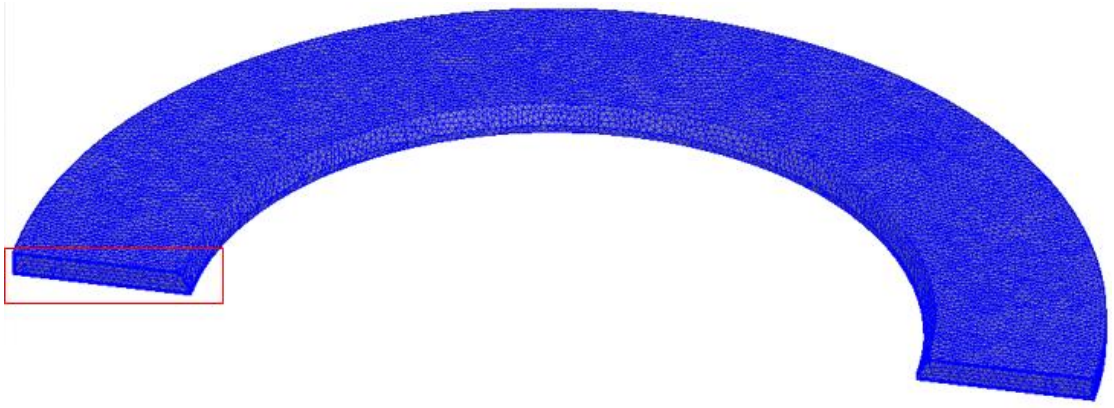

(a)

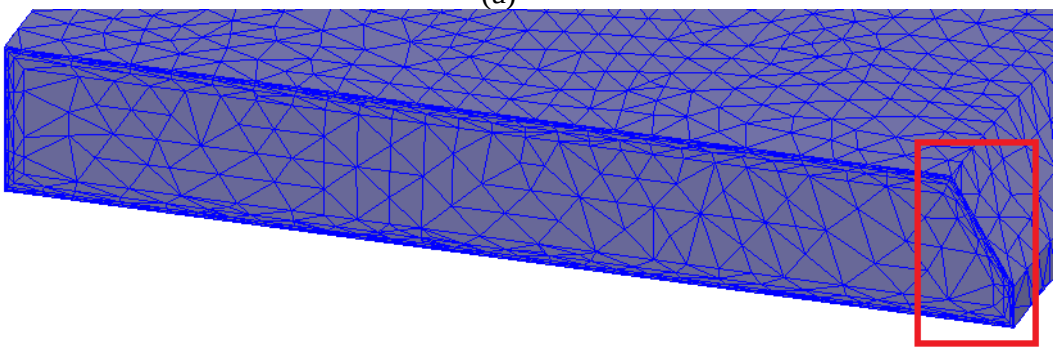

(b)

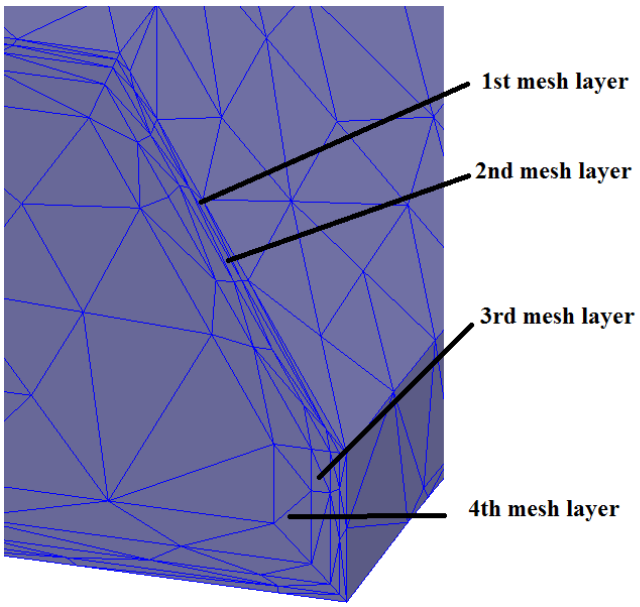

(c)

Figure 5.9 (a) Elements in the end plate; (b) elements in the four surface mesh layers on a cross-section plane; (c) elements in the four surface mesh layers in the region near the inner diameter of the end plate.

Mesh refinement is also applied to the finger plates as shown in Figure 5.10.

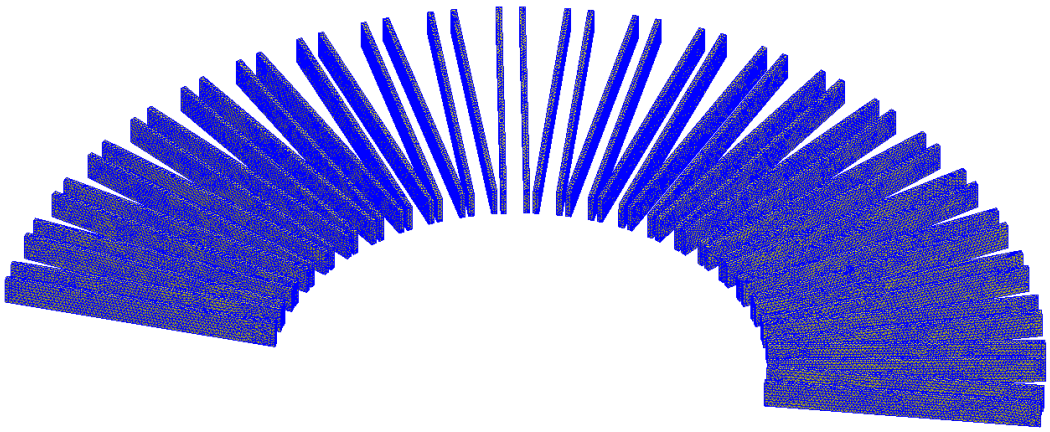

Figure 5.10 Elements in the finger plates.

After the mesh operations are set up for the critical regions in the simulation, automatic adaptive meshing is implemented to get a convergent mesh for the entire solving region. Figure 5.11 is the flowchart of the adaptive mesh refinement.

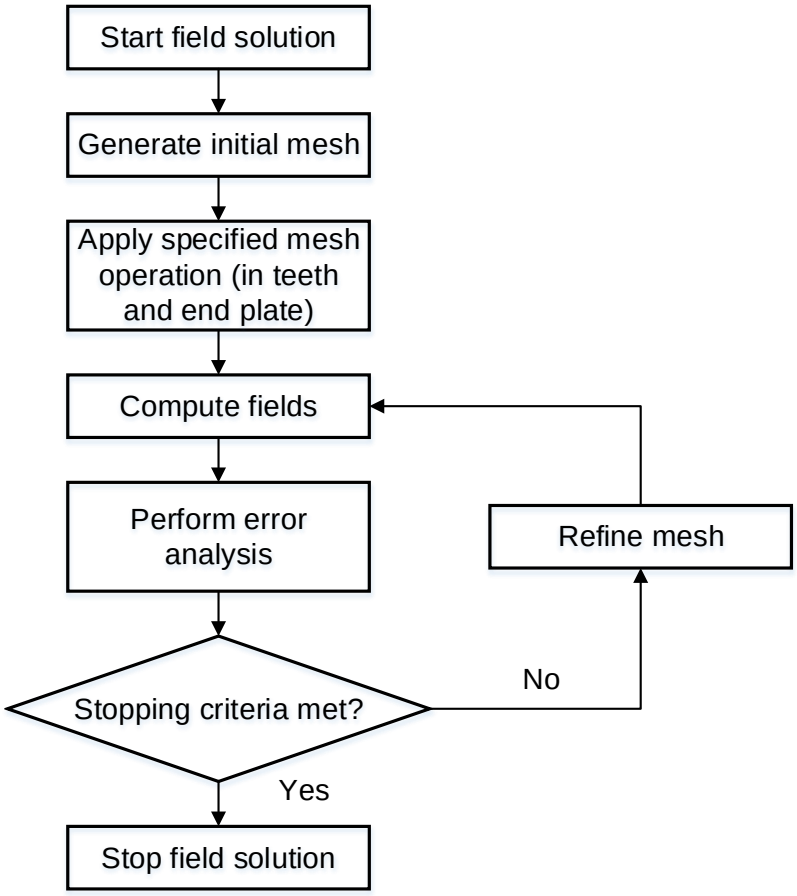

Figure 5.11 Flowchart of adaptive meshing.

Adaptive analysis iteratively refines the mesh in order to reduce the size of individual elements in areas of high error, thus improving the accuracy of the solution. For each step of the adaptive analysis, it firstly generates a field solution using the specified mesh. Then, the solution is analyzed by calculating an energy value based on the error in the solution. The Curl **H** is used to find the current density and then subtracts all input currents and other sources. For a perfect solution the error should be zero, but for the actual finite element simulation there is some amount of residual current density. An energy value calculated from this residual current density in each element is called the "energy error". When the energy error targets are not satisfied the mesh is refined by subdividing the elements with the highest "energy error" into smaller elements. The mesh refinement

continues until the total "percentage energy error" is smaller than the pre-specified value. The stopping criteria of the simulation is that the “percentage energy error” is less than 1%. Table 5.1 shows the convergence data of each step in the adaptive analysis.

Table 5.1 – Convergence data of adaptive meshing.

Pass	**1**	**2**	**3**	**4**	**5**
Energy error (%)	6.8907	3.1869	1.8199	1.218	0.94256
Delta energy (%)	N/A	0.71294	0.40746	0.05993	0.28043
Number of tetrahedrons	2281002	2554730	2861301	3204664	3589230

5.3 Electromagnetic Field Formulation and Calculation

5.3.1 Basic Electromagnetic Field equations and Assumptions

The differential form of the Maxwell’s macroscopic equations can be expressed as follows:

$$\text{Gauss's law: } \nabla \cdot \mathbf{D} = \rho_f \tag{5.5}$$

$$\text{Gauss's law for magnetism: } \nabla \cdot \mathbf{B} = 0 \tag{5.6}$$

$$\text{Faraday's law of induction: } \nabla \times \mathbf{E} = -\frac{\partial \mathbf{B}}{\partial t} \tag{5.7}$$

$$\text{Ampere's circuital law: } \nabla \times \mathbf{H} = \mathbf{J} + \frac{\partial \mathbf{D}}{\partial t} \tag{5.8}$$

where **D** is the displacement field vector, ρ_f is the free charge density, **B** is the magnetic flux density vector, **E** is the electric field vector, **H** is the magnetic intensity vector, and **J** is the free electric current density.

To apply the Maxwell's macroscopic equations to the analysis of the electro-magnetic field in the end region, it is necessary to specify the relationship between **D** and **E**, as well as that between **H** and **B**. The constitutive relations set up these relationships including the effects of the polarization **P** (bound charge) and the magnetization **M** (bound current). They are based on the equations of auxiliary fields:

$$\mathbf{D}(\mathbf{r},t) = [\varepsilon]\mathbf{E}(\mathbf{r},t) + \mathbf{P}(\mathbf{r},t) \tag{5.9}$$

$$\mathbf{H}(\mathbf{r},t) = \frac{1}{[\mu]}\mathbf{B}(\mathbf{r},t) - \mathbf{M}(\mathbf{r},t) \tag{5.10}$$

where $[\varepsilon]$ is the permittivity tensor, $[\mu]$ is the magnetic permeability tensor, and **r** is the coordinate of the position.

It is justifiable to neglect polarization **P** and free charge ρ_f in the analysis of the electromagnetic field of the generator end region. Since the silicon steel and carbon steel are soft magnetic materials, the effects of hysteresis loops of magnetic materials are neglected, and due to the absence of permanent magnets in the generator, the magnetization term **M** is not considered. Thus, the constitutive relation reduces to:

$$\mathbf{D}(\mathbf{r},t) = [\varepsilon]\mathbf{E}(\mathbf{r},t) \tag{5.11}$$

$$\mathbf{H}(\mathbf{r},t) = \frac{1}{[\mu]}\mathbf{B}(\mathbf{r},t). \tag{5.12}$$

In the generator end region, $[\varepsilon] = \varepsilon_0$. However, the $[\mu]$ can be nonlinear, time-dependent and position-dependent, which will be discussed in the following sections.

In the conductive region the ratio between the displacement current and the conductive current is:

$$\frac{\|\mathbf{J_D}\|}{\|\mathbf{J}\|} = \frac{\|\omega \mathbf{D}\|}{\|[\sigma]\mathbf{E}\|} = \frac{\|[\varepsilon]\mathbf{E}\|}{\|[\sigma]\mathbf{E}\|} 2\pi f \tag{5.13}$$

where $[\sigma]$ is the bulk conductivity tensor. Since $\left\|\frac{J_D}{J}\right\| \ll 1$ in the conductive region, the displacement current is neglected and (5.8) reduces to:

$$\nabla \times \mathbf{H} = \mathbf{J}. \tag{5.14}$$

Combining (5.7), (5.8), (5.11) and (5.12) yields:

$$\nabla^2 \mathbf{E} - [\mu][\sigma]\frac{\partial \mathbf{E}}{\partial t} = 0 \tag{5.15}$$

$$\nabla^2 \mathbf{H} - [\mu][\sigma]\frac{\partial \mathbf{H}}{\partial t} = 0. \tag{5.16}$$

In the non-conductive region where $\sigma = 0$ and the material properties are linear and isotropic, combining (5.7) and (5.8) yields:

$$\nabla^2 \mathbf{E} - [\mu][\varepsilon]\frac{\partial^2 \mathbf{E}}{\partial t^2} = 0 \tag{5.17}$$

$$\nabla^2 \mathbf{H} - [\mu][\varepsilon]\frac{\partial^2 \mathbf{H}}{\partial t^2} = 0. \tag{5.18}$$

Formulas (5.17) and (5.18) are the wave equations of electromagnetic field in the free space. In the analysis of a time-varying field, it takes a certain amount of time for the electromagnetic waves to be transmitted from the current source to the destination.

However, for the fundamental frequency and its lower harmonics, the corresponding wave length is:

$$\lambda_k = \frac{1}{f\sqrt{\mu\varepsilon}} = \frac{1}{kf_1\sqrt{\mu\varepsilon}} \tag{5.19}$$

where f is the frequency, f_1 is the fundamental frequency and k is the harmonic order. The dimensions of the generator are far shorter than the wave lengths of electromagnetic waves at the fundamental frequency and its lower harmonics, so the wave character of the field is not considered and the delay of the electromagnetic wave transmission from the sources to the destinations are neglected. Thus, the field distribution in the free space excited by current sources can be solved by Biot-Savart Law:

$$\mathbf{H_S}\left(\mathbf{r},t\right) = \frac{1}{4\pi}\int_{V'}\mathbf{J}\left(\mathbf{r}',t\right)\times\frac{\mathbf{r}-\mathbf{r}'}{\left\|\mathbf{r}-\mathbf{r}'\right\|^3}d^3r' \tag{5.20}$$

where **r'** is the coordinate of a certain current element. In this way the electromagnetic field can be treated as a quasi-static field, but the effects of eddy current in the conductive region are considered so the time-varying vortex equations (5.15) and (5.16) have to be solved at every time point.

To summarize, the general assumptions applied to the 3-D field analysis are:

1) Polarization and free charge are neglected;
2) Hysteresis loops of magnetic materials are not considered so the magnetization terms are eliminated from the field equations;
3) Displacement current is neglected in the conductive region;
4) The electromagnetic field is quasi-static and the delay of field transmission is neglected;

5) The impact of temperature on the conductivity or permeability of materials is ignored.

There are some additional assumptions for sub-regions in the field analysis, which is discussed in Section 5.3.3.

5.3.2 **T**- *Ω Formulation*

The magnetic field is calculated by 3D time-stepping FEAs. The governing equations are established based on the electric vector potential **T** and magnetic scalar potential *Ω*. The free current density vector is the sum of the source current density vector $\mathbf{J_s}$ and eddy current density vector $\mathbf{J_e}$. According to Kirchhoff's current law, $\nabla \cdot \mathbf{J} = 0$, and in the simulation the current sources (stator winding current and field winding currents) are uniformly distributed so $\nabla \cdot \mathbf{J_s} = 0$, then $\nabla \cdot \mathbf{J_e} = 0$. Therefore, it is reasonable to define a vector variable **T** rendering:

$$\nabla \times \mathbf{T} = \mathbf{J_e} \tag{5.21}$$

This vector is called electric vector potential representing the impact of eddy current on the field. Substituting (5.21) into (5.14) yields:

$$\nabla \times \left(\mathbf{H} - \mathbf{T} - \mathbf{H_s} \right) = 0 \tag{5.22}$$

So magnetic scalar potential φ that satisfies the following condition can be defined:

$$\nabla \Omega = \mathbf{H} - \mathbf{T} - \mathbf{H_s} \tag{5.23}$$

The electric vector potential **T** and magnetic scalar potential *Ω* form a pair of potential variables which can uniquely determine an electromagnetic field.

Substituting (5.12) and (5.23) into (5.6) leads to:

$$\nabla \cdot [\mu](\mathbf{T} + \mathbf{H}_s + \nabla\Omega) = 0 \tag{5.24}$$

It can be derived by combining (5.7), (5.12), (5.21) and (5.23) that:

$$\nabla \times \left([\sigma]^{-1} \nabla \times \mathbf{T} \right) + \frac{\partial}{\partial t}[\mu](\mathbf{T} + \nabla\Omega) = -\frac{\partial}{\partial t}[\mu]\mathbf{H}_s \tag{5.25}$$

Equations (5.24) and (5.25) are the primary governing equations of the electromagnetic field with **T**- Ω formulation.

5.3.3 Subdomains of the Solution Region

The entire solution domain $\mathbf{\Theta}$ is divided into three subdomains: the non-eddy-current domain $\mathbf{\Theta_1}$, the solid eddy-current domain $\mathbf{\Theta_2}$, and laminated core domain $\mathbf{\Theta_3}$. Subdomain $\mathbf{\Theta_1}$ contains the air region, as well as the rotor, retaining ring, shaft and armature/field windings because the eddy current in these metal components are not considered in the 3D FEA or can be neglected during steady-state operation. Press plate and finger plates are classified into $\mathbf{\Theta_2}$. Subdomain $\mathbf{\Theta_3}$ is the stator core. The forms of governing equations are different between the three types of subdomains.

5.3.3.1 **T**-φ formulation in the non-eddy-current subdomain $\mathbf{\Theta_1}$

Define **T** = **0** since no eddy current exists in $\mathbf{\Theta_1}$. So the magnetic field can be expressed by Ω only. Then the governing equations for this subdomain are:

$$\begin{cases} \nabla \cdot [\mu]\nabla\Omega = -\nabla \cdot [\mu]\mathbf{H}_s \\ \mathbf{H} = \mathbf{H}_s + \nabla\Omega \end{cases}. \tag{5.26}$$

The permeability tensor $[\mu]$ is a 3*3 diagonal matrix and isotropic for all components in $\mathbf{\Theta_1}$. In rotor and shaft, the $[\mu]$ is related to a pre-defined nonlinear **B**-**H** curve and is time-dependent and position-dependent based on local magnetic intensity.

5.3.3.2 **T**-φ formulation in the eddy-current subdomain $\mathbf{\Theta_2}$

According to (5.21), (5.23), (5.24) and (5.25), the governing field equations of $\mathbf{\Theta_2}$ are:

$$\begin{cases} \nabla\times\left(\left[\sigma\right]^{-1}\nabla\times\mathbf{T}\right)+\dfrac{\partial}{\partial t}\left[\mu\right]\left(\mathbf{T}+\nabla\Omega\right)=-\dfrac{\partial}{\partial t}\left[\mu\right]\mathbf{H}_{\mathbf{s}} \\ \nabla\cdot\left[\mu\right]\left(\mathbf{T}+\nabla\Omega\right)=-\nabla\cdot\left[\mu\right]\mathbf{H}_{\mathbf{s}} \\ \mathbf{H}=\mathbf{H}_{\mathbf{s}}+\mathbf{T}+\nabla\Omega \\ \mathbf{J}=\nabla\times\mathbf{T} \end{cases} . \tag{5.27}$$

The $[\mu]$ is isotropic and nonlinear in the press plate made of carbon steel. The effects of hysteresis loss and excess loss on the magnetic field are neglected because they are far less remarkable than that of the eddy current loss in the press plate.

5.3.3.3 **T**-φ formulation in the laminated core subdomain $\mathbf{\Theta_3}$

The field formulation in $\mathbf{\Theta_3}$ is the most complicated one due to the nonlinear and anisotropic material properties of the stator core. It is impossible to explicitly draw the structures of each lamination because it will inevitably result in a huge number of elements in the 3D FEA. The impact of the eddy current induced by the end leakage flux on the magnetic field is excluded from the calculation. The effects of classical core losses on the field are considered by introducing an additional field component and anisotropic conductivity in this subdomain. Specifically, the field equations in $\mathbf{\Theta_3}$ can be expressed as:

$$\begin{cases} \nabla\times\left(\left[\sigma\right]^{-1}\nabla\times\mathbf{T}\right)+\dfrac{\partial}{\partial t}\left[\mu\right]\left(\mathbf{T}+\nabla\Omega+\mathbf{H}_{\mathbf{s}}+\mathbf{H}_{\mathbf{p}}\right)=0 \\ \nabla\cdot\left[\mu\right]\left(\mathbf{H}_{\mathbf{s}}+\mathbf{T}+\nabla\Omega+\mathbf{H}_{\mathbf{p}}\right)=0 \end{cases} \tag{5.28}$$

where $\mathbf{H_p}$ is the additional magnetic field term due to core loss [185], and

$$\mathbf{H_p} = \mathbf{H_{pc}} + \mathbf{H_{ph}} + \mathbf{H_{pe}} \tag{5.29}$$

where $\mathbf{H_{pc}}$, $\mathbf{H_{ph}}$ and $\mathbf{H_{pe}}$ correspond to the effects of classical eddy current loss, static hysteresis loss and excess core loss respectively. Here the classical eddy current loss is caused by the time-varying radial/tangential flux.

For the term $\mathbf{H_{pc}}$, the classical eddy current loss density is normally given in the frequency domain as:

$$p_c = k_c \left(f B_m \right)^2 \tag{5.30}$$

where B_m is the flux density magnitude, and k_c is the classical eddy current loss coefficient obtained by:

$$k_c = \frac{\pi^2 \sigma d^2}{6} \tag{5.31}$$

where d is the thickness of laminations.

In the time domain, the density eddy current loss can be expressed as

$$p_c(t) = \frac{k_c}{2\pi^2} \cdot \frac{\partial \mathbf{B}}{\partial t} \cdot \frac{\partial \mathbf{B}}{\partial t} = \mathbf{H_{pc}} \cdot \frac{\partial \mathbf{B}}{\partial t} \tag{5.32}$$

Therefore, the equivalent field component $\mathbf{H_{pc}}$ is:

$$\mathbf{H_{pc}} = [k] \frac{\partial \mathbf{B}}{\partial t} = [k] \frac{\partial}{\partial t} [\mu] \left(\mathbf{H_s} + \mathbf{T} + \nabla \Omega + \mathbf{H_p} \right) \tag{5.33}$$

where $\mathbf{T} = \mathbf{0}$ and the tensor $[k]$ is defined as:

$$[k]=\begin{bmatrix} k_c/(2\pi)^2 & 0 & 0 \\ 0 & k_c/(2\pi)^2 & 0 \\ 0 & 0 & 0 \end{bmatrix} \tag{5.34}$$

Regarding the term $\mathbf{H_{ph}}$, the hysteresis loss density is computed in the frequency domain as

$$p_h = k_h f\left(B_m\right)^2 \tag{5.35}$$

where k_h is the hysteresis loss coefficient. The hysteresis loss in the time domain can be expressed as

$$p_h(t) = \mathbf{H_{ph}} \cdot \frac{\partial \mathbf{B}}{\partial t} \tag{5.36}$$

The equivalent field component $\mathbf{H_{ph}}$ is calculated by

$$\begin{cases} B = B_m \sin(\theta) \\ H_{ph} = H_m \cos(\theta) = \dfrac{k_h}{\pi} B_m \end{cases} \tag{5.37}$$

In (5.37), the *x*-, *y*- and *z*-direction field components are calculated individually, and B_m is obtained from a historical record of the maximum absolute value of flux density in each direction.

For the term $\mathbf{H_{pe}}$, the excess loss density is computed in the frequency domain as

$$p_e = k_e\left(fB_m\right)^{1.5} \tag{5.38}$$

where k_e is the excess loss coefficient. The excess loss in the time domain can be expressed as

$$p_e(t) = \mathbf{H_{pe}} \cdot \frac{\partial \mathbf{B}}{\partial t} \tag{5.39}$$

The equivalent field component $\mathbf{H_{pe}}$ is obtained by

$$\mathbf{H_{pe}} = \frac{k_e}{C_e}\left[\left(\frac{\partial B}{\partial t}\right)_m\right]^{-0.5} \frac{\partial \mathbf{B}}{\partial t} \tag{5.40}$$

where

$$\left(\frac{\partial B}{\partial t}\right)_m = \sqrt{\left(\frac{\partial B_x}{\partial t}\right)^2 + \left(\frac{\partial B_y}{\partial t}\right)^2 + \left(\frac{\partial B_z}{\partial t}\right)^2} \tag{5.41}$$

$$C_e = (2\pi)^{1.5} \cdot \frac{2}{\pi}\int_0^{\pi/2} \cos^{1.5}\theta d\theta = 8.763363 \tag{5.42}$$

The method of determining the core loss coefficients k_c, k_h and k_e is introduced in Section 5.4. The components $\mathbf{H_{ph}}$ and $\mathbf{H_{pe}}$ are computed in an iterative process at each time point [185]. So far, the effects of the lamination classic core losses on the transient magnetic field have been comprehensively analyzed. It should be noticed that in the stator core the permeability tensor $[\mu]$ is time/location-dependent, nonlinear and anisotropic:

$$[\mu] = \begin{bmatrix} \mu_x & & \\ & \mu_y & \\ & & \mu_z \end{bmatrix} = \begin{bmatrix} k_{lam}\mu_{fe} + (1-k_{lam})\mu_0 & & \\ & k_{lam}\mu_{fe} + (1-k_{lam})\mu_0 & \\ & & \dfrac{\mu_{fe}}{(1-k_{lam})\mu_{fe} + k_{lam}\mu_0}\mu_0 \end{bmatrix} \tag{5.43}$$

where μ_0 and μ_{fe} are the permeability of the vacuum (air) and steel respectively, k_{lam} is the stacking factor representing the ratio between the thickness of steel laminations and the

length of the stator core. In the transient analysis, μ_{fe} is time-varying and position-varying due to the nonlinear B-H curve of the silicon steel.

5.4 Electromagnetic Loss Formulation

5.4.1 Calculation of Loss Density Distribution in the Press Plate and Finger Plates

For an arbitrary location in the press plate and finger plates, the time-average eddy current loss density can be expressed as

$$\begin{aligned}\overline{p} &= \frac{2}{\sigma\tau}\int_{t_0}^{t_0+\frac{\tau}{2}}\left(J_r^{\,2}+J_t^{\,2}+J_z^{\,2}\right)dt \\ &= \frac{2}{\sigma\tau}\int_{t_0}^{t_0+\frac{\tau}{2}}\left[\left(\frac{1}{r}\frac{\partial T_z}{\partial\theta}-\frac{\partial T_\theta}{\partial z}\right)^2+\left(\frac{\partial T_r}{\partial z}-\frac{\partial T_z}{\partial r}\right)^2+\left(\frac{1}{r}\frac{\partial rT_\theta}{\partial r}-\frac{1}{r}\frac{\partial T_r}{\partial\theta}\right)^2\right]dt\end{aligned} \tag{5.44}$$

where τ is the electrical cycle, J_r, J_t and J_z are the radial, tangential and axial components of eddy current density respectively, and T_r, T_t and T_z are the radial, tangential and axial components of electric vector potential respectively. In this simulation, the hysteresis loss and excess loss of the press plate are ignored since they are negligible compared to the eddy current loss.

5.4.2 Calculation of the Stator Core Loss Density Distribution

The core loss density comprises the hysteresis loss density p_h, the excess loss density p_e, the classical eddy current loss density p_c caused by the radial/peripheral main fluxes and the additional eddy current loss density p_{cd} induced by end leakage flux. The first three terms are included in the conventional core loss models [188]

$$\begin{cases} p_h = \left\{ \left| H_r \dfrac{dB_r}{dt} \right|^{\frac{2}{\beta}} + \left| H_\theta \dfrac{dB_\theta}{dt} \right|^{\frac{2}{\beta}} + \left| H_z \dfrac{dB_z}{dt} \right|^{\frac{2}{\beta}} \right\} \\ p_e = \dfrac{1}{C_e} k_e \left\{ \left(\dfrac{dB_r}{dt} \right)^2 + \left(\dfrac{dB_\theta}{dt} \right)^2 + \left(\dfrac{dB_z}{dt} \right)^2 \right\}^{0.75} \\ p_c = \dfrac{1}{2\pi^2} k_c \left\{ \left(\dfrac{dB_r}{dt} \right)^2 + \left(\dfrac{dB_\theta}{dt} \right)^2 \right\} \end{cases} \tag{5.45}$$

where k_e and k_c are the excess and classical eddy current loss coefficients. The value of k_c is determined by the thickness of laminations and conductivity as discussed in Section 5.3.3.3. In the calculation

$$\beta = 2, C_e = \left(2\pi\right)^{1.5} \cdot \frac{2}{\pi} \int_0^{\frac{\pi}{2}} \cos^{1.5}\theta d\theta. \tag{5.46}$$

The hysteresis and excess loss coefficients k_h and k_e are determined by the manufacturer-provided loss curve (B_i, p_i) at the fundamental frequency through a curve regression algorithm. k_h and k_e are calculated by minimizing the function [188]:

$$F\left(k_h, k_e\right) = \sum_i \left[\left(p_i - k_c f_1^{\,2} B^2 \right) - k_h f_1 B^2 - k_e f_1^{1.5} B^{1.5} \right]^2 = \min \tag{5.47}$$

The time-average additional eddy current loss density is

$$\overline{p}_{cd} = \frac{2}{\sigma_{//} T} \int_{t_0}^{t_0 + \frac{T}{2}} \left\| \mathbf{J}_{//} \right\|^2 dt = \frac{2}{\sigma_{//} T} \int_{t_0}^{t_0 + \frac{T}{2}} \left\| \left(\nabla \times \mathbf{T} \right)_{//} \right\|^2 dt \tag{5.48}$$

where T is the electrical cycle. To summarize, the laminated core model incorporates the effects of nonlinear/anisotropic properties, eddy current reaction and classical core loss.

5.4.3 Calculation of the Copper Loss Density Distribution in the Stator Windings

In large generators, the stator windings consist of multiple insulated parallel copper strands, known as Roebel bars. These copper strands are connected in the end region and various types of transpositions have been used to mitigate circulating currents between strands [195], [196]. In the large generator investigated in this dissertation, 540° transposition is applied to the stator bars in the active part of the machine and the strands in the end region are not transposed. The configuration of the stator coil strands in a slot on a *radial-peripheral* cross section is demonstrated in Figure 5.12. There are two columns of strands, and the number of rows of strands is M_1 and M_2 for the top and bottom winding respectively. In addition to the general ohmic loss assuming uniform current density distribution in a strand, there are two major sources of losses in the copper strands: the skin-effect-associated losses and the eddy current losses caused by external impinging flux. The skin effect leads to the increase in the effective resistance and thus the loss of the strands due to the concentration of the ac currents in a small region near the surface of the conductor. The external fluxes that induce eddy currents in the strands include the airgap flux entering the slots caused by the difference between the magnetic potentials on the stator and rotor surfaces, and the slot leakage flux produced by the currents in the other strands of the same slot. It is infeasible to directly model and solve the eddy current in each strand in 3D FEAs because it requires extensively dense elements in the strands, which greatly increases the complexity and solution time of the simulations. The additional copper loss density is solved in post processing based on the dimensions of the stator bars and the flux distributions in the slots. To incorporate the loss related to skin effects, the approximate formula of ac resistivity is applied to modify the copper loss density [197]:

$$\bar{p}_{ac} = \frac{J^2}{2\sigma} \cdot \frac{\rho_{ac}}{\rho_{dc}} = \frac{I_s^{\,2}}{2\sigma(ab)^2} \cdot \sqrt{1 + \left(\frac{\kappa ab}{2\delta(a+b)} \right)^2} \tag{5.49}$$

where ρ_{ac} and ρ_{dc} are the ac and dc resistivity respectively, σ is the conductivity of material, I_s is the strand current, a and b are the width and height of a strand, δ is the skin depth, and the coefficient $\kappa \approx 1.2$. Here [197]

$$\delta = \sqrt{2/(\omega\mu\sigma)} \tag{5.50}$$

where ω is the frequency, and μ is the permeability of material. Only the fundamental frequency is considered when computing the ac loss density in each strand. Regarding the calculation of the eddy current density caused by external fluxes, since the impinging flux cannot penetrate deep axially through the active length of the stator coils due to the eddy current reaction, only the radial and peripheral flux densities are considered. The time-varying radial and peripheral flux densities are extracted from the 3D transient FEAs and the time-average eddy current loss density of a rectangular strand can be obtained by [197]:

$$\bar{p}_{ed} = \frac{\sigma\omega_1^2}{8}\sum_k k^2\left(\frac{B_{r,k}{}^2 a^2}{\xi_{a,k}}\cdot\eta\left(\xi_{a,k}\right)+\frac{B_{\theta,k}{}^2 b^2}{\xi_{b,k}}\cdot\eta\left(\xi_{b,k}\right)\right) \tag{5.51}$$

where ω_1 is the fundamental frequency, $B_{r,k}$ and $B_{\theta,k}$ are the magnitude of the kth-order harmonic radial and peripheral flux density respectively, and

$$\xi_{a,k} = a\sqrt{\frac{k\omega_1\mu\sigma}{2}},\ \xi_{b,k} = b\sqrt{\frac{k\omega_1\mu\sigma}{2}}.$$

In (5.51), the coefficient η is given by [197]:

$$\eta(\xi) = \frac{\sinh\xi - \sin\xi}{\cosh\xi - \cos\xi}. \tag{5.52}$$

Finally, the time-average strand copper loss density is

$$\bar{p}_{loss} = \bar{p}_{ac} + \bar{p}_{ed}. \tag{5.53}$$

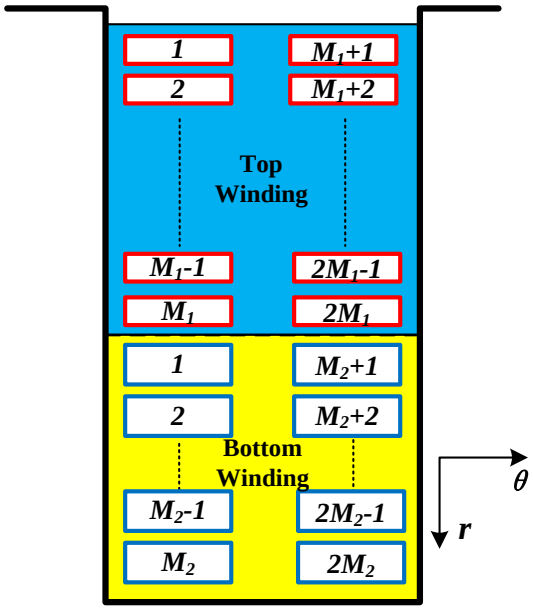

Figure 5.12 Stator coil configuration on a *radial-peripheral* cross section of a slot.

The axial distribution of $\bar{p}_{loss}$ should be solved for all strands of the top and bottom windings in a slot for thermal analyses.

5.5 Stationary 3D Thermal FEA Model

5.5.1 General Description of the Thermal FEA Model

Multi-physics modeling is important for the analysis of energy conversion systems [198], [199]. The transient electromagnetic study yields value for the heat generation density due to ohmic losses at each point of the domain. The thermal diffusivity of iron is about $2.3 \cdot 10^{-5}$ m^2/s. Since the heat transfer surface is in the order of 1 m^2, the time constant of conductive heat transfer is of the order of $4.3 \cdot 10^4$ s. Therefore, the variation in the electromagnetic behavior is several orders of magnitude faster than the thermal diffusion through the material. Thus, a steady state thermal simulation is carried out.

By assuming thermal steady state, it is expected that all teeth have a similar temperature distribution. Indeed, all heat transfer processes occurring in the generator have

a characteristic speed that is several orders of magnitude lower than the rotational speed of the machine. Therefore, the simulation can be further simplified by considering only one tooth and applying periodic boundary conditions on each side of the domain. The geometry considered in the thermal model is shown in Figure 5.13.

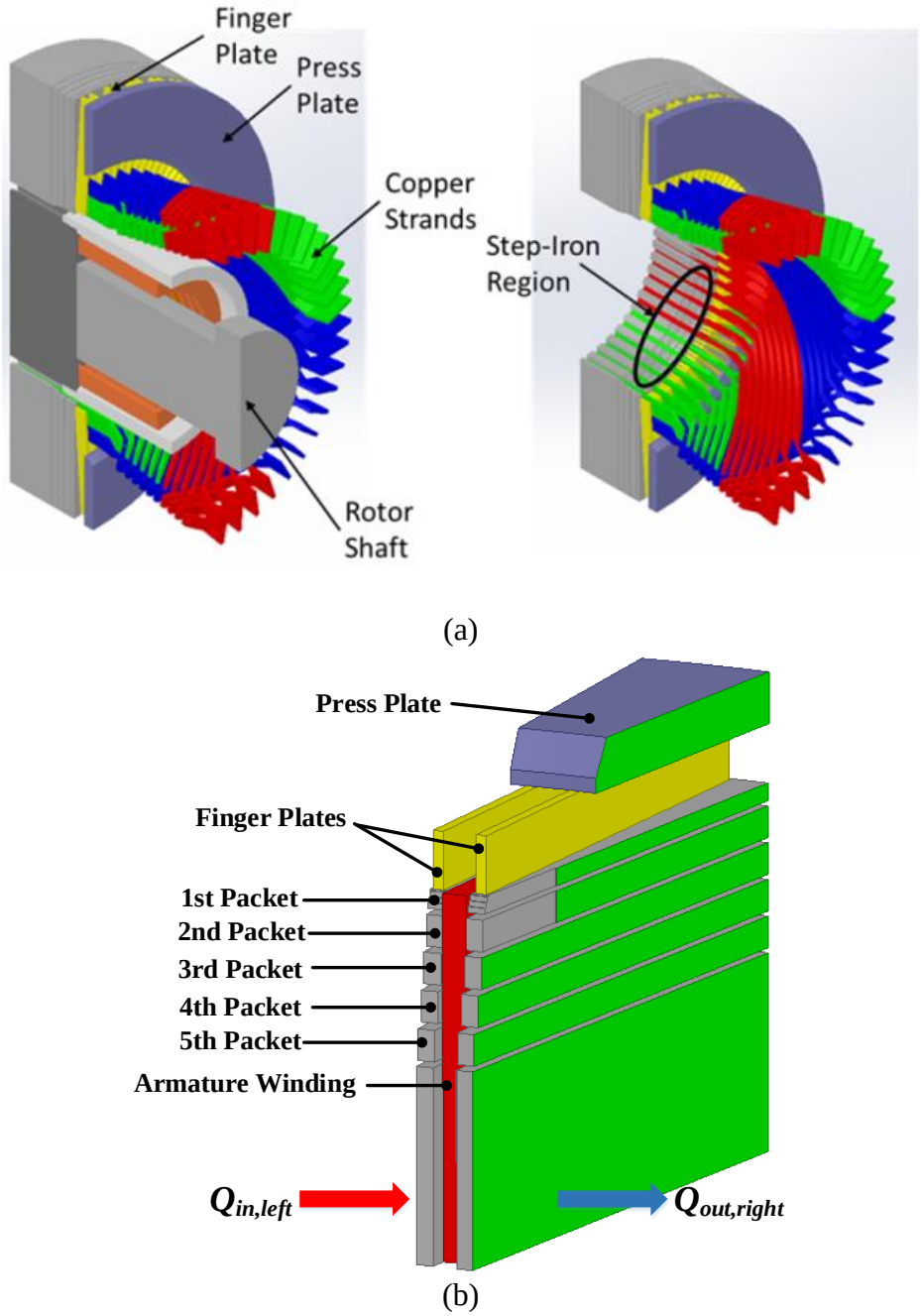

Figure 5.13 Geometry of (a) the transient electromagnetic simulation; (b) simplified model in the stationary 3D thermal simulation.

The mathematical governing equation of the stationary thermal field is

$$k\nabla^2 T + q_v = 0 \tag{5.54}$$

where T is the temperature field, k is the thermal conductivity tensor and q_v is the heat generation density. The distribution of heat generation density is obtained from the EM analysis by taking the average loss density over an electrical cycle at steady state, while the thermal conductivity in each component and the boundary conditions of (5.54) are described in Sections 5.5.2 and 5.5.3, respectively.

5.5.2 Material Properties

In the thermal model, the steel exhibits anisotropic properties due to the structure of laminations, resulting in a lower thermal conductivity in the axial direction. The thermal conductivity of the steel in the axial direction is defined to be 6.6 W/m-K. An equivalent thermal conductivity is introduced to account for the insulation between the copper strands. The algebraic expressions for both radial direction as well as axial and tangential direction appear in (5.55).

$$\hat{k}_r = \frac{t_{ins} + t_{cu}}{t_{ins}/k_{ins} + t_{cu}/k_{cu}}, \hat{k}_{z,\theta} = \frac{t_{ins}k_{ins} + t_{cu}k_{cu}}{t_{ins} + t_{cu}} \tag{5.55}$$

where t_{ins} and t_{cu} are the thickness of the insulation layer and copper in the stator strands respectively, and k_{ins} and k_{cu} are the thermal conductivity of insulation material and copper in the stator strands respectively. The thermal conductivity in radial direction is greatly diminished due to the strand insulation. The key material properties are summarized in Table 5.2.

Table 5.2 – Key material properties defined in the stationary thermal model.

Property	Unit	Value
steel thermal conductivity (r and θ)	[W/m-K]	23.0
steel thermal conductivity (z)	[W/m-K]	6.6
steel density	[kg/m^3]	8500
steel specific heat capacity	[J/kg-K]	460
copper density	[kg/m^3]	8960
copper specific heat capacity	[J/kg-K]	386
copper top bar equivalent thermal conductivity (r)	[W/m-K]	1.71
copper top bar equivalent thermal conductivity (z and θ)	[W/m-K]	338.5
copper bottom bar equivalent thermal conductivity (r)	[W/m-K]	2.20
copper bottom bar equivalent thermal conductivity (z and θ)	[W/m-K]	352.0

5.5.3 Boundary Conditions

Directly modeling the thin insulation layer between the copper coils and the iron stator body in an FEA simulation is challenging due to small thickness of the layer which can potentially cause badly conditioned elements or an exponential increase in the total number of elements. To overcome this challenge, the insulation layer is modelled as an infinitely thin thermal resistance layer boundary. The equivalent thermal resistance is defined to be 0.0173 m^2-K/W according to (5.56):

$$R_{layer} = \frac{l_{isl}}{k_{isl}} \tag{5.56}$$

where l_{isl} and k_{isl} are the thickness and thermal conductivity of the insulation layer, respectively, and are assumed to be 4.5 mm and 0.26 W/m-K, respectively.

The heat transfer rate along the stator windings is assumed to be negligible as compared to the heat removed by convection. Therefore, the axial extremities of the

coppers bars are subject to adiabatic boundary conditions. It is also assumed that the outer radius of the stator back-iron is not subject to any significant heat transfer, and the corresponding surface is therefore considered to be adiabatic. The inner portion of the stator is subject to convective heat transfer occurring in the air gap. The value of the convective heat transfer coefficient in the air gap was provided by the research sponsor. The radial vents provide bulk of the cooling power and are subject to convective boundary conditions. The convective heat transfer coefficients in the radial vents are calculated based on the coolant velocities measured by the research sponsor. The Dittus-Boelter correlation is adopted to compute the Nusselt number following (5.57). The hydraulic diameter is computed according to (5.58) and takes a value of 14 mm. Since the cross-sectional area of the channel increases along the flow path, the flow velocity and hence the convective heat transfer coefficient are functions of the radius. By assuming constant air properties over the range of temperatures considered, the expression shown in (5.58) is derived for the convective heat transfer coefficient in the radial vents as a function of the radius r and the velocity at the outer diameter of the stator u_o. The Nusselt number is corrected for entry effects by using (5.59). The air temperature in the radial vents is dependent on the radius. It is adapted using a first law balance based on the heat generated in each single stack, as shown in (5.60). Thereby, it is assumed that the amount of heat transferred to the fluid is proportional to the surface area of the vent.

$$Nu_{D_h} = 0.023\,\mathrm{Re}_{D_h}^{0.8}\,\mathrm{Pr}^{0.4} \tag{5.57}$$

$$D_h = \frac{4A_c}{P} \tag{5.58}$$

$$\frac{Nu_{D,entry}}{Nu_D} = 1 + \frac{C}{\left(x/D_h\right)^m} \tag{5.59}$$

$$T_{air,j}(r) = T_{in,j} + \frac{0.5\left(Q_{Gen,j} + Q_{Gen,j+1}\right)}{\dot{m}c_p}\frac{r^2 - r_i^2}{r_o^2 - r_i^2} \tag{5.60}$$

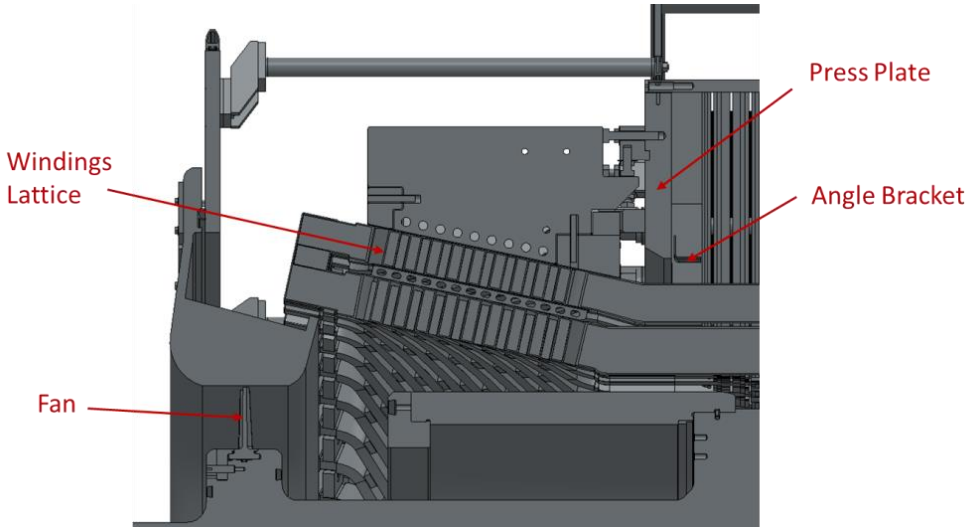

Figure 5.14 Domain of interest for the estimation of the convective heat transfer coefficients in the press plate and finger plates region.

The surfaces of the press plate, finger plates and top surface of the stator iron body are subject to convection boundary conditions. However, the intricate geometry, especially the baffling directing the flow at the bottom of the press plate, prevents the use of an existing correlation for the determination of the convective heat transfer coefficient. Therefore, a localized, 2-dimensional axis-symmetric computational fluid dynamics (CFD) study is performed to estimate the convective heat transfer coefficient on the surfaces of the press plate and the finger plates. The domain of interest for the CFD study is shown in Figure 5.14, and the simulation setup is demonstrated in Figure 5.15. The resulting flow field is shown in Figure 5.16. The flow acceleration due to the baffle below the press plate is shown in Figure 5.17. Finally, and as already mentioned, periodic boundary conditions are applied on each side surface of the tooth shown in Figure 5.13(b).

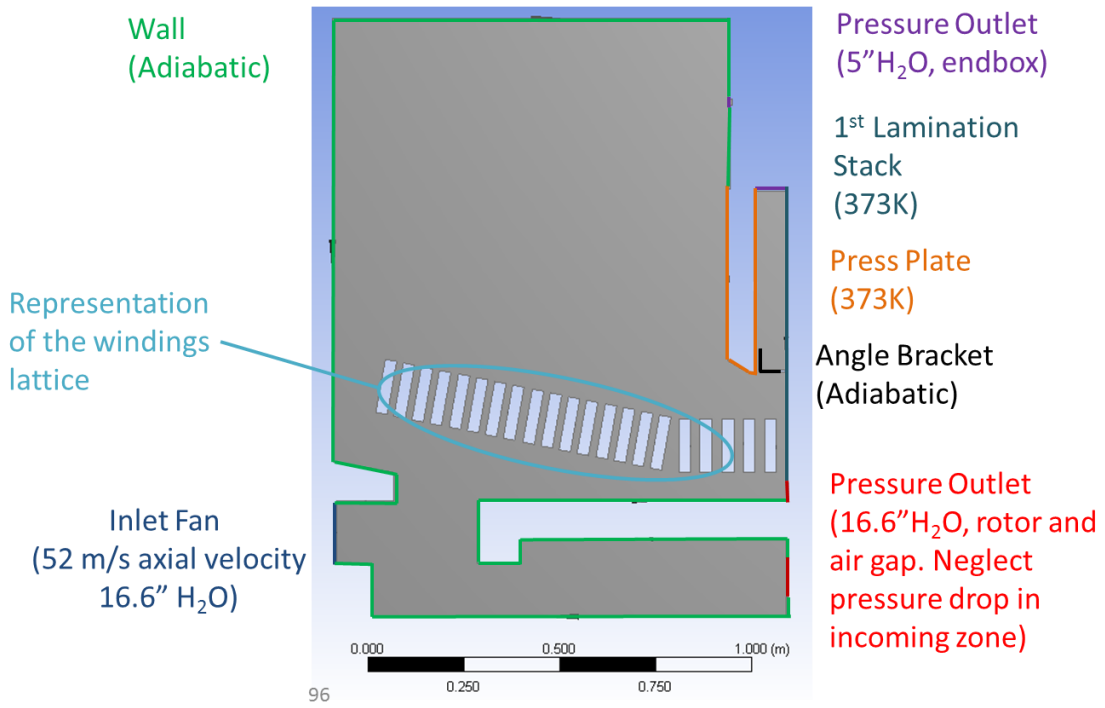

Figure 5.15 Setup of the 2D axis-symmetric simulation for the estimation of the convective heat transfer coefficients in the press plate and finger plates region.

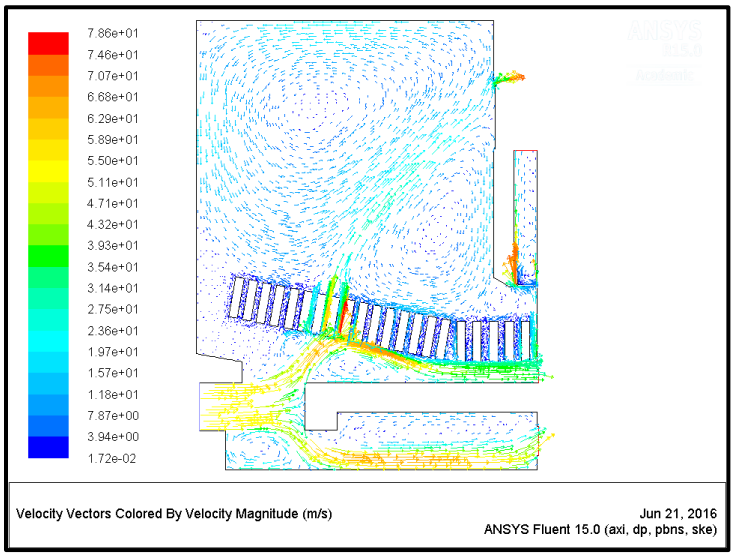

Figure 5.16 Flow field in the end-region of the generator calculated in the CFD simulation.

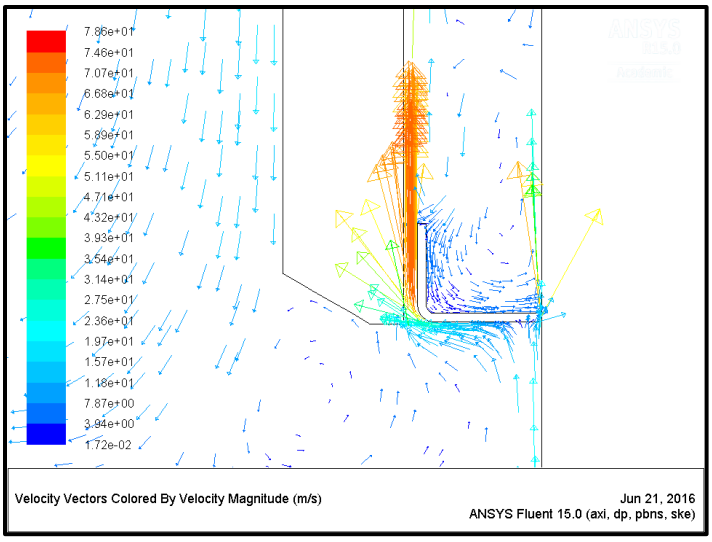

Figure 5.17 Flow acceleration due to baffle under the press plate.

5.6 Validation of the 3D Numerical Model

The 3D numerical model is validated by substituting the loss density distributions in all end components predicted by the transient 3D EM model into the stationary 3D thermal FEA to calculate the temperature distribution and comparing the estimated temperatures at different location with the measured data. Referring to the 3D thermal model presented in Figure 5.13(b), thermocouples are mounted in the 1st stator packet at the locations A and B, the 2nd stator packet at the location C with the same radius as A in the 1st packet, and on the top surface of the press plate at the positions D, E and F as shown in Figure 5.18. There is also a thermocouple mounted on the 1st (top) strand of the top winding with an axial distance of 5.3 mm to the core end (position G). Only open-circuit or short-circuit tests can be implemented for a large generator and it is difficult to measure the temperature when it generates the rated power after commissioning. The temperatures are therefore measured during the 110% O/C and 100% S/C tests at steady state.

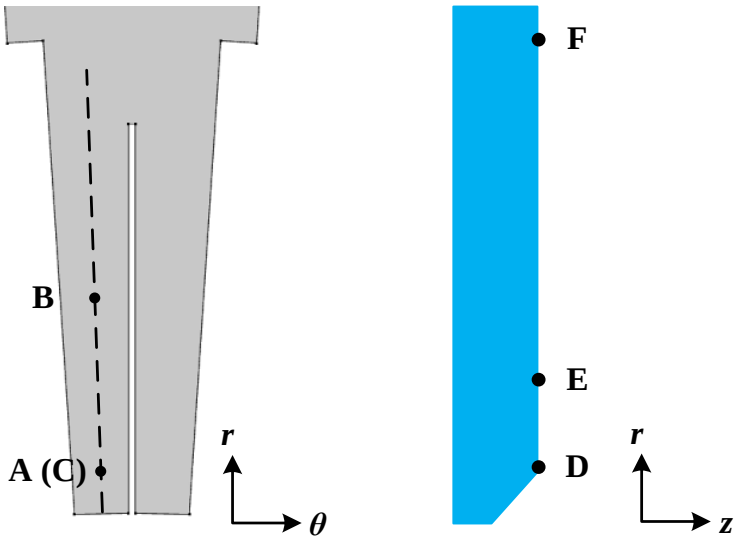

(a) (b)

Figure 5.18 Locations of thermocouples: (a) In the teeth of the outermost stator end packet; (b) On the top surface of the press plate.

Table 5.3 shows a comparison between the calculated and measured temperatures in the stator core and press plate. The largest absolute and percentage differences between the measured and predicted values are 3.7°C and 4.0% respectively. This validates the accuracy of the proposed method. It can be observed in Table 5.3 that the temperature in the teeth of the end packets in the S/C condition is slightly higher than the O/C condition, which is mainly due to the massive heat generated in the copper strands transferred to the stator core in the S/C test. However, the core loss density is relatively lower in the S/C test since the armature reaction mmf cancels the excitation mmf and the magnetic field in the stator core is weak. Furthermore, the ventilation ducts between end packets and the associated radial air flows are carefully designed to effectively dissipate the heat in the end core and avoid overheating. Thus, the temperatures at the S/C condition in Table 5.3 are also within acceptable limits. In both O/C and S/C tests, the temperature in the 2nd packet is lower than the 1st packet since the axial end leakage flux is shielded by the 1st packet and the resultant in-plane eddy current is weaker in the 2nd packet. The temperature of the press

plate is much higher in the S/C test than the O/C test because of the eddy current loss induced by the leakage flux that is excited by the stator end windings. The air flow between the press plate and the 1st packet is strengthened to prevent the heat generated in the press plate from being conducted to the stator that can potentially damage the insulation material between laminations.

Table 5.3 – Temperatures of the end stator core, press plate and top stator winding.

Condition	Position	A	B	C	D	E	F	G
110% O/C (°C)	**Measured**	61.3	56.9	58.1	52.2	53.5	53.5	97.5
	Predicted	63.4	56.5	58.2	54.3	53.1	53.3	98.3
100% S/C (°C)	**Measured**	73.7	77.8	64.6	114.1	95.8	99.7	129.8
	Predicted	74.6	75.2	67.1	110.7	92.1	102.4	130.4

5.7 Chapter Summary

This chapter describes a 3D FEA approach to calculate the electromagnetic field and losses in the end region that combines the modeling of anisotropic/nonlinear material properties, core loss effects, and the in-plane eddy currents caused by axial flux in the laminations. This approach is validated by the agreement between the calculated and measured temperatures and is used to analyze the magnetic field and loss distributions in the large generator end region.

CHAPTER 6. PARAMETRIC STUDY FOR THE DESIGN OF LARGE SYNCHRONOUS GENERATOR END REGION BASED ON THE 3-DIMENSIONAL NUMERICAL MODEL

Chapter 5 presents a validated 3-dimensional numerical approach to estimate the distributions of the magnetic field, loss density and temperature in the end region of large generators. Based on the 3D numerical model, this chapter studies the influences of various factors, including operating conditions, material properties and geometric structures, on the behaviors of the magnetic field and loss generation in the end region of large generators. First, the magnetic field and loss distributions in the end components in the open-circuit test condition, short-circuit test condition, and rated apparent power conditions are analyzed and compared by using the proposed 3D transient FEA method. Then, the impacts of different material properties and dimensions of the end metallic components, especially the press plate, on the magnetic flux and loss distributions in this region are evaluated by the 3D numerical model. Finally, a comparative study is carried out to evaluate the effectiveness of different designs of the end field/armature windings and end stator structures in reducing the losses in the end region, including the stepped profile of the end core packets, the assignment of the end tooth slits, the angle of the inclined armature end windings, and the relative axial lengths of the stator and rotor. The parametric study presented in this chapter establishes a favorable foundation for the analysis of the magnetic field behaviors in the end region and the design optimization for the end components of large synchronous generators.

6.1 Effects of Operating Conditions

The 3D numerical method is performed for the following five operating conditions: open-circuit test condition (110% rated terminal voltage), short-circuit test condition

(100% rated armature current), and rated apparent power with a 0.85 lagging power factor, a unity power factor and a 0.95 leading power factor conditions. This section analyzes and compares the magnetic and loss distributions in the press plate, finger plates, end stator core and stator end windings in different operating conditions.

6.1.1 Magnetic Field and Loss Distributions in the Press Plate

The press plate can be treated as a solid conductor, and the magnetic flux cannot penetrate deep into the press plate due to the eddy effects and is concentrated in a thin layer beneath the surface (skin effect). Figure 6.1 shows the distribution of the field intensity on the *q*-axis plane at the 0.95 leading pf condition. Since the press plate is made of highly nonlinear magnetic steel, the skin depth depends on the local saturation level. The radially inner surface has the strongest magnetic field and the skin depth is relatively larger, as shown in Figure 6.1.

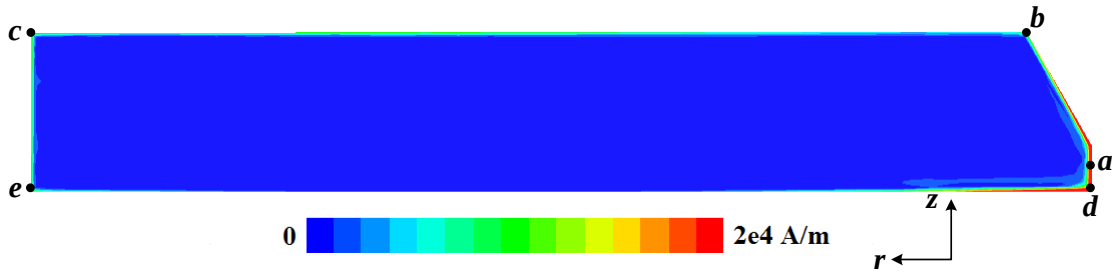

Figure 6.1 Distribution of the magnetic field intensity in the press plate on the *q*-axis cross-section plane at the 0.95 leading pf condition.

Figure 6.2 and Figure 6.3 show the surface distributions of magnetic field and loss density in the press plate in the 110% O/C and 0.95 leading pf conditions. The flux and loss densities rotate at synchronous speed with constant magnitudes. The flux and eddy currents in the press plate are produced by the field and armature end winding mmfs. According to the Biot-Savart Law, the field intensity is inversely proportional to the square of the distance between source currents and the destination. The distance from the press

plate to the armature end windings is much shorter than that to the field windings, thus the magnetic flux and eddy current are weakest in the O/C condition due to the absence of armature currents. The patterns of the field and loss distributions in the press plate at the 100% S/C, unity pf, and 0.85 lagging pf conditions resemble the pattern in the 0.95 leading pf condition shown in Figure 6.2(b) and Figure 6.3(b).

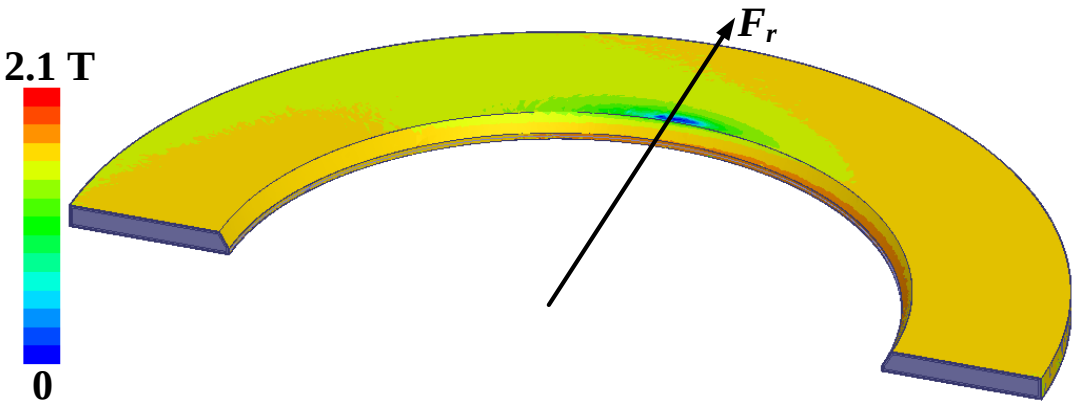

(a)

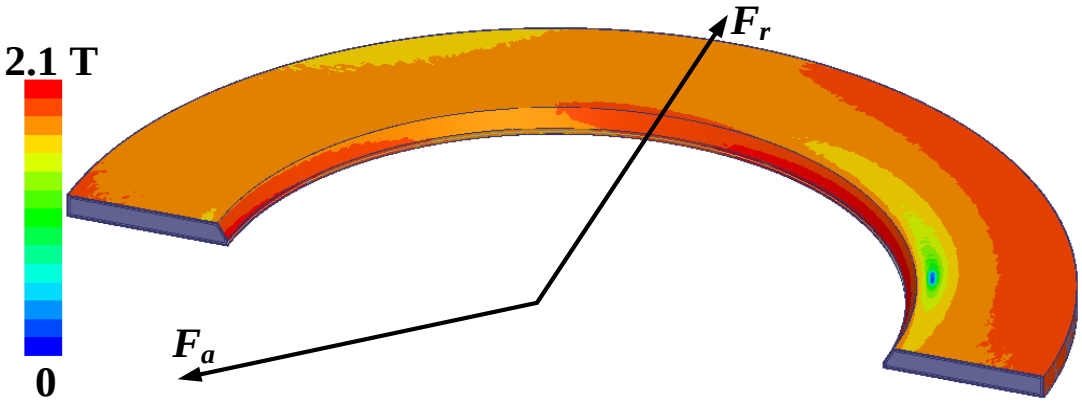

(b)

Figure 6.2 Magnetic flux density distribution on the surface of the press plate at one time instant. (a) 110% O/C condition; (b) 0.95 leading pf condition.

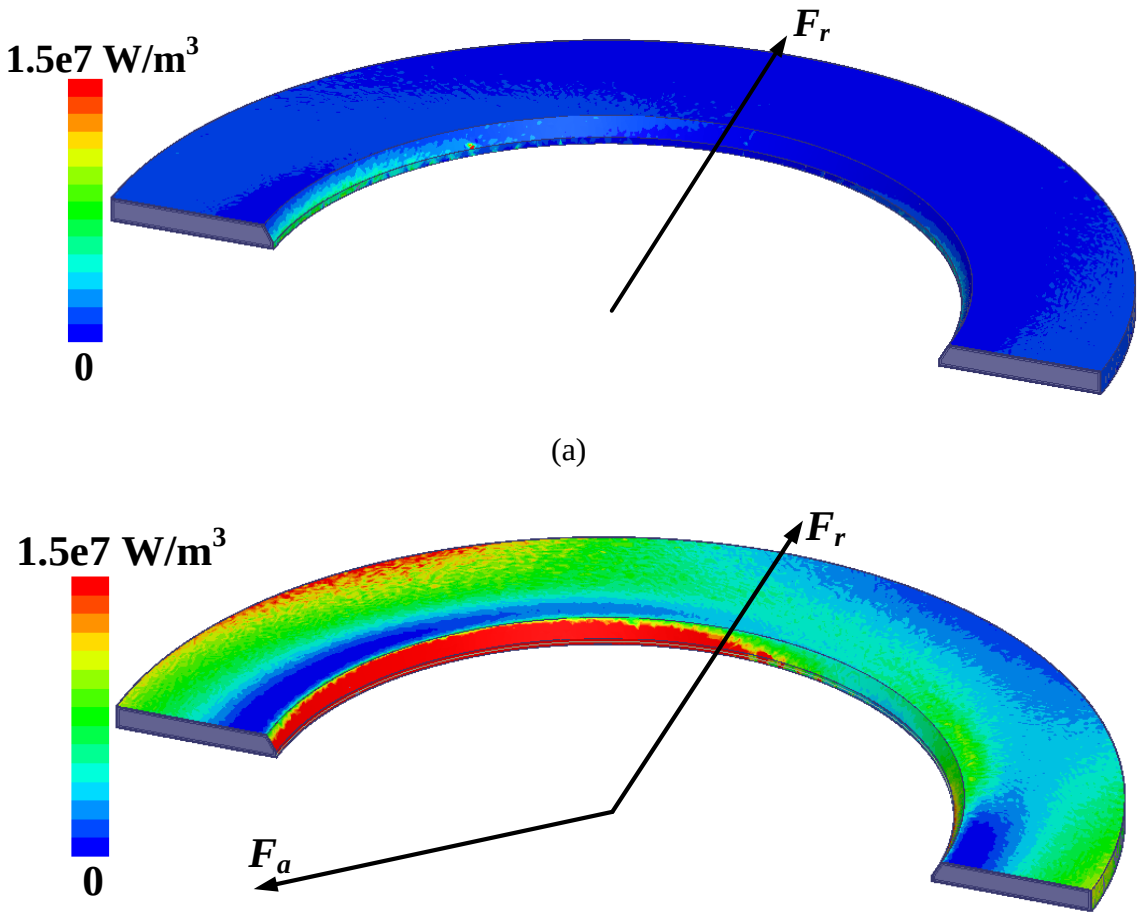

Figure 6.3 Loss density distribution on the surface of the press plate at one time instant. (a) 110% O/C condition; (b) 0.95 leading pf condition.

Figure 6.4 shows the surface distribution of flux and eddy current density vectors in the press plate at 0.95 leading pf condition. In the skin layer, the flux density vector is generally parallel to the surfaces, since the normal component is directly canceled by eddy effects. Thus in Figure 6.4(a), on the axially outer surface, the flux density vector only has radial and tangential components. The leakage flux induces eddy current parallel to the surfaces and orthogonal to the flux. The eddy current forms four main closed loops in the skin layer. The first two loops circulate between the radially inner surface and the axially outer surface. In these two loops, the eddy current flows peripherally beneath the radially inner surface, and then enters the skin layer of the axially outer surface and changes their

paths radially; when it approaches the region near the outer diameter of the press plate, it turns to the opposite peripheral direction and flows back to the radially inner surface. Each closed loop corresponds to one pole of the generator and they flow in opposite directions as illustrated in Figure 6.4(b). The other two closed loops exhibit similar patterns and appear in the skin layers of the axially inner surface and the radially outer surface.

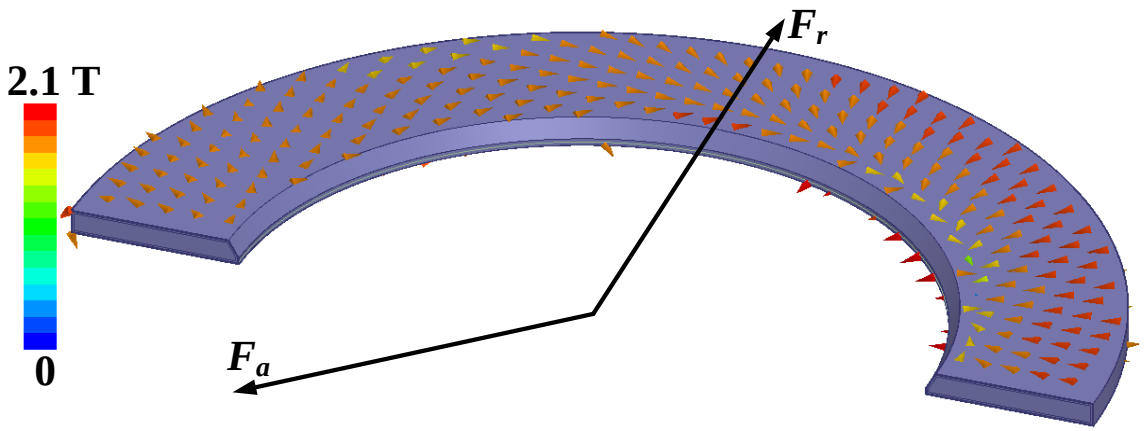

(a)

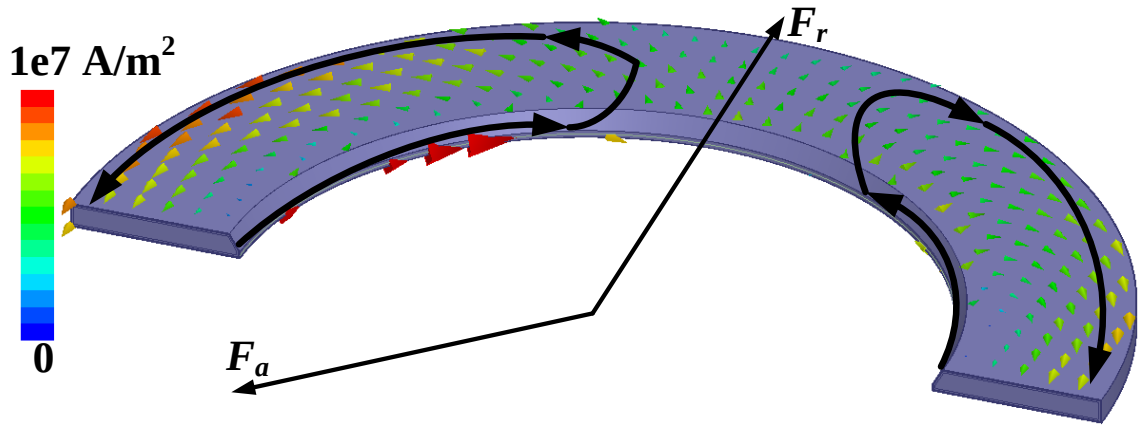

(b)

Figure 6.4 The distribution of the (a) flux density vector; (b) eddy current density vector on the surface of the press plate at one time instant in the 0.95 leading pf condition.

Analyses on the field and eddy current can be performed at each location in the press plate. A general principle is that the position of the peak radial/axial component of **B** generated by $\boldsymbol{F_r}$ or $\boldsymbol{F_a}$ respectively is close to the *radial-axial* plane aligned to $\boldsymbol{F_r}$ or $\boldsymbol{F_a}$,

while the peak tangential component of **B** is approximately located on the *radial-axial* plane orthogonal to $\boldsymbol{F_r}$ or $\boldsymbol{F_a}$. The composite **B** is the combination of the magnetic field vectors produced by $\boldsymbol{F_r}$ and $\boldsymbol{F_a}$. The impact of $\boldsymbol{F_a}$ is more significant and the composite **B** is closer to the vector generated by $\boldsymbol{F_a}$. The resultant **J** lies in the normal direction and leads **B** by approximately 45° in phase.

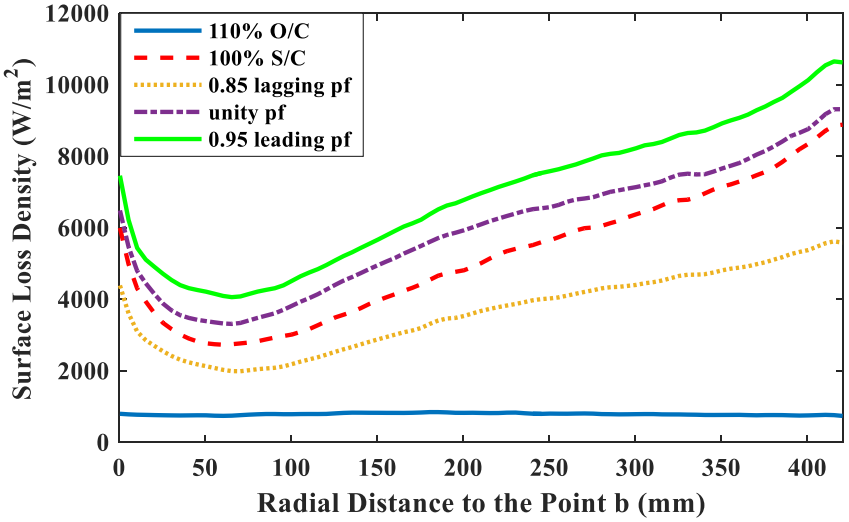

(a)

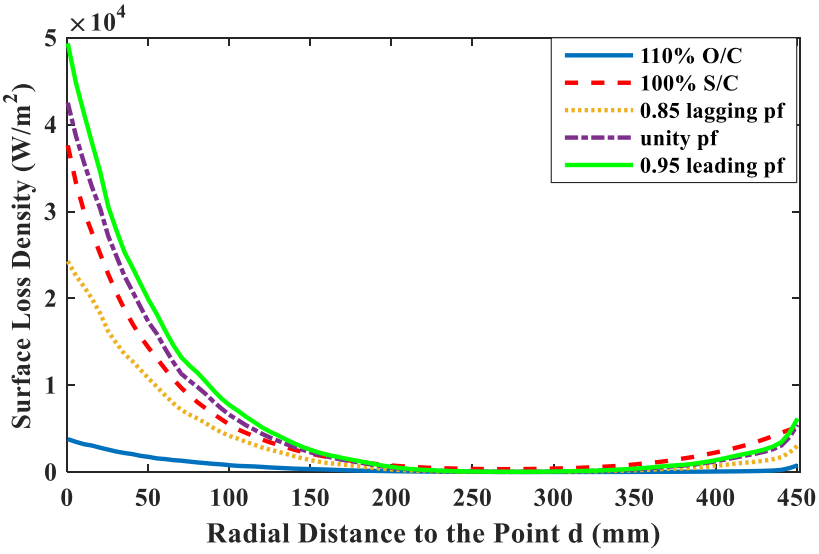

(b)

Figure 6.5 Radial distribution of surface eddy current loss density under five different operating conditions along the surface (a) ***bc***; (b) ***de*** in Figure 6.1.

Define the time-average surface loss density in W/m^2 to be

$$\bar{p}_A = \int_0^{h_0} \bar{p}_{loss} dh \tag{6.1}$$

where h is the vertical depth of a position in the skin layer from its corresponding point on the surface, and h_0 is a predefined depth that is sufficient for the eddy current density to attenuate to a negligible value. The $\bar{p}_A$ at point ***a*** in Figure 6.1 is 3.08e3 W/m^2, 4.30e4 W/m^2, 2.71e4 W/m^2, 4.59e4 W/m^2 and 5.38e4 W/m^2 for the five operating conditions of 110% O/C, 100% S/C, 0.85 lagging pf, unity pf and 0.95 leading pf condition respectively. The radial distributions of $\bar{p}_A$ on the surfaces ***bc*** and ***de*** are presented in Figure 6.5. The surface loss density of the surfaces ***bc*** and ***de*** is lower than that at the point ***a*** located on the radially inner surface. The total loss of the press plate of each operating condition appears in Table 6.1. The highest eddy current loss occurs in the power factor leading condition.

Table 6.1 – Total loss in the press plate.

Condition	**110% O/C**	**100% S/C**	**0.85 lagging**	**unity pf**	**0.95 leading**
Loss (kW)	4.2	47.9	32.3	53.5	59.4

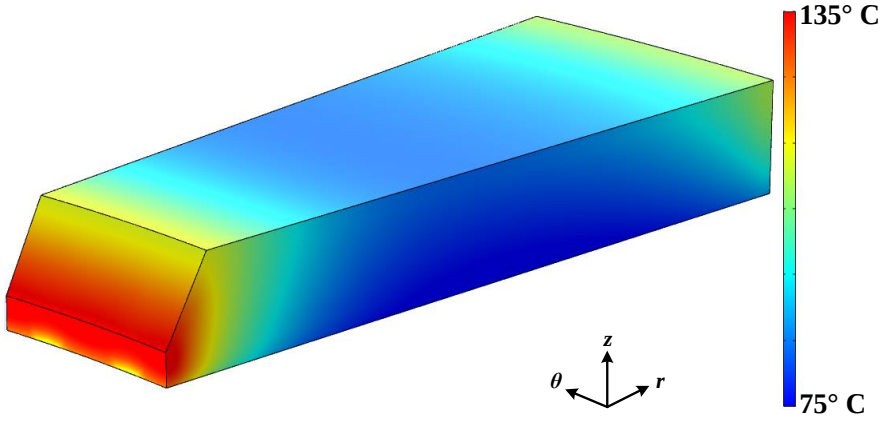

Figure 6.6 Temperature distribution in the press plate at 100% S/C condition.

Figure 6.6 demonstrates the temperature distribution in the press plate at 100% S/C condition. The highest temperature 138.3°C occurs at the radially inner surface and is also the hottest spot in the end region. The temperature declines in the radial direction with a slight rise near the outer diameter of the press plate.

6.1.2 Magnetic Field and Loss Distributions in the Finger Plates

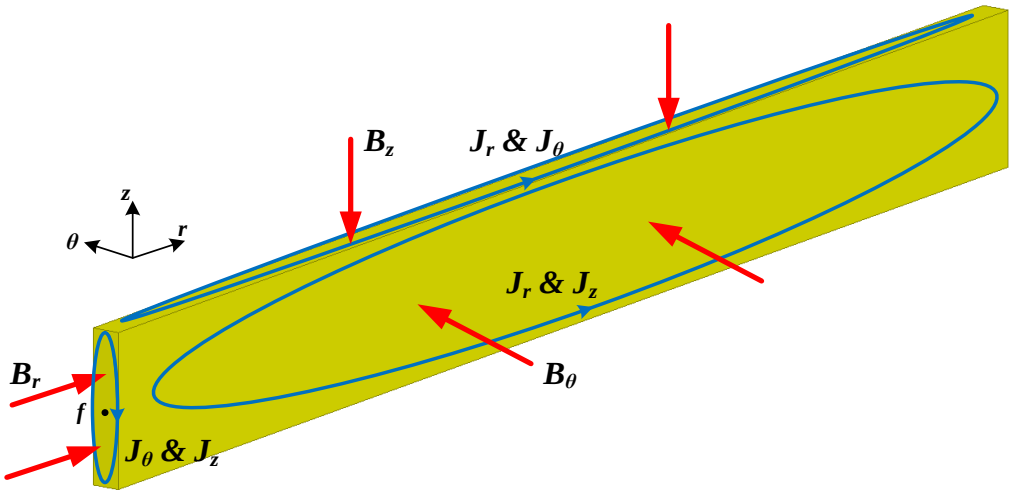

Figure 6.7 Magnetic field and the resultant eddy currents in a finger plate.

Eddy currents are also the primary source of losses in the finger plates. The finger plates are made of nonmagnetic steel with a lower permeability and conductivity thus the skin effect is not pronounced. Figure 6.7 shows the end leakage flux and eddy currents in a finger plate. The eddy current has the longest flowing path in *radial-axial* planes, thus the tangential flux is much more effective to produce eddy currents than the radial and axial components of flux.

Figure 6.8 shows the distributions of B and $\bar{p}_{loss}$ in the finger plates at the 110% O/C condition, in which their highest values appear at the radial tips and gradually decline along the radial direction. Similarly, the distributions of B and $\bar{p}_{loss}$ rotate at synchronous speed. The phase shift between the flux and eddy current densities in the finger plates is

about 90°. In O/C cases, B_r and B_z dominate the magnetic field and the B_θ is negligible, and Figure 6.9 shows the peripheral distribution of **B** components across the finger plates at point ***f*** in Figure 6.7. The peak value of B_r, B_z and B_θ is 0.187 T, 0.136 T and 0.022 T respectively. The phasors of B_r and B_z at point ***f*** are in opposite directions, and the phase angle between the B_r/B_z and B_θ is 90°. The higher-order harmonics of B_r/B_z are due to the field winding distribution, while fringing effects lead to the zigzag shape of the B_θ curve.

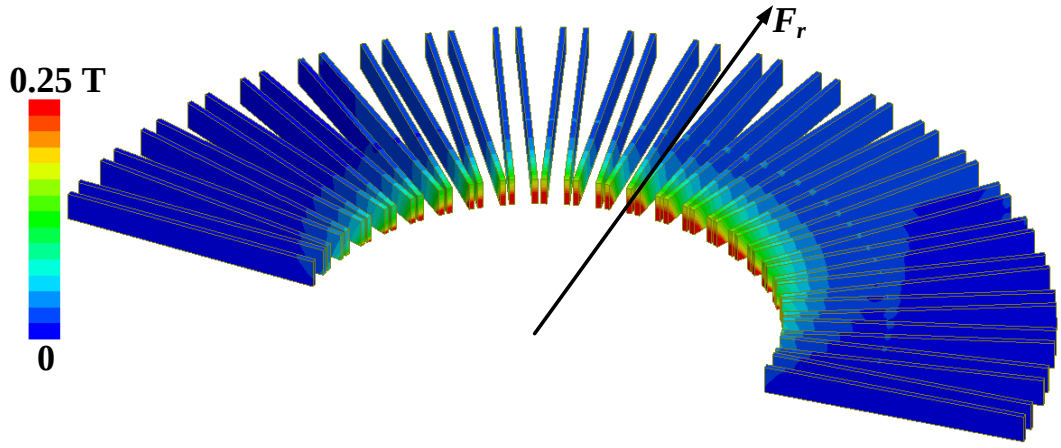

(a)

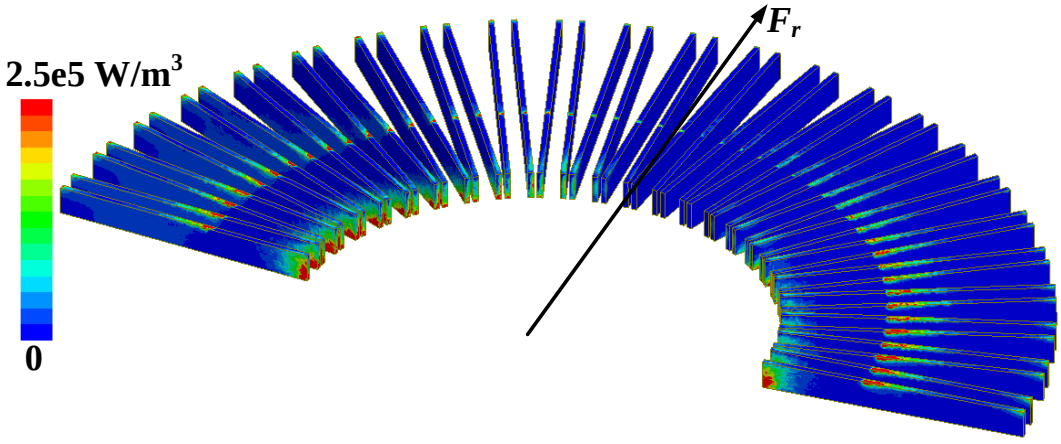

(b)

Figure 6.8 Distribution of (a) flux density; (b) eddy current loss density in the finger plates at one time instant in the 110% O/C condition.

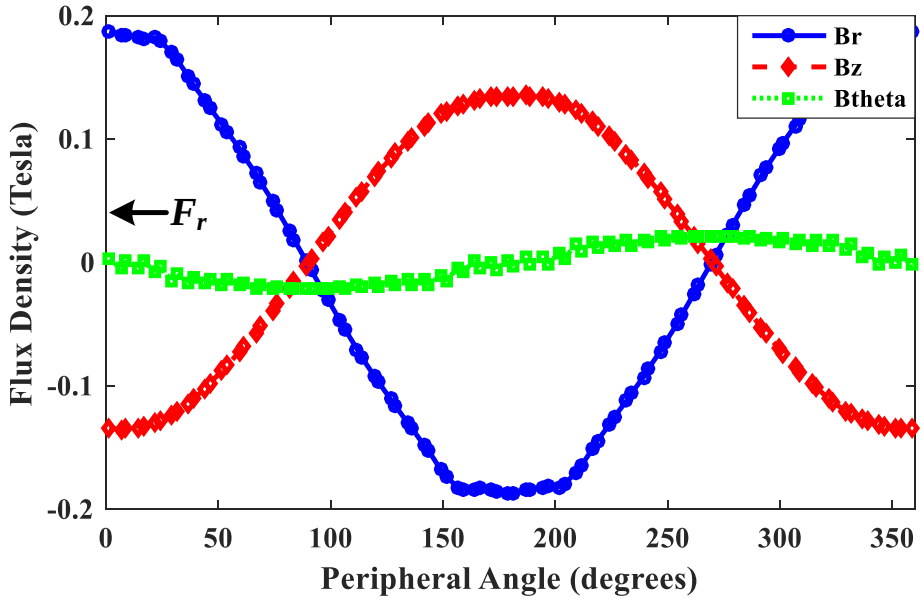

Figure 6.9 The peripheral distribution of the radial, axial and tangential flux density at the point ***f*** in Figure 6.7 under the 110% O/C condition.

The flux and loss distributions in the finger plates possess similar characteristics in the other four operating conditions. The flux and loss density distributions in the finger plates at the 0.95 leading pf condition appear in Figure 6.10. Contrary to the O/C case, in the other operating conditions, the major source of eddy currents is B_θ primarily excited by the adjacent stator windings. Therefore, the highest B_θ appears where the adjacent stator windings carry the largest current. The position of the peak B_θ is about 90° away from $\boldsymbol{F_a}$. As a result, the eddy current is about 90° apart from B_θ in phase, and its phasor is parallel to $\boldsymbol{F_a}$, as shown in Figure 6.10(b). The peripheral distributions of B_r, B_θ and B_z at the point ***f*** are shown in Figure 6.11. The peak value of B_r, B_θ and B_z is 0.158 T, 0.183 T and 0.182 T respectively. The higher-order harmonics of flux density are mainly caused by the fringing flux excited by the local stator end windings, and the distribution or short-pitch of armature/field windings.

The $\bar{p}_{loss}$ distributions on a *radial-axial* cross-section plane in the 110% O/C and 0.95 leading pf conditions are presented in Figure 6.12. In both cases the eddy current loss

is concentrated in the region near the radial tips. The total losses of the finger plates in different operating conditions are shown in Table 6.2. The total losses in the last four conditions are similar because the B_θ excited by the stator windings are the same. The total loss is much lower in the 110% O/C condition due to the absence of the stator current and the resultant tangential flux.

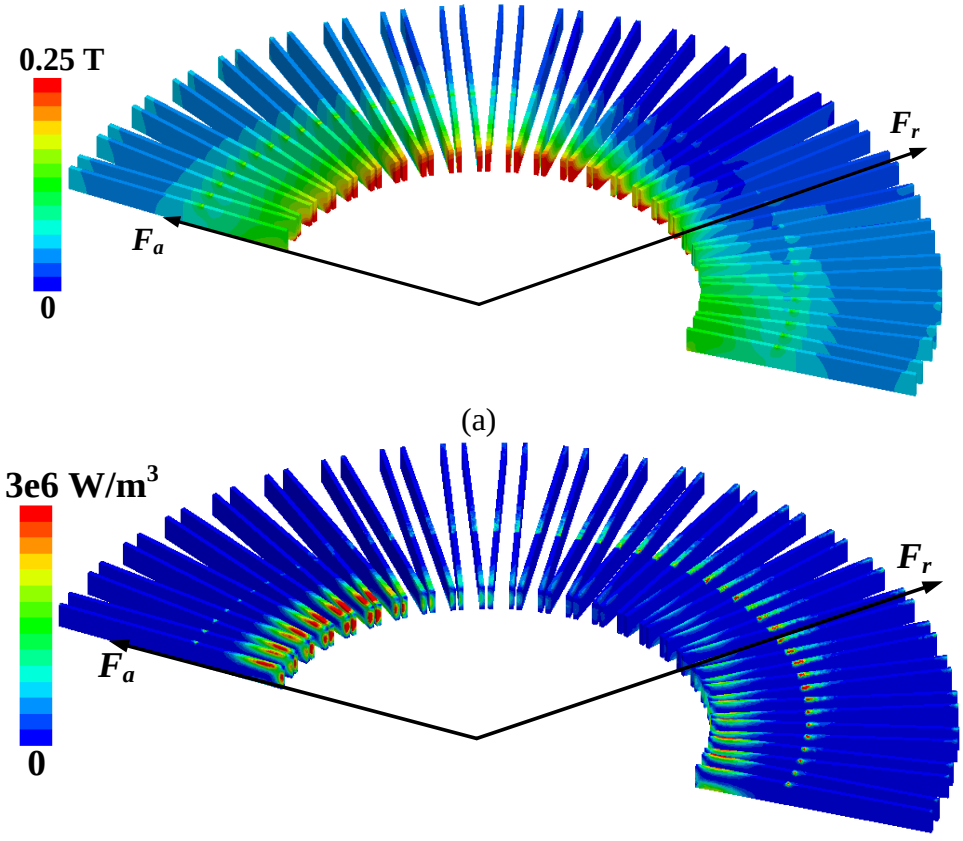

Figure 6.10 Distribution of (a) flux density; (b) eddy current loss density in the finger plates at one time instant in the 0.95 leading pf condition.

Table 6.2 – Total loss in the finger plates.

Condition	**110% O/C**	**100% S/C**	**0.85 lagging**	**unity pf**	**0.95 leading**
Loss (kW)	0.95	7.8	7.8	7.9	8.0

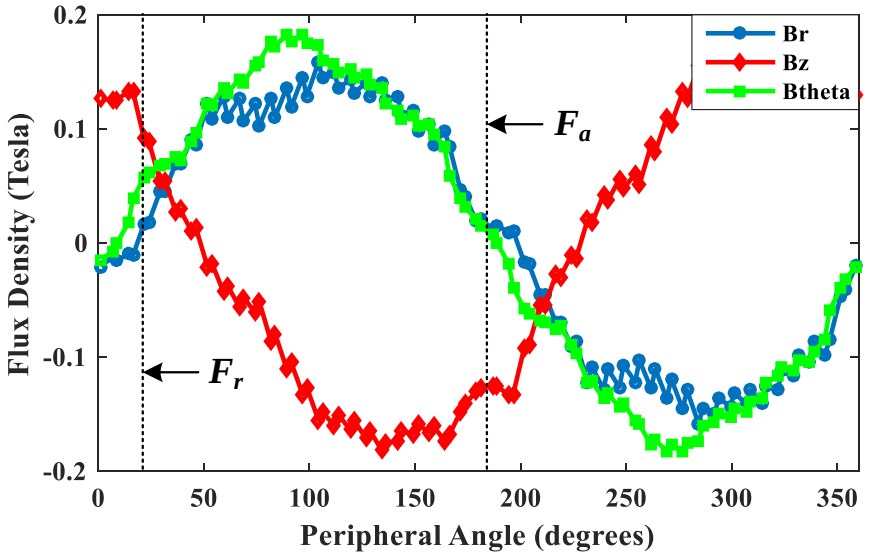

Figure 6.11 The peripheral distribution of the radial, axial and tangential flux density at the point ***f*** in Figure 6.7 under the 0.95 leading pf condition.

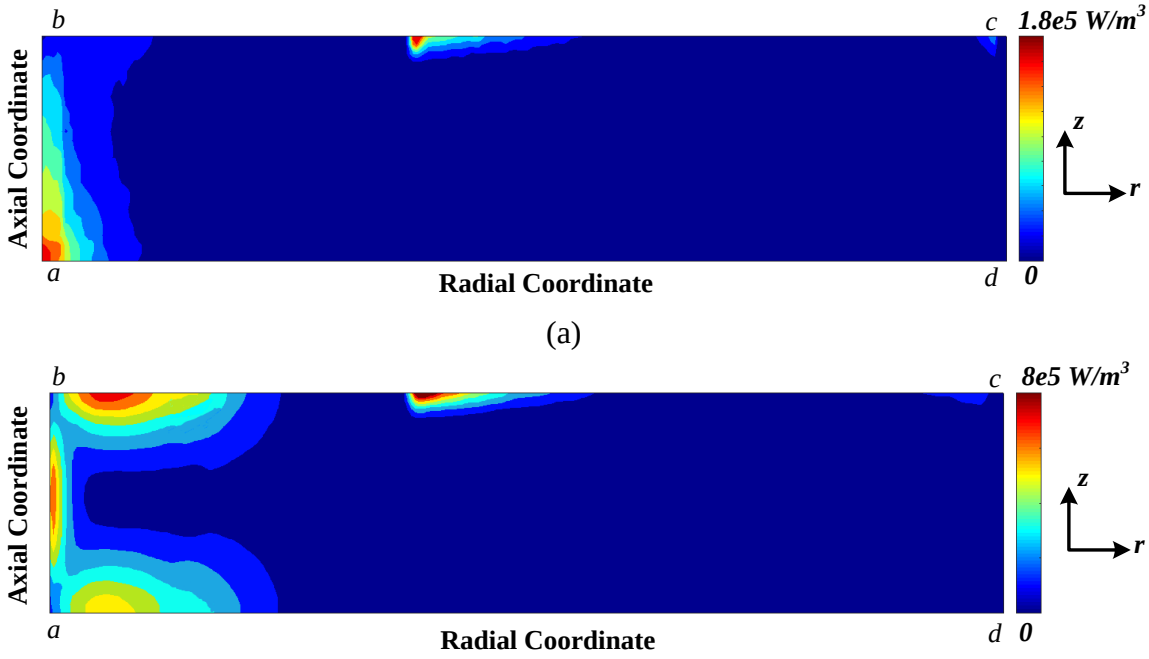

Figure 6.12 Time-average loss density in the finger plates on a *radial-axial* plane in the (a) 110% O/C condition; (b) 0.95 leading pf condition.

6.1.3 Magnetic Field and Loss Distributions in the End Stator Packets

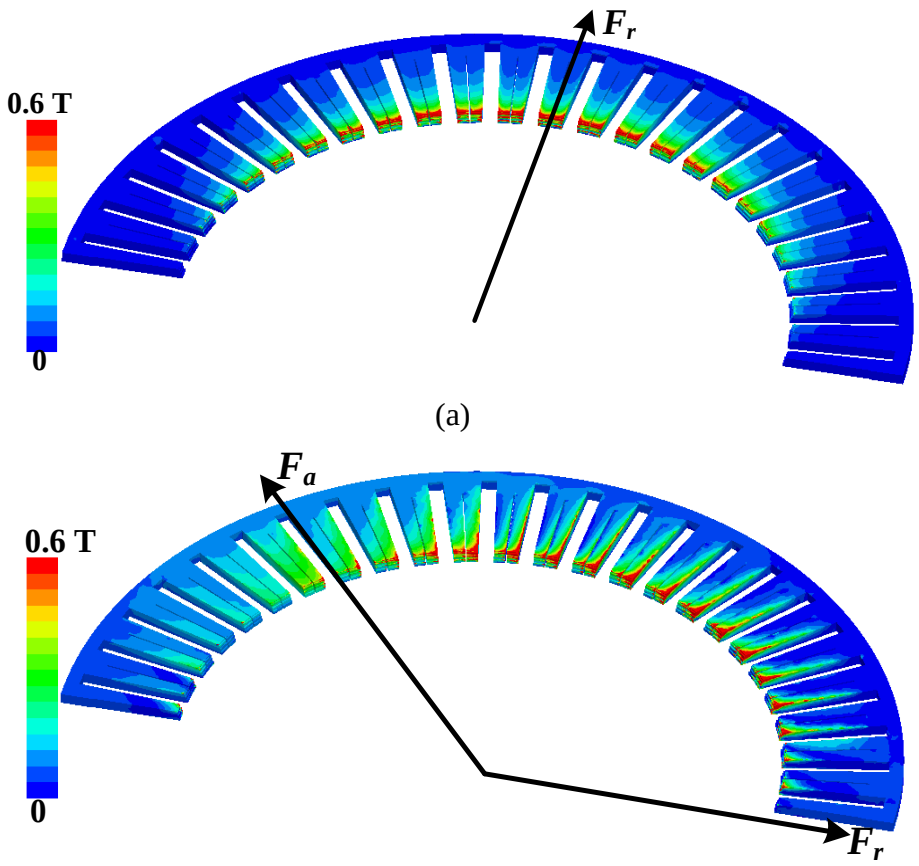

Figure 6.13 Distribution of axial flux density in the teeth of the 1st packet at one time instant at (a) 110% O/C condition; (b) 0.95 leading pf condition.

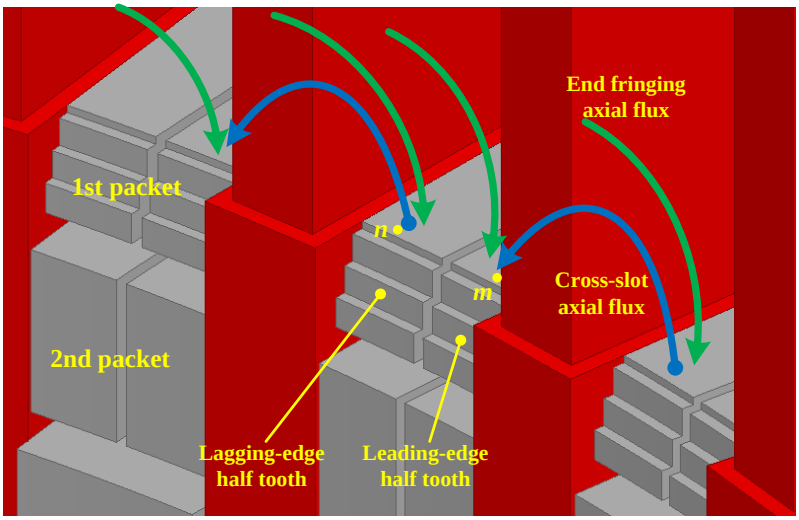

Figure 6.14 End fringing and cross-slot axial fluxes impinging the 1st packet.

The loops of the eddy currents induced by the tangential or radial main fluxes are constrained within the thin laminations, and therefore the resultant heat is mild and can be dissipated to the surrounding coolant without a significant temperature rise. However, the in-plane eddy currents induced by the axial flux are a main heat source in the stator end and may lead to partial overheating in stator end teeth. Generally, the 1st packet has the largest B_z because it absorbs the end leakage flux. Figure 6.13 shows the distributions of B_z in the teeth region of the 1st packet. The B_z decays from the tooth tip to the tooth bottom due to the increasing length of the axial flux path from the stator/rotor end windings to the end packets. Moreover, at 110% O/C condition, B_z exhibits symmetric distribution between the two halves of a tooth, while it is asymmetrically distributed in the 0.95 leading pf operation. This phenomenon is caused by the superposition of the end fringing and cross-slot axial fluxes as illustrated in Figure 6.14. The end fringing flux travels from the stator/rotor winding end turns to the end stator packets and its magnitude is approximately uniform across the stator tooth surface in the peripheral direction. Regarding the cross-slot axial flux, in the slot region the stator currents generate a difference in magnetic scalar potential between the two adjacent stator teeth and excite a peripherally traveling flux across the slot. The magnitude of the cross-slot axial flux density varies essentially linearly from zero at the slot bottom to its peak value at the slot opening. In Figure 6.14, the cross-slot flux reinforces the end fringing axial flux on one side of the tooth (leading-edge, i.e., the "downstream" side in the direction of rotor rotation) while it counteracts the end fringing axial flux on the other side (lagging-edge).

Figure 6.15 shows the B_z at the points ***m*** and ***n*** in Figure 6.14. At O/C condition, the axial fluxes impinging the points ***m*** and ***n*** are the same. In the S/C test condition, at the end-tooth tips, the end-fringing axial flux is weak since its components produced by the field and armature end windings cancel each other. Due to the cross-slot flux, the magnitude of B_z at the point ***n*** is slightly lower than that at the point ***m*** with a considerable

phase shift approaching 180°. In the 0.95 leading pf case, the B_z at the point ***n*** is significantly lower in magnitude with a small phase lag compared to that at the point ***m***. These conclusions about the B_z at the points ***m*** and ***n*** apply to any two axisymmetric points in the leading- and lagging-edge halves of tooth. The B_z in the end-core teeth at the lagging pf or unity pf conditions follows the same principles as that at the leading pf condition.

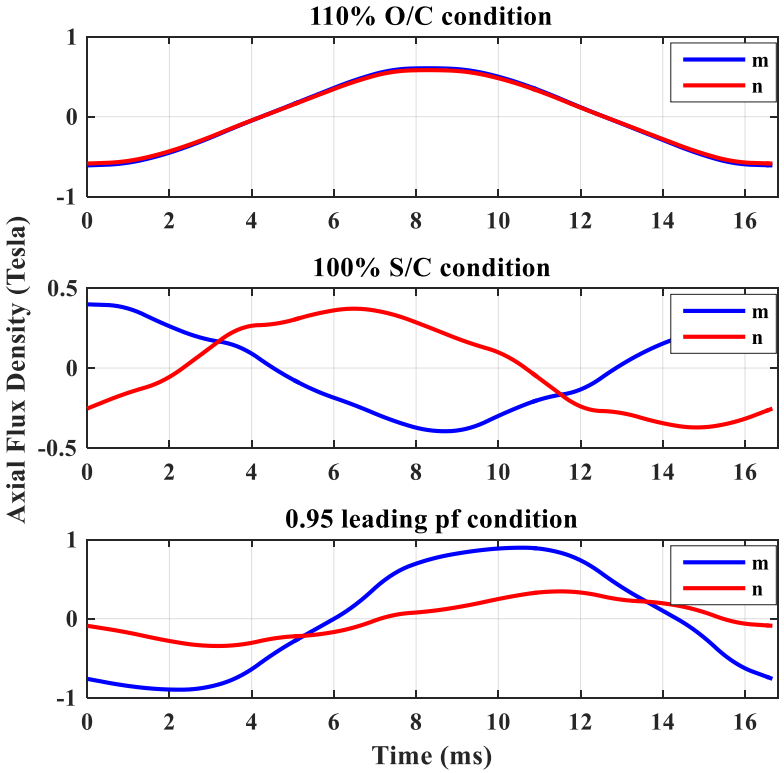

Figure 6.15 Time-varying axial flux density at the point ***m*** and ***n*** in Figure 6.14 under the 110% O/C, 100% S/C and 0.95 leading pf conditions.

Figure 6.16 presents the distribution of peak B_z along the radial line located in the center of the leading-edge half of the 1st packet's teeth. The highest value of B_z appears at 0.95 leading pf condition. The B_z declines as the power factor angle φ increases from the leading region to the lagging region in Figure 5.2.

Figure 6.17 shows the radial distribution of peak B_z impinging the leading-edge half tooth of each packet in the 0.95 leading pf condition. Generally, the B_z decreases from the

1st packet to the packets further into the stator main body, but the B_z is larger at the tooth tip of the 5th packet than at that of the 4th packet since the path of the fringing axial flux caused by the rotor mmf is shorter at the 5th packet. Figure 6.18 shows the axial flux density distribution in a plane located at the peripheral center of the leading-edge half end teeth. The axial flux is much stronger in the 1st and 2nd packet. Due to the smaller μ_z compared to μ_r and μ_θ and the presence of radial ducts between packets, the reluctance of the axial flux paths is significantly larger than in the radial direction, so when the end leakage flux axially penetrates an end packet, it then diverts to the radial direction and strengthens the main flux in this packet. The amount of the axial flux that travels across a radial duct and impinges the next end packet is limited. Because of this reason, it is shown in Figure 6.19 that the magnitude of B_θ and the resultant core loss in the back-iron increase axially from the 5th packet to the 1st packet. Another interesting phenomenon revealed by Figure 6.19 is that there are phase shifts between the values of B_θ in the yokes of different end packets. The 1st packet has the largest phase lag due to the reduced impact of rotor mmf on the main flux in the stator caused by the increased length of the air gap.

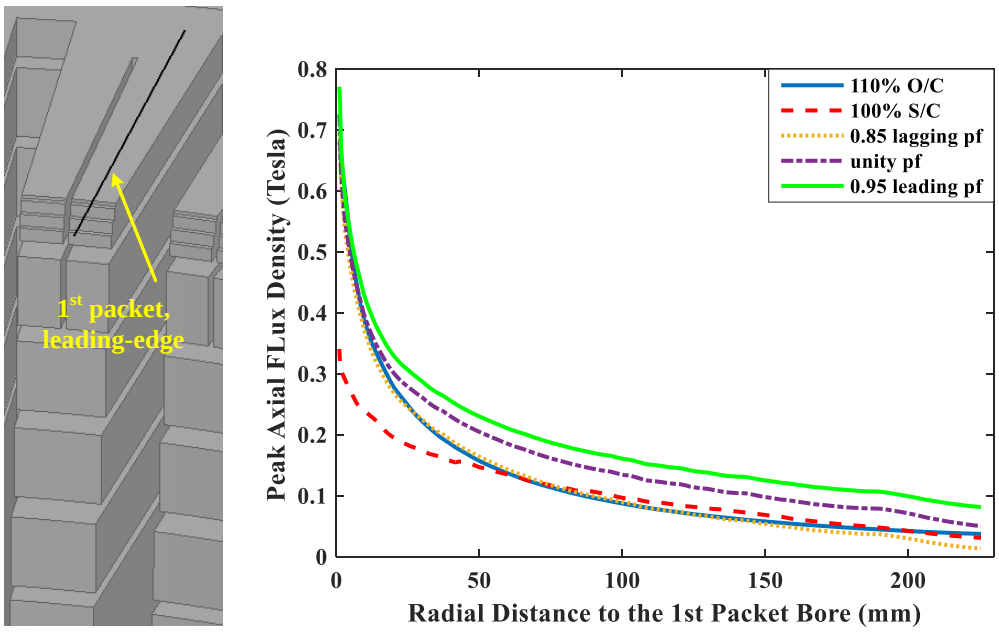

Figure 6.16 Peak axial flux density in the leading-edge half of the teeth in the 1st packet under different operating conditions.

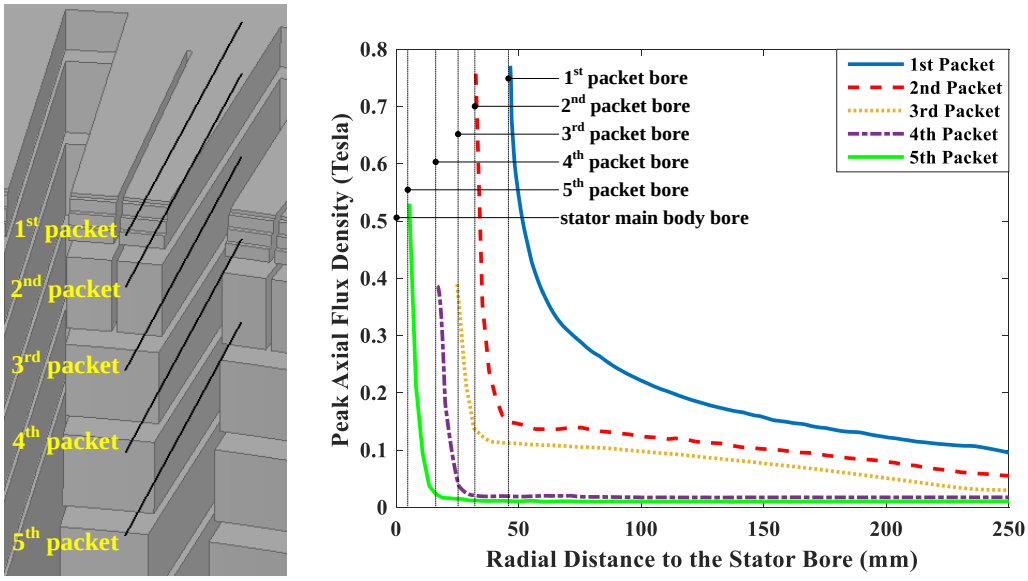

Figure 6.17 Peak axial flux density in the leading-edge half of the teeth in the 1st ~ 5th packets under the 0.95 leading pf condition.

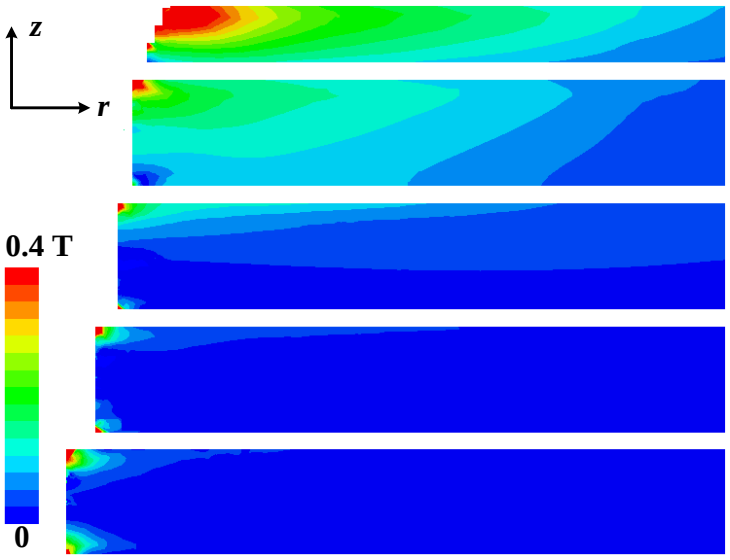

Figure 6.18 Distribution of axial flux density in the *radial-axial* cross section plane of the leading-edge half end teeth in the 0.95 leading pf condition.

The distribution of $\bar{p}_{c,\perp}$ in a lamination of the 1st packet is illustrated in Figure 6.20. The highest $\bar{p}_{c,\perp}$ appears at the tooth tips. The in-plane eddy current losses are symmetrically distributed in the two halves of the teeth in the O/C and S/C test conditions, while in the loading conditions the eddy current loss exhibits a significant asymmetric

distribution whose magnitude in the leading-edge half teeth is much higher. The loss distribution at the unity pf condition resembles that in the 0.95 leading pf condition with a slightly lower magnitude.

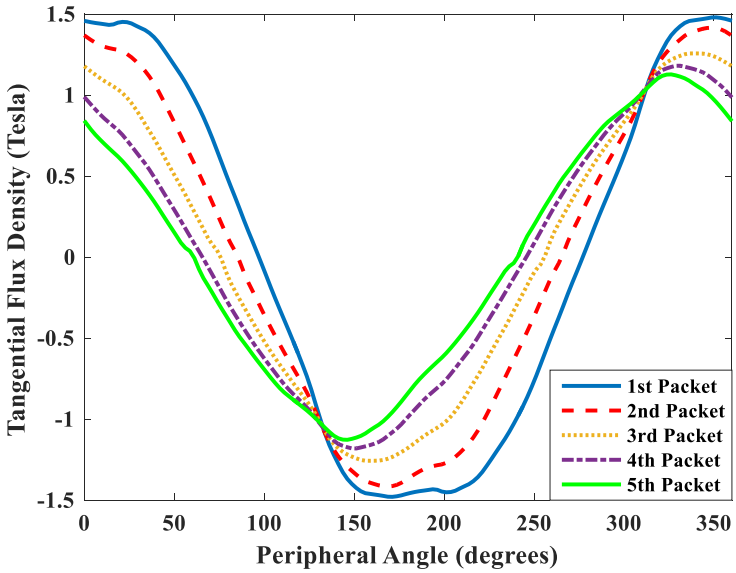

Figure 6.19 Peripheral distribution of tangential flux density along a circle 300 mm from the stator yoke inner diameter in the 0.95 leading pf condition.

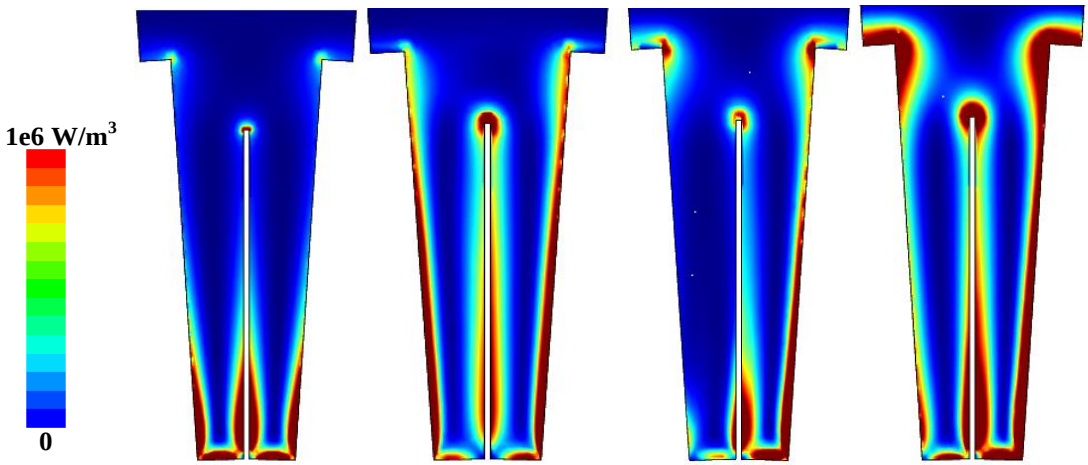

Figure 6.20 Time-average eddy current loss density caused by the axial flux in a lamination of the 1st packet at the (a) 110% O/C condition; (b) 100% S/C condition; (c) 0.85 lagging pf condition; (d) 0.95 leading pf condition.

Figure 6.21 shows the core losses in the three outermost packets. For each case, as the B_z declines axially from the core end into the stator main body, the eddy current loss also decreases from the 1st packet to the 3rd packet. In the loading conditions, both the conventional core loss and the additional eddy loss increase as the power factor changes from lagging to leading. The conventional core loss is very low in the S/C condition, but significant eddy current losses exist in the 1st and 2nd packet. The additional eddy current losses in the 4th and 5th packet and the main body packets reduce to small values in all cases. However, it has a comparative amount in outermost packets and is concentrated in the teeth and slot bottom, thus it has a huge impact on the temperatures in this region.

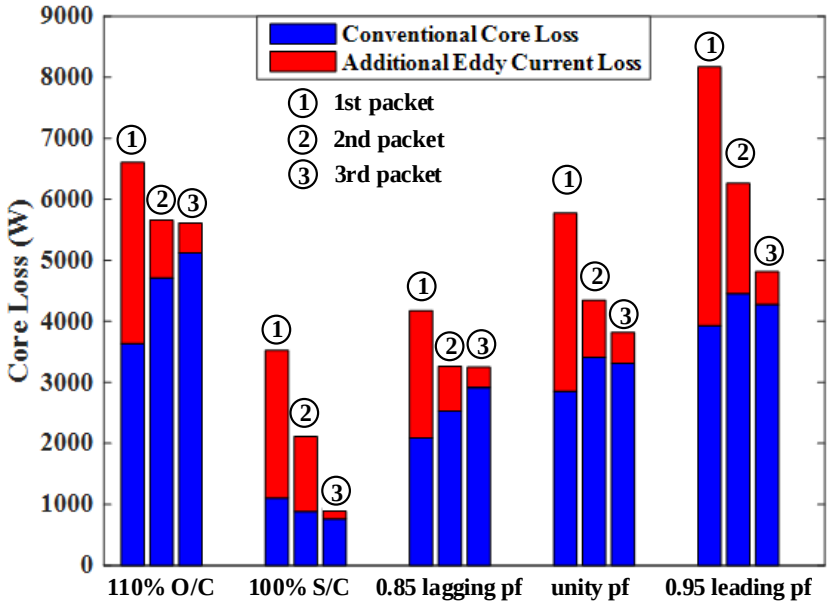

Figure 6.21 Core loss in the end packets under different operating conditions.

6.1.4 Magnetic Field and Loss Distributions in the End Stator Windings

The stepped shape with increased radii of the stator end packets exposes the stator coils to the intensive radial airgap flux and leads to the temperature rise of windings due to the resultant eddy currents. In the end region, the profile of the proximity loss induced by the slot leakage flux varies axially due to the variation of the slot configuration. This section

analyzes the characteristics of the magnetic field and loss distributions in the end stator windings in different operating conditions.

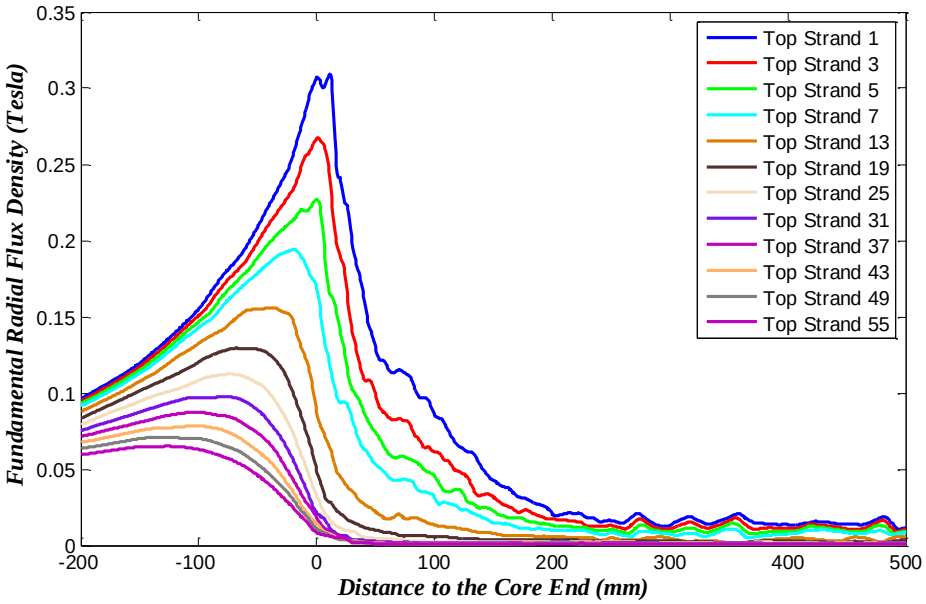

Figure 6.22 Distribution of the magnitude of the fundamental radial flux density in the copper strands of the end top stator winding at 110% O/C condition.

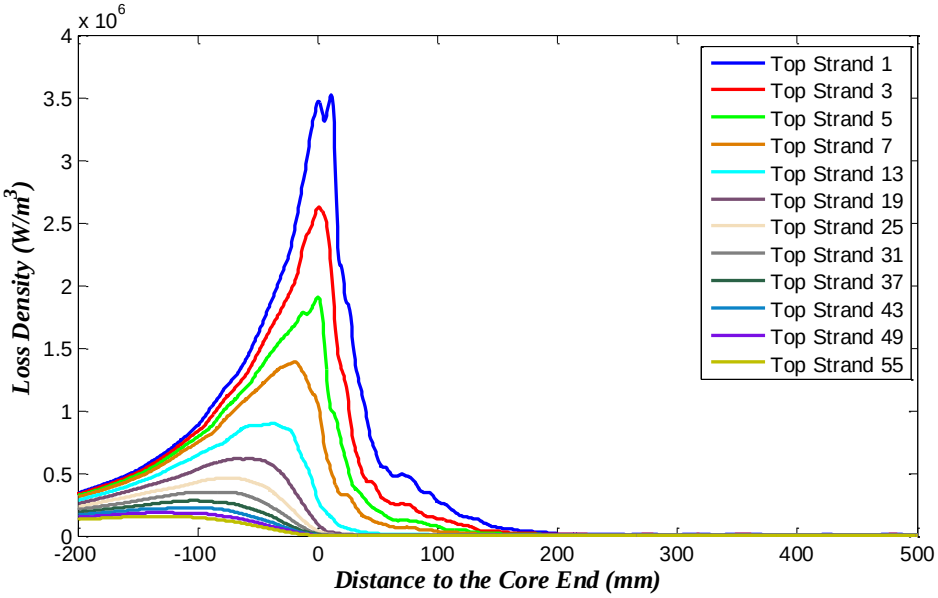

Figure 6.23 Distribution of loss density in the copper strands of the end top stator winding at 110% O/C condition.

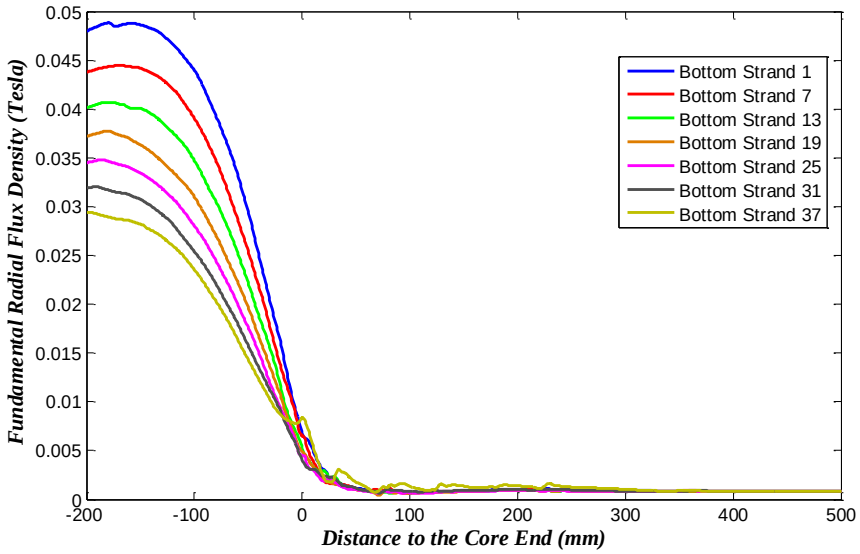

Figure 6.24 Distribution of the magnitude of the fundamental radial flux density in the copper strands of the end bottom stator winding at 110% O/C condition.

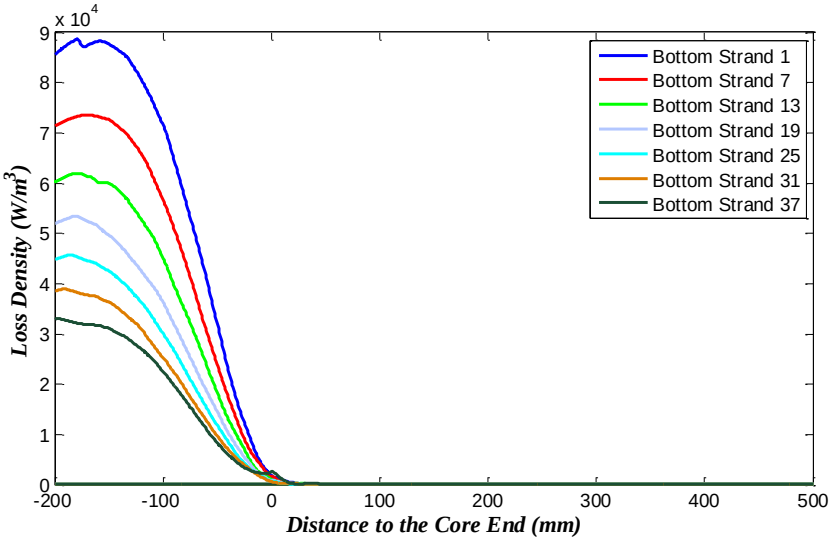

Figure 6.25 Distribution of loss density in the copper strands of the end bottom stator winding at 110% O/C condition.

In the open circuit test condition, the eddy current in the armature copper strands is mainly induced by the radial flux density coming from the air gap. The distributions of radial flux density and the corresponding loss density in the top and bottom layer windings are demonstrated in Figure 6.22 ~ Figure 6.25. In these figures, the strand 1 is the one

nearest to the air gap. In the region near the core-end, the radial flux density increases because the inner radius of the stator core increases and the top copper strands shunt more radial flux in that region. The copper strand nearest to the air gap has the highest radial flux and loss density, and the magnitude of radial flux density and loss density descend from the strand nearest to the air gap to the strand nearest to the yoke. The bottom bar has very low eddy current loss density. The loss density in the copper strands has the same distribution for different slots at 110% O/C condition.

At 100% S/C condition, since the field mmf and armature mmf counter each other, the magnetic field in the air gap is fairly weak, thus the radial flux density is very low in the copper strands. The eddy current is mainly induced by the peripheral flux excited by the local stator current. The distributions of peripheral flux density and the resultant proximity loss density are different between slots, depending on whether the top winding and the bottom winding belong to the same phase. The following results are based on the assumption that the top and the bottom windings in the slot are of the same phase.

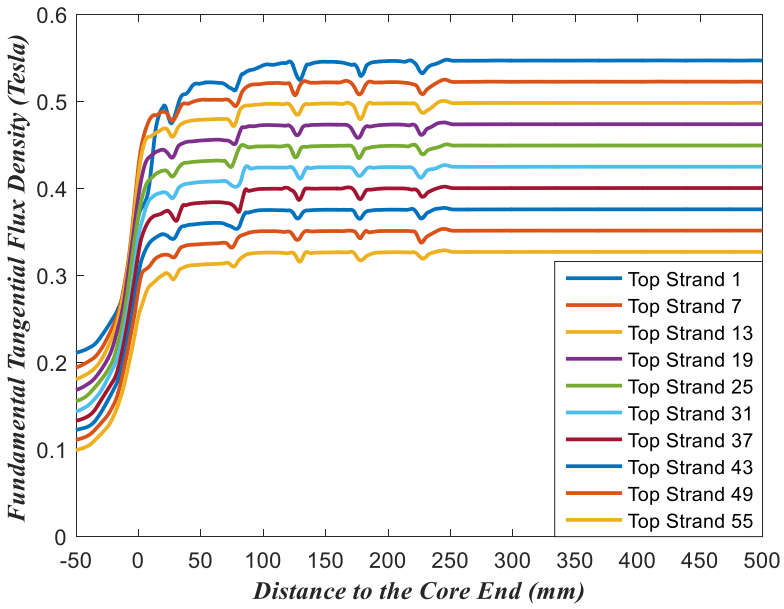

Figure 6.26 Distribution of the magnitude of the fundamental peripheral flux density in the copper strands of the end top stator winding at 100% S/C condition.

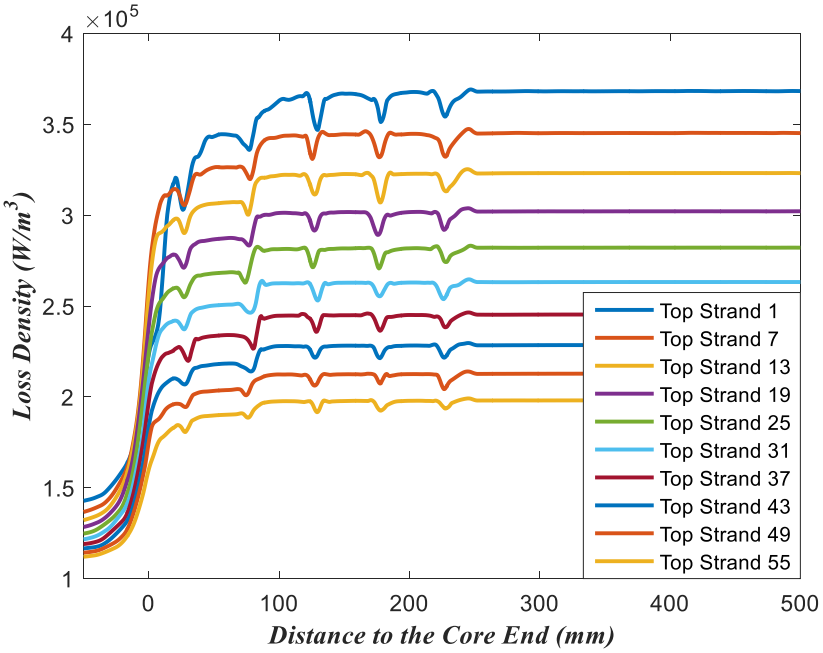

Figure 6.27 Distribution of loss density in the copper strands of the end top stator winding at 100% S/C condition.

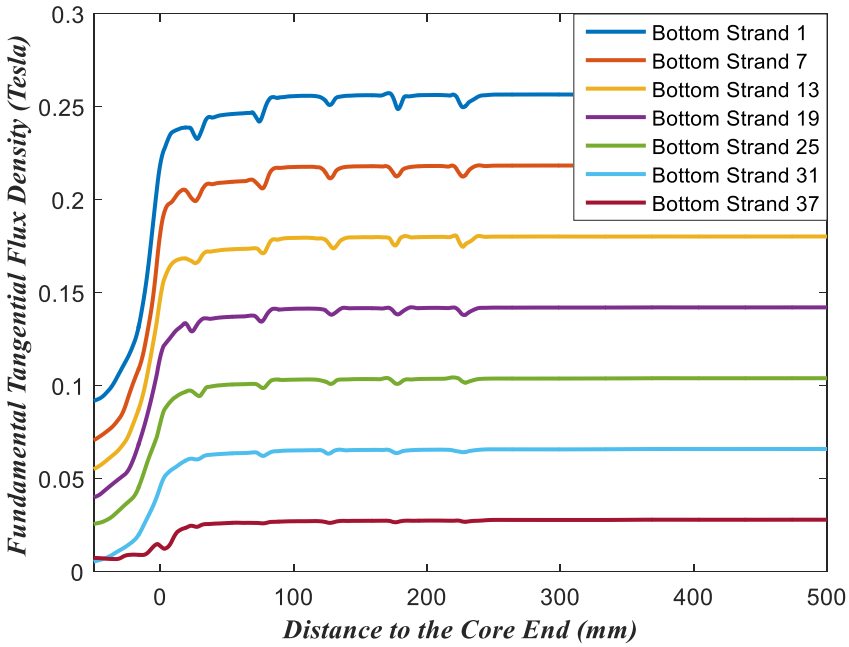

Figure 6.28 Distribution of the magnitude of the fundamental peripheral flux density in the copper strands of the end bottom stator winding at 100% S/C condition.

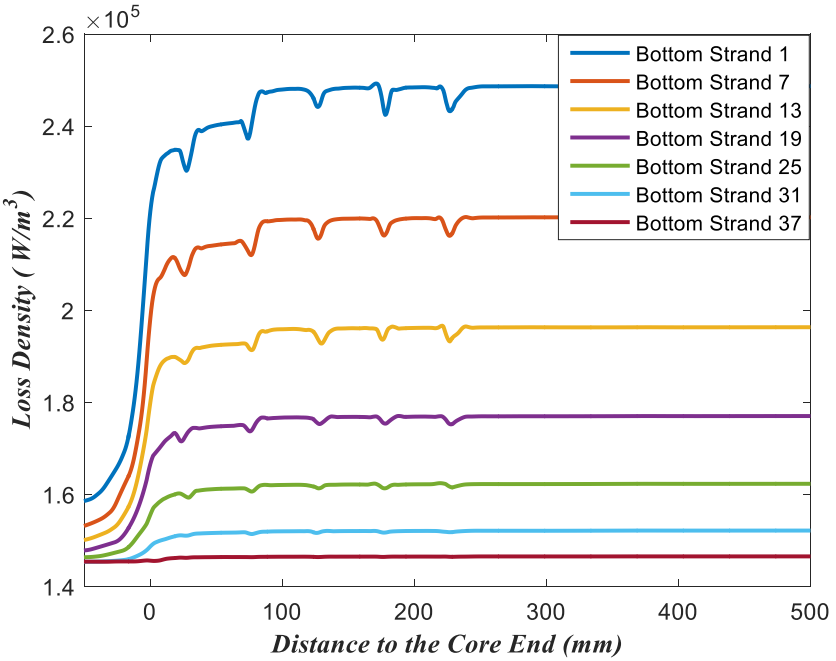

Figure 6.29 Distribution of loss density in the copper strands of the end bottom stator winding at 100% S/C condition.

Figure 6.26 ~ Figure 6.29 illustrate the distribution of peripheral flux density and loss density in the top and bottom windings. In the top winding or in the bottom winding, the peripheral flux density linearly increases from the strand nearest to the yoke to the strand nearest to the air gap. The average value of loss density is higher in the top winding, but the bottom winding also generates remarkable eddy current losses.

In rated apparent power conditions, both radial and peripheral fluxes can induce significant eddy currents in the stator copper strands. Figure 6.30 ~ Figure 6.34 show the radial/peripheral flux density and the loss density distribution in the top/bottom strands in the rated operating condition with a lagging power factor. The radial flux density is slightly lower than that in the 110% O/C case because the field mmf is countered by the armature mmf at rated MVA condition and the magnetic field in the air gap is weaker than that at 110% O/C condition. The peripheral flux density and proximity loss distributions, however, are close to the 100% S/C scenario because the peripheral leakage flux in the stator slots is mainly produced by the local stator currents and both conditions possess the

same armature currents. There is a significant rise of loss density in the top winding in the region near the core end, which is similar to the 110% O/C case.

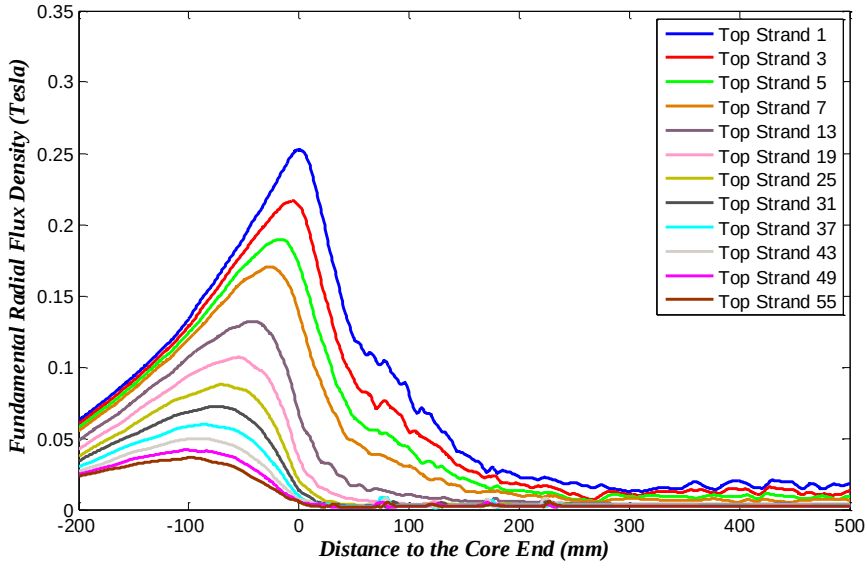

Figure 6.30 Distribution of the magnitude of the fundamental radial flux density in the copper strands of the end top winding at the rated condition.

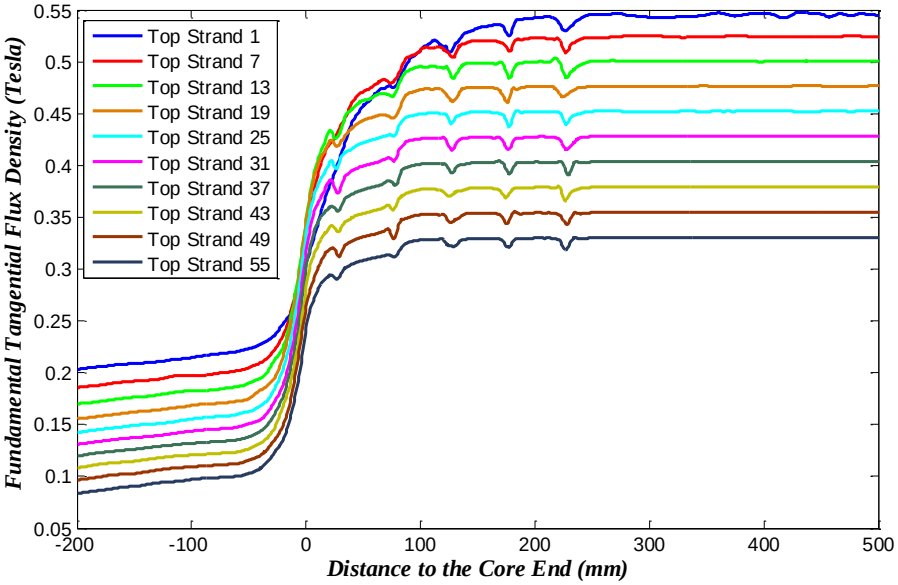

Figure 6.31 Distribution of the magnitude of the fundamental peripheral flux density in the copper strands of the end top winding at the rated condition.

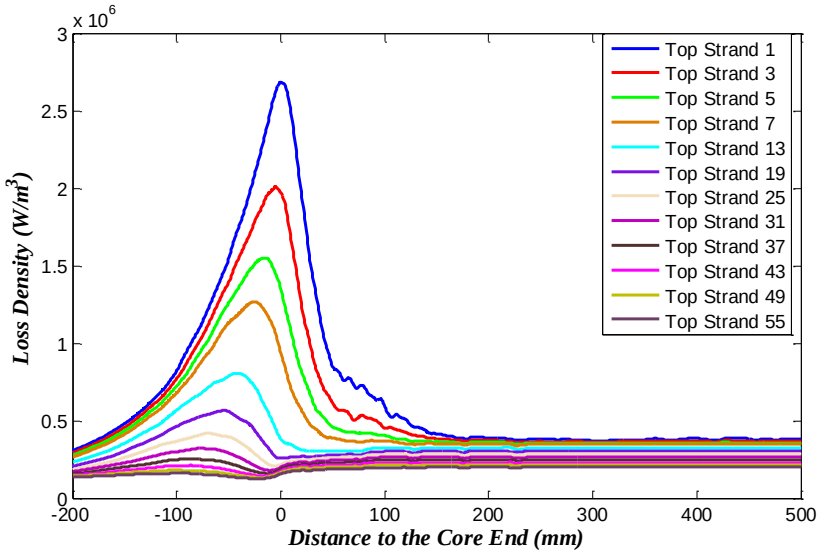

Figure 6.32 Distribution of loss density in the copper strands of the end top winding at the rated condition.

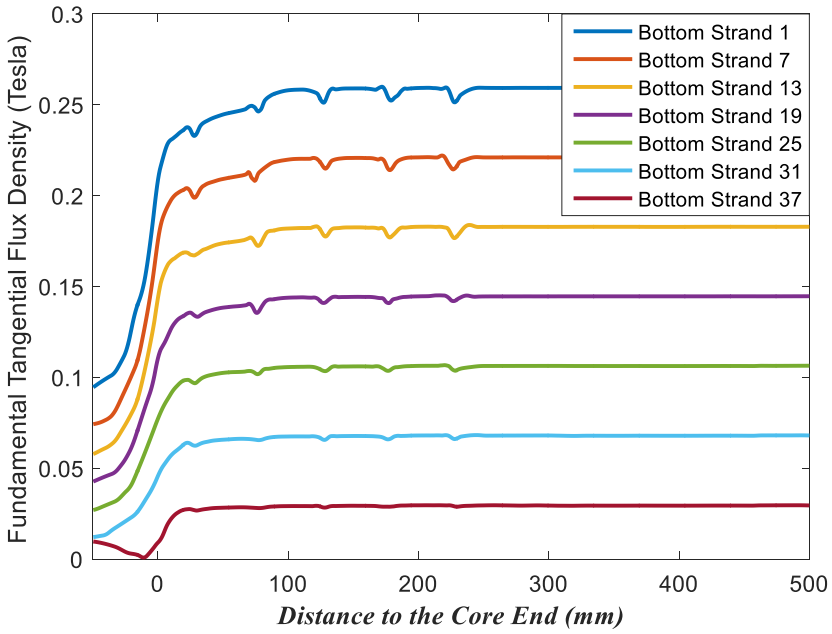

Figure 6.33 Distribution of the magnitude of the fundamental peripheral flux density in the copper strands of the end bottom winding at the rated condition.

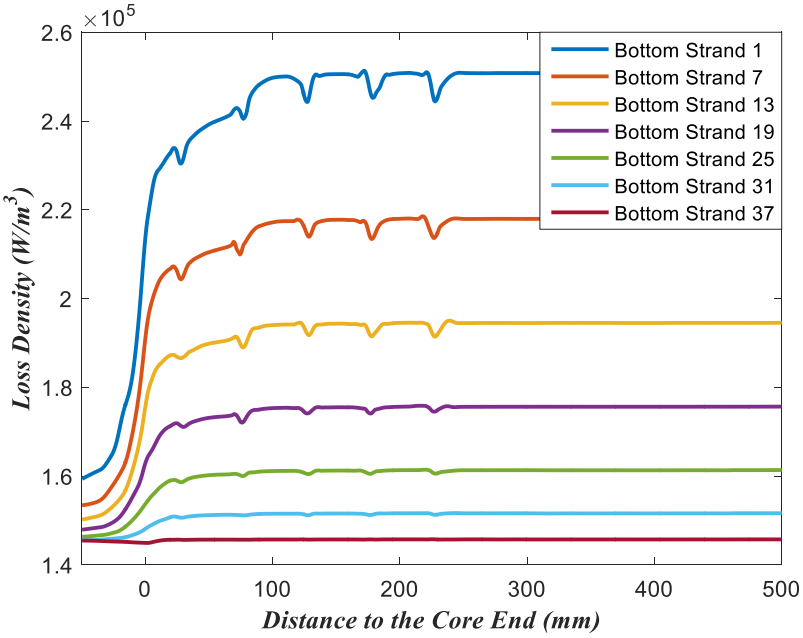

Figure 6.34 Distribution of loss density in the copper strands of the end bottom winding at the rated condition.

Critical conclusions based on the analysis in Section 6.1 include:

1) The loss in the press plate is lowest at 110% O/C condition. In the loading conditions, the press plate loss increases as the power factor changes from lagging to leading. The loss at 100% S/C is between the 0.85 lagging pf and unity pf conditions.
2) The eddy current loss in the finger plates is mainly determined by the tangential flux. The total loss of finger plates is smallest at 110% O/C condition. The loss distributions in the other four operating conditions are similar since the tangential flux excited by the adjacent stator windings are the same.
3) The eddy current loss induced by axial flux has a major impact on the temperatures of end packets. The axial flux is the combination of the end fringing flux and cross-slot flux, and its distribution in loading conditions exhibits asymmetric patterns.

4) In loading conditions, the loss in the end packets is larger when the power factor is leading. The additional eddy current loss decays axially from core-end to stator main body.
5) In the O/C condition, the radial airgap flux is the major source of eddy current in stator strands, while the peripheral leakage flux due to the proximity effects is the primary source of eddy current in the S/C condition. Both the radial and peripheral slot leakage fluxes can lead to eddy current losses in the loading conditions.

6.2 Effects of the Properties of End Metallic Components

The design of the end metallic components, such as the press plate and its metallic shield, also has an impact on the magnetic field and loss distributions in the end region of large generators. The press plate is a major end component of large generators that fastens the stator end-core packets and diverts the intensive leakage flux from impinging the stator core back-iron. In some scenarios, a metallic shield is installed beyond the press plate to bypass the end leakage flux and reduce the eddy currents in the press plate and stator. This section performs a comparative study based on the 3D numerical model to compare the magnetic field and losses in the end region of large generators with different designs of these metal components. All the results in this section are based on the rated condition with a rated apparent power and a 0.85 lagging power factor.

The original design in Figure 5.5 is called case A in this section where the press plate is made of magnetic steel. In cases B and C, the geometries of the press plate remain identical but its material is defined to be aluminum and copper respectively. The bulk conductivity defined in the model is 5.8e7 Siemens/m for aluminum and 3.8e7 Siemens/m for copper. Figure 6.35 shows the eddy current loss distribution in the press plate in cases A, B and C at rated operating condition. The eddy current loss is concentrated in the region near the inner diameter of the aluminum and copper press plate, while significant amount

of loss distributes in the region near the outer diameter (OD) of the magnetic steel press plate.

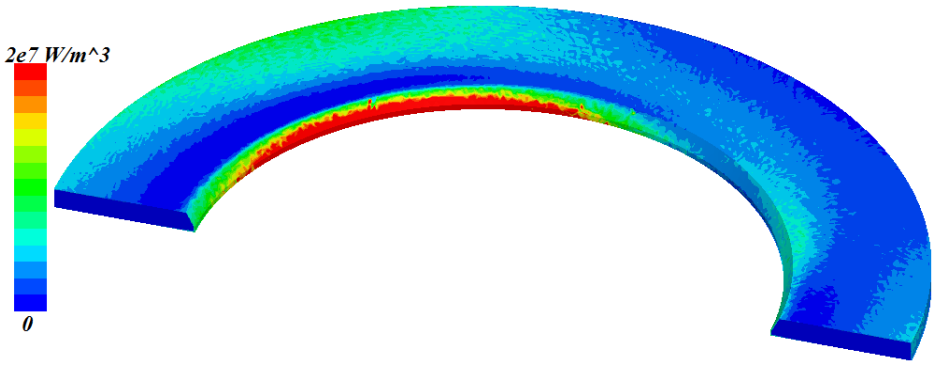

(a)

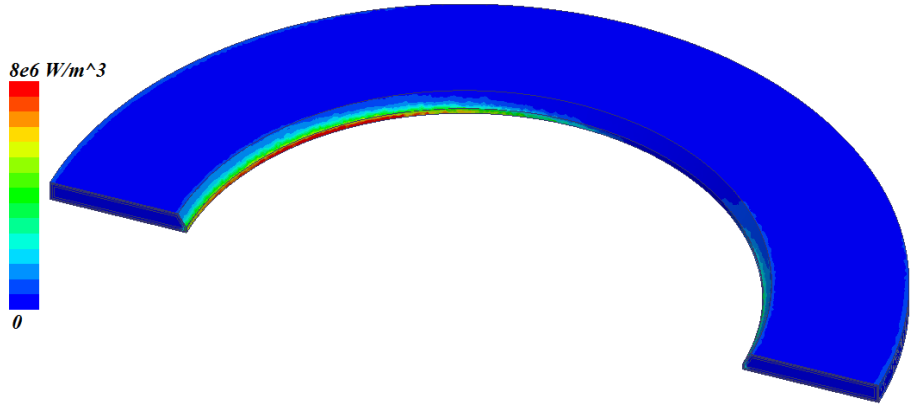

(b)

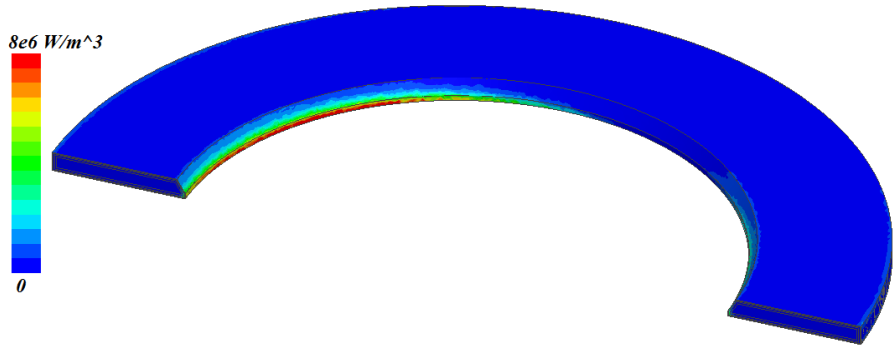

(c)

Figure 6.35 Loss density distribution at one time instant under the rated condition in the press plate made of (a) magnetic steel; (b) aluminum; (c) copper.

The total losses of the press plate in cases A, B and C are 34.1 kW, 10.5 kW and 8.5 kW respectively, while the highest time-average loss density at the inner surface is

1.54e7 W/m^3, 3.02e6 W/m^3 and 3.38e6 W/m^3 for the cases A~C respectively. The copper press plate has a lower total loss and a higher peak loss density compared to the aluminum press plate. The press plate made of magnetic materials results in significantly larger losses (case A). This phenomenon can be interpreted by the mechanism of the skin effect. For a conductor, the skin depth, the surface eddy current density and the eddy current loss per square meter can be expressed [25] as

$$\delta = \sqrt{\frac{1}{\pi f \mu \sigma}},\ J_0 = H_0 \cdot \sqrt{2\pi f \mu \sigma},\ P_{scl} = \frac{1}{2}\sqrt{\frac{\pi f \mu}{\sigma}} H_0^{\ 2} \tag{6.2}$$

where J_0 and H_0 are the surface current density and magnetic field intensity respectively. The surface eddy current density is proportional to the square root of the conductor permeability and conductivity, assuming the same impinging flux density primarily determined by stator/rotor mmfs. It can be concluded from (6.2) that generally the eddy current loss is larger in a press plate with a higher permeability and a lower conductivity.

In the teeth of the stator end core packets, the axial flux normal to the laminations is the dominant cause of the eddy currents. It is introduced in Section 6.1 that the axial flux and loss densities decay from the tooth tip to the bottom in each packet and decrease from the outermost lamination packet to the inner packets due to the increasing length of the axial flux path. In addition, the axial flux density in the leading-edge half tooth is higher because of the cross-slot flux generated by the armature windings. In Figure 6.36(a) associated with case A, intensive eddy current primarily induced by the axial flux and the radial component of end leakage flux appears in a thin layer under the surface of the 1st packet yoke. The densities of eddy current and radial flux rapidly attenuate as they penetrate deep into the 1st packet due to the skin effect as shown in Figure 6.36(b). However, significant eddy current induced by the axial flux still exists in the middle of the packet.

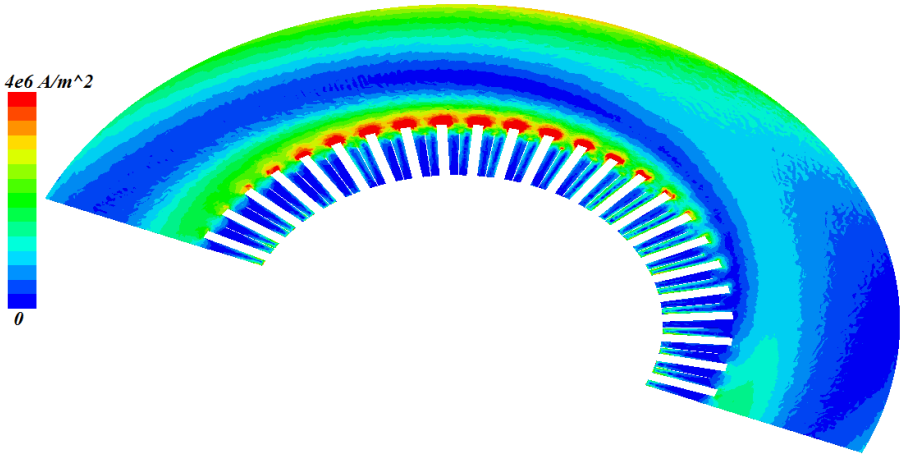

(a)

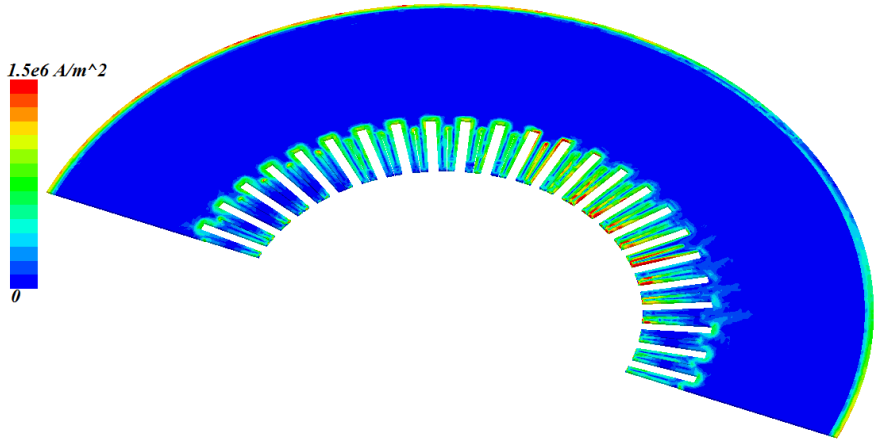

(b)

Figure 6.36 Eddy current density distribution at one time instant at rated condition of design A in the (a) surface layer elements of the 1st packet; (b) middle of the 1st packet.

Figure 6.37 shows the eddy current distribution in the surface elements of the 1st core end packet in case B. The eddy current in the stator core in case C has almost the identical distribution. It can be concluded from Figure 6.37 that the density of the surface eddy current in the back-iron of the 1st packet is much lower in cases B and C than that in case A. Figure 6.38 demonstrates the distribution of the time-average loss density in the 1st packet surface elements for all the cases analyzed in this section. The peak value of the time-average loss density at the stator yoke inner diameter (ID), or the bottom of the slot, is 8.6e6 W/m^3, 5.3e6 W/m^3 and 5.2e6 W/m^3. In case A, the stator yoke generates more loss in the surface layer since the permeability of magnetic steel is high and the reluctance of

the flux path around the stator yoke and the press plate ID is low, which strengthens the magnetic field in this region and leads to a more pronounced skin effect.

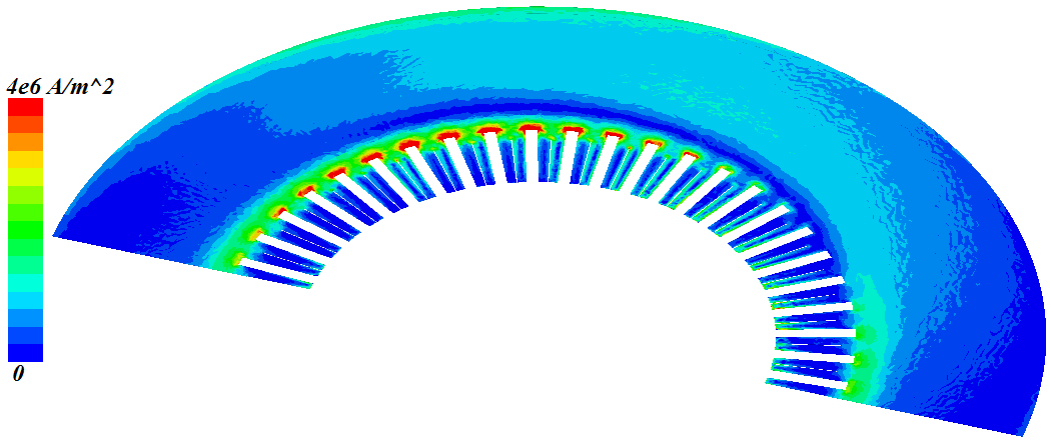

Figure 6.37 Eddy current density distribution at one time instant in the surface elements of the 1st packet with the press plate made of aluminum (case B).

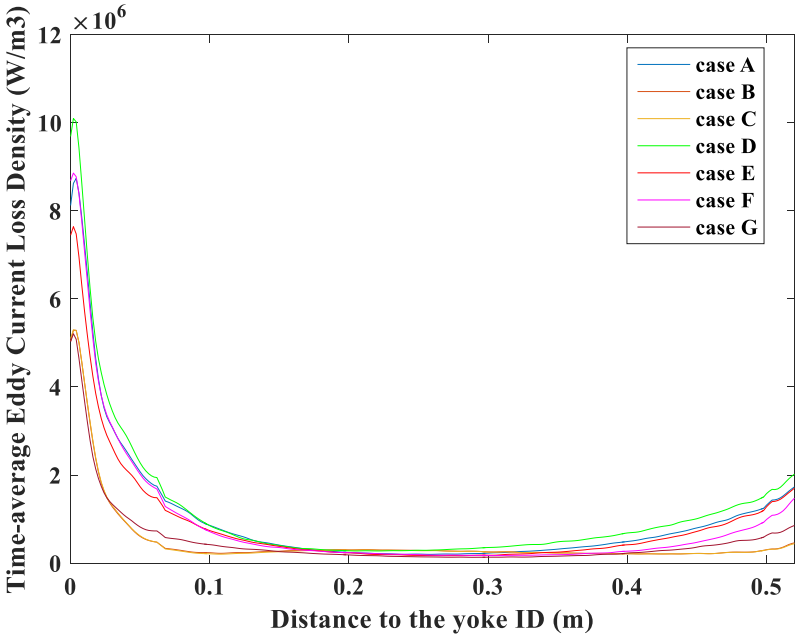

Figure 6.38 Radial distribution of the time-average eddy current loss density in the surface-layer elements of 1st packet yoke in the cases A~G.

The press plate (magnetic steel) ID increases by 70 mm in case D and decreases by 35 mm in case E. The total loss of the press plate in cases D and E is 18.8 kW and 46.8 kW respectively. The magnetic permeance between the end armature/field windings and the

inner edge of the press plate becomes smaller as its ID increases due to a larger distance to the windings, which greatly reduces the peak value of the eddy current density in this critical region, and vice versa. However, Figure 6.38 indicates that at the 1st end core packet yoke ID, the time-average loss density is 10.1e6 W/m^3 and 7.5e6 W/m^3 respectively in cases D and E. The press plate with a smaller ID can shield the stator core back-iron more effectively from the end leakage field thus resulting in a lower loss density in the stator. The patterns of loss distributions in cases D and E resemble that of case A presented in Figure 6.35(a).

In case F, the distance between the press plate and the 1st stator end core packet is shortened by 50 mm. The total loss density of the press plate is 27.1 kW in case F. The press plate loss is reduced due to two reasons: the distance between the press plate and the inclination part of the stator end windings is larger, which results in a longer flux path and a smaller magnetic permeance between the end windings and the press plate; the stator core back-iron shunts more flux at the press plate ID. It can be observed in Figure 6.38 that in case F, the peak loss density at the 1st packet yoke ID is 8.7e6 W/m^3, which is slightly higher than that in case A, but the loss density is lower in the region close to the stator OD.

In case G, an 8-mm-thick aluminum shield is mounted 15 mm away from the top and inner surfaces of the press plate. The total loss of the aluminum shield and the magnetic steel press plate is 20.7 kW and 5.41 kW respectively in case G. In Figure 6.39, significant eddy current is induced at the inner surface of the shield, but it can effectively keep the end leakage flux from penetrating the press plate, thus reducing its total loss to only 15.9% of the original value in case A. Since the shield does not have direct contact with the stator or finger plates, the thermal stress can be significantly relieved for the insulation material between the stator laminations. It can be inferred from Figure 6.38 that the loss distribution in the surface elements of the 1st core packet is similar to that in cases B and C.

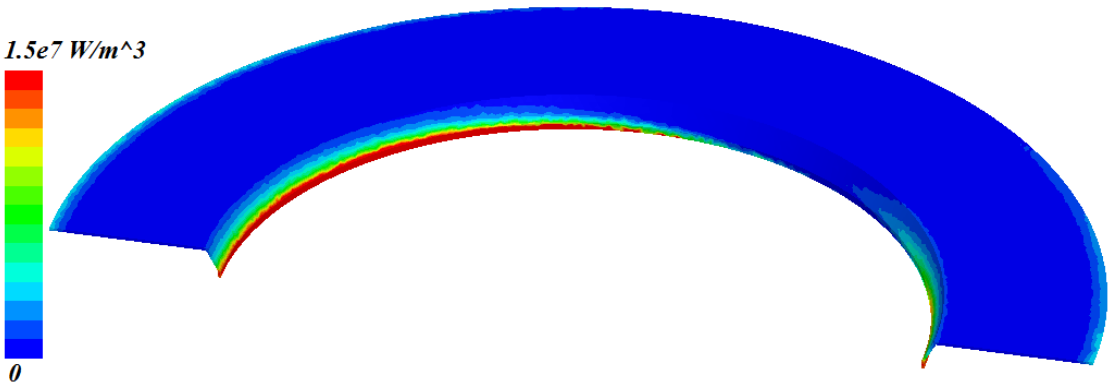

Figure 6.39 Eddy current loss density distribution at one time instant in the aluminum shield under the rated condition.

Table 6.3 – Total loss in the finger plates with different end metallic structures.

Case	A	B	C	D	E	F	G
Loss (kW)	7.82	7.87	8.06	7.79	8.41	0.46	7.84

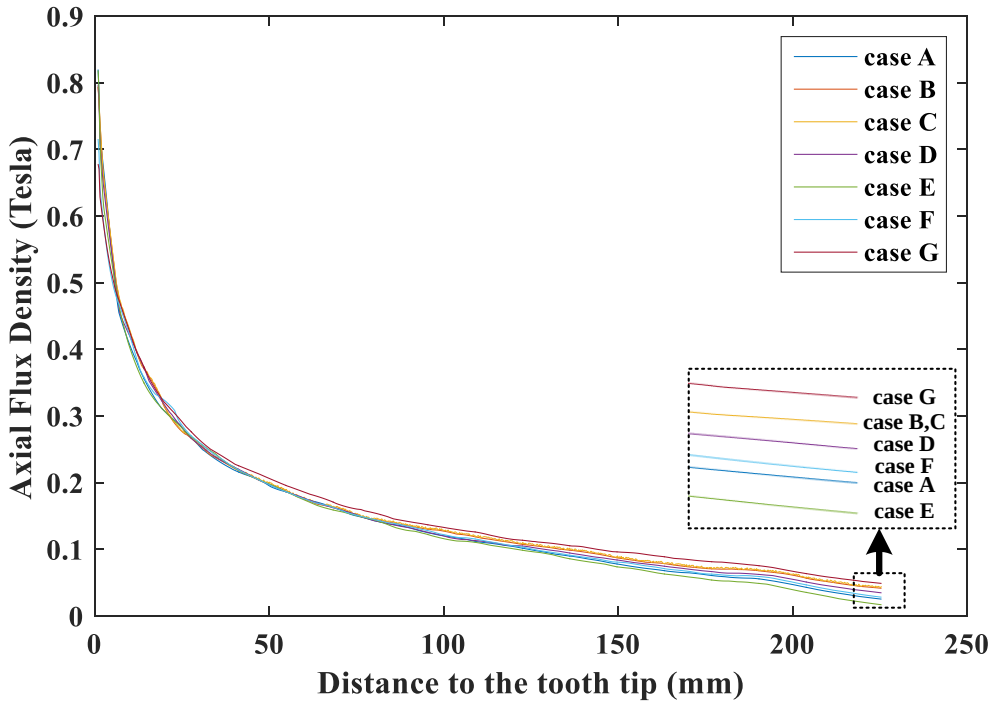

Figure 6.40 Peak axial flux density in the leading-edge half tooth of the 1st packet in the cases A~G under the rated condition.

The total loss of the finger plates is shown in Table 6.3. There is no direct relationship between the press plate material or dimension and the flux and loss distribution in finger plates except for case F, because the impact of the press structure on the tangential flux density at the finger plates ID is negligible. In case F, the height of the finger plates is lower and the length of eddy current loops in *radial-axial* planes is shorter, and the resultant loss of finger plates is merely 5.9% of that in case A.

Figure 6.40 shows the peak axial flux density in the leading-edge half tooth of the 1st packet for all cases. Although there are slight discrepancies of the axial flux density at the tooth bottom between the cases, the influence of different press plate properties on the eddy current loss distribution in the tooth portion is negligible according to the results of the simulations.

6.3 Effects of the End Stator and Winding Structures

In this section, a parametric study is carried out to evaluate the effectiveness of various designs of end stator profile and end winding structures in reducing the losses in the end components of large generators, including the stepped profile of the end core packets, the assignment of the end tooth slits, the angle of the inclined armature end windings, and the relative axial lengths of the stator and rotor. This section compares simulated results of various design concepts based on the rated condition, where the generator produces rated apparent power with a 0.85 lagging power factor. In this section the actual values of field quantities are expressed in a per unit (p. u.) system, in which the value of the initial point of a field quantity in the original design in Figure 5.5 is defined to be at 1 p. u.

6.3.1 Effect of the Stepped Profile of End Core Packets

The axial flux is the primary cause of the eddy currents in the end core. The goal of applying the stepped profiles of end packets is to increase the lengths of the paths of the axial fluxes generated by the armature/field end windings, thus decreasing the magnetic permeances between the end core and end armature/field windings, which significantly reduces the loss density at the tooth tip. Figure 6.41 shows two different stepped profiles of end packets (Designs A1 and A2). The IDs of the 1st and the 2nd packet in Design A1 are larger than those in Design A2.

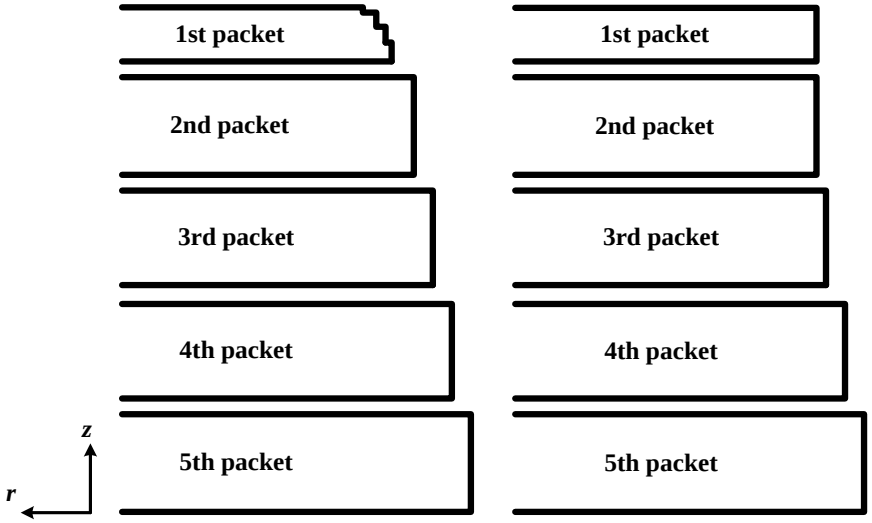

Figure 6.41 *Radial-axial* cross-section view of the stepped profile of the end core teeth of (a) the Design A1 – original design; (b) the Design A2.

It is explained in [12] that the axial flux and loss densities decrease from the core end to the stator main body due to the increasing length of the flux path, and the axial flux density is higher on the leading-edge (downstream of the rotation) half tooth due to the superposition of the end fringing flux and cross-slot flux. Hence generally the highest loss density occurs in the leading-edge half of the teeth of the 1st packet. Figure 6.42 shows the axial flux density distribution (in per unit) in the leading-edge half teeth of the 1st and the 2nd packet of the two designs. It can be concluded from Figure 6.42 that at the tooth tip of the 1st packet, the axial flux density is higher in Design A1 while at the tooth bottom the

axial flux densities are almost the same in Designs A1 and A2 because of the identical values of P_{re} and P_{ae}. However, the axial flux density at the tooth tip of the 2nd packet is slightly higher in Design A1 but in the rest of the teeth the axial flux density is higher in Design A2. The reason is that in Design A2 at the tooth tip the 1st packet effectively shields the end leakage flux from impinging the 2nd packet, while in the other regions, the 1st packet teeth in Design A2 are highly saturated, resulting in a larger reluctance in the radial direction, thus the axial flux in the 1st packet is less inclined to change its path to the radial direction but travels across the vent and enters the 2nd packet teeth instead. According to Figure 6.43, the resultant eddy current loss density is more intensive at the tooth tips of the 1st packet in Design A2 due to the higher axial flux.

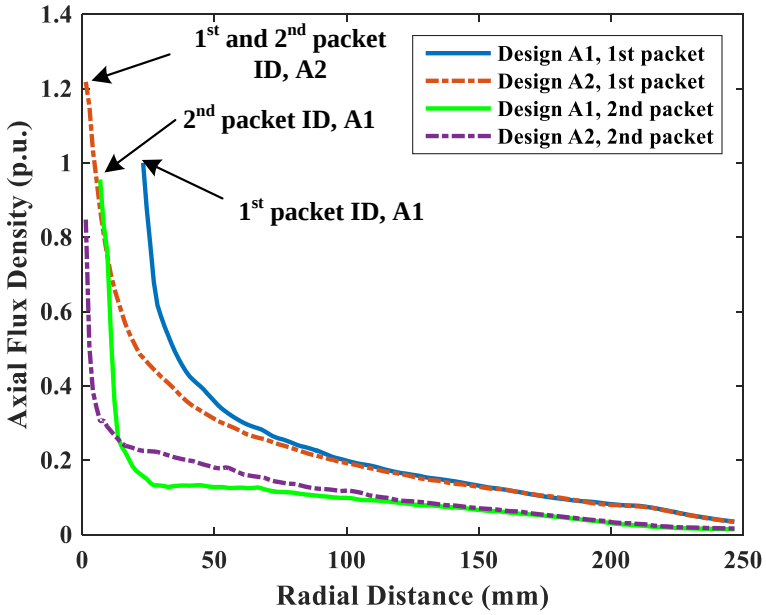

Figure 6.42 Radial distribution of the peak axial flux density impinging the leading-edge half teeth of the 1st and the 2nd packet of Designs A1 and A2.

The stepped profile has an influence on the flux and loss densities in the back-iron of end packets as well. Figure 6.44 shows that the tangential flux density in the back-iron of the 1st packet is higher in Design A2. In addition to the higher axial flux at the tooth tips,

the smaller 1st packet ID in Design A2 results in a lower radial reluctance in the air gap thus increasing the main flux in the 1st packet teeth and core back.

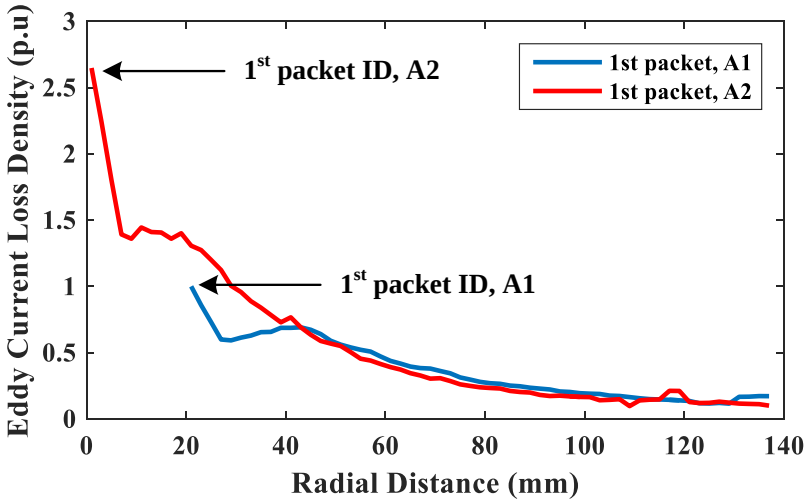

Figure 6.43 Radial distribution of the average additional eddy current loss density in a lamination of the leading-edge half tooth tips of the 1st packet of Designs A1 and A2.

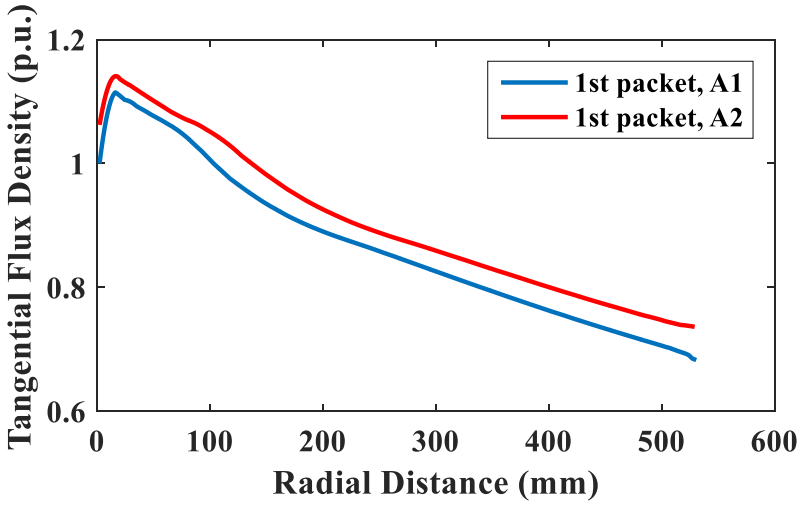

Figure 6.44 Radial distribution of the magnitude of the tangential flux density in the back-iron of the 1st packet of Designs A1 and A2.

6.3.2 Effect of the Tooth Slits

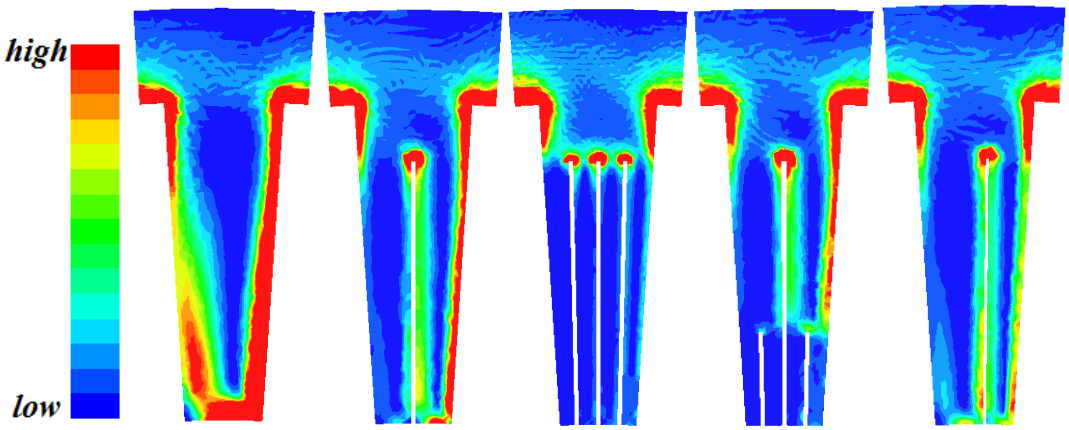

Figure 6.45 Additional eddy current loss density at the rated condition in a lamination of the 1st packet tooth in the Design (a) B1 – no slit; (b) B2 – original design, single slit; (c) B3 – three slits; (d) B4 – short sub-slits; (e) B5 – asymmetric single slit.

It is reported in [200] that the in-plane eddy current density caused by axial flux in end teeth is approximately proportional to the square of the tooth width. The slits in the end teeth equivalently shorten the tooth width and the eddy current paths, thus reducing the consequential losses. The effectiveness of different types of tooth slits are analyzed and Figure 6.45 compares the eddy current loss density distributions in a 1st packet tooth between the Designs B1~B5. Comparing the eddy current distributions shown in Figure 6.45(a) and (b) shows that the application of tooth slits effectively reduces the loss density in the tooth and alleviates the thermal stress. Increasing the number of slits can further decrease the eddy current loss and Figure 6.45(c) shows that the eddy current loss density in the tooth with three slits has been reduced to negligible values. The side effect of applying more slits is that they can significantly increase the level of saturation in the teeth, which leads to a higher reluctance in the radial direction, so the main flux is decreased and the axial flux is less likely to attenuate axially and is inclined to travel across the vent and penetrate the 2nd packet teeth. Figure 6.45(d) illustrates a tooth with a major slit in the center extended to the bottom and two shorter side sub-slits at the tip. This approach can significantly reduce the loss density at the tooth tip where the highest values of loss density and temperature appear, while the loss density distribution at the tooth bottom resembles

that in Design B2. The location of tooth slits can also affect the loss distributions. Figure 6.45(e) shows the asymmetric single slits adopted in Design B5. Comparing Figure 6.45(b) and (e) shows that Design B5 effectively shortens the eddy current paths thus reducing the losses in the leading-edge half tooth where the highest axial flux and eddy currents occur. The eddy current loss density is slightly higher in the lagging-edge half tooth in Design B5 than that in Design B2.

6.3.3 Effect of the Stator End Winding Inclination Angle

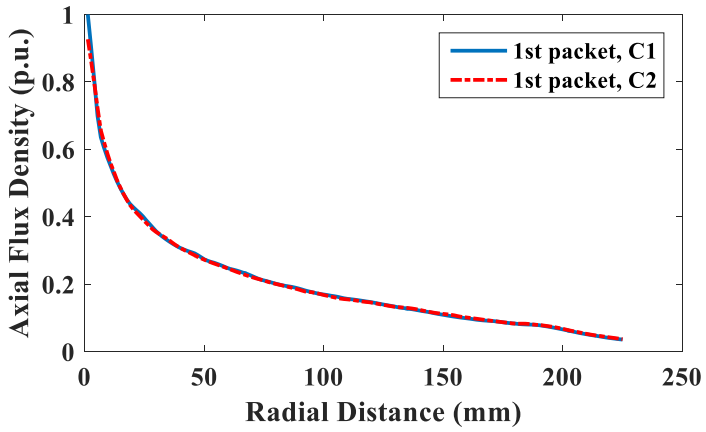

Figure 6.46 Radial distribution of the peak axial flux density impinging the leading-edge half teeth of the 1st packet of Designs C1 and C2.

For the original design (Design C1) in Figure 5.5, the angle of the inclination part of the armature end windings is 12 degrees to the generator axis, while this angle is increased to 32 degrees with the same length of winding extension in the end region in the simulation for the Design C2. Figure 6.46 shows the axial flux density distribution of the 1st packet teeth of both designs. The only difference between the results of the two designs is that the axial flux density at tooth ID is slightly lower in Design C2 compared to Design C1. Define P_{re} and P_{ae} to be the magnetic permeance factor between the press plate and the end field windings or end armature windings respectively. At the tooth tips, the permeance factor P_{re} is larger than P_{ae} and the axial field vector $\boldsymbol{B_z}$ is closer to the rotor mmf $\boldsymbol{F_r}$, hence the rotor-to-stator fringing flux is the dominant source of axial flux. Increasing the stator

winding inclination angle leads to larger values of P_{ae} and the associated field component $\boldsymbol{B}_{ae}$, which counteract the axial flux $\boldsymbol{B}_{re}$ contributed by the rotor mmf at the tooth tips. However, the influence of the stator winding inclination angle is limited and there is no noticeable difference between the loss densities in the end packet teeth.

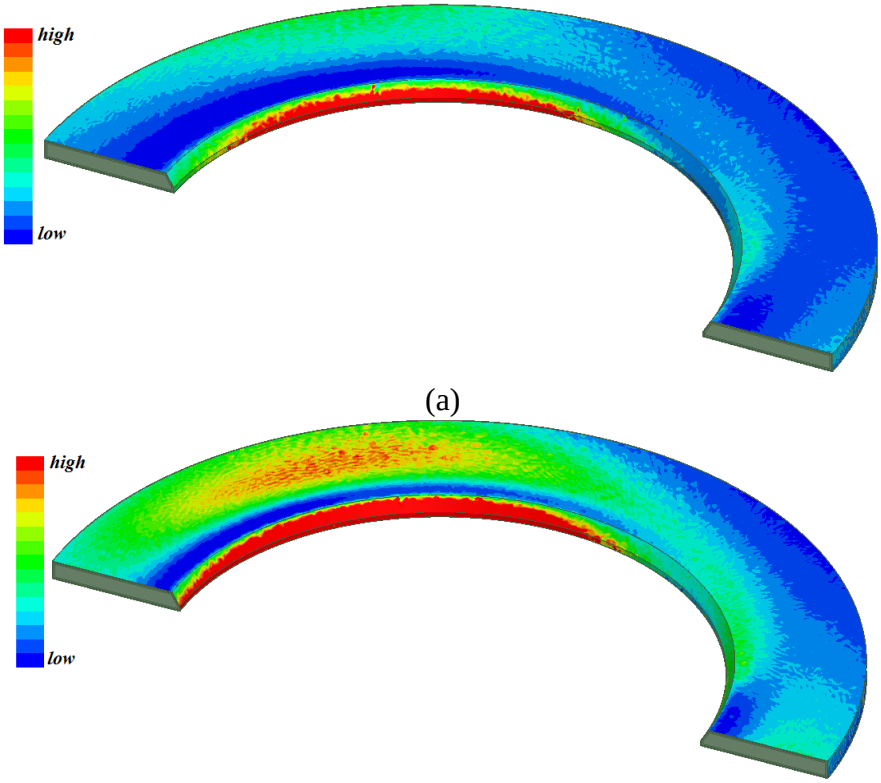

Figure 6.47 Eddy current loss density distribution at one time instant in the press plate under the rated condition of the Design (a) C1; (b) C2.

In addition, there exists significant difference between the loss distributions in the press plate and the 1st packet back-iron between the two designs. Figure 6.47 shows the loss distributions in the press plate and at the inner edge of the press plate, the eddy current loss density in Design C2 is 89% higher than in Design C1. Figure 6.48 demonstrates that the loss density beneath the top surface of the press plate in Design C2 is much higher than that in Design C1; the reason for this phenomenon is that the distance between the inner/top surfaces of the press plate to the stator end windings is shorter and the leakage flux on the surfaces is stronger according to the Biot-Savart Law.

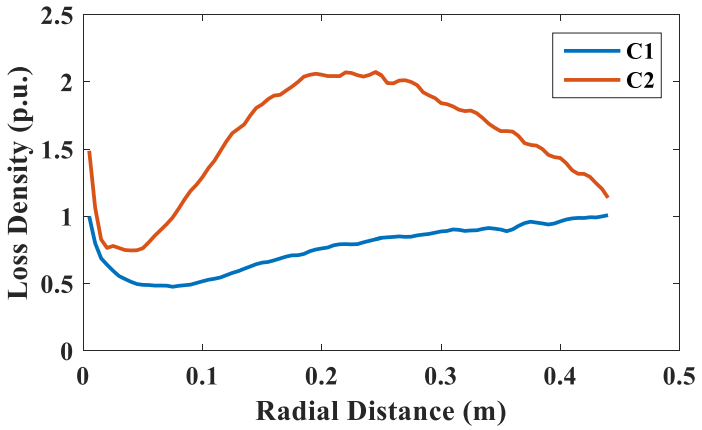

Figure 6.48 Radial distribution of the surface eddy current loss density at the top surface of Designs A1 and A2 under the rated condition.

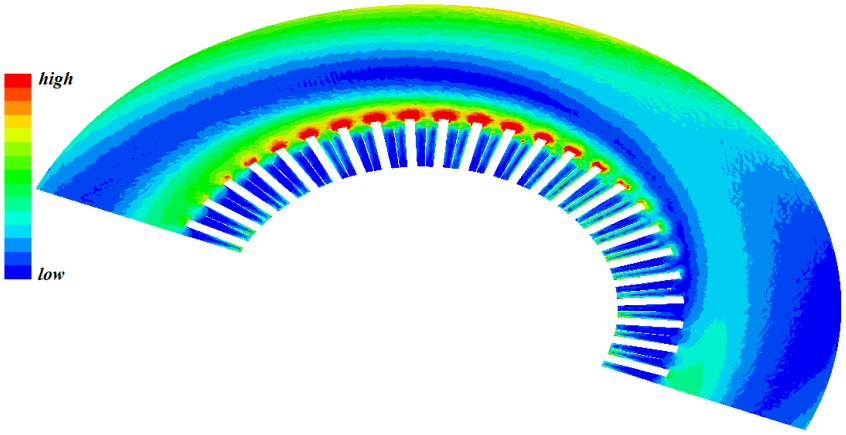

Figure 6.49 Eddy current density distribution at one time instant in the elements of the surface layer of the 1st packet in Design C1.

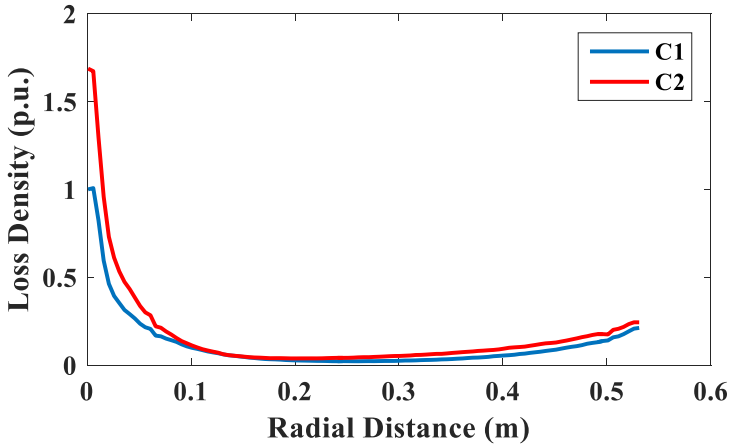

Figure 6.50 Radial distribution of the additional eddy current loss density in the surface-layer elements of 1st packet back-iron in Designs C1 and C2.

Regarding the losses in the end core, in Figure 6.49, intensive eddy current primarily induced by the axial flux and the radial end leakage flux appears in a thin layer under the surface of the 1st packet back-iron. However, the eddy current density rapidly attenuates axially into the 1st packet back-iron due to the skin effect. It can be concluded from Figure 6.50 that the larger angle of stator winding inclination in Design C2 results in stronger skin effects under the surfaces of the 1st packet back-iron, especially in the region near the back-iron ID.

6.3.4 Effect of the Stator End Winding Inclination Angle

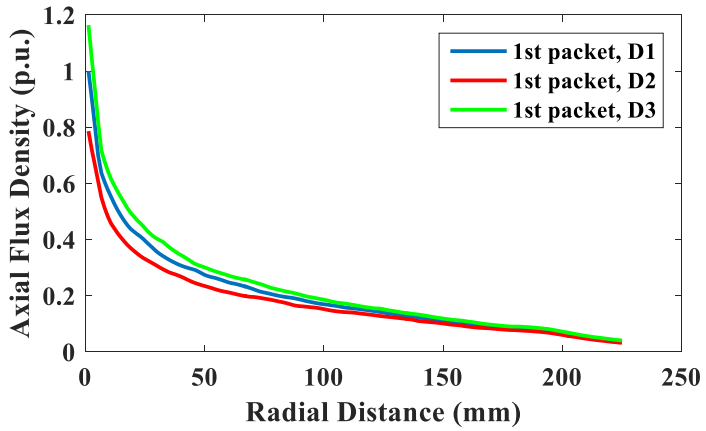

Figure 6.51 Radial distribution of the peak axial flux density impinging the leading-edge half teeth of the 1st packet of Designs D1~D3.

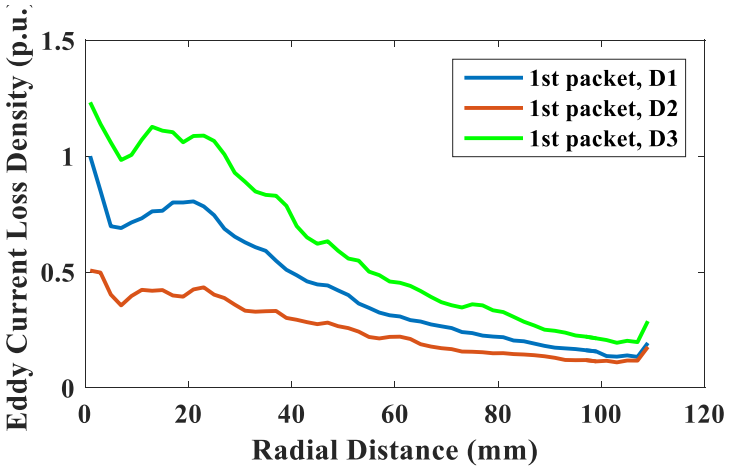

Figure 6.52 Radial distribution of the average additional eddy current loss density in a lamination of the leading-edge half tooth tips of the 1st packet of Designs D1~D3.

The axial extension of the rotor body into the end region in Figure 5.5 (Design D1) is decreased by 90 mm in Design D2 and increased by 60 mm in Design D3. Extending the rotor body effectively increases the permeance factor P_{re} and hence the axial rotor-to-stator fringing flux density at the tooth tips. This trend is illustrated in Figure 6.51. At the 1st packet ID, the axial flux density is 21% lower in Design D2 and 16% higher in Design D3 compared to Design D1. Similar conclusions can also be made for the resultant eddy current loss distributions in the end packet teeth based on the results of loss density in a lamination in the middle of the 1st packet presented in Figure 6.52.

6.4 Chapter Summary

This chapter presents a comprehensive parametric study on the impacts of various factors on the EM behaviors in the end region of large generators. First, the magnetic field and loss distributions in the end components under five operating conditions are analyzed and compared based on the 3D FEA model. Then, the impacts of different end metallic structures on the magnetic flux and loss distributions in this region are evaluated. Finally, a parametric study is performed to assess the effectiveness of different designs of the end field/armature windings and end stator structures in reducing the losses in the end region.

CHAPTER 7. FAST-SOLVING QUASI-3-DIMENSIONAL FINITE DIFFERENCE METHOD BASED SIMULATION OF THE LARGE GENERATOR END REGION

Purely analytical methods were developed in early years to analyze the leakage flux and the resultant losses in the end components of large generators, and they can be almost instantly performed by today's computers. However, their accuracy is confined by the strong assumptions for deriving the closed forms of magnetic field and the over-simplifications of the geometries and current filaments. Full 3D time-domain FEA described in Chapters 5 and 6 performs a precise modeling of the end structures and a rigorous representation of material properties, thus it is an effective tool for accurate calculation, but it takes a tremendous amount of computing time, making it less competitive for the initial design in which numerous candidates are required to be evaluated. Quasi-3D based approaches include the treatment of the complex geometries by mapping the end components onto a 2D *radial-axial* plane, thus they are an ideal design tool due to the balance between complexity and precision. However, an inherent assumption of quasi-3D methods is that the end geometries are peripherally consistent and all field quantities vary sinusoidally in the peripheral direction. In addition, only the magnetic field generated by end winding mmfs can be analyzed, and the cross-slot flux impinging the end core and the transverse flux in finger plates excited by local stator windings discussed in Chapter 6 have not been discussed in existing quasi-3D approaches. Regarding the calculation of the skin-layer eddy current distributions in the end metallic components, i.e., the press plate, to avoid adopting intensive mesh refinement in the region with pronounced eddy currents and thus reduce the computational effort, the surfaces of the conductors are usually modeled as surface impedance boundary conditions (SIBCs), but there are almost no reports about the implementation of SIBCs with finite difference (FD) formulation, or the inclusion of the

effects of nonlinear material or geometric edges/corners in quasi-3D calculations. Also, no existing quasi-3D method includes the calculation of the eddy current distributions in the copper strands in end stator windings, and the existing 1-D/2-D models without considering the stepped geometry are insufficient for the analysis of the axial variation of the strand eddy current distributions and significant temperature rise in the end region.

This chapter describes an improved fast-solving quasi-3D FD based method to analyze the magnetic field and loss distributions in the end region of large generators. To compensate the errors caused by the inherent assumption of classical quasi-3D formulation that the geometries of end components are peripherally consistent, regional conformal mappings based on Schwarz-Christoffel transformation are adopted to incorporate the impacts of the cross-slot flux caused by the local armature windings and slot/tooth geometry. When computing the field and loss distributions in the press plate, the effects of nonlinear material properties and a compensation method for the near corner effects are incorporated in the formulation of SIBCs to improve the accuracy. Furthermore, the axial variation of magnetic field and loss caused by stepped stator geometries and end fringing effects, the peripheral variation of the airgap flux caused by slotting effect, and the proximity effects between copper strands are incorporated in the calculation of the strand eddy current distributions near the core end.

7.1 Quasi-3D FD Scheme of the Generator End Region

The axial flux impinging the end stator core is the combination of the end fringing flux and cross-slot flux as illustrated in Figure 6.14. The end fringing flux is produced by the end armature/field winding mmfs, and travels from the winding end turns to the end stator. Its magnitude is approximately uniform across the stator tooth surface peripherally. Regarding the cross-slot axial flux, in the slot region the stator currents generate a difference in magnetic scalar potential between the two adjacent teeth and excite a

peripherally traveling flux across the slot. In Figure 6.14, the cross-slot flux reinforces the end fringing axial flux on one side of the tooth (leading-edge, i.e., the "downstream" side in rotation) while it counteracts the end fringing axial flux on the other side (lagging-edge).

In the fast calculation method proposed in this chapter, the quasi-3D simulation is used to determine the end fringing flux and the overall distribution of the magnetic field in the end region. The field governing equations are in terms of the complex magnetic scalar potential φ. All field quantities are expressed by complex variables. Since the fundamental component dominates the winding mmfs, higher-order harmonics are negligible and the complex values of field quantities represent their magnitudes and phase angles at fundamental frequency.

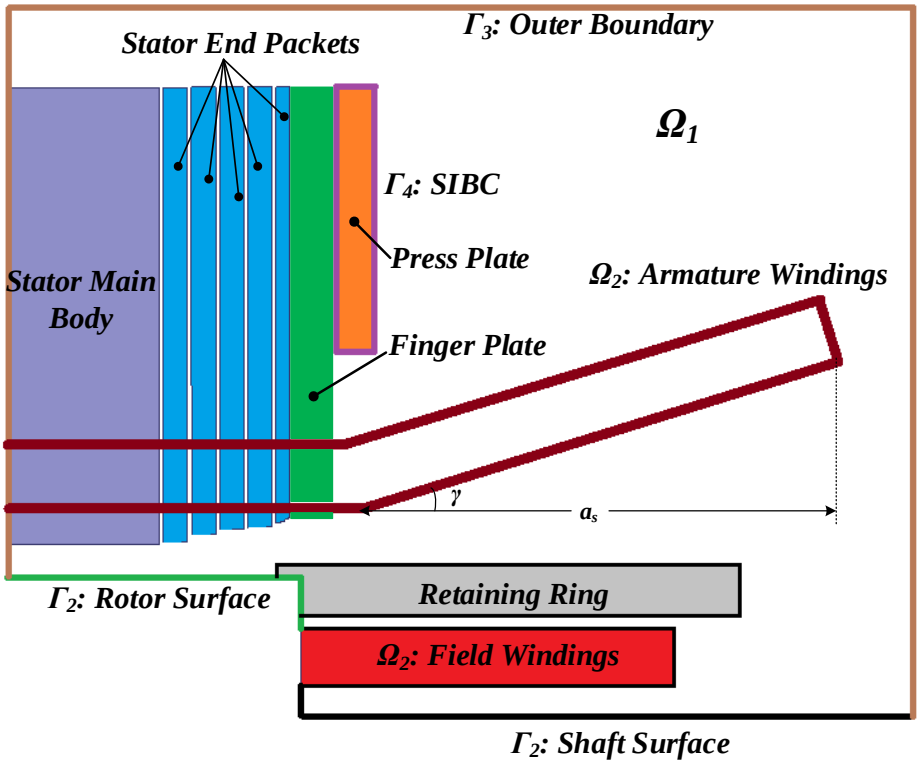

Figure 7.1 Radial-axial solving domain of the quasi-3D FD simulations.

Figure 7.1 shows the solution domain of the quasi-3D FD simulations. The major components in the model are the stator core end packets and main body, retaining ring,

press plate, and stator and rotor end windings. The stator core is represented up to an axial depth of 0.5 m from the core end surface, which is sufficient for the decay of the axial flux and the magnetic scalar potential distribution on the innermost plane (the left-side boundary in Figure 7.1) can representatively express the field in the stator main body. The radial ventilation ducts between the stator core end packets and the stepped shapes of the end core are explicitly represented in the model.

The basic assumptions of the quasi-3D formulation of the large generator end region are as follows:

1) The model geometries are consistent in the peripheral direction.
2) All field quantities vary sinusoidally in the peripheral direction at the fundamental frequency and all higher-order harmonics are neglected.
3) The influence of the temperature on the conductivity and permeability of materials is not considered.
4) The reaction of the eddy currents in the stator end core on the magnetic field is not directly represented in the model, but it is reflected by the modified anisotropic permeability tensor of stator core. However, the eddy current distribution in the stator end core can be estimated in post processing based on the flux density distribution solved in quasi-3D simulations.
5) The magnetic field and eddy current distributions in the press plate and other metallic components are not directly calculated by solving the electric vector potential distribution. The effects of eddy currents and the loss distribution are expressed by SIBCs on the conductor surfaces.
6) The radial mmf drop in the shaft is zero.
7) Magnetic flux cannot travel across the outer boundaries of the simulation model.

To incorporate the effects of the peripheral discontinuity of the slot/tooth geometries, a modified anisotropic permeability tensor in cylindrical coordinates is applied to the tooth portion of the laminated core based on the local proportions of slot and tooth widths and the stacking factor. In addition, since the in-plane eddy current reaction on the magnetic field in the stator cannot be explicitly expressed in quasi-3D formulations, a correction factor is defined for the axial components of the permeabilities in the tooth and the back-iron portion of the stator end packets respectively to represent the eddy current effects. Therefore, the anisotropic permeability of the stator end teeth is

$$\begin{cases} \mu_r = \dfrac{\mu_{e1} W_t + \mu_0 W_s}{W_t + W_s} \\ \mu_\theta = \dfrac{\left(W_t + W_s\right) \mu_{e1} \mu_0}{\mu_0 W_t + \mu_{e1} W_s} \\ \mu_z = \dfrac{\mu_{e2} k_{eddy,t} W_t + \mu_0 W_s}{W_t + W_s} \end{cases} \tag{7.1}$$

where

$$\begin{cases} \mu_{e1} = \mu_{fe} k_{lam} + \mu_0 \left(1 - k_{lam}\right) \\ \mu_{e2} = \dfrac{\mu_{fe} \mu_0}{\mu_0 k_{lam} + \mu_{fe} \left(1 - k_{lam}\right)} \\ k_{eddy,t} = \dfrac{\sqrt{2}}{\xi} \cdot \sqrt{\dfrac{\cosh \xi - \cos \xi}{\cosh \xi + \cos \xi}}, \; \xi = W_t \cdot \sqrt{\pi f_1 \mu_{e2} \sigma} \end{cases}$$

where k_{lam} is the stacking factor, W_t and W_s are the width of the tooth and slot respectively, μ_0 and μ_{fe} are the permeability of the air and steel respectively, f_1 is the fundamental frequency, and σ is the steel conductivity. In (7.1), μ_{fe} is calculated by an iterative process based on the nonlinear B-H curve. The effective permeability used for harmonic analyses based on the assumption of identical stored energy is

$$\mu_{fe} = \frac{2}{T} \cdot \frac{\int_0^T H_m \sin(\omega t) B\left[H_m \sin(\omega t)\right] dt}{{H_m}^2} \tag{7.2}$$

where T is the fundamental electrical cycle. Similarly, the three components of permeability tensor of the stator back iron are

$$\begin{cases} \mu_r = \mu_\theta = \mu_{fe} k_{lam} + \mu_0 \left(1 - k_{lam}\right) \\ \mu_z = \dfrac{\mu_{fe} \mu_0}{\mu_0 k_{lam} + \mu_{fe} \left(1 - k_{lam}\right)} \cdot k_{eddy,b} \end{cases} \tag{7.3}$$

where

$$k_{eddy,b} = \frac{\sqrt{2}}{\zeta} \cdot \sqrt{\frac{\cosh\zeta - \cos\zeta}{\cosh\zeta + \cos\zeta}}, \zeta = W_b \cdot \sqrt{\pi f_1 \mu_z \sigma}$$

where W_b is the peripheral width of back-iron segment. To account for the increased mmf drop in the airgap caused by the stator slots, the radial permeability of the airgap region is divided by the Carter's gap lengthening coefficient [201]. Notice that the Carter's coefficient has different values between the end packets depending on the inner radius of each packet.

To uniquely determine the excitations and boundary conditions for the simulation, both the armature and field winding fundamental mmfs and their relative phase shift must be specified for each operating condition. A 2D iterative FEA based method is selected to determine the operating point as discussed in Section 5.2.1.2. In Figure 7.1, the rotor surface is subject to the following Dirichlet boundary condition:

$$\varphi\big|_{\Gamma_1} = mmf_r - mmf_{ri} \tag{7.4}$$

where mmf_r is the fundamental field winding mmf and mmf_{ri} is the fundamental mmf drop in the rotor iron. The value of mmf_{ri} is obtained in post processing by integrating the magnetic field intensity lines radially from the rotor center to the outer diameter in 2D FEAs [163]. Based on-assumption 6), the boundary condition on the shaft surface is

$$\varphi\big|_{\Gamma_2} = 0. \tag{7.5}$$

The magnetic scalar potential on the outer surfaces of the model Γ_3 is subject to the Neumann boundary condition according to the assumption 7):

$$\left.\frac{\partial \varphi}{\partial n}\right|_{\Gamma_3} = 0. \tag{7.6}$$

The surfaces of the press plate Γ_4 are subject to SIBCs described in Section 7.3.

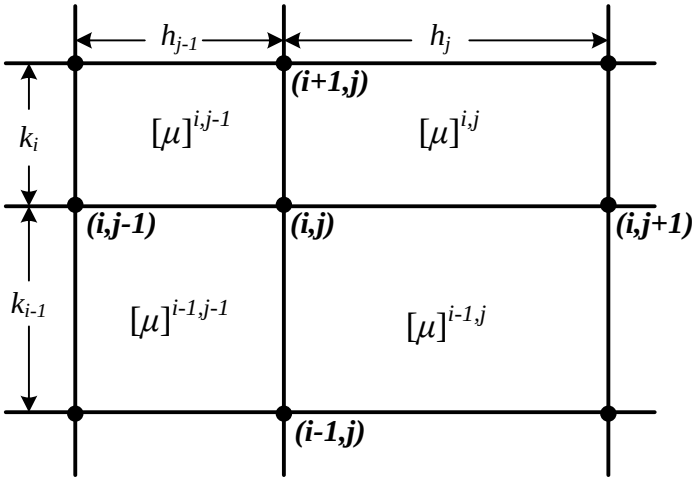

Figure 7.2 Quasi-3D FD grid.

Using the FD method, the solution domain is discretized into a FD mesh with about 30,000 nodes and classified into two sub-domains: the non-excitation sub-domain $\boldsymbol{\Omega_1}$ and the excitation sub-domain $\boldsymbol{\Omega_2}$ as shown in Figure 7.1. The sub-domain $\boldsymbol{\Omega_1}$ contains the stator core, finger plates, retaining ring and the air, while $\boldsymbol{\Omega_2}$ consists of the armature and field end windings. The governing equation of $\boldsymbol{\Omega_1}$ in terms of φ is

$$\frac{\partial}{\partial r}\left(\mu_r \frac{\partial \varphi}{\partial r}\right)+\frac{\mu_r}{r}\frac{\partial \varphi}{\partial r}-\frac{p^2}{r^2}\mu_\theta \varphi+\frac{\partial}{\partial z}\left(\mu_z \frac{\partial \varphi}{\partial z}\right)=0 \tag{7.7}$$

where p is the number of pole pairs. The quasi-3D FD formulation of (7.7) for the point (i,j) on the grid illustrated in Figure 7.2 is

$$B_{i,j}\varphi_{i-1,j}+T_{i,j}\varphi_{i+1,j}+L_{i,j}\varphi_{i,j-1}+R_{i,j}\varphi_{i,j+1}-D_{i,j}\varphi_{i,j}=0 \tag{7.8}$$

where

$$B_{i,j}=\frac{\mu_r{}^{i-1,j-1}h_{j-1}+\mu_r{}^{i-1,j}h_j}{2k_{i-1}}\left(1-\frac{k_{i-1}}{2r_i}\right)$$

$$T_{i,j}=\frac{\mu_r{}^{i,j-1}h_{j-1}+\mu_r{}^{i,j}h_j}{2k_i}\left(1+\frac{k_i}{2r_i}\right)$$

$$L_{i,j}=\frac{\mu_z{}^{i-1,j-1}k_{i-1}+\mu_z{}^{i,j-1}k_i}{2h_{j-1}}$$

$$R_{i,j}=\frac{\mu_z{}^{i-1,j}k_{i-1}+\mu_z{}^{i,j}k_i}{2h_j}$$

$$D_{i,j}=B_{i,j}+T_{i,j}+L_{i,j}+R_{i,j}+{p^2}\Big/{4r_i^2}\left(\mu_\theta{}^{i-1,j-1}k_{i-1}h_{j-1}+\mu_\theta{}^{i,j-1}k_i h_{j-1}+\mu_\theta{}^{i-1,j}k_{i-1}h_j+\mu_\theta{}^{i,j}k_i h_j\right).$$

For $\boldsymbol{\Omega_2}$, if the stator/rotor end windings are represented by current sheets, then the complicated $\mathbf{H_p}$ assignment or the formulation based on the three components of magnetic vector potential $\mathbf{A}$ is required, which significantly increases the computational complexity. To facilitate the formulation based on a single variable φ in free space, the field and armature windings are replaced by permanent magnets and the distribution of magnetization can generate the equivalent fundamental mmfs of the field and armature windings. Based on the relation $\mathbf{B}=[\mu](\mathbf{H}+\mathbf{M})$ and Gauss's law of magnetism $\nabla \cdot \mathbf{B} = 0$, the governing equation of $\boldsymbol{\Omega_2}$ is

$$\frac{\partial}{\partial r}\left(\mu_r \frac{\partial \varphi}{\partial r}\right)+\frac{\mu_r}{r}\frac{\partial \varphi}{\partial r}-\frac{p^2}{r^2}\mu_\theta \varphi+\frac{\partial}{\partial z}\left(\mu_z \frac{\partial \varphi}{\partial z}\right)=\frac{1}{r}\frac{\partial}{\partial r}\left(\mu_r r M_r\right)+\frac{\partial\left(\mu_z M_z\right)}{\partial z} \tag{7.9}$$

where M_r and M_z are the radial and axial equivalent magnetization respectively. The quasi-3D FD form of (7.9) is

$$B_{i,j}\varphi_{i-1,j} + T_{i,j}\varphi_{i+1,j} + L_{i,j}\varphi_{i,j-1} + R_{i,j}\varphi_{i,j+1} - D_{i,j}\varphi_{i,j} = F_{i,j} \tag{7.10}$$

where $B_{i,j}$, $T_{i,j}$, $L_{i,j}$, $R_{i,j}$ and $D_{i,j}$ are the same as the expressions in (7.8), and

$$F_{i,j} = \frac{1}{2r_i}\left[\begin{array}{l} \mu_r^{\,i,j-1}\left(r_i + \frac{1}{2}k_i\right)M_r^{\,i,j-1}h_{j-1} + \mu_r^{\,i,j}\left(r_i + \frac{1}{2}k_i\right)M_r^{\,i,j}h_j \\ \quad - \mu_r^{\,i-1,j-1}\left(r_i - \frac{1}{2}k_{i-1}\right)M_r^{\,i-1,j-1}h_{j-1} - \mu_r^{\,i-1,j}\left(r_i - \frac{1}{2}k_{i-1}\right)M_r^{\,i-1,j}h_j \end{array}\right]$$
$$+\frac{1}{2}\left[\mu_z^{\,i,j}M_z^{\,i,j}k_i + \mu_z^{\,i-1,j}M_z^{\,i-1,j}k_{i-1} - \mu_z^{\,i,j-1}M_z^{\,i,j-1}k_i - \mu_z^{\,i-1,j-1}M_z^{\,i-1,j-1}k_{i-1}\right].$$

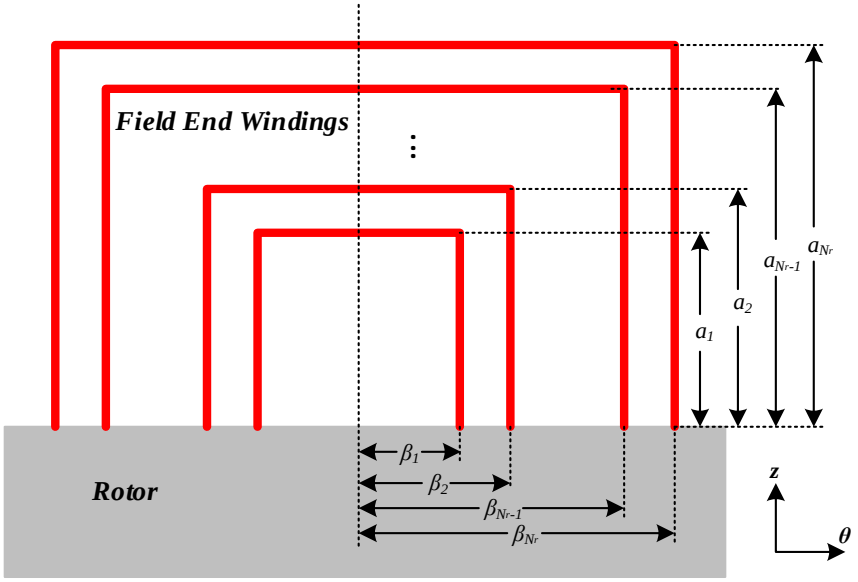

Figure 7.3 Topology of the field end windings.

The topology of the field end winding and the axial distribution of M_r are demonstrated in Figure 7.3 and Figure 7.4 respectively, and in Figure 7.4

$$M_{ri} = \frac{4I_r N_{tr}}{h_r \pi}\sum_{i}^{N_r}\sin\left(\frac{\beta_i}{p}\right), i = 1,2,...N_r \tag{7.11}$$

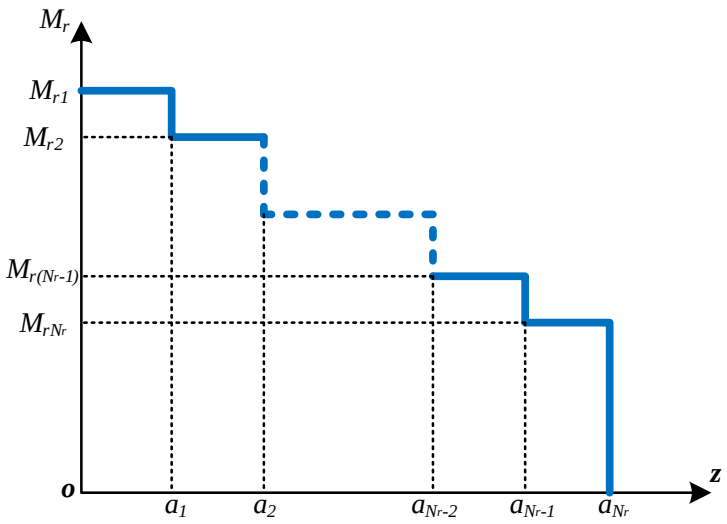

Figure 7.4 Distribution of M_r of field end windings.

where I_r is the rotor current, h_r is the thickness of the equivalent permanent magnet of field windings in Figure 7.1, N_r is the number of rotor bars per pole and N_{tr} is the number of turns per bar. The M_r of the straight part of the stator windings is

$$M_r = \frac{3\sqrt{2}}{h_s \pi} \frac{N_s I_a k_d k_p}{p} e^{-j\alpha} \tag{7.12}$$

where I_a is the stator phase current, h_s is the thickness of the equivalent permanent magnets of stator windings, N_s is the number of stator series turns per phase, and k_d and k_p are the stator winding distribution and pitch factor respectively. Define the phase angle of the rotor mmf to be zero, then α in (7.12) is the phase shift between the rotor and stator mmfs determined by 2D FEAs. The M_z of the rotor and straight stator windings is zero. The magnetization of the inclined stator winding is

$$\begin{cases} M_r = \dfrac{3\sqrt{2}}{h_s \pi} \dfrac{N_s I_a k_d k_p}{p} \cos\gamma \cdot \dfrac{a_s - z}{a_s} e^{-j\alpha} \\ M_z = -\dfrac{3\sqrt{2}}{h_s \pi} \dfrac{N_s I_a k_d k_p}{p} \cos\gamma \cdot \dfrac{a_s - z}{a_s} e^{-j\alpha} \end{cases} \tag{7.13}$$

where a_s is the axial extension of the inclined stator windings, γ is the inclination angle in Figure 7.1, and z is the axial position beyond the inclination point. Combining (7.8), (7.10) and all boundary conditions yields the matrix form of the governing equations $[\mathbf{K}][\boldsymbol{\varphi}]=[\mathbf{f}]$, where $[\mathbf{K}]$ is a sparse tridiagonal matrix with five nonzero diagonals related to the coefficients of the nodal magnetic scalar potentials, $[\boldsymbol{\varphi}]$ is the magnetic scalar potential vector, and $[\mathbf{f}]$ is a vector associated with boundary conditions and equivalent magnetizations. The distribution of the magnetic field can be obtained by solving the vector of $[\boldsymbol{\varphi}]$. The permeabilities of the stator core and the press plate depend on the flux density in each element due to the nonlinear B-H curves of magnetic steels, thus it is indispensable to incorporate the field-dependent harmonic permeability in (7.2) into the calculation and update the magnetic field distribution by iterations.

7.2 Calculation of the Magnetic Field and Loss in the End Core and Finger Plates

7.2.1 Analytical Calculation of the Cross-slot Flux Distribution

The quasi-3D simulation described in Section 7.1 is used to determine the end fringing flux in the end stator core, while the other essential component of magnetic field, the cross-slot flux generated by the local stator windings, is predicted by the conformal mapping method. The fundamentals of conformal transformation are introduced in Section 3.2.1. The sub-regions beyond the 1st packet and between two end packets shown in Figure 7.5 are modeled differently due to the differences in boundary conditions. Figure 7.6 shows the sequential conformal mappings to solve the cross-slot flux impinging the 1st packet. In Figure 7.6, the *Z* plane is the original geometry of a slot pitch and point *C'* is defined at the origin. The surfaces of stator core are assumed to be ideal magnetic iron boundaries, where the flux density vectors are orthogonal to these surfaces. Assuming that the *Z* plane is located at the inner diameter of the stator core and the drop of the mmf in steel produced by the local stator winding is ignored, then magnetic scalar potential of the upper and lower

boundaries in the Z plane is $\Omega_0=(I_{au}+I_{al})$ and 0 respectively, where I_{au} and I_{al} are the total current of the upper and lower winding in the slot respectively. The geometry in the Z plane is mapped to the T plane with the following Schwarz-Christoffel transformation [56], [180]:

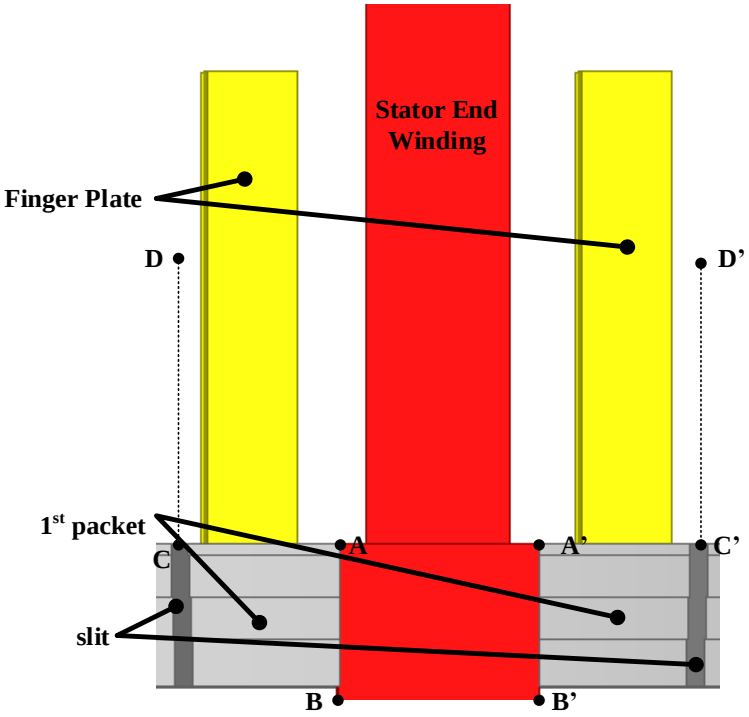

(a)

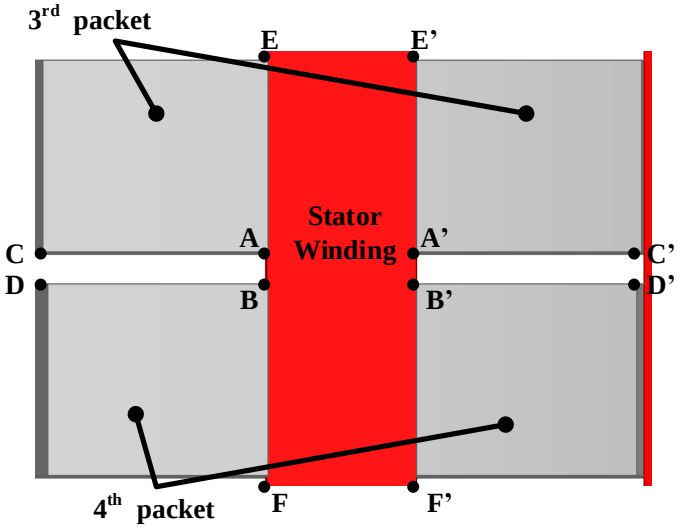

(b)

Figure 7.5 Regional solution domain (a) beyond the 1st end packet; (b) between the 3rd and 4th packet.

$$\frac{dz}{dt}=\frac{k}{\pi t}\cdot\frac{\sqrt{t-1}}{\sqrt{t-c}}$$
$$z=\frac{k}{\pi}\operatorname{arccosh}\left(\frac{2t-c-1}{c-1}\right)-\frac{k}{\pi\sqrt{c}}\operatorname{arccosh}\left(\frac{(c+1)t-2c}{(c-1)t}\right) \tag{7.14}$$

where $k=(W_s+W_t)/2$, $c=[(W_s+W_t)/W_s]^2$. The T plane is mapped to the upper half space in W plane, and then further onto an infinite strip in the S plane by the following transformations:

$$dt/dw=2w,\ t=w^2;\ ds/dw=1/(\pi w),\ s=\ln(w)/\pi. \tag{7.15}$$

Since the width of the strip in the S plane is 1, the flux density in the S plane is $B_{xS}=0$, $B_{yS}=\mu_0\,\Omega_0$, and the magnetic field in the Z plane is:

$$\mathbf{B_Z}=\mathbf{B_S}\left(\frac{\partial s}{\partial w}\cdot\frac{\partial w}{\partial t}\cdot\frac{\partial t}{\partial z}\right)^*=\mathbf{B_S}\left(\frac{\partial s}{\partial z}\right)^*. \tag{7.16}$$

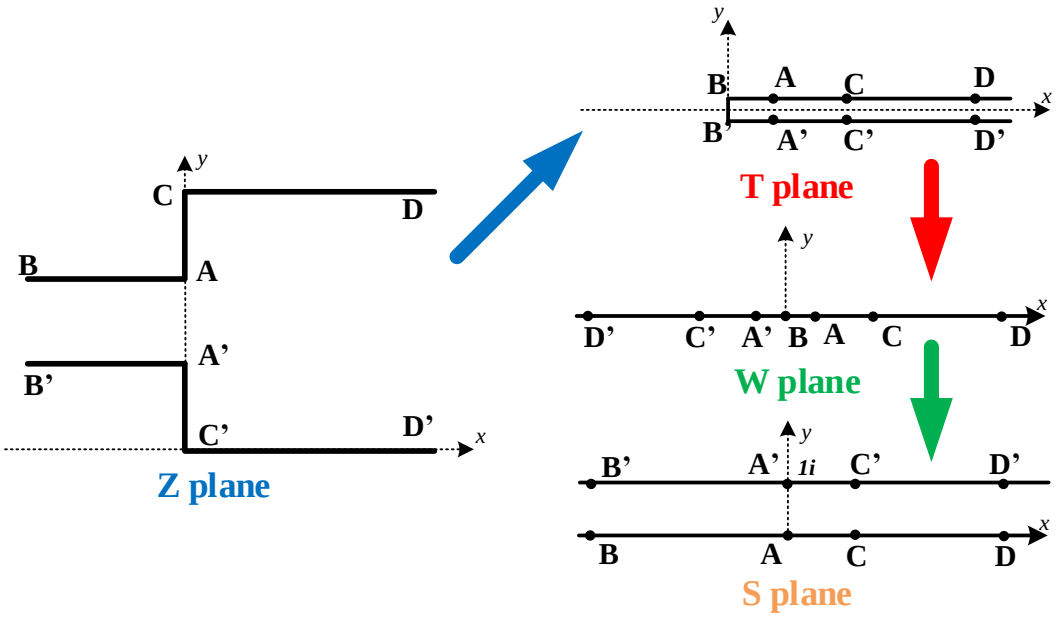

Figure 7.6 Sequential conformal mappings for the region beyond the 1st packet.

The B_x on the surfaces AC and $A'C'$ in the Z plane is the axial flux density on the 1st packet and the transverse flux in the finger plates can be obtained based on the

distribution of B_y between the boundaries *CD* and *C'D'*. For a slot where the upper and lower windings belong to the same phase, the magnitude of the cross-slot axial flux density varies essentially linearly from zero at the slot bottom to its peak value discussed above at the slot opening.

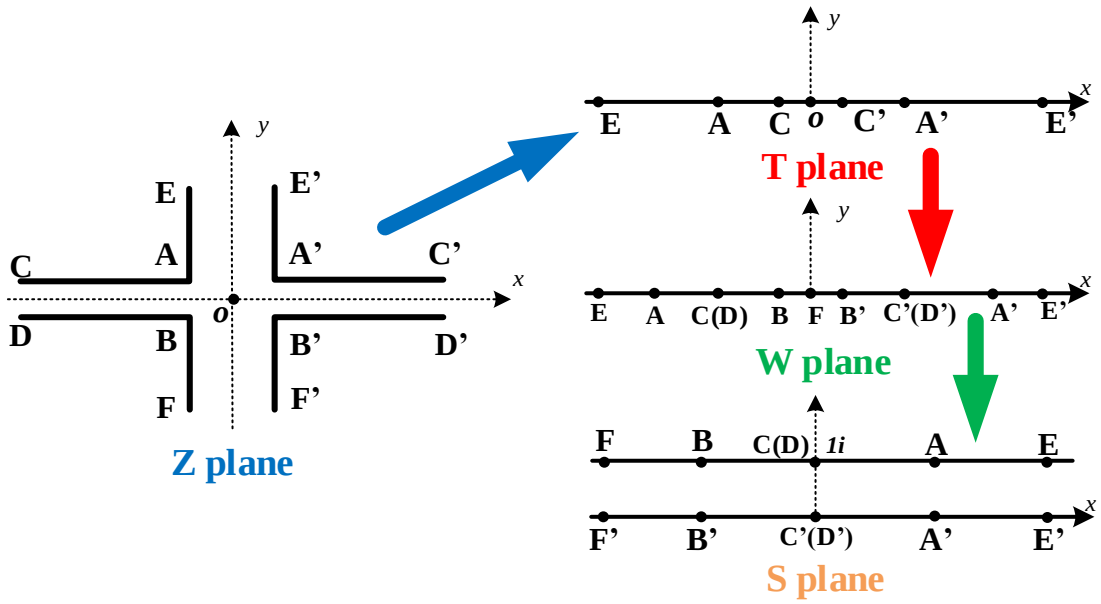

Figure 7.7 Sequential conformal mappings for the region between the 3rd and 4th end packets.

Figure 7.7 demonstrates the sequential conformal mappings for the region between the 3rd and 4th end packet. In the *Z* plane, the magnetic scalar potential on the boundaries in the right and left half planes is $\Omega_0=(I_{au}+I_{al})$ and 0 respectively. The first step is to map the upper half of *Z* plane to the upper infinite space in the *T* plane by Schwarz-Christoffel transformation:

$$\frac{dz}{dt}=-\frac{W_s}{\pi}\cdot\frac{\sqrt{1-t^2}}{t^2-a^2}$$
$$z=\frac{W_s}{\pi}\left(\arcsin t+\frac{\sqrt{1-a^2}}{2a}\operatorname{arccosh}\left(\frac{t^2-2a^2t^2+a^2}{a^2-t^2}\right)\right) \tag{7.17}$$

where $a = \sqrt{W_s^2/(W_s^2 + D^2)}$, and D is the axial distance between the two packets. The entire domain in the Z plane can be further mapped to the W plane:

$$t = \frac{a}{2}\left(w + \frac{1}{w}\right), \frac{dt}{dw} = \frac{a}{2}\left(1 - \frac{1}{w^2}\right). \tag{7.18}$$

The W plane is then mapped to the infinite strip in the S plane with the same function in (7.15). The magnetic field in the original Z plane is acquired in the same way as presented in (7.16). The B_y on the surfaces *AC*, *A'C'* and *BD*, *B'D'* is the axial cross-slot flux density on the 3rd and 4th packet respectively. The distribution of axial flux density inside of each end packet contributed by cross-slot flux is calculated by linear interpolation based on the its distribution on the surfaces.

7.2.2 Calculation of the Loss Densities in the Stator End Core and Finger Plates

There are four components of core loss: the hysteresis loss, excess loss, classical eddy current loss induced by the radial and peripheral main fluxes, and the eddy current loss caused by the axial flux. The first three types of core loss densities are [188]:

$$\begin{cases} p_h = k_h f_1 \left(B_r^2 + B_\theta^2 + B_z^2\right)^{\beta/2} \\ p_e = k_e f_1^{1.5} \left(B_r^2 + B_\theta^2 + B_z^2\right)^{0.75} \\ p_{c,//} = k_c f_1^2 \left(B_r^2 + B_\theta^2\right) \end{cases} \tag{7.19}$$

where k_h, k_e and k_c are the hysteresis, excess and classical eddy current loss coefficient respectively, and the parameter β=2. The distribution of B_r and B_θ can be solved in quasi-3D simulations, while B_z is the combination of the end fringing flux obtained in quasi-3D simulations and cross-slot flux computed by conformal mappings. Regarding the calculation of the eddy current loss density due to axial flux, to fully represent the

peripherally inconsitant tooth/slot geometries and incorporate the eddy current reaction, the electric vector potential **T** is introduced in the post-processing for laminations based on Faraday's induction law. To simplify the calculations, the vector **T** is selected to be only axially directed and this single component can fully represent the radial/peripheral eddy currents. The governing equation of the post-processing is:

$$\frac{1}{r}\frac{\partial}{\partial r}\left(r\frac{\partial T_z}{\partial r}\right)+\frac{1}{r^2}\frac{\partial^2 T_z}{\partial \theta^2}=j\left(2\pi f_1\right)k_{lam}\sigma\left(\mu_{e2}T_z+B_z\right). \tag{7.20}$$

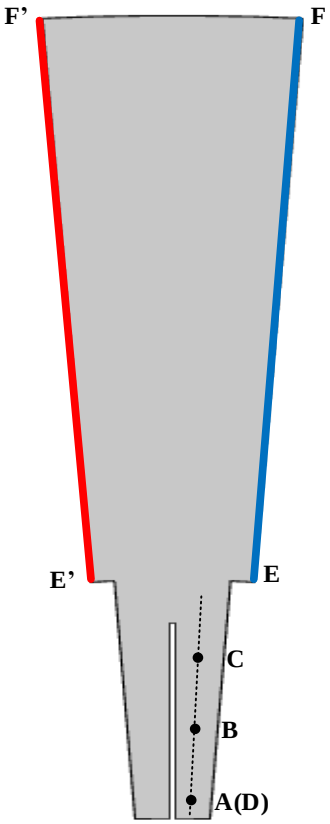

Figure 7.8 Solution domain of the post-processing for end packets.

The solution domain of the post-processing is shown in Figure 7.8. Only one slot pitch is represented by assigning the periodic boundary condition on the surfaces *EF* and *E'F'*:

$$T_z(r,\theta)\big|_{EF} = e^{j2\pi/N_{ss}} T_z(r,\theta-2\pi/N_{ss})\big|_{E'F'} \tag{7.21}$$

where N_{ss} is the number of stator slots. The eddy current loss density induced by B_z is

$$p_{c,\perp} = \frac{1}{2k_{lam}\sigma}\left\|\nabla\times(T_z\mathbf{a_z})\right\|^2 = \frac{1}{2k_{lam}\sigma}\left[\left(\frac{\partial T_z}{\partial r}\right)^2+\left(\frac{1}{r}\frac{\partial T_z}{\partial\theta}\right)^2\right]. \tag{7.22}$$

In finger plates, the eddy current loss density caused by axial/radial fluxes

$$p_{c,r(z)} \approx \sigma\left(\pi f_1 D_f B_{r(z)}\right)^2 \big/ 6 \tag{7.23}$$

where D_f is the peripheral thickness of a finger plate. The component induced by peripheral flux is gained in a post-processing on a *radial-axial* cross-sectional plane based on the following equations:

$$\begin{cases} \dfrac{1}{r}\dfrac{\partial}{\partial r}\left(r\dfrac{\partial T_\theta}{\partial r}\right)+\dfrac{\partial^2 T_\theta}{\partial z^2} = j(2\pi f_1)\sigma(\mu T_z + B_\theta) \\ p_{c,\theta} = \dfrac{1}{2\sigma}\left\|\nabla\times(T_\theta\mathbf{a}_\theta)\right\|^2 = \dfrac{1}{2\sigma}\left[\left(\dfrac{\partial T_\theta}{\partial r}\right)^2+\left(\dfrac{\partial T_\theta}{\partial z}\right)^2\right] \end{cases} \tag{7.24}$$

7.2.3 Simulation Results and Validation

The 3D time-domain FEA discussed in Chapters 5 and 6 is used as the benchmark to evaluate the effectiveness of the proposed fast-solving quasi-3D-formulation-based method. The full 3D FEA is validated by substituting the predicted loss density data into a 3D thermal FEA to solve the temperature distribution and comparing the calculated and measured temperatures. The details of the validation for the 3D FEAs are presented in section 5.6.

In this section, the results are based on the rated condition with a 0.85 lagging power factor. The distributions of the cross-slot flux are presented in Figure 7.9. The radial distribution of the peak B_z on the 1st packet is shown in Figure 7.10. The B_z in the leading-edge half tooth is higher than in the lagging-edge half because of the cross-slot flux and the conformal mappings described in section 7.2.1 can accurately capture its behavior. Good agreement is also achieved between the results of the eddy current loss distributions in stator end packets predicted by 3D FEAs and the proposed method, as demonstrated in Figure 7.11. Regarding the field and loss distributions in the finger plates, Figure 7.12 illustrates the eddy current loss density estimated by the proposed method and 3D FEAs, and Figure 7.13 shows that the peripheral flux distribution in finger plates can be precisely predicted by the conformal mapping method in section 7.2.1.

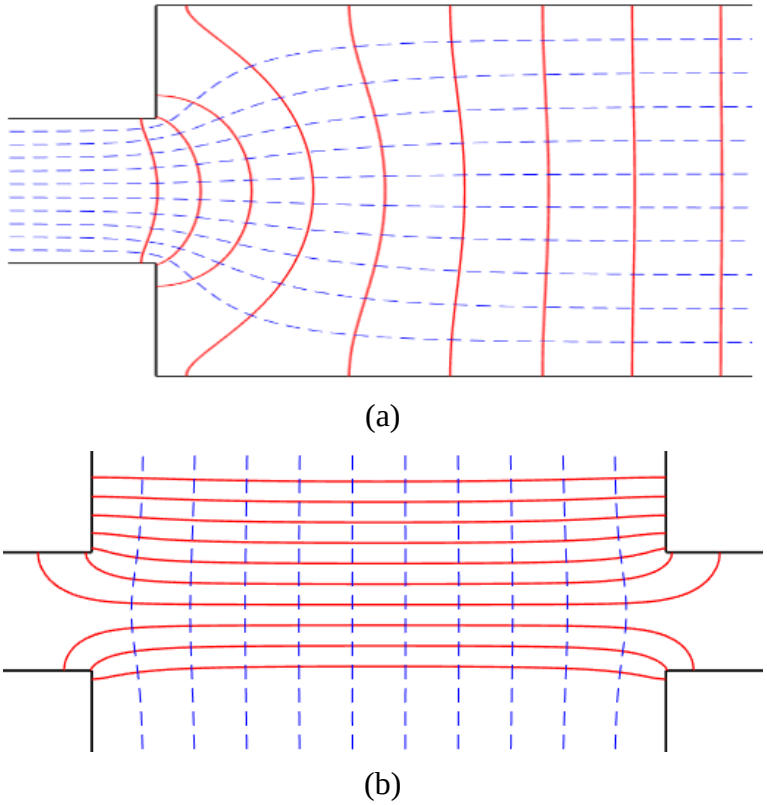

(a)

(b)

Figure 7.9 Flux (red) and equipotential (blue dashed) lines of the *Z* plane in (a) Figure 7.6; (b) Figure 7.7.

Since the quasi-3D simulation in section 7.1 and the post-processing in section 7.2.2 are based on 2D coordinates, the computational complexity is significantly reduced compared to 3D FEAs. It only takes a few minutes to perform a simulation with the proposed method, while the execution time of 3D FEAs can be many hours or even days.

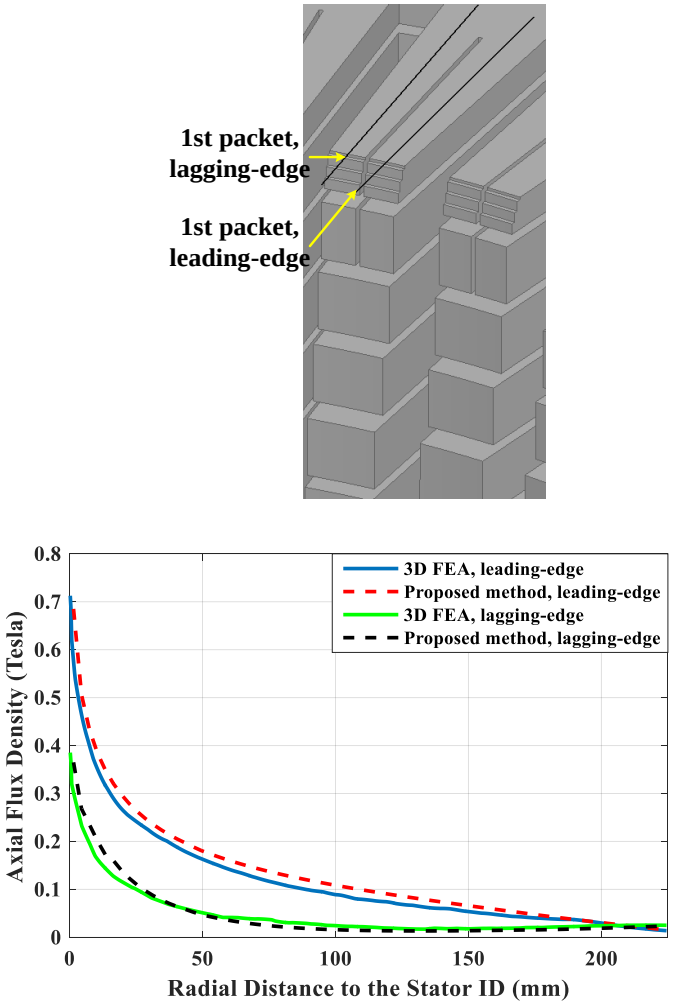

Figure 7.10 Peak axial flux density in the leading- and lagging-edge halves of a tooth in the 1st packet at rated condition.

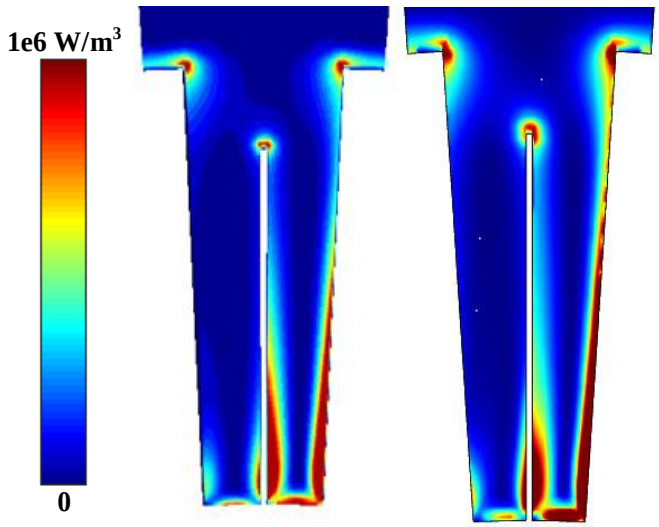

(a) (b)

Figure 7.11 Axial-flux-induced eddy current loss density of the 1st packet predicted by (a) the proposed method; (b) 3D FEA.

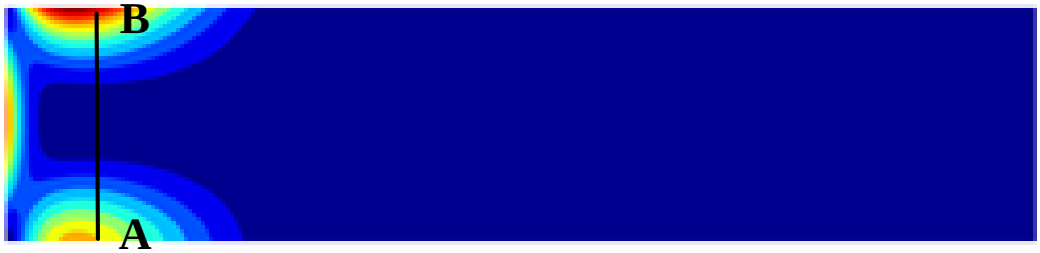

(a)

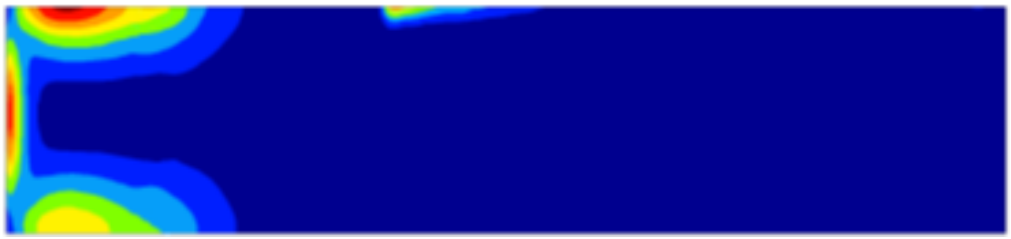

(b)

Figure 7.12 Loss density on a *radial-axial* plane of finger plates predicted by (a) the proposed method; (b) 3D FEA.

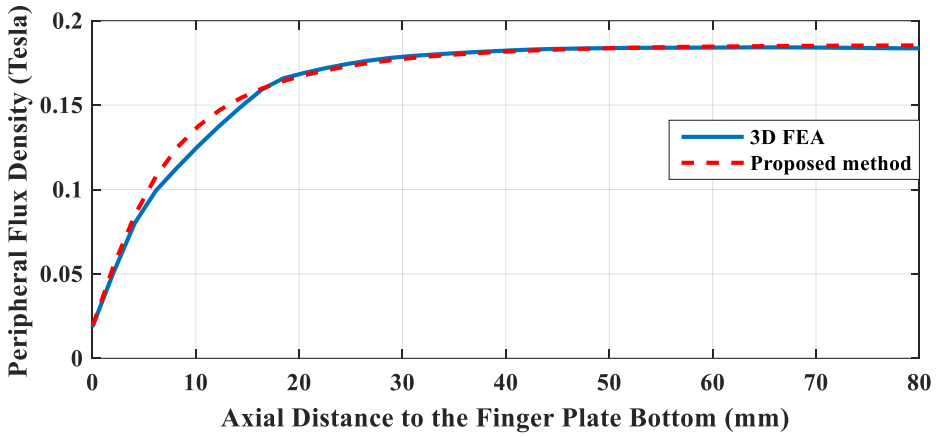

Figure 7.13 Peak peripheral flux density in a finger plate along the line *AB* in Fig. 11 at rated condition.

7.3 Calculation of the Magnetic Field and Loss in the Press Plate by SIBC

7.3.1 Formulation of the SIBC in the Quasi-3D FDM

This section presents the mathematical formulation of SIBC and the relevant implementation in the quasi-3D FD scheme and an iterative approach that compensates the impacts of the material nonlinearity and near corner effects.

SIBCs based on the assumption that the skin depth is less than the smallest feature size of the conductor can be applied to reduce the computational load [202]. SIBCs assume that the electromagnetic field in the conductor's skin layer can be described as an exponentially damped plane wave propagating through the conductor normal to its surface. Since the press plate inner radius is far larger than the skin depth, the curvature effect on the cylindrical surface impedance is neglected. In SIBCs, the relationship between the tangential electric and magnetic fields on the conductor surfaces is [202]

$$\mathbf{n}\times\mathbf{E} = Z_s\mathbf{n}\times(\mathbf{n}\times\mathbf{H}) \tag{7.25}$$

where **n** is the unit vector normal to the surface and Z_s is the surface impedance $Z_s = \sqrt{j\omega\mu_c / \sigma}$. Define t_1 and t_2 to be the two directions tangential to the surface and orthogonal to each other, then on the conductor surface

$$E_{t_2} = -Z_s H_{t_1}, E_{t_1} = Z_s H_{t_2}. \tag{7.26}$$

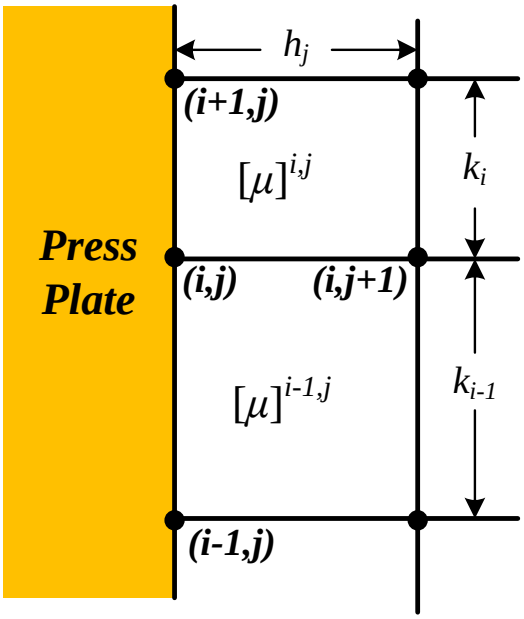

Figure 7.14 Quasi-3D FD grid on the axially outer surface of the press plate.

According to the boundary condition between different materials:

$$\mu_c H_{nc} = \mu_0 H_{n0} \tag{7.27}$$

where μ_c and μ_0 are the permeability of the conductor and the dielectric medium (air) respectively, and H_{nc} and H_{n0} are the component of **H** normal to the surface in the conductor and dielectric medium respectively. In this case, Faraday's law of induction $\nabla \times \mathbf{E} = -j\omega\mu\mathbf{H}$ can therefore be expressed as

$$\frac{\partial E_{t_2}}{\partial t_1} - \frac{\partial E_{t_1}}{\partial t_2} = -j\omega\mu_c H_{nc} = j\omega\mu_0 \frac{\partial \varphi}{\partial n}. \tag{7.28}$$

Substituting (7.26) into (7.28) yields

$$Z_s\left(\frac{\partial^2\varphi}{\partial {t_1}^2}+\frac{\partial^2\varphi}{\partial {t_2}^2}\right)=j\omega\mu_0\frac{\partial\varphi}{\partial n}. \tag{7.29}$$

Taking a node (*i,j*) on the axially outer surface of the press plate in Figure 7.1 of the press plate as an example shown in Figure 7.14, the quasi-3D FD formulation of (7.29) is

$$B_{i,j}\varphi_{i-1,j}+T_{i,j}\varphi_{i+1,j}+R_{i,j}\varphi_{i,j+1}-D_{i,j}=0 \tag{7.30}$$

where

$$B_{i,j}=\frac{Z_s h_j}{k_{i-1}}\left(1-\frac{k_{i-1}}{2r_i}\right),\ T_{i,j}=\frac{Z_s h_j}{k_i}\left(1+\frac{k_i}{2r_i}\right)$$

$$R_{i,j}=\frac{1}{2}j\omega\left({\mu_z}^{i-1,j}k_{i-1}+{\mu_z}^{i,j}k_i\right),\ D_{i,j}=B_{i,j}+T_{i,j}+R_{i,j}+\frac{p^2}{2{r_i}^2}\left(Z_s k_{i-1}h_j+Z_s k_i h_j\right)$$

7.3.2 Consideration of Nonlinear Material Property and Near Corner Effects

Since the surface impedance is related to the permeability of the conductor, the material nonlinearity has a significant impact on the magnetic field. The effective permeability used for harmonic analyses based on the assumption of identical stored energy is [1]

$$\mu_c=\frac{2}{T}\cdot\frac{\int_0^T H_m\sin(\omega t)B\left[H_m\sin(\omega t)\right]dt}{{H_m}^2}. \tag{7.31}$$

The procedure is then to find the effective permeability of each peak value of sinusoidal **H**. Note that the tangential components of **H** are continuous at the surface and

the normal component of **H** in the conductor can be found by $H_{nc} = \mu_0 H_{n0} / \mu_c$. Generally, for a magnetic material $\mu_c >> \mu_0$ and the normal component of magnetic field is instantly eliminated by the eddy current effect as it penetrates the conductor, so H_{nc} is negligible when updating μ_c on the conductor surface in the iterative process.

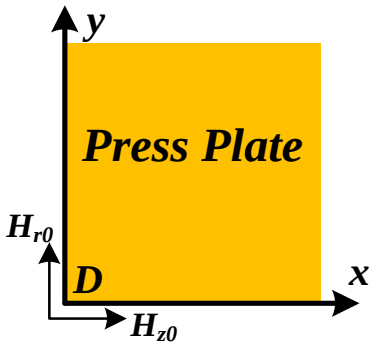

Figure 7.15 Transverse magnetic fields near the corner edge between the axially inner surface and radially inner surface of the press plate.

After the surface impedance Z_s is determined, the eddy current loss per square meter is obtained based on the Poynting [1] vector as follows:

$$P = -\mathrm{Re}\frac{1}{2}\left(\mathbf{E_t} \times \mathbf{H_t}^*\right) = \sqrt{\frac{\omega\mu_c}{8\sigma}}\left(\mathbf{H_t} \cdot \mathbf{H_t}^*\right) = \sqrt{\frac{\omega\mu_c}{8\sigma}}\left(\hat{H}_{t_1}{}^2 + \hat{H}_{t_2}{}^2\right). \tag{7.32}$$

On the other hand, the classical model of SIBC is only valid for an infinite conductor half plane and this limitation can introduce significant errors when the conductor surface has sharp corners. To reduce the error, a compensation method is used to modify the surface impedance near corners [203], [204]. For example, on the radially inner surface of the press plate in Figure 7.1, when the location is near the corner edge shown in Figure 7.15, for the transverse magnetic field H_z, the modified surface impedance is

$$Z_{s,\theta z} = \frac{-E_\theta}{H_z}\Big|_S = Z_s\left(1 - \frac{H_{r0}}{H_{z0}} e^{-\sqrt{j\omega\mu_c\sigma}x}\right). \tag{7.33}$$

The following empirical expression proposed in [203] is utilized to determine the near-corner surface impedance for the parallel component of the magnetic field H_θ:

$$Z_{s,z\theta} = \frac{E_z}{H_\theta}\Big|_S = \frac{1}{\sigma\delta}\left[\left(1 - e^{-\frac{1.07x}{\delta}}\cos\frac{0.76x}{\delta}\right) + j\left(1 - 2e^{-\frac{2.8x}{\delta}}\cos\frac{-1.55x}{\delta}\right)\right] \qquad (7.34)$$

The determination of the surface permeability for nonlinear conductors and obtaining the information of H_{r0} and H_{z0} in (7.33) require iterative procedures, which can be paralleled to the nonlinear iterations for determining the permeability of the stator core. Note that the expression of $\mathbf{E_t}$ in (7.32) should be modified correspondingly near corners according to the local surface impedance.

7.3.3 Simulation Results and Validation

The 3D time-domain FEA is used as the benchmark to evaluate the effectiveness of the proposed SIBC in the quasi-3D FDM. Dense meshes are set up in the 3D FEA beneath the surfaces of the press plate to capture the eddy current distribution. The full 3D FEA is validated by substituting the predicted loss density data into a 3D thermal FEA to solve the temperature distribution and comparing the calculated temperatures with measured results. The details of the 3D EM and thermal FEAs and their validation are presented in Chapter 5. Three thermocouples are mounted on the top surface at the locations shown in Figure 5.18 and the comparison in Table 5.3 shows agreement between the results of FEAs and physical measurements. The press plate is made of magnetic steel in this case.

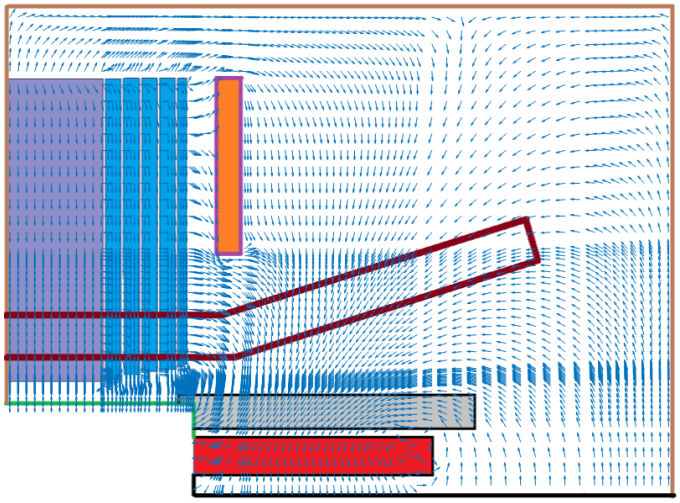

Figure 7.16 Radial-axial vectors of the magnetic field in the generator end region in the *d*-axis plane in case 1.

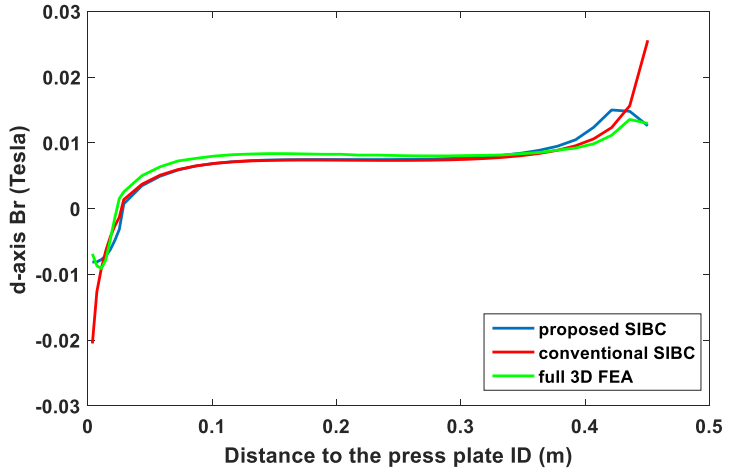

(a)

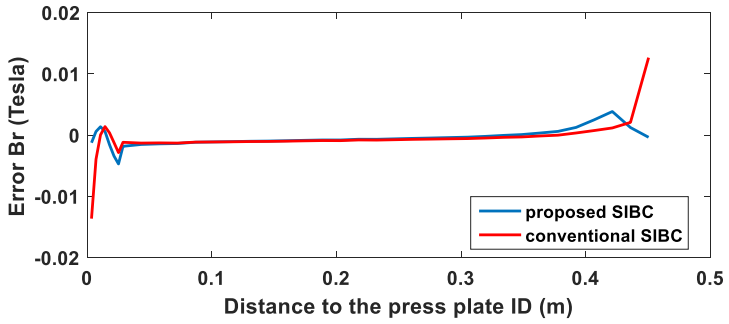

(b)

Figure 7.17 (a) Radial flux density in the *d*-axis plane on the axially outer surface in case 1; (b) comparison of the errors of the radial flux densities predicted by the proposed SIBC and the conventional SIBC.

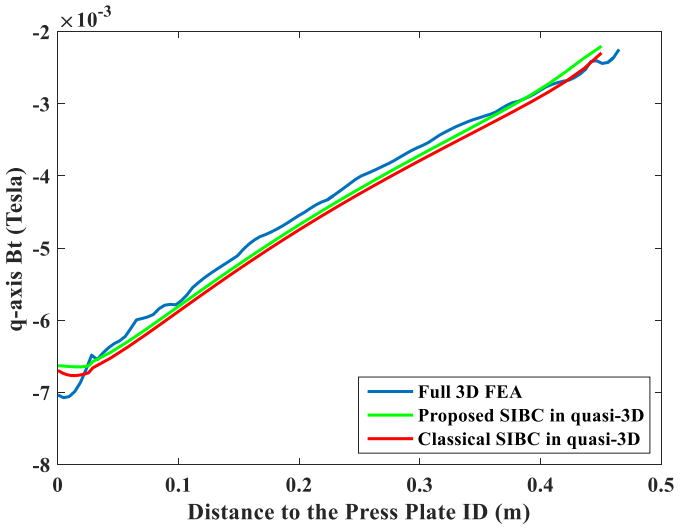

Figure 7.18 Tangential flux density in the *q*-axis plane on the axially outer surface in case 1.

Two simulations are performed with both full 3D FEAs and quasi-3D FDMs: the 110% open-circuit condition with an aluminum (case 1) and a magnetic steel (case 2, original case) press plate respectively. Figure 7.16 shows the flux density vectors in the *d*-axis *radial-axial* cross-sectional plane in the end region of case 1. Figure 7.17 and Figure 7.18 illustrate the radial flux density in the *d*-axis plane and tangential flux density in the *q*-axis plane on the axially outer surface of the press plate in Figure 7.1. The results of the proposed SIBC show good agreement with the results of the full 3D FEA, while the conventional SIBC method leads to a significant error in the result of radial flux density (transverse flux) near the corners as indicated in Figure 7.17(b). Figure 7.19 shows the agreement between the results of the radial distribution of the surface eddy current loss densities (in W/m^2) generated by the proposed SIBC and full 3D FEA for case 1. There remain small discrepancies between the loss densities calculated by the proposed SIBC and the 3D FEA in a tiny region closest to the corners as demonstrated in Figure 7.19 due to the fact that in this region, the eddy current distribution is also dependent on the flux impinging the adjacent surfaces (the inner surface or the outer surface) but SIBC can only represent the impact of the flux penetrating into the same surface. Regarding case 2, Figure

7.20 shows that the proposed SIBC can effectively reduce the error caused by the nonlinear B-H curves of the steel with nonlinear iterations, while the conventional SIBC may lead to an unaccepted error in the region with high saturation. In this case study, the relative permeability of the magnetic steel is assumed to be μ_r=500 when applying the classical SIBCs.

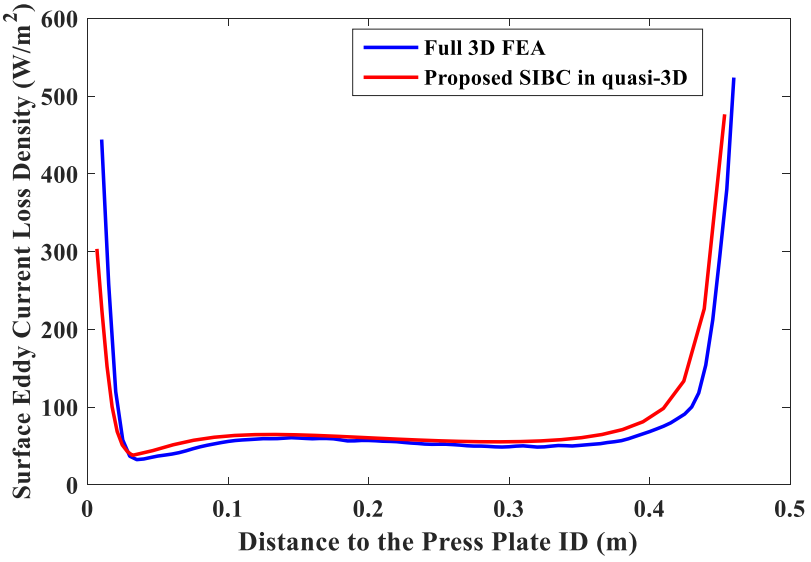

Figure 7.19 Surface eddy current loss density on the axially outer surface in case 1.

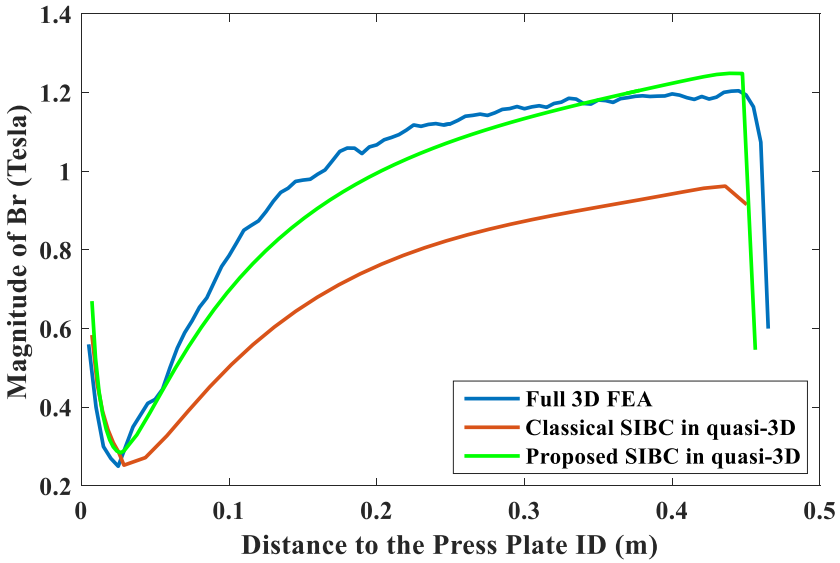

Figure 7.20 Magnitude of the fundamental component of radial flux density on the axially outer surface in case 2.

It takes hours or even days to perform a single benchmark full 3D FEA simulation. However, the computing time of the proposed quasi-3D FDM is merely 10~30 seconds, depending on the operating condition and the complexity of the definition on the boundary conditions and excitations. This significantly reduced computional effort and the agreement between the results of the proposed SIBC and fully 3D FEAs prove that the approach proposed in this section is an effective tool for the evaluation of design candidates at the initial stage.

7.4 Calculation of the Magnetic Field and Loss in the Stator Copper Strands

Estimating the loss and monitoring the temperature of stator windings is crucial for the reliability and safe operation of electric machine systems [205]-[208]. This section presents a computationally efficient method to analyze the eddy current loss of the stator winding strands in the end stator region of large synchronous generators. It is necessary to estimate and reduce the stator coil losses, including the circulating current losses and eddy current losses at the design stage for large synchronous generators to avoid the overheating of stator windings. Generally, stator windings are composed of numerous strands that are connected in the end region. Circulating currents occur due to the disparities of electromagnetic forces between strands and generate extra loss and heat. Various methods have been proposed to predict the circulating currents and it is popular to utilize Roebel transposition to decrease the associated losses [195], [196], [209].

There are essentially three sources that contributes to the eddy current losses in stator coils. The first component is the skin effect that can be mitigated by properly selecting the size of the strands. The second source of eddy currents is the airgap flux entering the slots caused by the difference between the magnetic scalar potentials on the stator and rotor surfaces. The third source is the slot leakage flux generated by the local strand currents (proximity effect). Numerical methods, e.g., finite element/difference

analyses, are proposed to estimate the eddy current losses of stator coils [210], [211]. They provide trustworthy results with a precise modelling of the geometries, but are unsuitable for the initial design that requires the evaluation of numbers of design candidates due to the time-consuming computations. Analytical formulations, including the 1-D single-slot models [212], 2-D single-slot and machine models [213], are reported to be efficient and provide insights into the nature of the eddy current distributions in stator strands. However, the existing methods assume that the machine structures and therefore the strand eddy current distributions maintain constant in the axial direction. In the end region of a large generator as depicted in Figure 5.5, the inner radii of the stator packets gradually increase with a stepped shape to prolong the paths of the end fringing axial flux produced by the end windings and reduce the resultant in-plane eddy currents in lamination. Consequently, at the slot openings, the radial airgap flux impinging the copper strands strengthens while the slot leakage flux becomes weaker. The existing 1-D/2-D models without considering the stepped geometry are insufficient for the analysis of the axial variation of the strand eddy current distributions and significant temperature rise in this region.

In this section, the 3-D distributions of the strand eddy losses in the stepped region are solved with all three components incorporated, i.e., the skin effect, airgap flux and proximity effect related copper losses. The quasi-3D formulation described in section 7.1 that maps the end structures onto a *radial-axial* plane is adopted to calculate the airgap flux distribution with an accurate modelling of the stepped stator, material nonlinearities and the end fringing effect. To compensate the inherent limitation of quasi-3D methods that the slot/tooth geometries are not explicitly modeled, the conformal mapping method is adopted and the airgap flux impinging each strand in a slot is further derived. In addition, the transverse cross-slot leakage flux distributions with different slot/coil configurations are obtained by applying the subdomain model in a single-slot region. The proposed method does not require a 3-D numerical modelling of the complex geometries of the generator

end region and stator strands, thus it is computationally efficient and can be used for the initial design of a large generator. The benchmark 3D time-domain FEAs and physical measurements are used to validate the proposed fast calculation method.

7.4.1 Conformal Mapping Method for the Calculation of the Airgap Flux Distributions

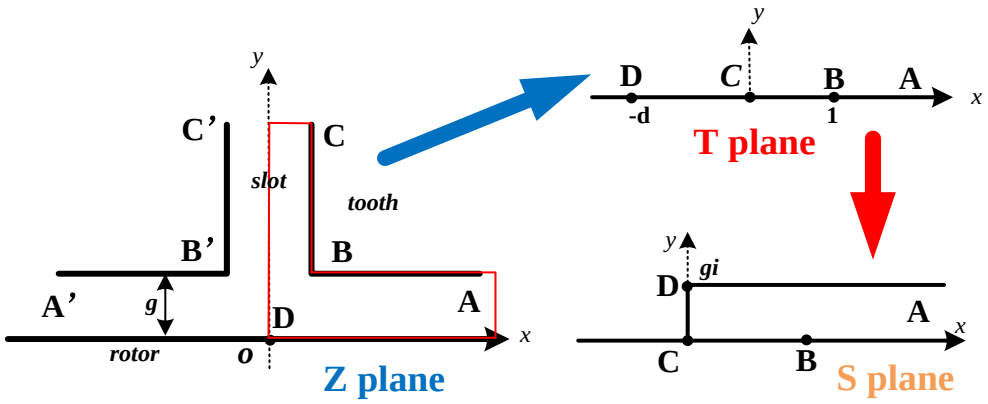

Figure 7.21 Sequential conformal mappings for the airgap-slot region.

The quasi-3D formulation in section 7.1 is used to estimate the radial end fringing airgap flux impinging the end core packets. However, it is insufficient to obtain an accurate solution of the airgap flux distributions in the stator slots by using the quasi-3D method due to the absence of an explicit slot/tooth modelling. A post-processing with sequential conformal mappings for a slot-airgap region is performed to compensate this limitation, as demonstrated in Figure 7.21. Since the impinging flux cannot penetrate deep axially through the active length of the stator coils due to the eddy current reaction, only the radial and peripheral airgap flux densities are calculated. In Figure 7.21, the *Z* plane is the original geometry of a slot pitch. Define the magnetic scalar potential on the rotor (y=0) and stator surfaces (*ABC* and *A'B'C'*) to be Ω_0 and zero respectively, where Ω_0 is the difference between the complex potentials at the rotor and stator surfaces. Due to the symmetry of the magnetic field, only the right half slot encompassed by red lines in the *Z* plane is analyzed. The geometry of the *Z* plane is mapped to the *T* plane of the upper half space with the following Schwarz-Christoffel transformation [56]:

$$\frac{dz}{dt} = \frac{g}{\pi t}\sqrt{\frac{t-1}{t+d}}, t = \frac{2g}{\pi}\left(\frac{1}{\sqrt{d}}\tan^{-1}\frac{p}{\sqrt{d}} + \frac{1}{2}\ln\frac{1+p}{1-p}\right) \tag{7.35}$$

where

$$d = \left(2g/b_s\right)^2,\ p = \sqrt{\frac{t+d}{t-1}}$$

and g is the radial airgap depth, and b_s is the slot width. The T plane is then mapped to a slotless infinite strip with the same depth g in the S plane by the Schwarz-Christoffel transformation:

$$\frac{ds}{dt} = -\frac{g}{\pi}\sqrt{\frac{1}{t\left(t+d\right)}}. \tag{7.36}$$

The relationship between the magnetic fields in the Z and S planes is [180]:

$$\mathbf{B_z} = \mathbf{B_s}\left(\frac{ds}{dz}\right)^* = \mathbf{B_s}\left(\frac{ds}{dt}\cdot\frac{dt}{dz}\right)^* = \mathbf{B_s}\left(-\sqrt{\frac{t}{t-1}}\right)^*. \tag{7.37}$$

The airgap flux lines within a slot pitch of the Z plane are presented in Figure 7.22, where the magnetic field in the left half of the airgap/slot is calculated by utilizing the symmetry of the field in this region. Figure 7.22 shows that significant airgap flux exists in the strands around the slot opening, but the flux density attenuates rapidly as it propagates into the slot because of the parallel flux paths in the adjacent teeth.

The end fringing effect is not included in the calulation above. To utilize the advantages of both the quasi-3D and conformal mapping methods, for the airgap region ($y \le g$) of the Z plane, in (7.37) $\mathbf{B_s}$ of the S plane is replaced by the magnetic field $\mathbf{B_q}$ at the same location obtained from the quasi-3D simulation, while for the slot region ($y > g$), the value $\mathbf{B_s}$ in (7.37) is simply substituted by the $\mathbf{B_q}$ on the stator surface predicted by the

quasi-3D method. Because the inner diameters of the end core packets are different as shown in Figure 5.5 and Figure 7.1, the effective airgap depth *g* in Figure 7.21 also varies axially. Therefore, the conformal mappings should be performed for each individual *radial-peripheral* cross-section in the stepped-stator region.

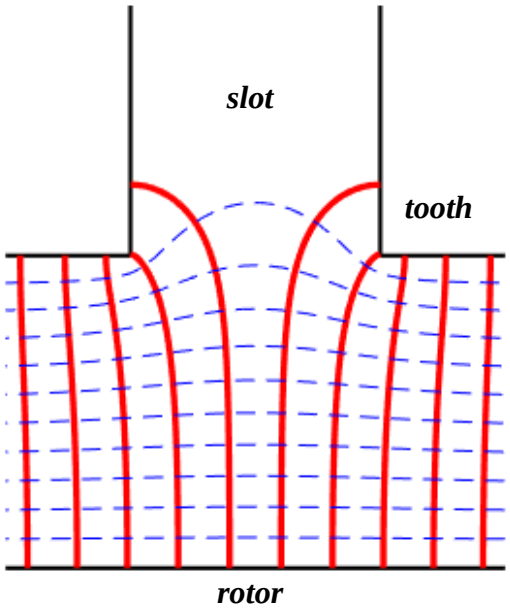

Figure 7.22 Flux (red solid) and equipotential (blue dashed) lines of the *Z*-plane solution domain in Figure 7.21.

7.4.2 Calculation of the Cross-slot Leakage Flux Distribution in End Stator Slots

The subdomain field model is adopted to calculate the slot leakage field produced by stator coils in a single slot pitch. The basic descriptions of the subdomain field method appear in [214]. The analytical model is based on the following assumptions:

1) The stator and rotor are infinitely permeable;
2) The stator/rotor surfaces are subject to ideal iron boundaries with orthogonal **B** vectors;
3) The impact of circulating currents in the end region is ignored and the current density is uniformly distributed in conductor area;
4) The eddy current reaction on magnetic field is neglected;

5) The axial variation of the slot leakage field is not comprehensively considered, and 2D analysis is performed for each *radial-peripheral* cross-section.

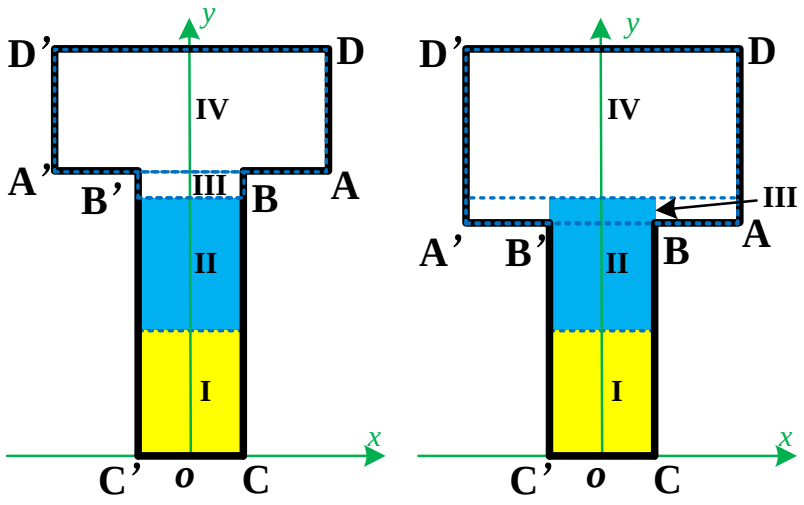

Figure 7.23 Solution domain with the slot configuration of (a) the stator main body; (b) end stepped packets.

There are two types of slot/coil configuration analyzed in this section. Figure 7.23 presents the single-slot solution region with double-layer distributed windings with all subdomains. In the stator main body, the stator inner radius is smaller than that of the top winding strand as shown in Figure 7.23(a), but the opposite scenario of Figure 7.23(b) appears as the stator inner radius becomes larger in the end stepped region.

The magnetic field is formulated by the Poisson equation of magnetic vector potential **A**, and only the *z*-component is considered in the 2D field. Due to the neglect of eddy current reaction and circulating currents according to assumptions 3) and 4), the governing equation is

$$\frac{\partial^2 A_z}{\partial x^2} + \frac{\partial^2 A_z}{\partial y^2} = -\mu_0 J \tag{7.38}$$

where μ_0 is the air/copper permeability and J is the current density. The boundary conditions of A_z of both cases in Figure 7.23 are

1) The rotor surface *DD'* and the stator surface *ABCC'B'A'* are subject to ideal iron boundary condition: $\partial A_z / \partial n = 0$, where *n* is the normal direction.
2) The magnetic field is parallel to the lines *AD* and *A'D'*: $\partial A_z / \partial y = 0$.

The solution of A_Z in (7.38) is the combination of a particular solution and a homogeneous solution. The particular solution is determined to comply with the Poisson equation associated with the source current density, while the homogeneous solution is selected to satisfy the boundary conditions. The homogeneous solution can be expressed in the following form:

$$\begin{aligned} A_{zh}(x,y) &= A_0 xy + B_0 x + C_0 y + D_0 \\ &+ \sum_{n=1}^{\infty} \left[\left(A_n \sinh k_n y + B_n \sinh k_n y \right) \cdot \cos k_n x + \left(C_n \sinh k_n y + D_n \sinh k_n y \right) \cdot \sin k_n x \right]. \end{aligned} \tag{7.39}$$

Due to the symmetry of the magnetic field distribution in two halves of the slot $B_x(x,y) = B_x(-x,y)$, $B_y(x,y) = -B_y(-x,y)$, and in all subdomains C_n=D_n=0. For the case Figure 7.23(a), in the subdomain I, it can be inferred from the boundary conditions $\left(\partial A_{z1}/\partial y\right)\big|_{CC'} = 0, \left(\partial A_{z1}/\partial x\right)\big|_{BC,B'C'} = 0$ that $A_{10} = B_{10} = C_{10} = 0$, $B_{1n} = 0, k_{1n} = k_n = n\pi / b_s$, $n = \text{even}$. Define D_{10} to be zero, and a feasible solution of A_{z1} is:

$$\begin{aligned} A_{z1} &= A_{zp1} + A_{zh1} = -\frac{1}{2}\mu_0 J_I y^2 + \sum_{neven} A_{1n} \cos k_n x \cosh k_n y \\ \Rightarrow B_{x1} &= \partial A_{z1}/\partial y = -\mu_0 J_I y + \sum_{neven} k_n A_{1n} \cos k_n x \sinh k_n y, \\ B_{y1} &= -\partial A_{z1}/\partial x = \sum_{neven} k_n A_{1n} \sin k_n x \cosh k_n y \end{aligned} \tag{7.40}$$

where J_I is the current density of the bottom-layer winding in subdomain I.

For the subdomain II, according to the boundary condition $\left(\partial A_{z2}/\partial x\right)\big|_{BC,B'C'}=0$, the coefficients $A_{20}=B_{20}=0$ and $k_{2n}=k_{1n}=k_n$. Therefore, the distributions of A_{z2} and the magnetic field in subdomain II can be expressed as

$$\begin{aligned}
A_{z2} &= A_{zp2}+A_{zh2}=-\frac{1}{2}\mu_0 J_{II}\left(y-h_1\right)^2+C_{20}y+D_{20}\\
&\quad+\sum_{neven}\left(A_{2n}\cosh k_n y+B_{2n}\sinh k_n y\right)\cos k_n x \;\Rightarrow\\
B_{x2} &= -\mu_0 J_{II}\left(y-h_1\right)+C_{20}+\sum_{neven}k_n\left(A_{2n}\sinh k_n y+B_{2n}\cosh k_n y\right)\cos k_n x\\
B_{y2} &= \sum_{neven}k_n\left(A_{2n}\cosh k_n y+B_{2n}\sinh k_n y\right)\sin k_n x
\end{aligned} \tag{7.41}$$

where J_{II} is the current density of the top-layer winding in subdomain II, and h_1 is the height of the bottom-layer winding.

The boundary conditions and thus the homogeneous solution of the subdomain III have the same forms as the subdomain II. The particular solution does not exist in subdomain III due to the absence of source current. Therefore, A_{z3} is as follows:

$$\begin{aligned}
&A_{z3}=A_{zh3}=C_{30}y+D_{30}+\sum_{neven}\left(A_{3n}\cosh k_n y+B_{3n}\sinh k_n y\right)\cos k_n x\\
&\Rightarrow B_{x3}=C_{30}+\sum_{neven}k_n\left(A_{3n}\sinh k_n y+B_{3n}\cosh k_n y\right)\cos k_n x\\
&B_{y3}=\sum_{neven}k_n\left(A_{3n}\cosh k_n y+B_{3n}\sinh k_n y\right)\sin k_n x.
\end{aligned} \tag{7.42}$$

The particular solution of the subdomain IV is also zero. Based on the boundary condition $\left(\partial A_{z4}/\partial y\right)\big|_{AD,A'D',DD'}=0$, the coefficients of the homogeneous solution of A_{z2} satisfy $A_{40}=C_{40}=0$, $k_{4n}=m_n=n\pi/b_a$, $n=\text{odd}$, where b_a is the slot pitch in the airgap. The symmetry condition $B_y\left(x,y\right)=-B_y\left(-x,y\right)$ implies $B_{40}=0$. Thus, substituting these conditions into (7.39) yields:

$$
\begin{aligned}
&A_{z4} = A_{zh4} = D_{40} + \sum_{nodd} \left(A_{4n} \cosh m_n y + B_{4n} \sinh m_n y \right) \cos m_n x \\
&\Rightarrow B_{x4} = \sum_{nodd} m_n \left(A_{4n} \sinh m_n y + B_{4n} \cosh m_n y \right) \cos m_n x \\
&\quad B_{y4} = \sum_{nodd} m_n \left(A_{4n} \cosh m_n y + B_{4n} \sinh m_n y \right) \sin m_n x.
\end{aligned} \tag{7.43}
$$

The coefficients A_{1n}~A_{4n}, B_{1n}~B_{4n}, C_{20} and C_{30} should be determined to predict the slot leakage field. The continuity of magnetic field, which indicates that the values of B_x and B_y calculated in two adjacent subdomains should be equal on the boundary between them, is used to determine the coefficients [214]. Comparing the fields of subdomains I and II on $y=h_1$:

$$
\begin{cases}
A_{1n} \sinh k_n h_1 = A_{2n} \sinh k_n h_1 + B_{2n} \cosh k_n h_1 \\
A_{1n} \cosh k_n h_1 = A_{2n} \cosh k_n h_1 + B_{2n} \sinh k_n h_1 \ (n = \text{even}). \\
C_{20} = -\mu_0 J_I h_1
\end{cases} \tag{7.44}
$$

The following relations can be obtained based on the conditions on the boundary $y=h_2$ between the subdomains II and III:

$$
\begin{cases}
A_{2n} = A_{3n},\ B_{2n} = B_{3n},\ (n = \text{even}) \\
C_{30} = -\mu_0 J_I h_1 - \mu_0 J_{II} \left(h_2 - h_1 \right)
\end{cases}. \tag{7.45}
$$

The relations on the boundary $y=h_3$ between the subdomains III and IV is complex due to the difference between the x-axis cycles of A_{z3} and A_{z4} in (7.42), (7.43). Combining $B_{x3}|_{BB'}$ and the boundary condition $B_x|_{AB,A'B'}=0$ yields the Fourier series:

$$
\begin{aligned}
&B_{x3}\big|_{AA'} = \frac{2}{b_a} \sum_{nodd} \left(\int_0^{b_s/2} B_{x3}\big|_{AA'} \cos m_n x dx \right) \cos m_n x \\
&= \sum_{nodd} \left[\frac{4C_{30}}{n\pi} - \sum_{ieven} \left(A_{3i} \sinh k_i h_3 + B_{3i} \cosh k_i h_3 \right) \cdot \frac{2nib_s}{i^2 {b_a}^2 - n^2 {b_s}^2} \cos\left(\frac{i\pi}{2} \right) \right] \sin\left(\frac{n\pi b_s}{2b_a} \right) \cos m_n x.
\end{aligned} \tag{7.46}
$$

Similarly, $B_{y4}|_{BB'}$ is reorganized into the following form of Fourier series:

$$\begin{aligned} B_{y4}\Big|_{BB'} &= \frac{2}{b_s}\sum_{neven}\left(\int_0^{b_s/2} B_{y4}\Big|_{BB'}\sin k_n x dx\right)\sin k_n x \\ &= \sum_{neven}\left[\sum_{iodd}\left(A_{4i}\cosh m_i h_3 + B_{4i}\sinh m_i h_3\right)\cdot\frac{2nib_a}{i^2 b_s{}^2 - n^2 b_a{}^2}\sin\left(\frac{i\pi b_s}{2b_a}\right)\right]\cos\left(\frac{n\pi}{2}\right)\sin k_n x. \end{aligned} \tag{7.47}$$

Combining (7.42), (7.43), (7.46) and (7.47) leads to the relations below:

$$\begin{cases} m_n\left(A_{4n}\sinh m_n h_3 + B_{4n}\cosh m_n h_3\right) \\ \quad = \left[\dfrac{4C_{30}}{n\pi} - \sum_{ieven}\left(A_{3i}\sinh k_i h_3 + B_{3i}\cosh k_i h_3\right)\cdot\dfrac{2nib_s}{i^2 b_a{}^2 - n^2 b_s{}^2}\cos\left(\dfrac{i\pi}{2}\right)\right]\sin\left(\dfrac{n\pi b_s}{2b_a}\right),\ n = \text{odd} \\ k_n\left(A_{3n}\cosh k_n h_3 + B_{3n}\sinh k_n h_3\right) \\ \quad = \left[\sum_{iodd}\left(A_{4i}\cosh m_i h_3 + B_{4i}\sinh m_i h_3\right)\cdot\dfrac{2nib_a}{i^2 b_s{}^2 - n^2 b_a{}^2}\sin\left(\dfrac{i\pi b_s}{2b_a}\right)\right]\cos\left(\dfrac{n\pi}{2}\right),\ n = \text{even} \end{cases}. \tag{7.48}$$

It can be obtained by applying the boundary condition $B_{x4}|_{DD'}=0$ on the edge $y=h_4$ to (7.43) that:

$$A_{4n}\sinh m_n h_4 + B_{4n}\cosh m_n h_4 = 0\ (n = \text{odd}). \tag{7.49}$$

The coefficients A_{1n}~A_{4n}, B_{1n}~B_{4n}, C_{20} and C_{30} can be obtained by solving the set of equations (7.44), (7.45), (7.48) and (7.49). The modelling for the case Figure 7.23(b) is conducted in a similar way.

7.4.3 Calculation of the Strand Loss Distributions in the Stepped-stator Region

The fundamental radial and peripheral components of the airgap and slot leakage flux densities are extracted and combined at the position of each strand. Accordingly, the average eddy current loss density of a rectangular strand can be obtained by:

$$P_e = \frac{\sigma\omega^2}{24}\left(\frac{3{B_r}^2a^2}{\xi_a}\cdot\frac{\sinh\xi_a-\sin\xi_a}{\cosh\xi_a-\cos\xi_a}+\frac{3{B_\theta}^2b^2}{\xi_b}\cdot\frac{\sinh\xi_b-\sin\xi_b}{\cosh\xi_b-\cos\xi_b}\right) \tag{7.50}$$

where

$$\xi_a = a\sqrt{\frac{\omega\mu\sigma}{2}},\ \xi_b = b\sqrt{\frac{\omega\mu\sigma}{2}}$$

where ω is the fundamental frequency, a and b are the width and height of a strand, and σ is the conductivity of copper. To include the loss due to skin effects, the approximate formula of AC resistivity is applied to modify the DC loss density [197]:

$$P_{ac} = \frac{J^2}{2\sigma}\cdot\frac{\rho_{ac}}{\rho_{dc}} = \frac{I^2}{2\sigma\left(abN_{st}\right)^2}\cdot\sqrt{1+\left(\frac{\kappa ab}{2\delta\left(a+b\right)}\right)^2},\ \delta = \sqrt{\frac{2}{\omega\mu\sigma}} \tag{7.51}$$

where ρ_{ac} and ρ_{dc} are the AC and DC resistivities, I is the winding current, N_{st} is the number of strands in a winding, and $\kappa \approx 1.2$. Finally, the average strand copper loss density is $P = P_e + P_{ac}$.

7.4.4 Simulation Results and Validation

The 3D transient electromagnetic FEA is used as the benchmark to evaluate the proposed efficient method. The 3D FEA is validated by substituting the predicted loss density distributions in all end components, including the copper loss density in all strands, into a 3D thermal FEA to solve the temperature distribution and comparing the results with measured data. The thermal conductivities of the stator and windings exhibit anisotropy

due to the insulation materials. The details of the 3D FEAs are presented in Chapters 5 and 6. The configuration of the stator coil strands in a slot is shown in Figure 5.12. There are two columns of strands, and the number of rows is M_1 and M_2 for the top and bottom winding respectively. There are thermocouples mounted on the 1st (top) strand of the top winding in the stepped-stator region. Results in section 5.6 show the agreement between the results of the 3D time-domain FEAs and measurements.

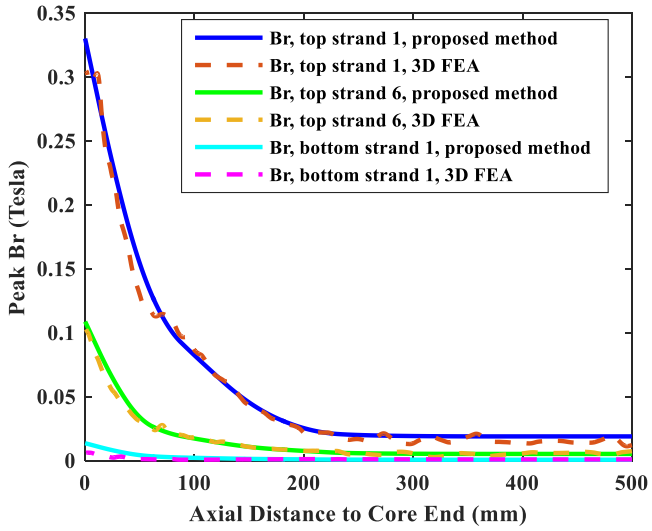

(a)

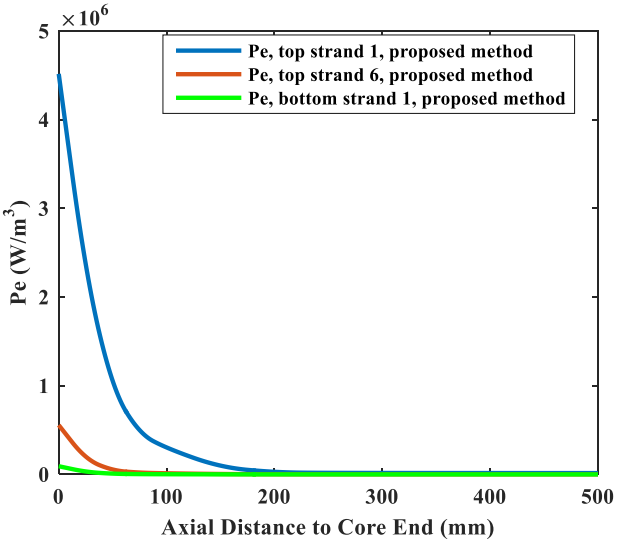

(b)

Figure 7.24 Axial distribution of (a) B_r; (b) P_e of 3 strands at the 110% open-circuit condition in the stepped-stator region.

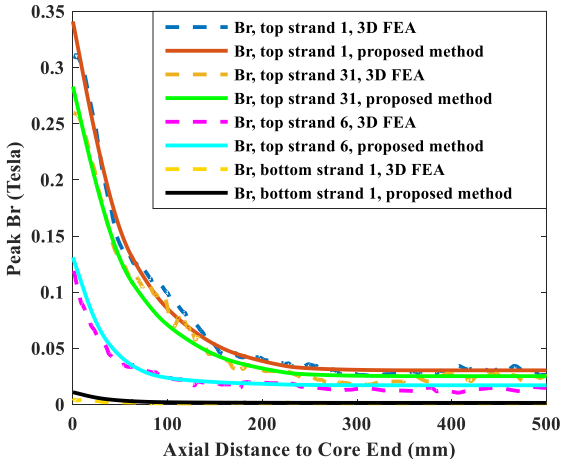

(a)

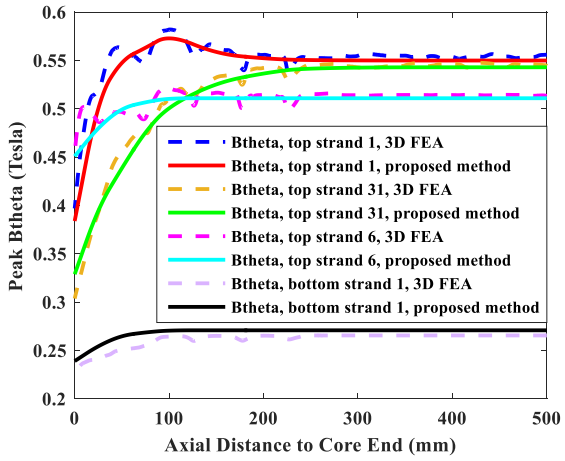

(b)

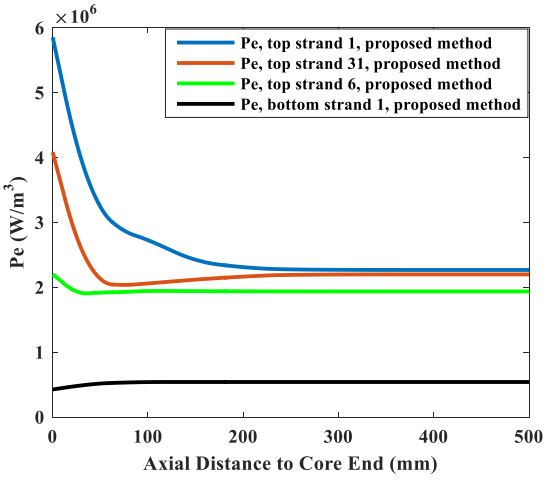

(c)

Figure 7.25 Axial distribution of (a) B_r; (b) B_θ; (c) P_e at rated condition in the stepped-stator region.

In this section, two simulations based on the open-circuit condition with 110% terminal voltage and the rated condition with a 0.85 lagging power factor are performed. Here M_1=30 and M_2=20. The axial distributions of the peak B_r and P_e of 3 strands at the open-circuit condition are presented in Figure 7.24. The radial flux and eddy current densities increase axially in the end region due to the larger stator inner radius and the exposure of the stator coils to the airgap flux. The B_r declines as the flux penetrates radially into a slot. The peripheral flux is very weak in the open-circuit condition because of the absence of stator currents. The axial distributions of the peak B_r, B_θ and eddy current loss density of 4 strands at the rated condition are shown in Figure 7.25. In the simulation, the slot is assumed to be at the center of a phase belt. The B_r increases in the stepped-stator region, while the value of B_θ drops when approaching the core end. The differences between the values of B_r and B_θ in the top-layer strands 1 and 31 are caused by that the slot leakge flux reinforces the airgap flux on one side of the slot but they counter each other in the other half slot. The B_θ rises almost linearly from the slot bottom to its peak value at the slot opening. Good agreement is achieved between the results of the 3D FEAs and the proposed method, as demonstrated in Figure 7.24 and Figure 7.25. Since the quasi-3D simulation in section 7.1 and the analytical methods in sections 7.4.1 and 7.4.2 are based on 2D coordinates, the computational complexity is significantly reduced compared to 3D FEAs. It only takes a few minutes or even less than a minute to perform a simulation with the proposed fast method, while the execution time of 3D FEAs can be many hours or even days.

7.5 Chapter Summary

This chapter presents a fast-solving quasi-3D FD based method to predict the magnetic field and loss distributions in the end region of large generators. Regional conformal mappings based on Schwarz-Christoffel transformation are adopted to model the cross-slot axial flux in end core teeth. The effects of nonlinear material properties and

near corner effects are incorporated in the formulation of SIBCs that estimate the losses in end metallic components. Finally, the eddy current distribution in the stator copper strands in the end stepped region is computed. The accuracy of the proposed fast-solving method is validated by the agreement between the results of the analytical method and full 3D FEAs.

CHAPTER 8. CONCLUSIONS, CONTRIBUTIONS AND RECOMMENDATIONS FOR FUTURE WORK

This chapter concludes this dissertation by first reviewing the objective of this research and proposed solution framework, summarizing the technical development and major contributions, and finally presenting the list of outcomes such as journal and conference papers related to this dissertation.

In addition, section 8.4 presents the recommended future research directions that can extend the scope of this dissertation.

8.1 Conclusions

The objective of the proposed research is to develop the accurate and efficient multi-physics models for SRMs and the end regions of LSGs, so as to further exploit fast and efficient methods for the design optimization that aim to improve their performances.

In Chapters 3 and 4, the generalized and fast-solving analytical EM and thermal models of SRMs are first developed and a multi-objective optimization method combining an ANN regression model and PSO algorithm is proposed based on the analytical models. The multi-physics model is validated by the experiment and FEA counterparts. Particularly for the proposed electromagnetic model of SRMs expressed in polar coordinates in Chapter 3, results show that the percentage differences between the performance values predicted by the analytical method and those generated by FEAs and experimental measurements are less than 5% at all rotor positions, operating points with different machine topologies; moreover, by applying the enhanced EM model in Cartesian coordinates incorporating the method of conformal mapping, the accuracy of the permeance prediction in the rotor-slot and stator-slot subregions can be significantly improved with a percentage error less than

10% for all permeance parameters. The results in Chapter 4 show that the proposed fast-solving multi-objective optimization framework can effectively improve the performances of an SRM design. It can generate the design Pareto front within about half an hour with the evaluation of over 60,000 design candidates.

A comprehensive multi-physics 3D-FEA-based model is introduced in Chapter 5 that predicts the magnetic field, loss and temperature distributions in the end region of large synchronous generators. This mathematical model is validated by the agreement between the calculated and measured temperatures, and the largest absolute and percentage differences between the measured and predicted values are 3.7 °C and 4.0% respectively. In Chapter 6, the 3D-FEA model is used to analyze the impacts of different operating and design parameters on the magnetic field and loss distributions in the stator end region. The key conclusions on the impacts of the operating conditions discussed in section 6.1 are: the loss in the press plate is lowest at 110% O/C condition, while in the loading conditions, the press plate loss increases as the power factor changes from lagging to leading, and the loss at 100% S/C is between the 0.85 lagging pf and unity pf conditions; the eddy current loss in the finger plates is mainly determined by the tangential flux, and the total loss of finger plates is smallest at 110% O/C condition, while the loss distributions in the finger plates in the other four operating conditions are similar since the tangential flux excited by the adjacent stator windings are the same; the eddy current loss induced by axial flux has a major impact on the temperatures of end packets, and the axial flux is the combination of the end fringing flux and cross-slot flux, and its distribution in loading conditions exhibits asymmetric patterns; in loading conditions, the loss in the end packets is larger when the power factor is leading; the additional eddy current loss decays axially from core-end to stator main body. On the other hand, the critical conclusions on the influences of different end component structures on the loss distributions in the end region discussed in sections 6.2 and 6.3 include the following: changing the material of the press plate from magnetic

steel to nonmagnetic materials such as copper and aluminum can significantly reduce the eddy current loss in the press plate and outermost core packet; the eddy current loss is higher in the press plate with a smaller inner diameter due to a closer distance to the end armature windings, but it can also shield the stator core back-iron more effectively from the end leakage field thus resulting in a lower loss density in the end stator; the total loss in the finger plates can be reduced by decreasing the distance between the press plate and the outermost core packet; the losses in the press plate and end core can be reduced by applying a thin-layer metallic shield beyond the press plate; the stepped profile and slitting structure of the end teeth can effectively reduce the in-plane eddy current in the end packets; the loss in the press plate increases with a larger inclination angle of the end armature windings; the eddy current loss in the end core packets is positively correlated with the length of the rotor body.

Since it is time-consuming to perform the 3D FEA model for each candidate design of the end structures in a large generator, Chapter 7 proposes a quasi-3D-FD-based fast-solving model, which is an optimal solution to be adopted at the initial design stage and is verified by the agreement between its results and the outputs of the pre-validated full 3D FEA model.

8.2 Contributions

The main contributions of this dissertation are summarized as follows:

1) A comprehensive analytical framework is proposed to predict the electromagnetic behaviors of an SRM. The merits of the proposed method are inherent in three aspects. The first aspect is that it provides comprehensive discussions on the boundary conditions of magnetic potentials at arbitrary rotor positions, compared to the previous publications that are only suitable for the unaligned position [52], [215]. The method is further improved by applying conformal mappings to the rotor-slot and stator-slot regions to eliminate the errors

caused by the inaccurate representation of their geometries [53], [216], [217]. The second aspect is that it possesses the advantage of conventional MECs that can incorporate steel saturation, and the merit of Maxwell's equation-based methods that can adaptively model the field in the air region, so it simultaneously overcomes the two difficulties. The third aspect is that the simulation time of the analytical method is merely a few seconds, compared to 2~5 minutes for a 2D FEA and more than 5 minutes for a 3D FEA with the same time step. Generally, in the process of iterative and multi-objective design optimization, the performances of thousands of design candidates need to be evaluated when applying intelligent search algorithms to find an optimal design for a specific cost function. Applying the proposed method can significantly reduce the computational time by hours or even days in this process. The proposed method therefore provides a reliable foundation for the prediction of the performance of an SRM as well as accelerating the process of design optimization.

2) The method described in Chapter 4 implements the multi-objective optimization for SRMs, and it not only explicitly predicts the electromagnetic (EM) performances of an SRM candidate with arbitrary geometries and topology, but also rigorously incorporates the machine control and thermal effects in the design process. Furthermore, the optimization method includes a DoE method that identifies the relationship between the design variables and performance indices with artificial neural networks (ANNs) trained by the samples generated by maximin Latin hypercube designs (MLHDs) that are accurate, flexible and adaptive over the entire design space, and the vector-based multi-objective PSO to find the Pareto optimal solutions. The incorporated DoE method can greatly reduce the time of the optimization process compared to classical evolutionary stochastic algorithms, which involve the simulations for a huge number of SRM design candidates and are coupled with a time-consuming FEA solver [66].

3) A comprehensive 3-D numerical approach is proposed in Chapter 5 to predict the multi-physics fields of the end region of a large synchronous generator. Regarding the EM

analysis, compared to existing 3-D FEA methods, it builds an accurate geometric model of the end windings and metallic components, and incorporates the effects of the nonlinear and anisotropic material properties, in-plane eddy currents in stator laminations and core loss into calculation [173], [218], [219].

4) Based on the 3-D numerical model described in Chapter 5, Chapter 6 carries out a parametric study to analyze the impacts of operating conditions and different material properties and structures of end components on the magnetic field and loss distributions in the end region [173], [220]. This sets up a solid foundation for the design optimization of the end structure of large synchronous generators.

5) Considering the reality that it takes hours or even days to run a single 3-D FEA simulation to predict the field and loss distributions in the large generator end region, a quasi-3D finite-difference based approach is proposed to accelerate the calculation. In the proposed approach, regional conformal mappings are adopted to incorporate the impacts of the cross-slot flux caused by the local armature windings and slot/tooth geometry to eliminate the errors in traditional quasi-3D methods that are caused by the assumption of peripheral consistency of magnetic field and geometries [221]. Compared to the existing surface impedance boundary condition formulations, the effects of nonlinear material properties and a compensation method for the near corner effects are incorporated to improve the accuracy [164]. Furthermore, for the first time this dissertation introduces the phenomenon of the axial variation of magnetic field and loss caused by stepped stator geometries in the end stator windings, and end fringing effects, the peripheral variation of the airgap flux caused by slotting effect, and the proximity effects between copper strands are incorporated in the calculation of the strand eddy current distributions near the core end [222].

8.3 Outcomes of This Dissertation

The literature review and research work presented in this dissertation have resulted in a number of publications, listed as follows:

Journal papers:

[1] **S. Li**, S. Zhang, J. Dang, T. G. Habetler, and R. G. Harley, "Analytical calculation of the phase inductance profile of switched reluctance machines," *IEEE Trans. Energy Convers.*, accepted.

[2] **S. Li**, N. A. Gallandat, J. R. Mayor, T. G. Habetler, and R. G. Harley, "Calculating the electromagnetic field and losses in the end region of a large synchronous generator under different operating conditions with three-dimensional transient finite element analysis," *IEEE Trans. Ind. Appl.*, vol. 54, no. 4, pp. 3281-3293, Jul./Aug. 2018.

[3] **S. Li**, S. Zhang, C. Gong, T. G. Habetler, and R. G. Harley, "An enhanced analytical calculation of the phase inductance profile of switched reluctance machines," *IEEE Trans. Ind. Appl.*, accepted.

[4] **S. Li**, S. Zhang, T. G. Habetler, and R. G. Harley, "Modeling, design optimization and applications of switched reluctance machines – A review," *IEEE Trans. Ind. Appl.*, accepted.

[5] S. Zhang, **S. Li**, R. G. Harley, and T. G. Habetler, "Performance evaluation and comparison of multi-objective optimization algorithms for the analytical design of switched reluctance machines," *CES Trans. Elec. Mach. Syst.*, vol. 1, no. 1, pp. 58-65, Mar. 2017.

[6] C. Gong, **S. Li**, T. G. Habetler, J. A. Restrepo, and B. Soderholm, "Direct position control for ultra-high speed switched reluctance machines based on low-cost non-intrusive reflective sensors," *IEEE Trans. Ind. Appl.*, accepted.

Conference papers:

[1] **S. Li**, S. Zhang, J. Dang, T. G. Habetler, and R. G. Harley, "Calculating the unsaturated inductance of 4/2 switched reluctance motors at arbitrary rotor positions based on partial differential equations of magnetic potentials," in *Proc. North American Power Symposium (NAPS)*, Charlotte, NC, 2015, pp. 1-8.

[2] **S. Li**, S. Zhang, C. Jiang, J. R. Mayor, T. G. Habetler, and R. G. Harley, "A fast control-integrated and multiphysics-based multi-objective design optimization of switched reluctance machines," in *Proc. IEEE Energy Convers. Congr. & Expo. (ECCE)*, Cincinnati, OH, Oct. 1-5, 2017, pp. 730-737.

[3] **S. Li**, C. Gong, N. A. Gallandat, J. R. Mayor, and R. G. Harley, "Analyzing the impact of press plate structure on the flux and loss distributions in the end region of large generators by transient 3-dimensional finite-element method with an improved core loss model," in *Proc. IEEE Int. Elec. Mach. Drives Conf. (IEMDC)*, Miami, FL, May 21-24, 2017.

[4] **S. Li**, C. Gong, N. A. Gallandat, J. R. Mayor, and R. G. Harley, "Implementation of surface impedance boundary conditions in the quasi three-dimensional finite-difference simulations of generator end regions," in *Proc. IEEE Int. Elec. Mach. Drives Conf. (IEMDC)*, Miami, FL, May 21-24, 2017.

[5] **S. Li**, S. Zhang, T. G. Habetler, and R. G. Harley, "A survey of electromagnetic – thermal modeling and design optimization of switched reluctance machines," in *Proc. IEEE Int. Elec. Mach. Drives Conf. (IEMDC)*, Miami, FL, May 21-24, 2017.

[6] S. Zhang, **S. Li**, R. G. Harley, and T. G. Habetler, "A multi-objective analytical design approach of switched reluctance machines with integrated active current profile

optimization," in *Proc. IEEE Int. Elec. Mach. Drives Conf. (IEMDC)*, Miami, FL, May 21-24, 2017.

[7] **S. Li**, S. Zhang, T. G. Habetler, and R. G. Harley, "Fast and accurate analytical calculation of the unsaturated phase inductance profile of 6/4 switched reluctance machines," in *Proc. IEEE Energy Convers. Congr. & Expo. (ECCE)*, Milwaukee, WI, Sept. 18-22, 2016.

[8] **S. Li**, N. A. Gallandat, J. R. Mayor, and R. G. Harley, "Calculating the electromagnetic field and losses in the end region of large synchronous generators under different operating conditions with three-dimensional transient finite element analysis," in *Proc. IEEE Energy Convers. Congr. & Expo. (ECCE)*, Milwaukee, WI, Sept. 18-22, 2016.

[9] S. Zhang, **S. Li**, J. Dang, R. G. Harley, and T. G. Habetler, "Multi-objective design and optimization of generalized switched reluctance machines with particle swarm intelligence," in *Proc. IEEE Energy Convers. Congr. & Expo. (ECCE)*, Milwaukee, WI, Sept. 18-22, 2016.

[10] **S. Li**, C. Gong, L. Du, J. R. Mayor, R. G. Harley, and T. G. Habetler, "Fast calculation of the magnetic field and loss distributions in the stator core end packets and finger plates of large synchronous generators," in *IEEE Energy Convers. Congr. & Expo. (ECCE)*, Portland, OR, Sept. 23-27, 2018.

[11] **S. Li**, C. Gong, L. Du, J. R. Mayor, R. G. Harley, and T. G. Habetler, "Parametric study for the design of the end region of large synchronous generators based on three-dimensional transient finite element analysis," in *IEEE Energy Convers. Congr. & Expo. (ECCE)*, Portland, OR, Sept. 23-27, 2018.

[12] **S. Li**, C. Gong, J. R. Mayor, R. G. Harley, and T. G. Habetler, "Efficient calculation of the strand eddy current loss distributions in the end stepped-stator region of large

synchronous generators," in *IEEE Energy Convers. Congr. & Expo. (ECCE)*, Portland, OR, Sept. 23-27, 2018.

[13] S. Zhang, **S. Li**, R. G. Harley, and T. G. Habetler, "An efficient multi-objective Bayesian optimization approach for automated analytical design of switched reluctance machines," in *IEEE Energy Convers. Congr. & Expo. (ECCE)*, Portland, OR, Sept. 23-27, 2018.

[14] S. Zhang, **S. Li**, R. G. Harley, and T. G. Habetler, "Visualization and data mining of multi-objective electric machine optimizations with self-organizing maps: a case study on switched reluctance machines," in *IEEE Energy Convers. Congr. & Expo. (ECCE)*, Portland, OR, Sept. 23-27, 2018.

There are some other publications completed during the Ph.D. study that are indirectly related to, or not associated with this dissertation, as follows:

Journal papers:

[1] **S. Li**, S. Zhang, C. Jiang, L. He, R. G. Harley, and T. G. Habetler, "An enhanced active DC-flux-injection-based approach for thermal monitoring of induction machines with closed-loop control schemes," *IEEE Trans. Ind. Appl.,* (to be) submitted.

[2] E. Q. -Manriquez, E. N. Sanchez, R. G. Harley, **S. Li**, and R. A. Felix, "Neural inverse optimal control for induction motors via rapid control prototyping," *IEEE Trans. Power Electron*., accepted.

Conference papers:

[1] **S. Li**, S. Zhang, C. Jiang, L. He, and R. G. Harley, "An enhanced active DC-flux injection based approach for thermal monitoring of induction machines with direct torque

control schemes," in *Proc. IEEE Energy Convers. Congr. & Expo. (ECCE)*, Cincinnati, OH, Oct. 1-5, 2017, pp. 3537-3544.

[2] C. Jiang, **S. Li**, and T. G. Habetler, "A review of condition monitoring of induction motors based on stray flux," in *Proc. IEEE Energy Convers. Congr. & Expo. (ECCE)*, Cincinnati, OH, Oct. 1-5, 2017, pp. 5424-5430.

[3] S. Zhang, **S. Li**, L. He, J. A. Restrepo, and T. G. Habetler, "A high-frequency torque injection-based rotor thermal monitoring scheme for direct-torque-controlled interior permanent magnet synchronous machines," in *Proc. IEEE Energy Convers. Congr. & Expo. (ECCE)*, Cincinnati, OH, Oct. 1-5, 2017, pp. 3552-3558.

[4] S. Zhang, **S. Li**, L. He, J. A. Restrepo, and T. G. Habetler, "A high-frequency rotating flux injection based rotor thermal monitoring scheme for direct-torque-controlled interior permanent magnet synchronous machines," in *Proc. IEEE Int. Elec. Mach. Drives Conf. (IEMDC)*, Miami, FL, May 21-24, 2017.

[5] H. Shao, **S. Li**, and T. G. Habetler, "Calculating the unsaturated direct and quadrature axes magnetizing inductances of synchronous reluctance machines based on Maxwell's equations and magnetic equivalent circuit," in *Proc. North American Power Symposium (NAPS)*, Morgantown, WV, Sept. 17-19, 2017.

[6] E. Q. -Manriquez, E. N. Sanchez, R. G. Harley, **S. Li**, and R. A. Felix, "Neural sliding mode control for induction motors using rapid control prototyping," in *Proc. International Federation of Automatic Control (IFAC)*, Toulouse, France, Jul. 9-14, 2017.

[7] **S. Li**, Y. Deng, and R. G. Harley, "Staircase modulation of modular multilevel converters with minimal total harmonic distortion and maximal number of output voltage levels," in *Proc. IEEE Energy Convers. Congr. & Expo. (ECCE)*, Milwaukee, WI, Sept. 18-22, 2016.

[8] C. Gong, **S. Li**, and T. G. Habetler, "Analysis of the rotor robustness of ultra-high speed switched reluctance machines over 1 million rpm using cohesive zone model," in *IEEE Energy Convers. Congr. & Expo. (ECCE)*, Portland, OR, Sept. 23-27, 2018.

[9] H. Shao, **S. Li**, and T. G. Habetler, "Analytical calculation of the air-gap flux density and magnetizing inductance of synchronous reluctance machines," in *IEEE Energy Convers. Congr. & Expo. (ECCE)*, Portland, OR, Sept. 23-27, 2018.

[10] C. Gong, **S. Li**, and T. G. Habetler, "Rotor dynamic analysis of ultra-high speed switched reluctance machines over 1 million rpm," in *IEEE Energy Convers. Congr. & Expo. (ECCE)*, Portland, OR, Sept. 23-27, 2018.

There are some manuscripts in preparation to be submitted to referred journals.

8.4 Recommendations for Future Work

8.4.1 Enhancement of the Electromagnetic Model of SRMs

Chapter 3 has presented a comprehensive analytical framework to predict the EM performances of SRMs, but assumptions on the boundary conditions of magnetic potentials between adjacent stator-slot and rotor-slot sub-regions are made to derive the closed-form solutions of magnetic field in the air region. These assumptions may lead to errors in the calculation. It is recommended to adopt the subdomain method proposed in [214] for permanent magnet machines that can rigorously express these boundary conditions to eliminate the associated errors. The subdomain method is based on the theory that the magnetic potentials and the normal/tangential components of the magnetic field on the boundaries between two adjacent sub-regions are equal.

8.4.2 Enhancement of the Multi-Objective Optimization Algorithms for SRMs

Chapter 4 describes a multi-objective optimization approach for SRMs that combines the design of experiments (DoE) and evolutionary algorithms. These methods are time-consuming and computationally intensive, and cannot guarantee global optimal solutions. It is recommended to apply gradient based methods to the optimization model to accelerate calculation and achieve global optimality. On the other hand, it is recommended to introduce robust optimization methods to incorporate the effects of manufacturing defects or other uncertain factors on the results of the multi-objective optimization.

8.4.3 Improvement of the Fast-Solving Approach for the Large Generator End Region

There are several aspects related to the fast-solving quasi-3D based method in Chapter 7 for the end region of large generators that can be improved in future work:

1) The fast-solving electromagnetic model is recommended to be coupled with a corresponding fluid-dynamic/thermal model to further estimate the temperature distribution in the generator end region;
2) It is recommended to construct a regional 3-D model for the stator end teeth to accurately estimate the impinging axial flux and eddy current distributions inside a tooth where magnetic saturation is significant.
3) In the method to calculate the strand eddy current distributions related to proximity effects in stator end windings, it is recommended to include the circulating currents to improve the accuracy.

REFERENCES

[1] S. J. Salon, "Finite element analysis of electrical machines," *Kluwer Academic Publishers*, 1995.

[2] S. Li, S. Zhang, T. G. Habetler, and R. G. Harley, "A survey of electromagnetic – thermal modeling and design optimization of switched reluctance machines," in *Proc. Int. Elect. Mach. & Drives Conf. (IEMDC)*, Miami, FL, May. 21-24, 2015, pp. 1-7.

[3] A. G. Jack, J. W. Finch, and J. P. Wright, "Adaptive mesh generation applied to switched-reluctance motor design," *IEEE Trans. Ind. Appl.*, vol. 28, no. 2, pp. 370-375, Mar./Apr. 1992.

[4] K. Koibuchi, T. Ohno, and K. Sawa, "A basic study for optimal design of switched reluctance motor by finite element method," *IEEE Trans. Magn.*, vol. 33, no. 2, pp. 2077-2080, Mar. 1997.

[5] J. Dang, *et al*., "Practical considerations for the design and construction of a high-speed SRM with a flux-bridge rotor," *IEEE Trans. Ind. Appl*., vol. 51, no. 6, pp. 4515-4520, Nov./Dec. 2015.

[6] C. Lu, P. Zhou, D. Lin, Bo. He, and D. Sun, "Multiply connected 3-D transient problem with rigid motion associated with T-Ω formulation," *IEEE Trans. Magn.*, vol. 50, no. 2, Feb. 2014.

[7] D. Lin, P. Zhou, Q. M. Chen, N. Lambert, and Z. J. Cendes, "The effects of steel lamination core losses on 3D transient magnetic fields," *IEEE Trans. Magn.*, vol. 46, no. 8, pp. 3539-3542, Aug. 2010.

[8] W. Yao, J. -M. Jin, and P. T. Krein, "A highly efficient domain decomposition method applied to 3-D finite-element analysis of electromechanical and electric machine problems," *IEEE Trans. Energy Convers*., vol. 27, no. 4, pp. 1078-1086, Dec. 2012.

[9] P. Zhou, B. He, C. Lu, D. Lin, and N. Chen, "Transient simulation of electrical machines using time decomposition method," in *Proc. Int. Elect. Mach. & Drives Conf. (IEMDC)*, Miami, FL, May. 21-24, 2015, pp. 1-6.

[10] Y. Tang, and J. A. Kline, "Modeling and design optimization of switched reluctance machine by boundary element analysis and simulation," *IEEE Trans. Energy Convers*., vol. 11, no. 4, pp. 673-680, Dec. 1996.

[11] A. M. Omekanda, C. Broche, and M. Renglet, "Calculation of the electromagnetic parameters of a switched reluctance motor using an improved FEM-BIEM-application to different models for the torque calculation," *IEEE Trans. Ind. Appl*., vol. 33, no. 4, pp. 914-918, Jul./Aug. 1997.

[12] M. B. Fauchez, "Magnetic analysis of a switched reluctance motor using a boundary element – finite element coupling method," *IEEE Trans. Magn*., vol. 24, no. 1, pp. 475-478, Jan. 1988.

[13] T. C. O'Connell, and P. T. Krein, "A time-harmonic three-dimensional vector boundary element model for electromechanical devices," *IEEE Trans. Energy Convers*., vol. 25, no. 3, pp. 606-618, Sept. 2010.

[14] A. D. Brovont, "Exploring the boundary element method for optimization-based machine design," in *Proc. Int. Elect. Mach. & Drives Conf. (IEMDC)*, Miami, FL, May. 21-24, 2015, pp. 1-7.

[15] J. Song, C. -C. Lu, and W. C. Chew, "Multilevel fast multipole algorithm for electromagnetic scattering by large complex objects," *IEEE Trans. Antennas Propag*., vol. 45, no. 10, pp. 1488-1493, Oct. 1997.

[16] D. M. Araujo, J. -L. Coulomb, O. Chadebec, and L. Rondot, "A hybrid boundary element method-reluctance network method for open boundary 3-D nonlinear problems," *IEEE Trans. Magn*., vol. 50, no. 2, Feb. 2014.

[17] L. Shen, J. Wu, S. Yang, and X. Huang, "Fast flux linkage measurement for switched reluctance motors excluding rotor clamping devices and position sensors," IEEE Trans. Instrum. Meas., vol. 62, no. 1, pp. 185-191, Jan. 2013.

[18] S. Song, M. Zhang, and L. Ge, "A new decoupled analytical modeling method for switched reluctance machine," *IEEE Trans. Magn.*, vol. 51, no. 3, Mar. 2015.

[19] A. Khalil, and I. Husain, "A Fourier series generalized geometry-based analytical model of switched reluctance machines," *IEEE Trans. Ind. Appl*., vol. 43, no. 3, pp. 673-684, May/Jun. 2007.

[20] H. P. Chi, R. L. Lin, and J. F. Chen, "Simplified flux linkage model for switched reluctance motors," *IEE Proc. Electr. Power Appl.,* vol. 152, no. 3, pp. 577-583, Mar. 2005.

[21] W. Ding, and D. Ling, "A fast analytical model for an integrated switched reluctance starter/generator," *IEEE Trans. Energy Convers.,* vol. 25, no. 4, pp. 948-956, Dec. 2010.

[22] B. Fahimi, G. Suresh, J. Mahdavi, and M. Ehsami, "A new approach to model switched reluctance motor drive application to dynamic performance prediction, control, and design," in *Proc. 29th IEEE Annu. Power Electron. Spec. Conf.,* Fukuoka, Japan, May 1998, vol. 2, pp. 2097-2102.

[23] D. A. Torrey, X. -M. Niu, and E. J. Unkauf, "Analytical modelling of variable-reluctance machine magnetisation characteristics," *IEE Proc. Electric Power Appl*., vol. 142, no. 1, pp. 14-22, Jan. 1995.

[24] J. M. Stephenson, and J. Corda, "Computation of torque and current in doubly salient reluctance motors from nonlinear magnetization data," *Proc. Inst. Elect. Eng*., vol. 126, no. 5, May 1979.

[25] D. N. Essah, and S. D. Sudhoff, "An improved analytical model for the switched reluctance motor," *IEEE Trans. Energy Convers*., vol. 18, no. 3, pp. 349-356, Sept. 2003.

[26] X. -D. Xue, K. W. E. Cheng, and S. L. Ho, "A self-training numerical method to calculate the magnetic characteristics for switched reluctance motor drives," *IEEE Trans. Magn*., vol. 40, no. 2, pp. 734-737, Mar. 2004.

[27] S. Mir, I. Husain, and M. E. Elbuluk, "Switched reluctance motor modeling with on-line parameter identification," *IEEE Trans. Ind. Appl*., vol. 34, no. 4, pp. 776-783, Jul./Aug. 1998.

[28] D. A. Torrey, and J. H. Lang, "Modeling a nonlinear variable-reluctance motor drive," *Proc. Inst. Electr. Eng*., vol. 137, no. 5, pp. 314-326, Sept. 1990.

[29] B. Loop, D. N. Essah, and S. Sudhoff, "A basis function approach to the nonlinear average value modeling of switched reluctance machines," *IEEE Trans. Energy Convers*., vol. 21, no. 1, pp. 60-68, Mar. 2006.

[30] X. -D. Xue, K. W. E. Cheng, and S. L. Ho, "Simulation of switched reluctance motor drives using two-dimensional bicubic spline," *IEEE Trans. Energy Convers*., vol. 17, no. 4, pp. 471-477, Dec. 2002.

[31] D. W. J. Pulle, "New data base for switched reluctance drive simulation," *Proc. Inst. Electr. Eng. -B*, vol. 138, no. 6, pp. 331-337, Nov. 1991.

[32] S. U. Rehman, and D. G. Taylor, "Piecewise modeling and optimal commutation of switched reluctance motors," in *Proc. Int. Symp. Ind. Electron*., Athens, Greece, Jul. 1995, vol. 1, pp. 266-271.

[33] X. D. Xue, K. W. E. Cheng, and S. L. Ho, "A position stepping method for predicting performances of switched reluctance motor drives," *IEEE Trans. Energy Convers*., vol. 22, no. 4, pp. 839-847, Dec. 2007.

[34] S. Song, M. Zhang, and L. Ge, "A new fast method for obtaining flux-linkage characteristics of SRM," *IEEE Trans. Ind. Electron.*, vol. 62, no. 7, pp. 4105-4117, Jul. 2015.

[35] Z. Lin, D. S. Reay, B. W. Williams, and X. He, "Online modeling for switched reluctance motors using B-spline neural networks," *IEEE Trans. Ind. Electron.*, vol. 54, no. 6, pp. 3317-3322, Dec. 2007.

[36] L. A. Belfore, and A. A. Arkadan, "Modeling faulted switched reluctance motors using evolutionary neural networks," *IEEE Trans. Ind. Electron*., vol. 44, no. 2, pp. 226-233, Apr. 1997.

[37] S. Song, L. Ge, and M. Zhang, "Data-reconstruction-based modeling of SRM with few flux-linkage samples from torque-balanced measurement," *IEEE Trans. Energy Convers.*, vol. 31, no. 2, pp. 424-435, Jun. 2016.

[38] C. Lin, W. Wang, M. McDonough, and B. Fahimi, "An extended field reconstruction method for modeling of switched reluctance machines," *IEEE Trans. Magn.*, vol. 48, no. 2, pp. 1051-1054, Feb. 2012.

[39] W. Zhu, B. Fahimi, and S. Pekarek, "A field reconstruction method for optimal excitation of permanent magnet synchronous machines," *IEEE Trans. Energy Convers*., vol. 21, no. 2, pp. 305-313, Jun. 2006.

[40] D. Lin, P. Zhou, S. Stanton, and Z. J. Cendes, “An analytical circuit model of switched reluctance motors,” *IEEE Trans. Magn*., vol. 45, no. 12, pp. 5368-5375, Dec. 2009.

[41] J. M. Kokernak and D. A. Torrey, “Magnetic circuit model for the mutually coupled switched-reluctance machine,” *IEEE Trans. Magn*., vol. 36, no.2, pp. 500-507, Mar. 2000.

[42] R. Krishnan, “Switched reluctance motor drives, Modeling, Simulation, Analysis, Design, and Applications,” *CRC Press*, 2001.

[43] A. Michaelides, C. Pollock, and C. Jolliffe, “Analytical computation of minimum and maximum inductances in single and two phase switched reluctance motors,” *IEEE Trans. Magn.*, vol. 33, no. 2, pp. 2037-2040, Mar. 1997.

[44] H. Chen, C. Sun, and Q. Wang, “Analysis of flux-linkage characteristics of switched reluctance linear generator,” *IEEE Trans. Appl. Supercond*., vol. 24, no. 3, Jun. 2014.

[45] F. E. Fleming, and C. S. Edrington, “Real-time emulation of switched reluctance machines via magnetic equivalent circuits,” *IEEE Trans. Ind. Electron*., vol. 63, no. 6, pp. 3366-3376, Jun. 2016.

[46] N. K. Sheth, and K. R. Rajagopal, "Calculation of the flux-linkage characteristics of a switched reluctance motor by flux tube method," *IEEE Trans. Magn*., vol. 41, no. 10, pp. 4069-4071, Oct. 2005.

[47] A. Radun, “Analytically computing the flux linked by a switched reluctance motor phase when the stator and rotor poles overlap,” *IEEE Trans. Magn*., vol. 36, no. 4, pp. 1996-2003, Jul. 2000.

[48] M. Moallem, and G. E. Dawson, "An improved magnetic equivalent circuit method for predicting the characteristics of highly saturated electromagnetic devices," *IEEE Trans. Magn.*, vol. 34, no. 5, pp. 3632-3635, Sept. 1998.

[49] W. Uddin, and Y. Sozer, “Analytical modeling of mutually coupled switched reluctance machines under saturation based on design geometry,” *IEEE Trans. Ind. Appl.*, vol. 53, no. 5, pp. 4431-4440, Sept./Oct. 2017.

[50] Q. Yu, and D. Gerling, “Analytical modeling of a canned switched reluctance machine with multilayer structure,” *IEEE Trans. Magn.*, vol. 49, no. 9, pp. 5069-5082, Sept. 2013.

[51] S. -H. Mao, D. Dorrell, and M. -C. Tsai, “Fast analytical determination of aligned and unaligned flux linkage in switched reluctance motors based on a magnetic circuit model,” *IEEE Trans. Magn.*, vol. 45, no. 7, pp. 2935-2942, Ju. 2009.

[52] S. Li, S. Zhang, J. Dang, T. G. Habetler, and R. G. Harley, “Calculating the unsaturated inductance of 4/2 switched reluctance motors at arbitrary rotor positions based on partial differential equations of magnetic potentials,” in *Proc. North American Power Symposium (NAPS)*, Charlotte, NC, Oct. 4-6, 2015, pp. 1-8.

[53] S. Li, S. Zhang, T. G. Habetler, and R. G. Harley, “Fast and accurate analytical calculation of the unsaturated phase inductance profile of 6/4 switched reluctance machines,” in *Proc. IEEE Energy Convers. Congr. and Expo. (ECCE)*, Milwaukee, WI, Sept. 18-22, 2016.

[54] A. Radun, "Analytical calculation of the switched reluctance motor's unaligned inductance," *IEEE Trans. Magn.*, vol. 35, no. 6, pp. 4473-4481, Nov. 1999.

[55] E. Ilhan, M. F. J. Kremers, E. T. Motoasca, J. J. H. Paulides, and E. A. Lomonova, “Spatial discretization methods for air gap permeance calculations in double salient traction motors,” *IEEE Trans. Ind. Appl.*, vol. 48, no. 6, pp. 2165-2172, Nov./Dec. 2012.

[56] T. C. O’Connell, and P. T. Krein, “A Schwarz-Christoffel-based analytical method for electric machine field analysis,” *IEEE Trans. Energy Convers.*, vol. 24, no. 3, pp. 565-577, Sept. 2009.

[57] Z. Djelloul-Khedda, K. Boughrara, F. Dubas, and R. Ibtiouen, “Nonlinear analytical prediction of magnetic field and electromagnetic performances in switched reluctance machines,” *IEEE Trans. Magn.*, vol. 53, no. 7, Jul. 2017.

[58] M. F. Momen, and I. Husain, “Design and performance analysis of a switched reluctance motor for low duty cycle operation,” *IEEE Trans. Ind. Appl.*, vol. 41, no. 6, pp. 1612-1618, Nov./Dec. 2005.

[59] J. Faiz, B, Ganji, C. E. Carstensen, K. A. Kasper, and R. W. De Doncker, "Temperature rise analysis of switched reluctance motors due to electromagnetic losses," *IEEE Trans. Magn.*, vol. 45, no. 7, pp. 2927-2934, Jul. 2009.

[60] F. R. Jawad, I. Iranpur, and P. Pillay, "Thermal model for a switched reluctance motor of TEFC design during steady and transient operation," *Elect. Mach. Power Syst.*, vol. 26, no. 10, pp. 77-91, 1998.

[61] G. J. Li, J. Ojeda, E. Hoang, M. Lecrivain, and M. Gabsi, "Comparative studies between classical and mutually coupled switched reluctance motors using thermal-electromagnetic analysis for driving cycles," *IEEE Trans. Magn.*, vol. 47, no. 4, Apr. 2011.

[62] N. Arbab, W. Wang, C. Lin, J. Hearron, and B. Fahimi, "Thermal modeling and analysis of a double-stator swtiched reluctance motor," *IEEE Trans. Energy Convers.*, vol. 30, no. 3, pp. 1209-1217, Sept. 2015.

[63] S. Inamura, T. Sakai, and K. Sawa, "A temperature rise analysis of switched reluctance motor due to the core and copper loss by FEM," *IEEE Trans. Magn.*, vol. 39, no. 3, pp. 1554-1557, May 2003.

[64] K. N. Srinivas, and R. Arumugam, "Analysis and characterization of switched reluctance motors: Part II—Flow, thermal, and vibration analyses," *IEEE Trans. Magn.*, vol. 41, no. 4, pp. 1321-1332, Apr. 2005.

[65] C. M. Bednar, J. R. Mayor, and S. A. Semidey, "Parametric, self-segmenting steady state thermal estimation for switched reluctance machines," in *Proc. PMED 2014*, pp. 1-6, 2014.

[66] S. Li, S. Zhang, C. Jiang, J. R. Mayor, T. G. Habetler, and R. G. Harley, "A fast control-integrated and multiphysics-based multi-objective design optimization of switched reluctance machines," in *Proc. IEEE Energy Convers. Congr. and Expo. (ECCE)*, Cincinnati, OH, Oct. 1-5, 2017, pp. 730-737.

[67] W. Jiang, and T. M. Jahns, "Coupled electromagnetic-thermal analysis of electric machines including transient operation based on finite-element techniques," *IEEE Trans. Ind. Appl.*, vol. 51, no. 2, pp. 1880-1889, Mar./Apr. 2015.

[68] X. D. Xue, K. W. E. Cheng, and S. L. Ho, “Optimization and evaluation of torque-sharing functions for torque ripple minimization in switched reluctance motor drives,” *IEEE Trans. Power Electron*., vol. 24, no. 9, pp. 2076-2090, Sept. 2009.

[69] J. Ye, B. Bilgin, and A. Emadi, “An offline torque sharing function for torque ripple reduction in switched reluctance motor drives,” *IEEE Trans. Energy Convers*., vol. 30, no. 2, pp. 726-735, Jun. 2015.

[70] J. Ye, B. Bilgin, and A. Emadi, “An extended-speed low-ripple torque control of switched reluctance motor drives,” *IEEE Trans. Power Electron*., vol. 30, no. 3, pp. 1457-1470, Mar. 2015.

[71] K. Russa, I. Husain, and M. E. Elbuluk, “Torque-ripple minimization in switched reluctance machines over a wide speed range,” *IEEE Trans. Ind. Appl*., vol. 34, no. 5, pp. 1105-1112, Sept./Oct. 1998.

[72] D. G. Taylor, M. J. Woolley, and M. Illic-Spong, “Design and implementation of a linearizing and decoupling feedback transformation for switched reluctance motors,” in *Proc. 17th symp. Incremental Motion Control Systems and Devices*, Champaign, IL, Jun. 1988, pp. 173-184.

[73] M. Ilic’-Spong, R. Marino, S. Peresada, and D. Taylor, “Feedback linearizing control of switched reluctance motors,” *IEEE Trans. Automat. Contr*., vol. AC-32, pp. 371-379, May 1987.

[74] R. Mikail, I. Husain, Y. Sozer, M. S. Islam, and T. Sebastian, “Torque-ripple minimization of switched reluctance machines through current profiling,” *IEEE Trans. Ind. Appl.*, vol. 49, no. 3, pp. 1258-1267, May/Jun. 2013.

[75] I. Husain, and M. Ehsani, “Torque ripple minimization in switched reluctance motor drives by PWM current control,” *IEEE Trans. Power Electron.*, vol. 11, no. 1, pp. 83-88, Jan. 1996.

[76] N. T. Shaked, and R. Rabinovici, “New procedures for minimizing the torque ripple in switched reluctance motors by optimizing the phase-current profile,” *IEEE Trans. Magn.*, vol. 41, no. 3, pp. 1184-1192, Mar. 2005.

[77] J. M. Stephenson, A. Hughes, and R. Mann, "Torque ripple minimisation in a switched reluctance motor by optimum harmonic current injection," *IEE Proceedings - Electric Power Applications*, vol. 148, p. 322, 2001.

[78] S. K. Sahoo, S. Dasgupta, S. K. Panda, and X. Jian-Xin, "A Lyapunov function-based robust direct torque controller for a switched reluctance motor drive system," *IEEE Trans. Power Electron*., vol. 27, no.2, pp. 555-564, Feb. 2012.

[79] R. B. Inderka and R. W. A. A. De Doncker, "DITC-direct instantaneous torque control of switched reluctance drives," *IEEE Trans. Ind. Appl*., vol. 39, no. 4, pp. 1046-1051, Jul./Aug. 2003.

[80] K. Russa, I. Husain, and M. Elbuluk, "A self-tuning controller for switched reluctance motors," *IEEE Trans. Power Electron*., vol. 15, no. 3, pp. 545–552, May 2000.

[81] N. C. Sahoo, J. X. Xu, and S. K. Panda, "Low torque ripple control of switched reluctance motors using iterative learning," *IEEE Trans. Energy Convers*., vol. 16, no. 4, pp. 318-326, Dec. 2001.

[82] S. K. Sahoo, S. K. Panda, and J. X. Xu, "Iterative Learning-Based High-Performance Current Controller for Switched Reluctance Motors," *IEEE Trans. Energy Convers*., vol. 19, no. 3, pp. 491-498, Sept. 2004.

[83] D. S. Reay, T. C. Green, and B. W. Williams, "Neural networks used for torque ripple minimization from a switched reluctance motor," in *Proc. EPE'93*, vol. 6, 1993, pp. 1-6.

[84] Z. Lin, D. S. Reay, B. W. Williams, and X. He, "Torque Ripple Reduction in Switched Reluctance Motor Drives Using B-Spline Neural Networks," *IEEE Trans. Ind. Appl.*, vol. 42, no. 6, pp. 1445-1453, Nov./Dec. 2006.

[85] S. Mir, M. E. Elbuluk, and I. Husain, "Torque-ripple minimization in switched reluctance motors using adaptive fuzzy control," *IEEE Trans. Ind. Appl.*, vol. 35, no.2, pp. 461-468, Mar./Apr. 1999.

[86] J. W. Lee, H. S. Kim, B. I. Kwon, and B. T. Kim, "New Rotor Shape Design for Minimum Torque Ripple of SRM Using FEM," *IEEE Trans. Magn*., vol. 40, no. 2, pp. 754-757, Mar. 2004.

[87] Y. K. Choi, H. S. Yoon, and C. S. Koh, "Pole-Shape Optimization of a Switched-Reluctance Motor for Torque Ripple Reduction," *IEEE Trans. Magn*., vol. 43, no. 4, pp. 1797-1800, Apr. 2007.

[88] D. -H. Lee, T. H. Pham, and J.-W. Ahn, "Design and operation characteristics of four-two pole high-speed SRM for torque ripple reduction," *IEEE Trans. Ind. Electron.*, vol. 60, no. 9, pp. 3637-3643, Sept. 2013.

[89] C. Sahin, A. E. Amac, M. Karacor, and A. Emadi, "Reducing torque ripple of switched reluctance machines by relocation of rotor moulding clinches," *IET Electric Power Applications*, vol. 6, pp. 753-760, 2012.

[90] P. C. Desai, M. Krishnamurthy, N. Schofield, and A. Emadi, "Novel switched reluctance machine configuration with higher number of rotor poles than stator poles: concept to implementation," *IEEE Trans. Ind. Electron*., vol. 57, no.2, pp. 649-659, Feb. 2010.

[91] H. Sahraoui, H. Zeroug, and H. A. Toliyat, "Switched Reluctance Motor Design Using Neural-Network Method with Static Finite-Element Simulation," *IEEE Trans. Magn*., vol. 43, no. 12, pp. 4089-4095, Dec. 2007.

[92] M. N. Anwar, and I. Husain, "Radial force calculation and acoustic noise prediction in switched reluctance machines," *IEEE Trans. Ind. Appl*., vol. 36, no. 6, pp. 1589-1597, Nov./Dec. 2000.

[93] M. N. Anwar, I. Husain, and A. V. Radun, "A comprehensive design methodology for switched reluctance machines," *IEEE Trans. Ind. Appl*., vol. 37, no. 6, pp. 1684-1692, Nov./Dec. 2001.

[94] K. Kiyota, T. Kakishima, A. Chiba, and M. A. Rahman, "Cylindrical rotor design for acoustic noise and windage loss reduction in switched reluctance motor for HEV applications," *IEEE Trans. Ind. Appl.*, vol. 52, no. 1, pp. 154-162, Jan./Feb. 2016.

[95] S. M. Castano, B. Bilgin, E. Fairall, and A. Emadi, "Acoustic noise analysis of a high-speed high-power switched reluctance machine: frame effects," *IEEE Trans. Energy Convers.*, vol. 31, no. 1, pp. 69-77, Mar. 2016.

[96] C. Pollock, and C. -Y. Wu, "Acoustic noise cancellation techniques for switched reluctance drives," *IEEE Trans. Ind. Appl.*, vol. 33, no. 2, pp. 477-484, Mar./Apr. 1997.

[97] J. -W. Ahn, S. -G. Oh, J. -W. Moon, and Y. -M. Hwang, "A three-phase switched reluctance motor with two-phase excitation," *IEEE Trans. Ind. Appl.*, vo. 35, no. 5, pp. 1067-1075, Sept./Oct. 1999.

[98] N. Kurihara, J. Bayless, H. Sugimoto, and A. Chiba, “Noise reduction of switched reluctance motor with high number of poles by novel simplified current waveform at low speed and low torque region,” *IEEE Trans. Ind. Appl*., vol. 52, no. 4, pp. 3013-3021, Jul./Aug. 2016.

[99] J.-W. Ahn, S.-J. Park, and D.-H. Lee, “Hybrid excitation of SRM for reduction of vibration and acoustic noise,” *IEEE Trans. Ind. Electron.*, vol. 51, no. 2, pp. 374-380, Apr. 2004.

[100] S. J. Evangeline, and S. S. Kumar, “Torque ripple minimization of switched reluctance drives – a survey,” in *Proc. PEMD 2010*, pp. 1-6.

[101] C. Gan, J. Wu, Q. Sun, W. Kong, H. Li, and Y. Hu, “A review on machine topologies and control techniques for low-noise switched reluctance motors in electric vehicle applications,” *IEEE Access*, accepted.

[102] M. Hasegawa, N. Tanaka, A. Chiba, and T. Fukao, "The operation analysis and efficiency improvement of switched reluctance motors with high silicon steel," in *Proc. Power Conversion Conference, (PCC-Osaka 2002)*, vol. 3, pp. 981-986, 2002.

[103] H. Hayashi, K. Nakamura, A. Chiba, T. Fukao, K. Tungpimolrut, and D. G. Dorrell, "Efficiency improvements of switched reluctance motors with high-quality iron steel and enhanced conductor slot fill," *IEEE Trans. Energy Convers*., vol. 24, no. 4, pp. 819-825, Dec. 2009.

[104] Y. Takano, et al., "Torque density and efficiency improvements of a Switched Reluctance Motor without rare earth material for hybrid vehicles," in *Proc. Energy Conversion Congress and Exposition (ECCE-2010)*, pp. 2653-2659.

[105] A. Chiba, et al., "Torque Density and Efficiency Improvements of a Switched Reluctance Motor Without Rare-Earth Material for Hybrid Vehicles," *IEEE Trans. Ind. Appl.*, vol. 47, no. 3, pp. 1240-1246, May/ Jun. 2011.

[106] A. Michaelides and C. Pollock, "Design and performance of a high efficiency 5-phase switched reluctance motor," in *Proc. 7th Int. Conf. Electrical Machines and Drives*, 1995, pp. 266-270.

[107] S. Xueguan, P. Youngchul, L. Jian, and L. Joonho, "Optimization of Switched Reluctance Motor for Efficiency Improvement Using Response Surface Model and

Kriging Model," in *Computational Sciences and Optimization (CSO)*, 2011 Fourth International Joint Conference on, 2011, pp. 259-260.

[108] M. Sugiura, Y. Ishihara, H. Ishikawa, and H. Naitoh, "Improvement of efficiency by stepped-skewing rotor for switched reluctance motors," in *2014 International Power Electronics Conference (IPEC-Hiroshima 2014 - ECCE-ASIA)*, 2014, pp. 1135-1140.

[109] D. S. Reay, C. Shang, and B. W. Williams, "Efficiency improvements in switched reluctance motor position and torque control using adaptive fuzzy systems," in *Proc. 5th IEEE Int. Conf. Fuzzy Systems*, 1996, vol. 2, pp. 800-805.

[110] I. Kioskeridis and C. Mademlis, "Maximum efficiency in single-pulse controlled switched reluctance motor drives," *IEEE Trans. Energy Convers*., vol. 20, no. 4, pp. 809-817, Dec. 2005.

[111] J. Faiz and R. Fazai, "Optimal Excitation Angles of a High Speed Switched Reluctance Generator by Efficiency Maximization," in *Proc. Int. Power Electronics and Motion Control Conference (EPE-PEMC 2006)*, 2006, pp. 287-291.

[112] C. Sikder, I. Husain, and Y. Sozer, "Switched reluctance generator control for optimal power generatioin with current regulation," *IEEE Trans. Ind. Appl.*, vol. 50, no. 1, pp. 307-316, Jan./Feb. 2014.

[113] W. U. N. Fernando and M. Barnes, "Electromagnetic Energy Conversion Efficiency Enhancement of Switched Reluctance Motors with Zero-Voltage Loop Current Commutation," *IEEE Trans. Energy Convers.*, vol. 28, no. 3, pp. 482-492, Sept. 2013.

[114] L. G. B. Rolim, R. Hanitsch, E. H. Watanabe, and W. I. Suemitsu, "Development of a high-efficiency switched reluctance drive using soft-switching techniques," in *Proc. 6th Int. Conf. Power Electronics and Variable Speed Drives*, 1996, pp. 203-207.

[115] H. Keunsoo, L. Cheewoo, K. Jaehyuck, R. Krishnan, and O. Seok-Gyu, "Design and development of low-cost and high-efficiency variable-speed drive system with switched reluctance motor," *IEEE Trans. Ind. Appl.*, vol. 43, no.3, pp. 703-713, May/Jun. 2007.

[116] S. Woothipatanapan, A. Jangwanitlert, and P. Chancharoensook, "Efficiency improvement of converter for switched reluctance motor drives by mixed parallel operation of IGBT and MOSFET," in *Proc. TENCON 2010*, pp. 1841-1846.

[117] K. Kiyota and A. Chiba, "Design of switched reluctance motor competitive to 60-kW IPMSM in third-generation hybrid electric vehicle," *IEEE Trans. Ind. Appl.*, vol. 48, no. 6, pp. 2303-2309, Nov./Dec. 2012.

[118] R. T. Naayagi and V. Kamaraj, "A Comparative Study of Shape Optimization of SRM using Genetic Algorithm and Simulated Annealing," in *Proc. INDICON*, 2005, pp. 596-599.

[119] E. Afjei, A. Siadatan, and H. Torkaman, "Magnetic modeling, prototyping, and comparative study of a quintuple-set switched reluctance motor," *IEEE Trans. Magn.*, vol. 51, no. 8, pp. 1-7, Aug. 2015.

[120] N. Vattikuti, V. Rallabandi, and B. G. Fernandes, "A novel high torque and low weight segmented switched reluctance motor," in *Power Electronics Specialists Conference, 2008. PESC 2008. IEEE*, 2008, pp. 1223-1228.

[121] A. Labak and N. C. Kar, "A novel five-phase pancake shaped switched reluctance motor for hybrid electric vehicles," in *Vehicle Power and Propulsion Conference, 2009. VPPC '09. IEEE*, 2009, pp. 494-499.

[122] M. Moallem, O. Chee-Mun, and L. Unnewehr, "Effect of rotor profiles on the torque of a switched-reluctance motor," *IEEE Tran. Ind. Appl.*, vol. 28, no.2, pp. 364-369, Mar./Apr. 1992.

[123] T. Yifan, "Switched reluctance motor with fractionally pitched windings and bipolar currents," in *Proc. 33rd IAS Annual Meeting*, 1998, vol. 1, pp. 351-358.

[124] K. Tungpimolrut, et.al., "Torque improvement of three-phases full bridge converter based switched reluctance motor with DC assisted winding," in *Proc. Electrical Machines and Systems (ICEMS)*, Sapporo, Japan, Oct. 2012, pp. 1-5.

[125] Z. Xiaoshu, H. Yingjie, and J. Gu, "Optimization research of turn-on angle and turn-off angle based on switched reluctance starter/generator system," in *Electrical and Computer Engineering (CCECE), 2015 IEEE 28th Canadian Conference on*, 2015, pp. 864-869.

[126] R. Suryadevara and B. G. Fernandes, "Modified direct instantaneous torque control of switched reluctance motor with high torque per ampere and reduced source current ripple," in *Proc. Int. Power Electronics Conference (IPEC-Hiroshima 2014 - ECCE-ASIA)*, 2014, pp. 2433-2437.

[127] X. D. Xue, K. W. E. Cheng, T. W. Ng, and N. C. Cheung, "Multi-objective optimization design of in-wheel switched reluctance motors in electric vehicles," *IEEE Trans. Ind. Electron*., vol. 57, no. 9, pp. 2980-2987, Sept. 2010.

[128] A. M. Omekanda, "A new technique for multi-dimensional performance optimization of switched reluctance motors for vehicle propulsion," *IEEE Trans. Ind. Appl.*, vol. 39, no. 3, pp. 672-676, May/Jun. 2003.

[129] J.-H. Choi, S. Kim, J.-M. Shin, J. Lee and S.-T. Kim, "The multi-object optimization of switched reluctance motor," in *Proc. IEEE Int. Conf. EMECS*, 2004, vol. 4-B, no. 4, pp. 184-189.

[130] H. Cheng, H. Chen and Z. Yang, "Design indicators and structure optimisation of switched reluctance machine for electric vehicles," *IET Electr. Power Appl*., vol. 9, no. 4, pp. 319-331, Apr. 2015.

[131] J. W. Jiang, B. Bilgin, B. Howey, and A. Emadi, "Design optimization of switched reluctance machine using genetic algorithm," in *Proc. International Electric Machines & Drives Conference (IEMDC)*, Coeur d'Alene, ID, May 2015, pp. 1671-1677.

[132] S. Smaka, S. Konjicija, S. Masic and M. Cosovic, "Multi-Objective design optimization of 8/14 switched reluctance motor," in *Proc. IEEE Int. Elect. Mach. Drives Conf.*, pp. 468–475, May 2013.

[133] E. Öksüztepe, "In-wheel switched reluctance motor design for electric vehicles by using pareto based multi objective differential evolution algorithm," *IEEE Trans. Veh. Technol.*, Oct. 2016, in press.

[134] C. Ma and L. Qu, "Multiobjective optimization of switched reluctance motors based on design of experiments and particle swarm optimization," *IEEE Trans. Energy Convers.*, vol. 30, no. 3, pp. 1144-1153, Sept. 2015.

[135] Z. Ren, D. Zhang and C.-S. Koh, "Multi-objective worst-case scenario robust optimal design of switched reluctance motor incorporated with FEM and kriging," in

Proc. International Conference on Electrical Machines and Systems (ICEMS), Bushan, Oct. 2013, pp. 716-719.

[136] D. Ilea, M. M. Radulescu, F. Gillon, P. Brochet, "Multi-objective optimization of a switched reluctance motor for light electric traction applications," in *Proc. of 2010 IEEE Vehicle Power and Propulsion Conference (VPPC 2010)*, 2010, Lille, pp. 1-6.

[137] B. Mirzaeian, M. Moallem, V. Tahani, and C. Lucas, "Multiobjective optimization method based on a genetic algorithm for switched reluctance motor design," *IEEE Trans. Magn*., vol. 38, no. 3, pp. 1524-1527, May 2002.

[138] S. Zhang, S. Li, J. Dang, T. G. Habetler, and R. G. Harley, "Multi-objective design and optimization of generalized switched reluctance machines with particle swarm intelligence," in *Proc. IEEE Energy Conversion Congress and Exposition (ECCE)*, Milwaukee, WI, pp. 1-7, Sept. 2016.

[139] J. H. Pisch, Y. Li, P. C. Kjaer, J. J. Gribble, and T. J. E. Miller, " Pareto-Optimal firing angles for switched reluctance motor control," in *Proc. 2nd Int. Conf. Genetic Algorithms Eng. Syst.: Innov. Appl.*, 1997, pp. 90–96

[140] C. Ma, L. Qu, R. Mitra, P. Pramod, and R. Islam, "Vibration and torque ripple reduction of switched reluctance motors through current profile optimization," in *Proc. Applied Power Electronics Conference and Exposition (APEC)*, Long Beach, CA, Mar. 2016, pp. 3279-3285.

[141] M. M. Borujeni, A. Rashidi, and S. M. S. Nejad, "Optimal four quadrant speed control of switched reluctance motor with torque ripple reduction based on EM-MOPSO," in *Proc. Power Electronics, Drives Systems & Technologies Conference (PEDSTC)*, Tehran, Feb. 2015, pp. 310-315.

[142] M. M. Namazi, M. M. Borujeni, A. Rashidi, S. M. S. Nejad and J.-W Ahn, "Torque ripple reduction of switched reluctance motor drive with adaptive sliding mode control and particle swarm optimization," in *Proc. Int. Conf. Adv. Intell. Mechatron. (AIM)*, Busan, 2015, pp. 371-376.

[143] J. Tegopoulos and E. Kriezis, "Eddy current distribution in cylindrical shells of infinite length due to axial currents part I: shells of one boundary," *IEEE Trans. Power Apparatus and Systems*, pp. 1278-1286, 1971.

[144] J. Tegopoulos and E. Kriezis, "Eddy current distribution in cylindrical shells of infinite length due to axial currents part II: Shells of finite thickness," *IEEE Trans. Power Apparatus and Systems,* pp. 1287-1294, 1971.

[145] P. Hammond, "The calculation of the magnetic field of rotating machines. Part 1: The field of a tubular current," *Proc. IEE-Part C: Monographs,* vol. 106, pp. 158-164, 1959.

[146] D. Ashworth and P. Hammond, "The calculation of the magnetic field of rotating machines. Part 2: The field of turbo-generator end-windings," *Proc. IEE-Part A: Power Engineering,* vol. 108, pp. 527-538, 1961.

[147] P. Lawrenson, "The magnetic field of the end-windings of turbo-generators," *Proc. IEE-Part A: Power Engineering,* vol. 108, pp. 538-549, 1961.

[148] J. Tegopoulos, "Flux impinging on the end plate of turbine generators," *Power Apparatus and Systems, Part III. Transactions of the American Institute of Electrical Engineers,* vol. 81, pp. 700-706, 1962.

[149] J. Tegopoulos, "Current sheets equivalent to end-winding currents of turbine-generator stator and rotor," *Power Apparatus and Systems, Part III. Transactions of the American Institute of Electrical Engineers,* vol. 81, pp. 695-700, 1962.

[150] J. Tegopoulos, "Determination of the magnetic field in the end zone of turbine generators," *IEEE Trans. Power Apparatus and Systems,* vol. 82, pp. 562-572, 1963.

[151] J. A. Tegopoulos and R. H. Boyer, "Magnetic Vector Potential as a Result of Elementary Currents Between Two Parallel Planes," *IEEE Trans. Power Apparatus and Systems,* vol. 82, pp. 559-562, 1963.

[152] A. Reece and A. Pramanik, "Calculation of the end-region field of ac machines," *Proc. IEE,* 1965, pp. 1355-1368.

[153] R. Stoll and P. Hammond, "Calculation of the magnetic field of rotating machines. Part 4: Approximate determination of the field and the losses associated with eddy currents in conducting surfaces," *Proc. IEE,* 1965, pp. 2083-2094.

[154] R. Stoll and P. Hammond, "Calculation of the magnetic field of rotating machines. Part 5: Field in the end region of turbogenerators and the eddy-current loss in the end plates of stator cores," *Proc. IEE,* vol. 113, pp. 1793-1804, 1966.

[155] D. Ban, D. Zarko, and I. Mandic, "Turbogenerator end-winding leakage inductance calculation using a 3-D analytical approach based on the solution of Neumann integrals," *IEEE Trans. Energy Convers.,* vol. 20, pp. 98-105, 2005.

[156] C. Carpenter, "The application of the method of images to machine end-winding fields," *Proc. IEE-Part A: Power Engineering,* vol. 107, pp. 487-500, 1960.

[157] C. Carpenter, "Comparison of alternative formulations of 3-dimensional magnetic-field and eddy-current problems at power frequencies," *Proc. IEE,* 1977, pp. 1026-1034.

[158] J. R. Bowler, "Eddy current calculations using half‐space Green’s functions," *Journal of applied physics,* vol. 61, pp. 833-839, 1987.

[159] A. Schramm and D. Gerling, "Analytical calculation of the end winding leakage inductance based on the solution of Neumann integrals," in *Industrial Electronics, 2005. ISIE 2005. Proceedings of the IEEE International Symposium on*, 2005, pp. 851-855.

[160] M. Freese, "Analytic calculation of turbo generator end winding inductances using Neumann’s formula," in *Power Electronics Electrical Drives Automation and Motion (SPEEDAM), 2010 International Symposium on*, 2010, pp. 1597-1602.

[161] M. Freese, "Comparison between an analytic method and a numerical calculation to determine the end winding inductances of a turbo generator," in *Proc. International Conference on Electrical Machines (ICEM), Rom, Italy*, 2010.

[162] P. Hammond, "The calculation of the magnetic field of rotating machines. Part 3: Eddy currents induced in a solid slab by a circular current loop," *Proc. IEE-Part C: Monographs,* vol. 109, pp. 508-515, 1962.

[163] G. K. M. Khan, G. W. Buckley, R. B. Bennett, and N. Brooks, “An integrated approach for the calculation of losses and temperatures in the end-region of large turbine generators,” *IEEE Trans. Energy Convers.*, vol. 5, no. 1, pp. 183-194, Mar. 1990.

[164] S. Li, C. Gong, N. A. Gallandat, J. R. Mayor, and R. G. Harley, “Implementation of surface impedance boundary conditions in the quasi three-dimensional finite-difference simulations of generator end regions,” in *Proc. IEEE Int. Elect. Mach. Drives Conf. (IEMDC),* Miami, May 21-24, 2017.

[165] V. C. Silva, Y. Marechal, and A. Foggia, “Surface impedance method applied to the prediction of eddy currents in hydrogenerator stator end regions,” *IEEE Trans. Magn.*, vol. 31, no. 3, pp. 2072-2075, May 1995.

[166] R. Lin, A. Haavisto, and A. Arkkio, “Axial flux and eddy-current loss in active region of a large-sized squirrel-cage induction motor,” *IEEE Trans. Magn.*, vol. 46, no.11, pp. 3933-3938, Nov. 2010.

[167] Y. Liang, X. Bian, H. Yu, and C. Li, “Finite-element evaluation and eddy-current loss decrease in stator end metallic parts of a large double-canned induction motor,” *IEEE Trans. Ind. Electron*., vol. 62, no. 11, pp. 6779-6785, Nov. 2015.

[168] K. Yamazaki, *et al*., “Eddy current analysis considering lamination for stator core ends of turbine generators,” *IEEE Trans. Magn.*, vol. 44, no. 6, pp. 1502-1505, Jun. 2008.

[169] L. Wang, *et al*., “Influence of underexcitation operation on electromagnetic loss in the end metal parts and stator step packets of a turbogenerator," *IEEE Trans. Energy Convers.*, vol. 29, no. 3, pp. 748-757, Sept. 2014.

[170] Y. Yao, *et al.*, “3-D eddy current analysis in the end region of a turbogenerator by using reduced magnetic vector potential,” *IEEE Trans. Magn.*, vol. 42, no. 4, pp. 1323-1326, Apr. 2006.

[171] K. Ito, *et al*., “Simulation for design purposes of magnetic fields in turbine-driven generator end region,” *IEEE Trans. Power Apparatus and Systems*, vol. PAS-99, no. 4, pp. 1586-1596, Jul./Aug. 1980.

[172] P. J. Tavner, J. Penman, R. L. Stoll, and H. O. Lorch, “Influence of winding design on the axial flux in laminated-stator cores,” *Proc. IEE*, vol. 125, no. 10, pp. 948-956, Oct. 1978.

[173] S. Li, *et al.*, “Analyzing the impact of press plate structure on the flux and loss distributions in the end region of large generators by transient 3-dimensional finite-element method with improved core loss model,” in *Proc. IEMDC*, 2017.

[174] H. M. Hamalainen, J. Pyrhonen, J. Nerg, and J. Puranen, “3-D finite element method analysis of additional load losses in the end region of permanent-magnet generators,” *IEEE Trans. Magn.*, vol. 48, no. 8, pp. 2352-2357, Aug. 2012.

[175] B. Mecrow, A. Jack, and C. Cross, "Electromagnetic design of turbogenerator stator end regions," *Proc. IEE-C Generation, Transmission and Distribution*, 1989, pp. 361-372.

[176] F. Huo, J. Han, W. Li, X. Zhou, Y. Zhang, Y. Li, *et al.*, "Influence of Copper Shield Structure on 3-D Electromagnetic Field, Fluid and Temperature Fields in End Region of Large Turbogenerator," *IEEE Trans. Energy Convers.*, vol. 28, pp. 832-840, 2013.

[177] L. Wang, F. Huo, W. Li, Y. Zhang, Q. Li, Y. Li, *et al.*, "Influence of metal screen materials on 3-D electromagnetic field and eddy current loss in the end region of turbogenerator," *IEEE Trans. Magn.*, vol. 49, pp. 939-945, 2013.

[178] C. S. Helrich, "The classical theory of fields: electromagnetism," *Springer Science & Business Media*, 2012.

[179] M. Aubertin, T. Henneron, F. Piriou, P. Guerin, and J. –C. Mipo, “Periodic and anti-periodic boundary conditions with the Lagrange multipliers in the FEM,” *IEEE Trans. Magn.*, vol. 46, no. 8, pp. 3417-3420, Aug. 2010.

[180] D. Zarko, D. Ban, and T. A. Lipo, “Analytical calculation of magnetic field distribution in the slotted air gap of a surface permanent-magnet motor using complex relative air-gap permeance,” *IEEE Trans. Magn.*, vol. 42, no. 7, pp. 1828-1837, Jul. 2006.

[181] R. W. Scharstein, and D. S. Daniel, “Magnetostatic field of a conductor of semicircular cross section in a highly permeable half-space: exact analytic solution for infinite permeability with perturbative correction,” *IEEE Trans. Magn.*, vol. 38, no. 6, pp. 3594-3606, Nov. 2002.

[182] H. A. Wheeler, “Inductance formulas for circular and square coils,” *Proc. IEEE*, vol. 70, no. 12, pp. 1449-1450, Dec. 1982.

[183] J. Kim, and R. Krishnan, “High efficiency single-pulse controlled switched reluctance motor drive for high speed (48k rpm) application: analysis, design, and experimental verification,” in *Proc. IEEE IAS Annual meeting*, Edmonton, AB, Canada, Oct. 5-9, 2008, pp. 1-8.

[184] S. R. MacMinn, and W. D. Jones, "A very high speed switched-reluctance starter-generator for aircraft engine applications," in *Proc. NAECON*, Dayton, OH, May 22-26, 1989, vol. 4, pp. 1758-1764.

[185] P. Zhou, D. Lin, C. Lu, N. Chen, and M. Rosu, "A new algorithm to consider the effects of core losses on 3-D transient magnetic fields," *IEEE Trans. Magn.*, vol. 50, no. 2, Feb. 2014.

[186] X. Sun, Y. Shen, S. Wang, G. Lei, Z. Yang, and S. Han, "Core losses analysis of a novel 16/10 segmented rotor switched reluctance BSG motor for HEVs using nonlinear lumped parameter equivalent circuit model," *IEEE/ASME Trans. Mechatronics*, vol. 23, no. 2, pp. 747-757, Apr. 2018.

[187] J. Corda, and S. M. Jamil, "Experimental determination of equivalent-circuit parameters of a tubular switched reluctance machine with solid-steel magnetic core," *IEEE Trans. Ind. Electron*., vol. 57, no. 1, pp. 304-310, Jan. 2010.

[188] D. Lin, P. Zhou, W. N. Fu, Z. Badics, and Z. J. Cendes, "A dynamic core loss model for soft ferromagnetic and power ferrite materials in transient finite element *analysis*," *IEEE Trans. Magn.*, vol. 40, no. 2, pp. 1318-1321, Mar. 2004.

[189] J. -W. Ahn, S. -G. Oh, J. -W. Moon, and Y. -M. Hwang, "A three-phase switched reluctance motor with two-phase excitation," *IEEE Trans. Ind. Appl*., vol. 35, no. 5, pp. 1067-1075, Sept./Oct. 1999.

[190] J. Ye, B. Bilgin, and A. Emadi, "An extended-speed low-ripple torque control of switched reluctance motor drives," *IEEE Trans. Power Electron*., vol. 30, no. 3, pp. 1457-1470, Mar. 2015.

[191] L. He, Y. Li, and R. G. Harley, "Adaptive multi-mode power control of a direct-drive PM wind generation system in a microgrid," *IEEE J. Emerg. Sel. Topics Power Electron*., vol. 1, no. 4, pp. 217-225, Dec. 2013.

[192] L. He, Y. Li, and R. G. Harley, "Novel adaptive power control of a direct-drive PM generation system in a micro grid," in *Proc. IEEE PEMWA*, Denver, CO, Jul. 16-18, 2012, pp. 1-8.

[193] F. A. C. Viana, G. Venter, and V. Balabanov, "An algorithm for fast optimal Latin hypercube design of experiments," *Int. J. Numer. Meth. Eng.*, vol. 82, pp. 135-156, Apr. 2010.

[194] J. -W. Park, R. G. Harley, and G. K. Venayagamoorthy, “Adaptive-critic-based optimal neurocontrol for synchronous generators in a power system using MLP/RBF neural networks,” *IEEE Trans. Ind. Appl*., vol. 39, no. 5, pp. 1529-1540, Sept./Oct. 2003.

[195] J. Haldemann, “Transpositions in stator bars of large turbogenerators,” *IEEE Trans. Energy Convers*., vol. 19, no. 3, pp. 553-560, Sept. 2004.

[196] M. Fujita, Y. Kabata, T. Tokumasu, K. Nagakura, M. Kakiuchi, and S. Nagano, “Circulating currents in stator coils of large turbine generators and loss reduction,” *IEEE Trans. Ind. Appl*., vol. 45, no. 2, pp. 685-693, Mar./Apr. 2009.

[197] R. F. Dana, and Y. Chow, "Edge condition of the field and a.c. resistance of a rectangular strip conductor," *IEE Proc. H - Microwaves, Antennas and Propagation*, vol. 137, no. 2, pp. 133-140, 1990.

[198] L. He, J. R. Mayor, R. G. Harley, H. Liles, G. Zhang, and Y. Deng, “Multiphysics modeling of the dynamic response of a vacuum automatic circuit recloser,” IEEE Trans. Ind. Appl., vol. 50, no. 6, pp. 3697-3707, Nov./Dec. 2014.

[199] L. He, J. R. Mayor, R. G. Harley, H. Liles, G. Zhang, and Y. Deng, “Multi-physics modeling of the dynamic response of a circuit breaker recloser system,” in *Proc. IEMDC*, Chicago, IL, May 12-15, 2013, pp. 1001-1008.

[200] P. J. Lawerenson, “The magnetic field of the end-windings of turbo-generators,” *Proceedings of the IEE – Part A: Power Engineering*, vol. 107, no. 42, pp. 538-549, Dec. 1961.

[201] O. Laldin, S. D. Sudhoff and S. Pekarek, "Modified Carter's coefficient," *IEEE Trans. Energy Convers.*, vol. 30, no. 3, pp. 1133-1134, Sept. 2015.

[202] M. Yi, M. Ha, Z. Qian, A. Aydiner, and M. Swaminathan, “Skin-effect-incorporated transient simulation using the Laguerre-FDTD scheme,” *IEEE Trans. Microw. Theory Techn.*, vol. 61, no. 12, pp. 4029-4039, Dec. 2013.

[203] E. M. Deeley, “Surface impedance near edges and corners in three-dimensional media,” *IEEE Trans. Magn*., vol. 26, no. 2, pp. 712-714, Mar. 1990.

[204] J. Wang, J. D. Lavers, and P. Zhou, “Modified surface impedance boundary condition applied to eddy current problems,” *IEEE Trans. Magn.*, vol. 28, no. 2, pp. 1197-1200, Mar. 1992.

[205] L. He, S. Cheng, Y. Du, R. G. Harley, and T. G. Habetler, “A dc-flux-injection approach for thermal monitoring of induction machines with direct torque control,” in *Proc. ECCE*, Denver, CO, Sept. 15-19, 2013, pp. 2115-2122.

[206] L. He, S. Cheng, R. G. Harley, and T. G. Habetler, “A torque-injection-based approach for thermal monitoring of induction machines with direct torque control,” in *Proc. IEMDC*, Chicago, IL, May 12-15, 2013, pp. 93-99.

[207] L. He, S. Cheng, Y. Du, R. G. Harley, and T. G. Habetler, “Stator temperature estimation of direct-torque-controlled induction machines via active flux or torque injection,” IEEE Trans. Power Electron., vol. 30, no. 2, pp. 888-899, Dec. 2015.

[208] L. He, J. Restrepo, S. Cheng, R. G. Harley, and T. G. Habetler, “An improved DC-signal-injection method with active torque-ripple mitigation for thermal monitoring of field-oriented-controlled induction motors,” in Proc. ECCE, Montreal, QC, Sept. 20-24, 2015, pp. 4447-4454.

[209] X. Bian, and Y. Liang, "Circuit network model of stator transposition bar in large generators and calculation of circulating current," *IEEE Trans. Ind. Electron.*, vol. 62, no. 3, pp. 1392-1399, Mar. 2015.

[210] D. A. Gonzalez, and D. M. Saban, "Study of the copper losses in a high-speed permanent-magnet machine with form-wound windings," *IEEE Trans. Ind. Electron.*, vol. 61, no. 6, pp. 3038-3045, Jun. 2014.

[211] S. Iwasaki, *et al*., "Influence of PWM on the proximity loss in permanent-magnet brushless AC machines," *IEEE Trans. Ind. Appl.*, vol. 45, no. 4, pp. 1359-1367, Jul./Aug. 2009.

[212] A. S. Thomas, Z. Q. Zhu, and G. W. Jewell, "Proximity loss study in high speed flux-switching permanent magnet machine," *IEEE Trans. Magn.*, vol. 45, no. 10, pp. 4748-4751, Oct. 2009.

[213] Y. Amara, P. Reghem, and G. Barakat, "Analytical prediction of eddy-current loss in armature windings of permanent magnet brushless AC machines," *IEEE Trans. Magn.*, vol. 46, no. 8, pp. 3481-3484, Aug. 2010.

[214] L. J. Wu, Z. Q. Zhu, D. Staton, M. Popescu, and D. Hawkins, "Analytical model for predicting magnet loss of surface-mounted permanent magnet machines accounting for slotting effect and load," *IEEE Trans. Magn.*, vol. 48, no. 1, pp. 107-117, Jan. 2012.

[215] S. Li, S. Zhang, J. Dang, T. G. Habetler, and R. G. Harley, "Analytical calculation of the phase inductance profile of switched reluctance machines," *IEEE Trans. Energy Convers*., accepted.

[216] S. Li, S. Zhang, C. Gong, T. G. Habetler, and R. G. Harley, "An enhanced analytical calculation of the phase inductance profile of switched reluctance machines," *IEEE Trans. Ind. Appl*., accepted.

[217] S. Li, S. Zhang, T. G. Habetler, and R. G. Harley, "Modeling, design optimization and applications of switched reluctance machines – A review," *IEEE Trans. Ind. Appl*., accepted.

[218] S. Li, N. A. Gallandat, J. R. Mayor, T. G. Habetler, and R. G. Harley, "Calculating the electromagnetic field and losses in the end region of a large synchronous generator under different operating conditions with three-dimensional transient finite element analysis," *IEEE Trans. Ind. Appl.*, vol. 54, no. 4, pp. 3281-3293, Jul./Aug. 2018.

[219] S. Li, N. A. Gallandat, J. R. Mayor, and R. G. Harley, "Calculating the electromagnetic field and losses in the end region of large synchronous generators under different operating conditions with three-dimensional transient finite element analysis," in *Proc. IEEE Energy Convers. Congr. & Expo. (ECCE)*, Milwaukee, WI, Sept. 18-22, 2016.

[220] S. Li, C. Gong, L. Du, J. R. Mayor, R. G. Harley, and T. G. Habetler, "Parametric study for the design of the end region of large synchronous generators based on three-dimensional transient finite element analysis," in *IEEE Energy Convers. Congr. & Expo. (ECCE)*, Portland, OR, Sept. 23-27, 2018.

[221] S. Li, C. Gong, L. Du, J. R. Mayor, R. G. Harley, and T. G. Habetler, "Fast calculation of the magnetic field and loss distributions in the stator core end packets and finger plates of large synchronous generators," in *IEEE Energy Convers. Congr. & Expo. (ECCE)*, Portland, OR, Sept. 23-27, 2018.

[222] S. Li, C. Gong, J. R. Mayor, R. G. Harley, and T. G. Habetler, "Efficient calculation of the strand eddy current loss distributions in the end stepped-stator region of large

synchronous generators," in *IEEE Energy Convers. Congr. & Expo. (ECCE)*, Portland, OR, Sept. 23-27, 2018.

VITA

Sufei Li was born in Shiyan, China in 1988. He received the B.S. degree in electrical engineering from Shanghai Jiao Tong University, Shanghai, China, in 2011, and the dual M.S. degree in electrical and computer engineering from Shanghai Jiao Tong University and Georgia Institute of Technology, Atlanta, GA, USA, in 2014. He has been pursuing the Ph.D. degree at the School of Electrical and Computer Engineering, Georgia Institute of Technology since August 2014.

Sufei Li has been working on the design and control of electric machines in the electric power group at Georgia Institute of Technology. His research interests include the multi-physics modeling, design, control and condition monitoring of electric machines, computational intelligence applied to electric machines and power systems, and the control of power converters. He was a research and development intern at Siemens Inc., Charlotte NC in 2016, and in Ansys Inc., Canonsburg PA in 2017. Sufei Li is an IEEE student member since 2015, and served as the president of PES Student Branch Chapter at Georgia Tech in the year 2015 to 2016.